MODELING, DESIGN, AND ADJOINT SENSITIVITY

ANALYSIS OF NANO-PLASMONIC STRUCTURES

MODELING, DESIGN, AND ADJOINT SENSITIVITY

ANALYSIS OF NANO-PLASMONIC STRUCTURES

By

Osman S. Ahmed, M.Sc., B.Sc.

A Thesis

Submitted to the School of Graduate Studies

in Partial Fulfillment of the Requirements

for the Degree

Doctor of Philosophy

McMaster University

To Abdelrahman and Aisha

DOCTOR OF PHILOSOPHY (2013)   McMaster University
(Electrical and Computer Engineering)   Hamilton, Ontario

TITLE: **MODELING, DESIGN, AND ADJOINT SENSITIVITY ANALYSIS OF NANO-PLASMONIC STRUCTURES**

AUTHORS: Osman S. Ahmed
M.Sc.
Department of Engineering Physics
(Faculty of Engineering, Cairo University, Egypt)
B.Sc.
Department of Electronics and Electrical Communications Engineering
(Faculty of Engineering, Cairo University, Egypt)

SUPERVISORS: Mohamed H. Bakr
Professor, Department of Electrical and Computer Engineering
B.Sc., M.Sc. (Cairo University, Egypt)
Ph.D. (McMaster University, Canada)
P.Eng. (Province of Ontario)

Xun Li
Professor, Department of Electrical and Computer Engineering
B.Sc. (Shandong University, China)
M. Sc. (Wuhan Research Institute, China)
Ph. D. (Beijing Jiaotong University, China)
P.Eng (Province of Ontario)

Number of Pages: xviii, 250

ABSTRACT

We propose novel techniques for modeling, adjoint sensitivity analysis, and optimization of photonic and nano-plasmonic devices. The scope of our work is generalized to cover microwave, terahertz and optical regimes. It contains original approaches developed for different categories of materials including dispersive and plasmonic materials. Artificial metamaterials are also investigated and modeled. The modeling technique exploits the time-domain transmission line modeling (TD-TLM) technique. Generalized adjoint variable method (AVM) techniques are developed for sensitivity analysis of the modeled devices. Although TLM-based, they can be generalized to other time-domain modeling techniques like finite difference time-domain method (FDTD) and time-domain finite element method (FEM).

We propose to extend the application of TLM-based AVM to photonic devices. We develop memory efficient approaches that overcome the limitation of excessive memory requirement in TLM-based AVM. A memory reduction of 90% can be achieved without loss of accuracy and at a more efficient calculation procedure. The developed technique is applied to slot waveguide Bragg gratings and a challenging dielectric resonator antenna problem.

We also introduce a novel sensitivity analysis approach for materials with dispersive constitutive parameters. To our knowledge, this is the first wide-band AVM approach that takes into consideration the dependence of material properties on the frequency. The approach can be utilized for design optimization of innovative nano-

plasmonic structures. The design of engineered metamaterial is systematic and efficient. Beside working with engineered new designs, dispersive AVM can be utilized in bio-imaging applications. The sensitivity of the objective function with respect to dispersive material properties enables the exploitation of parameter and gradient based optimization for imaging in the terahertz and optical regimes. Material resonance interaction can be easily investigated by the provided sensitivity information.

In addition to the developed techniques for simulation-based optimization, several analytical optimization algorithms are proposed to foster the parameter extraction and design optimization in terahertz and optical regimes. In terahertz time-domain spectroscopy, we have developed an efficient parameter based approach that utilizes the pre-known information about the material. The algorithm allows for the estimation of the optical properties of sample materials of unknown thicknesses. The approach has been developed based on physical analytical dispersive models. It has been applied with the Debye, Lorentz, Cole-Cole, and Drude model.

Furthermore, we propose various algorithms for design optimization of coupled resonators. The proposed algorithms are utilized to transform a highly non-linear optimization problem into a linear one. They exploit an approximate transfer function of the coupled resonators that avoids negligible multiple reflections among them. The algorithms are successful for the optimization of very large-scale coupled microcavities (150 coupled ring resonators).

ACKNOWLEDGMENTS

It is not easy to acknowledge the invaluable support and dedication I received from my supervisor, Dr. Mohamed Bakr. His innovative, simple, and insightful ideas formed a base towards fruitful achievements during the course of my work. His supervision is a model that stimulates excellence. Dr. Bakr makes every effort to maintain a perfect academic environment for me and for every graduate student in the group.

I am also grateful to my co-supervisor, Dr. Xun Li, for his advice, scientific contribution, and encouragement during the research development. I also would like to thank Dr. Natalia Nikolova and Dr. Matiar Howlader, members of my supervisory committee, for their useful discussion and interesting ideas.

I also wish to thank Dr. Mohamed Swillam, a former postdoctoral fellow at McMaster University, for the fruitful collaboration. His insight and advices elevated the quality of the conducted research.

I would like also to thank the administrative team at the Department of Electrical and Computer Engineering, McMaster University. I wish to express my appreciation to Cheryl Gies for her constant support.

Special thanks to my colleagues at McMaster University, Reza Amineh, Li Liu, Yu Zhang, Yifan Zhang, Ali Khalatpour, Sadegh Dadash, Kaveh Moussakhani, Mohamed Elsherif, and Mohamed Negm. I really enjoyed being part of you.

I would like to dedicate this thesis to my mother, Reda Shamseldin, who taught me the value of hard work. She dedicated her lifetime to ensure that I acquire the best education. I am indebted to my beloved father who did his best to support me and made my life easy and comfortable. All the love goes to my sister, Fatima, and my brothers who saved no effort to support me pursuing academic excellence. Special thanks to my sister in law, Aml Ibrahim, for her constant encouragement.

Last but not least, I thank my wife, Arwa Ibrahim, for standing beside me. Her perseverance is inspiring and her dedication is motivating. I am indebted to her for my entire success. I would like also to thank my son, Abdelrahman, for his remarkable understanding and patience. Aisha and Abdelrahman, my special children, I love you.

CONTENTS

LIST OF FIGURES

xiii

1 INTRODUCTION

Nano-scale light manipulation has stimulated the emergence of various promising multidisciplinary fields of sciences and the growth of new technologies [1]-[18]. Study of the applications of new materials has become of prime importance due to the extra-ordinary light matter interaction in the nano-scale range. Nano-photonics is proposed for the evolution of diverse applications in biology, chemistry, material science, etc. [4], [19], and [20]. It has wide applications for on-chip optical interconnects that mitigate challenges facing the current integration technology. Due to the high level of miniaturization, high density of device integration can be realized [1]-[4].

This thesis focuses on modeling nano-plasmonic structures that can guide, trap, and steer light to unprecedented limits [21]. The term plasmonics is utilized for the new emerging field describing light interaction with the noble metal surface electrons [22]. This interaction was utilized before in the history (4th century A. D.) by means of metallic nano-particles embedded in glass. For example, the Lycurgus glass cup (see Fig. 1.1) demonstrates the resonance light interaction with the tiny gold particles. The glass cup transmits red, while appearing green in response to the incident light from the outside [23]. The strong light interaction with the tiny particles was subject to a simple mathematical explanation by Gustav Mie's paper in 1908 [24].

Fig. 1.1. The Lycurgus glass cup; light interaction with miniaturized gold particles gives rise to resonance at the red light wavelength. © Trustees of the British Museum

Recently, nano-plasmonics has been proposed to bridge the gap between low-speed copper interconnects and bulky optical interconnects [3], [25]-[27]. The ability of light confinement to sub 100-nm has enabled plasmonics to serve as miniaturized fast optical interconnects for on-chip digital data transmission. Thus, the link capacity can be increased up to 1000 times the speed of the usual copper interconnects that suffer from loss, delay, and crosstalk.

Another important application of plasmonics is the lens effect [5]-[14]. Nano-plasmonic structures trap, steer, and guide light to the subwavelength scale. Numerous configurations have been proposed for focusing the light utilizing the resonant interference at subwavelength limit [12]. Some of these configurations are modeled and studied in this dissertation. The lens effect can be exploited in the complementary metal-oxide semiconductor (CMOS) image sensor [13]. It has a wide application in optical microscopy as well.

The size, material, and geometrical properties of the plasmonic structures are key elements in the respective application. In nano-plasmonics, light can be guided to subwavelength scale at a metal dielectric interface [8]. Basic plasmonic waveguide configurations include metal-dielectric-metal (MDM), dielectric-metal-dielectric (DMD), and most recently the hybrid configuration. While MDMs provide a larger light modal localization, inherent metal losses limit the light propagation length. DMD configurations are proposed for long-range applications; most importantly, for bio-sensing applications. The hybrid configuration provides large localization with minimal propagation losses.

In this thesis, we provide novel techniques for modeling, sensitivity analysis, and optimization of a variety of nano-photonic devices including nano-plasmonics. We consider wide range of materials including artificial materials (metamaterials).

1.1 MOTIVATION

Photonics and nano-plasmonics have witnessed a drastic increase in device complexity, along with the availability of a wide variety of materials. Analytical solutions of such structures are not available. As a result, full vectorial time-domain modeling is necessary [9]. Among the promising time-domain modeling techniques, transmission line modeling (TLM) is proposed as a physics-based, stable, and accurate technique for multi-physics simulation. Modeling of nano-plasmonic structures using TLM provides a circuit model that is exploited for modeling optical electronic junctions. It enables efficient simulation of on-chip optical interconnects. The accuracy is consistent with other

numerical time-domain modeling techniques, such as the finite difference time-domain (FDTD) method.

Computer aided design (CAD) tools are usually exploited to avoid the repetition of expensive fabrication and measurement cycles. CAD tools provide prediction for the achievable response and means for fine-tuning the proposed design. The full vectorial simulation is rich of information about the scattered field in the entire computational domain. Experience with computational electromagnetics suggests exploiting the entire calculations, rather than the required response only, to estimate the effect of the design parameters. For design optimization and sensitivity analyses, gradient information is mandatory. Efficient gradient-based techniques are developed for design optimization and parameter extraction inverse problems. Efficient approaches are proposed to avoid calculation of extra simulations.

The adjoint variable method (AVM) is a well-established modality proposed for gradient calculations with minimal computational effort. It provides sensitivity of the objective function with respect to the design variables, using at most one extra simulation. This is far more efficient than the conventional finite difference approaches that scale linearly with the number of design parameters.

One of the main challenges for the AVM calculation is handling large structures. The calculation of the gradient information of a general time-domain objective function requires storing a large number of computational information at each time step. This storage increases with the increase in structure complexity and size. This forfeits the advantage of utilizing AVM due to the large memory overhead. Advanced computational

platforms may not be able to handle the memory requirements of the AVM problem. Two possible approaches can be utilized to overcome this limitation. One of them is through the development of AVM techniques for frequency-dependent objective functions. This eliminates the need to store extensive time-domain information. Another approach is through elegant computational approaches that eliminate the redundant calculations and the subsequent extra storage throughout the whole simulation. Utilizing the latter approach, gradients of a general time-domain objective functions are estimated with minimum memory overhead.

Adjoint sensitivity algorithms have been developed for numerous time and frequency-domain computational techniques. However, these approaches are limited to the non-dispersive materials. By extending the AVM technique to the dispersive media, various phenomena and applications are explored. For example, dispersive AVM can be utilized for bio-sensing, spectroscopy, and imaging applications, where the sample under study is inherently frequency dependent. For nano-plasmonic design optimization, the AVM algorithm is adapted to take into consideration the frequency dependence of the metal properties.

In addition to simulation-based modeling and sensitivity approaches, we develop efficient optimization algorithms that address wide spectrum of applications. These algorithms are exploited for time-domain terahertz spectroscopy and the design of very large scale coupled microcavities.

Terahertz technology has been proposed recently for imaging and spectroscopy techniques. The availability of sources and detectors at this range (0.3 THz to 3THz)

drives a large number of disciplines working towards imaging applications. The characteristics of terahertz wave, including high penetration and good resolution, compared to the infra-red and visible light regimes, made it a promising solution for concealed weapon detection (carried on person beneath clothing) [28], food inspection, etc. Terahertz time-domain signals are also utilized in the spectroscopy of different categories of materials. A material sample is illuminated with an ultra-short terahertz pulse to estimate the optical characteristics of the sample. The transmissivity can be measured to extract the material information. This is a typical inverse problem dealing with responses of unknown materials. However, the uncertainty in the sample thickness measurements limits the accuracy of the parameter extraction. Efficient physics-based approaches enable the extraction of the sample material properties and thickness simultaneously.

1.2 CONTRIBUTIONS

The author has contributed to the efficient modeling of nano-plasmonic devices using the transmission line modeling (TLM). A full 3D dispersive TLM in-house software is developed for photonic and nano-plasmonic structures [29], [30]. The software can model plasmonic material dispersion characteristics and other materials characterized by the Debye and Lorentz models. The solver has been exploited for modeling and studying plasmonic subwavelength focusing structures and metamaterials. A perfectly matched layer (PML) has been optimized to ensure the elimination of

spurious reflected waves. The software has been used in the optimization of different plasmonic devices [31].

We present a memory efficient approach for TLM-based adjoint techniques [32]-[35]. We achieve 90% reduction in the memory requirement of the AVM approach as compared to the original algorithms. The computational efficiency is improved as all redundant calculations are avoided. The technique is developed and applied to benchmark microwave structures and to optical structures. A spectral AVM approach, for the TLM technique, has also been implemented to increase the efficiency of the approach in the case of frequency-domain objective functions.

We have proposed an AVM theory for sensitivity calculations of structures involving dispersive materials [36]-[38]. The technique is based on the *Z*-domain formulation, which allows for AVM calculations for a general dispersion function. The developed approach has been applied for the sensitivity calculation with materials of the Debye, Drude, and Lorentz models. It has been applied to 2D and 3D structures for general time-domain objective functions, and for the special case of frequency-dependent objective functions. We have applied our approach to complex metamaterial plasmonic resonator antenna. The computational efficiency of our approach was demonstrated, and its accuracy was compared to central difference approaches.

In terahertz spectroscopy, we have proposed an efficient approach to the parameter estimation of a sample material of unknown thickness [39]-[41]. The uncertainty in the thickness measurements induces large error margin for the optical parameter estimation. To overcome this limitation, a physics-based parameter estimation technique was

developed based on the parameterization of the optical material frequency dependence. This reduces the number of unknown parameters, which enhances the convergence of the nonlinear optimization problem. The approach has been successfully applied to the terahertz characterization of doped semiconductors. The estimation of the plasmonic effect has been also demonstrated.

Our work is not limited to simulation-based techniques. We have also proposed two simple structured optimization methods for the design optimization of coupled microcavities [42]-[47]. They can be utilized for filter design with tens of coupled microcavities in few seconds. These techniques are based on adopting simplified transfer functions that transform the nonlinear optimization problem of the highly coupled parameters to a linear one with a global solution.

In the first technique, the microcavity coupling parameters are assumed to vary around known mean values. A perturbation-based approach is developed to formulate the design problem in terms of the perturbation parameters. The design problem is then cast as a linear least square design problem with a unique solution that can be obtained in few seconds for tens of design parameters. This can be contrasted with other approaches that converge to a local solution only.

Another efficient approach to filter design, using a large number of cascaded microcavities, is based on the linear phase filter (LPF) approximation. An approximate objective function is exploited to solve the design as a linear programming (LP) problem. This allows for a fast and efficient solution of large scale problems. In addition, no initial design is required. The LP solver can find a feasible starting point by solving an initial

feasibility problem. The computational time is less than one second for structures that contain up to 150 coupled microcavities.

The work in this thesis has resulted in a number of published articles in highly ranked peer reviewed journals in the field. It has been also presented widely to the photonics and nano-plasmonics community at the recognized international conferences. These publications are cited throughout the thesis and are listed in the Bibliography.

1.3 THESIS OUTLINE

The thesis intends to explain in full detail the developed techniques and approaches for the modeling, design, and sensitivity analysis of nano-plasmoic structures. However, some examples are included for audiences of general microwave background. Although the thesis is mainly focused on simulation-based techniques, analytical and convex optimization approaches are also demonstrated. The thesis is organized into two parts. Part 1 includes Chapters 2-4, which cover the simulation-based modeling and sensitivity analysis approaches and their applications. Part 2 includes Chapters 5 and 6, which cover the analytical optimization approaches.

In Chapter 2, the theory of transmission line modeling of nano-plasmonic devices is introduced. The application of the modeling technique to challenging nano-plasmonic structures is also included. Chapter 3 is dedicated to explain the memory efficient AVM approach to transmission line modeling. This technique is applied to several microwave and photonic structures. In Chapter 4, the theory of the AVM for dispersive materials is explained, exploiting the transmission line approach.

Chapter 5 is dedicated to terahertz time-domain spectroscopy approaches. An efficient optimization approach is developed and the results demonstrate its validity and accuracy.

In Chapter 6, the convex formulations of the coupled resonator optical structures are presented. These formulations allow for the efficient design of a large number of coupled resonators. The responses are optimized to achieve optical filters of enhanced performance. Finally, the work is concluded in Chapter 7.

1.4 REFERENCES

[1]   W. L. Barnes, A. Dereux, and T. W. Ebbesen, "Surface Plasmon subwavelength optics," *Nature*, vol. 424, pp. 824-830, 2003.

[2]   S. I. Bozhevolnyi, V. S. Volkov, E. Devaux, and T. W. Ebbesen, "Channel Plasmon-Polariton guiding by subwavelength metal grooves," *Phys. Rev. Lett*., vol. 95, p. 046802, 2005.

[3]   E. Ozbay, "Plasmonics: Merging photonics and electronics at nanoscale dimensions," *Science*, vol. 311, pp. 189-193, 2006.

[4]   C. Genet and T. W. Ebbesen, "Light in tiny holes," *Nature*, vol. 445, pp. 39-46, 2007.

[5]   F. J. Garcia-Vidal, L. Martin-Moreno, H. J. Lezec, and T. W. Ebbesen, "Focusing light with a single subwavelength aperture flanked by surface corrugations," *Appl. Phys. Lett*. vol. 83, pp.4500-4502, 2003.

[6]   B. Guo, Q. Gan, G. Song, J. Gao, and L. Chen, "Numerical study of a high-resolution far-field scanning optical microscope via a surface plasmon modulated light source," *IEEE J. Lightwave Technol.*, vol. 25, pp. 830-833, 2007.

[7]   H. Shi, C. Du, and X. Luo, "Focal length modulation based on a metallic slit surrounded with grooves in curved depths," *Appl. Phys. Lett.*, vol. 91, p. 093111, 2007.

[8]   H. Atwater, "The promise of plasmonics," *Sci. Am*, vol. 296, pp. 56-63, 2007.

[9]   B. Lee, S. Kim, H. Kim, and Y. Lim, "The use of plasmonics in light beaming and focusing," *Prog. in Quantum Electronics*, vol. 34, pp. 47-87, 2010.

[10]   Z. Sun and H. K. Kim, "Refractive transmission of light and beam shaping with metallic nano-optic lenses," *Appl. Phys. Lett.*, vol. 85, pp. 642-644, 2004.

[11]   H. Shi, C. Wang, C. Du, X. Luo, X. Dong, and H. Gao, "Beam manipulating by metallic nano-slits with variant widths," *Opt. Express*, vol. 13, pp. 6815-6820, 2005.

[12]   L. Verslegers, P. B. Catrysse, Z. Yu, and S. Fan, "Planar metallic nanoscale slit lenses for angle compensation," *Appl. Phys. Lett*. vol. 95, p. 071112, 2009.

[13]   L. Verslegers, P. B. Catrysse, Z. Yu, J. S. White, E. S. Barnard, M. L. Brongersma, and S. Fan, "Planar lenses based on nanoscale slit arrays in a metallic film," *Nano Lett.*, vol. 9, pp. 235-238, 2009.

[14]   D. Choi, Y. Lim, S. Roh, I. Lee, J. Jung, and B. Lee, "Optical beam focusing with a metal slit array arranged along a semicircular surface and its optimization with a genetic algorithm," *Appl. Opt.*, vol. 49, pp. A30-A35, 2010.

[15]   J. Homola, S. S. Yee, and G. Gauglitz, "Surface plasmon resonance sensors: review," *Sens. Actuators B*, vol. 54, pp. 3-15, 1999.

[16]   R. D. Harris and J. S. Wilkinson, "Waveguide surface plasmon resonance sensors," *Sens. Actuators B*, vol. 29, pp. 261-267, 1995.

[17]   B. Luk'yanchuk, N. I. Zheludev, S. A. Maier, N. J. Halas, P. Nordlander, H.Giessen, and C. T. Chong, "The Fano resonance in plasmonic nanostructures and metamaterials," *Nature Mater*., vol. 9, pp. 707-715, 2010.

[18]   H. A. Atwater and A. Polman, "Plasmonics for improved photovoltaic devices," *Nature Mater*., vol. 9, pp. 205-213, 2010.

[19]   S. M. Williams, K. R. Rodriguez, S. Teeters-Kennedy, A. D. Stafford, S. R. Bishop, U. K. Lincoln, and J. V. Coe, "Use of the extraordinary infrared transmission of metallic subwavelength arrays to study the catalyzed reaction of methanol to formaldehyde on copper oxide," *J. Phys. Chem. B*, vol. 108, pp. 11833-11837, 2004.

[20]   T. W. Ebbersen, H. J. Lezec, H. F. Ghaemi, T. Thio, and P. A. Wolff, "Extraordinary optical transmission through sub-wavelength hole arrays," *Nature*, vol. 391, pp. 667-669, 1998.

[21]   S. A. Maier, *Plasmonics: Fundamentals and Applications*, Springer, 2007.

[22]   S. A. Maier, M. L. Brongersma, P.G. Kik, S. Meltzer, A. A. G. Requicha, and H. A. Atwater, "Plasmonics- a route to nanoscale optical devices," *Adv. Mater*., vol. 13, pp. 1501-1505, 2001.

[23]   S. A. Maier and H. A. Atwater, "Plasmonics: Localization and guiding of electromagnetic energy in metal/dielectric structures," *J. Appl. Phys.*, vol. 98, pp. 1-10, 2005.

[24]   G. Mie, "Beitrige zur Optik trüber Medien, speziell kolloidaler Metallösungen (Contributions to the optics of turbid media, especially colloidal metal suspensions)," *Ann. Phys.*, vol. 25, pp. 376-445, 1908.

[25]   M. J. Kobrinsky, B. A. Block, J.-F. Zheng, B. C. Barnett, E. Mohammed, M. Reshotko, F. Robertson, S. List, I. Young, K. Cadien, "On chip optical interconnects," *Intel Techno. J.*, vol. 8, pp. 129-142, 2004.

[26]   D. K. Gramotnev and S. I. Bozhevolnyi, "Plasmonics beyond the diffraction limit," *Nature Photon.*, vol. 4, pp. 83-91, 2010.

[27]   R. Zia, J. A. Schuller, A. Chandran, and M. L Brongersma, "Plasmonics: the next chip-scale technology," *Mater. Today*, vol. 9, pp. 20-27, 2006.

[28]   R. Appleby and H. B. Wallace, "Standoff detection of weapons and contraband in the 100 GHz to 1 THz region," *IEEE Trans. Antennas Propag.*, vol. 55, pp. 2944-2956, 2007.

[29]   O. S. Ahmed, M. A. Swillam, M. H. Bakr, and Xun Li, "Modeling and design of nano-plasmonic structures using transmission line modeling," *Opt. Express*, vol. 18, pp. 21784-21797, 2010.

[30]   O. S. Ahmed, M. A. Swillam, M. H. Bakr, and X. Li, "Transmission line modeling of nano-plasmonic devices," *Integrated Photonics Research, Silicon*

and Nanophotonics (IPRSN), OSA Technical Digest (CD): IMA3. 1-3, Toronto 2011.

[31] M. H. El Sherif, O. S. Ahmed, M. H. Bakr, "Derivative free optimization of nano-plasmonic structures," *The 31st Prog. In Electromag. Research Symposium* (PIERS), Kuala Lumpur, Malaysia 2012.

[32] O. S. Ahmed, M. H. Bakr, and X. Li, "A memory-efficient implementation of TLM-based adjoint sensitivity analysis," *IEEE Trans. Antennas Propag.*, vol. 60, pp. 2122-2125, 2012.

[33] O. S. Ahmed, M. H. Bakr, and X. Li, "Memory efficient adjoint sensitivity analysis exploiting 3D time-domain transmission line modeling," *2012 IEEE MTT-S International Microwave Symposium Digest*, Montreal 2012.

[34] O. S. Ahmed, M. H. Bakr, M. A. Swillam, and X. Li, "Efficient sensitivity analysis of photonic structures with transmission line modeling," in *Proc. SPIE*, vol. 8412, Photonics North 2012, 841213, Montreal 2012.

[35] O. S. Ahmed, M. H. Bakr, X. Li, "Efficient formulation for TLM-based adjoint sensitivity analysis," *The 28th Int. Review of Prog. in Applied Comput. Electromag.* (ACES), Columbus, Ohio 2012.

[36] O. S. Ahmed, M. H. Bakr, X. Li, and T. Nomura, "Adjoint variable method for two-dimensional plasmonic structures," *Opt. Lett.*, vol. 37, pp. 3453-3455, 2012.

[37] O. S. Ahmed, M. H. Bakr, X. Li, and T. Nomura, "A time-domain adjoint variable method for materials with dispersive constitutive parameters*," IEEE Trans. Microwave Theory Tech.*, vol. 60, pp. 2959-2971, 2012.

[38] O. S. Ahmed, M. H. Bakr, X. Li, and T. Nomura, "Wideband sensitivity analysis of plasmonic structures," in *Proc. SPIE*, vol. 8619, Photonics West 2013, Physics and Simulation of Optoelectronic Devices XXI, 86190R, San Francisco 2013.

[39] O. S. Ahmed, M. A. Swillam, M. H. Bakr, and X. Li, "Efficient optimization approach for accurate parameter extraction with terahertz time-domain spectroscopy," *IEEE J. of Lightwave Technol.*, vol. 28, pp. 1685–1692, 2010.

[40] O. S. Ahmed, M. A. Swillam, M. H. Bakr, and X. Li, "Accurate characterization of doped semiconductors with terahertz spectroscopy," in *Proc. SPIE*, vol. 8007, Photonics North 2011, 80071K, Ottawa 2011.

[41] O. S. Ahmed, M. A. Swillam, M. H., Bakr, and X. Li, "Efficient and accurate parameter extraction approach for terahertz time domain spectroscopy," in *Proc. SPIE*, vol. 7938, Photonics West 2011, Terahertz Technology and Applications IV, 793805, San Francisco 2011.

[42] O. S. Ahmed, M. A. Swillam, M. H. Bakr, and X. Li, "Efficient design optimization of ring resonator-based optical filters," *IEEE J. of Lightwave. Technol.*, vol. 29, pp. 2812-2817, 2011.

[43] M. A. Swillam, O. S. Ahmed, M. H., Bakr, and X. Li, "Filter design using multiple coupled microcavities," *IEEE Photon. Technol. Lett.*, vol. 23, pp. 1160-1162, 2011.

[44] M. A. Swillam, O. S. Ahmed, and M. H. Bakr, "Efficient design of coupled microcavities at optical frequencies," Micromachines, vol. 3, pp. 204-217, 2012.

[45] M. A. Swillam, O. S. Ahmed, M. H. Bakr, and X. Li, "Microcavity filter design using convex optimization methodology," *Integrated Photonics Research, Silicon and Nanophotonics* (IPRSN), OSA Technical Digest (CD): IWD4. 1-3, Toronto 2011.

[46] O. S. Ahmed, M. A. Swillam, M. H. Bakr, and X. Li, "A perturbation approach for the design of coupled resonator optical waveguides (CROWs)," in *Proc. SPIE*, vol. 8264, Photonics West 2012, Integrated Optics: Devices, Materials, and Technologies XVI, 82640H, San Francisco 2012.

[47] M. A. Swillam, O. S. Ahmed, M. H. Bakr, and X. Li, "Highly efficient design methodology for very large scale coupled microcavities," in *Proc. SPIE*, vol. 8412, Photonics North 2012, 841215, Montreal 2012.

2 TIME-DOMAIN TRANSMISSION LINE MODELING OF NANO-PLASMONIC STRUCTURES

Fast approaches to the modeling of electromagnetic wave propagation are achieved utilizing simplified analytical models [1]-[4]. In order to derive the analytical model, the physical problem has to be approximated by applying a set of assumptions. Similar iterative semi-analytical approaches are incorporated to remove some restrictions on the proposed test design [4]. Usually the analytical or semi-analytical models are of limited application for simple structures. Though many assumptions have to be included, we have to rely on the prediction of the response provided by this approximate analytical form, to test, design, and optimize the suggested device or structure. The design cycle can thus be fast and efficient. On the other hand, utilizing the ever-increasing computational power, one can simulate accurately these simple structures in a fraction of a second with no assumptions made. Moreover, computational techniques can simulate complex geometry and material combinations that have no analytical or semi-analytical solution.

The fabrication of nano-scale plasmonic devices is very time consuming [5]-[7]. It relies on resources that sometimes are not available at one design institute. The cost and time required to complete a single design is a challenge. Studying the effect of one parameter may require hundreds of different fabrication-measurement cycles. In order to

overcome these restrictions, numerical simulation has become a mandatory step in any design cycle [8], [9]. The design has to be first simulated utilizing the full vectorial Maxwell equations. The computational problem is discretized to ensure that the solver can handle the finest feature of the design. A complex three-dimensional design can be simulated typically in few hours. Tuning the design requires affordable computational cost. Using an efficient optimization approach, we can ensure optimal structure design before moving to the expensive fabrication cycles.

One of the main motivations for numerical simulation is the ability to model multi-physics problems. The design problem usually incorporates multiple physics phenomena that interact with each other. Simplified models aim to avoid these interactions by some mathematical manipulation. However, many interesting phenomena take place because of the presence of weak coupling between them. It is thus of prime importance to ensure accuracy of the modeling of the interaction between one physical phenomenon and another to avoid errors that would deteriorate the quality of the simulated system. A single platform is usually utilized – the transmission line method is an example – to avoid complex physics interfacing.

The transmission line method (TLM) provides a universal approach to model electromagnetic-based structures [10] and semiconductor based laser structures [11]. It has also been utilized to model circuit components [12], [13], micro-electro-mechanical systems (MEMS) [14], and electro-magnetic compatibility (EMC) problems [15]. The drift and diffusion processes have also been modeled with TLM [16]. Mechanical and heat systems are also modeled [17], [18]. Time-domain TLM is unconditionally stable

[19]-[21], which allows for any excitation, ranging from time-domain impulses to Gaussian-modulated sinusoids. The accuracy of the calculated results is still dependent on the temporal and spatial discretization parameters. However, the application of the TLM in photonics area has been so far limited to few basic structures using simple boundary conditions [22].

This chapter describes in detail the theory of the time-domain transmission line modeling technique. The algorithm is demonstrated for modeling dispersive materials. The challenge of having a perfect absorbing boundary condition is also addressed. The TLM technique is proven to be accurate through modeling challenging plasmonic structures.

2.1 TRANSMISSION LINE MODELING

In transmission line modeling, the electromagnetic problem is transformed into a circuit problem. A transmission line circuit replaces each cell in the computational domain. The modeling problem (calculation of fields at every point in space at every time instant) includes a solution of a network of transmission lines. The electric fields and magnetic fields are mapped to their corresponding voltages and currents, respectively. Constitutive parameters are modeled by local circuit parameters [20].

TLM is known to be a physics-based unconditionally stable technique [23], [24]. However, fine time and space discretization enables accurate modeling of the structure features and provides accurate wideband results. The calculation of the electric and magnetic fields is done in the same location within the computational cell and time

instant without any spatial or temporal shifts, which allows for highly accurate results of complex anisotropic material modeling. TLM as a time-domain technique avoids field divergence scenarios that are common for frequency domain solvers.

In the last two decades, TLM has witnessed drastic advances for modeling a variety of different complex materials [25]-[30]. Different cell configurations are proposed to enhance the accuracy and the efficiency of the technique. The symmetric condensed node (SCN) is utilized for the formulation of 3-D TLM [21]. It represents a natural extension from simpler 1-D and 2-D nodes. It can be demonstrated to consist of combinations of series and shunt nodes that are utilized for modeling 2-D problems. Among all possible circuital representations, we focus on the SCN node. The *Z*-domain formulation proposed by [28]-[30] is utilized. This simplifies and generalizes the modeling of complex dispersive and anisotropic materials. The use of extra stubs is avoided as it complicates the flow of the technique. However, equivalence between the required extra storage and the extra stubs can be shown.

2.1.1   Maxwell Equations and the Transmission Line Representation

Maxwell equations are utilized to calculate and predict the electromagnetic waves inside a medium. The solutions of these equations are accurate in the macroscopic domain where quantum mechanical effects are negligible, e.g., light quantization (photons) [31]. For time-domain numerical simulations, Maxwell equations are solved locally to predict both electric and magnetic fields (E, H), associated with the electromagnetic wave, at each node inside the computational domain, and at each time

instant throughout the numerical simulation. Maxwell equations in their differential form in an isotropic media are as follows [32]:

$$\nabla \times \boldsymbol{H} = \boldsymbol{J}_e + \sigma_e * \boldsymbol{E} + \frac{\partial}{\partial t}\left[\varepsilon_0 \boldsymbol{E} + \varepsilon_0 \chi_e * \boldsymbol{E}\right]$$
$$-\nabla \times \boldsymbol{E} = \boldsymbol{J}_m + \sigma_m * \boldsymbol{H} + \frac{\partial}{\partial t}\left[\mu_0 \boldsymbol{H} + \mu_0 \chi_m * \boldsymbol{H}\right]$$

(2.1)

where $\boldsymbol{J}_e$ and $\boldsymbol{J}_m$ are the impressed current and voltage densities, respectively. In (2.1), the material constitutive parameters are as follows: σ_e is the electric conductivity, σ_m is the magnetic resistivity, χ_e is the electrical susceptibility, and χ_m is the magnetic susceptibility. The symbol ($*$) represents a time-domain convolution operation. Equation (2.1) represents the full vectorial Maxwell equations with all field components included. For Cartesian coordinates, $\boldsymbol{E} = [E_x \quad E_y \quad E_z]$, $\boldsymbol{H} = [H_x \quad H_y \quad H_z]$, $\boldsymbol{J}_e = [J_{ex} \quad J_{ey} \quad J_{ez}]$, and $\boldsymbol{J}_m = [J_{mx} \quad J_{my} \quad J_{mz}]$.

Maxwell equations rarely have analytical solutions for problems of complicated geometry and material inhomogeneity. However, they provide the base for any full wave numerical solver, as they are locally valid at any spatial point in the domain at any time instant. Usually the electromagnetic (EM) structure is discretized spatially in all directions. For the Cartesian coordinates, the spatial steps are Δx, Δy, and Δz in the x, y, and z directions, respectively. For a uniform structured grid, $\Delta x = \Delta y = \Delta z = \Delta l$. The EM structure is solved at each time instant with zero initial conditions. The time sampling step is denoted as Δt. In general, spatial and temporal steps have to satisfy accuracy limits and synchronism constraints.
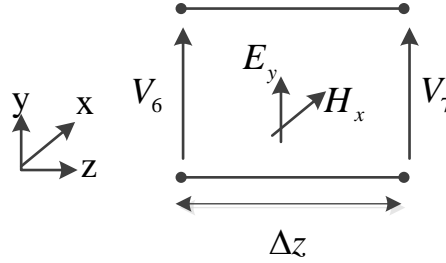
Fig. 2.1. The 1-D node configuration for wave propagation in z direction. Port numbers are chosen in accordance to the full 3D case [28].

The spatial discretization Δl is usually constrained by the finest feature of the photonic structure. Another limit for Δl in the case of bulk structures is defined by the smallest excitation wavelength λ_{min}. In this case, the maximum spatial discretization $\Delta l = \lambda_{min}/10$. On the other hand, the time sampling step Δt is usually determined as a function of the spatial steps for all the numerical techniques [9], [12], and [20]. In TLM, Δt is chosen throughout the whole domain to ensure one to one mapping between the circuit model and the electromagnetic model. This mapping is assumed at free space (vacuum). Synchronism of the signal propagation throughout an inhomogeneous media is ensured by means of extra storage as will be explained shortly.

For clear representation of the TLM theory, the one-dimensional model is utilized to demonstrate how the EM model can be mapped to the corresponding circuit model. For the one-dimensional propagation of a plane wave in the z direction (Cartesian coordinates), the electric and magnetic fields are invariant with the x and y directions. Transverse electromagnetic (TEM) wave polarization is supported (see Fig. 2.1). For the

y polarized wave (electric field E_y and magnetic field H_x), Maxwell equations (2.1) are

reduced to:

$$\frac{\partial E_y}{\partial z} = J_{mx} + \sigma_m * H_x + \mu_0 \frac{\partial H_x}{\partial t} + \mu_0 \frac{\partial}{\partial t}\left(\chi_m * H_x\right)$$

$$\frac{\partial H_x}{\partial z} = J_{ey} + \sigma_e * E_y + \varepsilon_0 \frac{\partial E_y}{\partial t} + \varepsilon_0 \frac{\partial}{\partial t}\left(\chi_e * E_y\right)$$

(2.2)

The mapping of the EM equations (2.2) to a circuit equations requires the normalization

rules [28]. The electric and magnetic fields are mapped and normalized as

$$E_y = -V_y / \Delta l \quad , \quad H_x = -I_x / \Delta l = -i_x / (\Delta l \eta_0)$$

(2.3)

where V_y is the potential parameter in volts, I_x is the current quantity in amperes, and i_x

is the normalized current in volts, where η_0 is the free space wave impedance. Similarly,

the current and voltage densities are mapped as [28]:

$$J_{ey} = -I_{ey} / \Delta l^2 = -i_{ey} / (\Delta l^2 \eta_0) \quad , \quad J_{mx} = -V_{mx} / \Delta l^2$$

(2.4)

where i_{ey} and V_{mx} have dimensions of volts.

By substituting (2.3) and (2.4) in (2.2), it is rewritten as:

$$\frac{\partial V_y}{\Delta l \partial z} = \frac{V_{mx}}{\Delta l^2} + \sigma_m * \frac{i_x}{\eta_0 \Delta l} + \mu_0 \frac{\partial i_x}{\eta_0 \Delta l \partial t} + \mu_0 \frac{\partial}{\eta_0 \Delta l \partial t}\left(\chi_m * i_x\right)$$

$$\frac{\partial i_x}{\eta_0 \Delta l \partial z} = \frac{i_{ey}}{\eta_0 \Delta l^2} + \sigma_e * \frac{V_y}{\Delta l} + \varepsilon_0 \frac{\partial V_y}{\Delta l \partial t} + \varepsilon_0 \frac{\partial}{\Delta l \partial t}\left(\chi_e * V_y\right)$$

(2.5)

Similar to the derivation in [28], we define the normalized spatial and time derivatives:

$$\frac{\partial}{\partial z} = \frac{1}{\Delta l} \frac{\partial}{\partial \bar{z}}, \quad \frac{\partial}{\partial t} = \frac{1}{\Delta t} \frac{\partial}{\partial \bar{t}}$$

(2.6)

From (2.5), the constitutive parameters can also be mapped and normalized to the corresponding circuit parameters as follows:

$$r_m = \frac{\sigma_m \Delta l}{\eta_0}, \quad g_e = \sigma_e \Delta l \eta_0, \quad L_n = 1, \quad C_n = 1 \tag{2.7}$$

where r_m, g_e, L_n, and C_n are the normalized resistance, conductance, inductance and capacitance, respectively. By substitution of (2.6) and (2.7) in (2.5), one gets:

$$\frac{\partial V_y}{\partial z} = V_{mx} + r_m * i_x + L_n \frac{\partial i_x}{\partial \overline{t}} + L_n \frac{\partial}{\partial \overline{t}} \left(\chi_m * i_x \right)$$
$$\frac{\partial i_x}{\partial z} = i_{ey} + g_e * V_y + C_n \frac{\partial V_y}{\partial \overline{t}} + C_n \frac{\partial}{\partial \overline{t}} \left(\chi_e * V_y \right) \tag{2.8}$$

In (2.8), the time sampling $\Delta t = \Delta l / c$, where $c = 1/\sqrt{\mu_0 \varepsilon_0}$ is the light speed in free space. From the definition of Δt, the network speed in the one-dimensional case is the same as the light speed in free space. Equation (2.8) represents the circuit model for the calculation of the electric and magnetic fields (i.e. V_y and i_x). We apply the conventional transformation for the time derivatives to the normalized frequency domain $\overline{s}$, where $s = \overline{s} / \Delta t$ as follows from (2.6). Equation (2.8) is transformed using the convolution theorem to [28]:

$$D_z V_y = V_{mx} + r_m i_x + L_{nx} \overline{s} i_x + L_{nx} \overline{s} \chi_m i_x \tag{2.9}$$

$$D_z i_x = i_{ey} + g_e V_y + C_{ny} \overline{s} V_y + C_{ny} \overline{s} \chi_e V_y \tag{2.10}$$

where $D_z V_y = V_7 - V_6$ and $D_z i_x = i_6 + i_7$ with the port numbers are chosen for compatibility with the three dimensional (3D) case in Section 2.2 (Fig. 2.7).

Equations (2.9) and (2.10) can be realized with the circuits provided in Figs. 2.2 and 2.3. In Fig. 2.2, a series node is utilized for the calculation of the x polarized magnetic field (i_x). While in Fig. 2.3, a shunt node is utilized for the calculation of the y polarized electric field (V_y). Using two different node configurations, we calculate the electric and magnetic fields at the same instant in time and at the same space point. This represents the condensed formulation that can be extended to the 2D or 3D case towards the symmetrical condensed node (SCN) that is usually exploited for the full vectorial time-domain simulation.
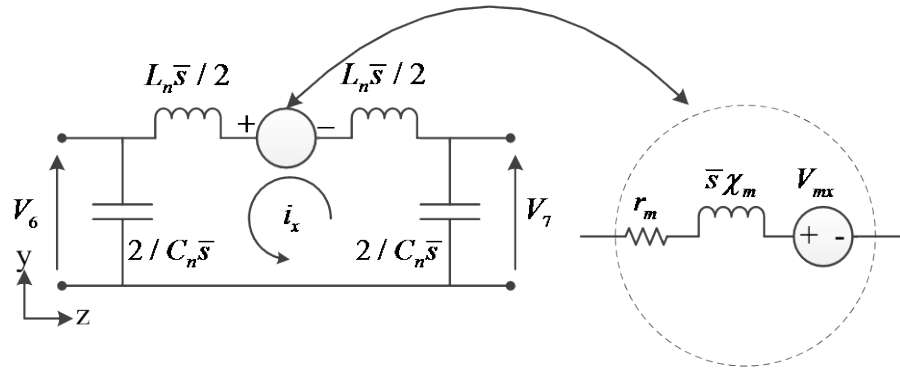
Fig. 2.2. Circuit model of a computational node for one dimensional EM problem (series case).
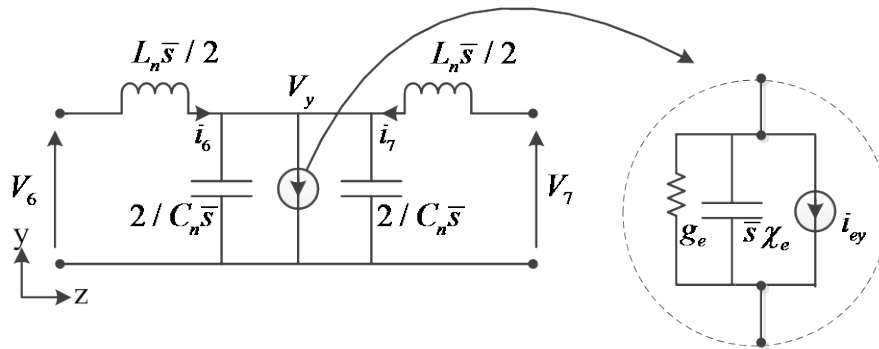
Fig. 2.3. Circuit model of a computational node for one dimensional EM problem (shunt case).
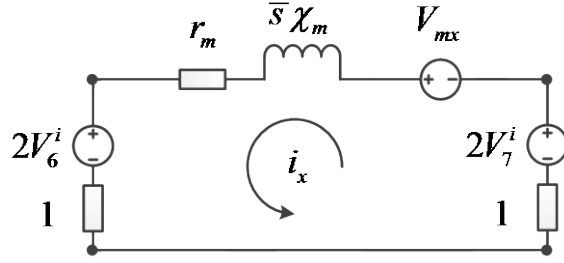
Fig. 2.4. Thevenin equivalent circuit for the series node.
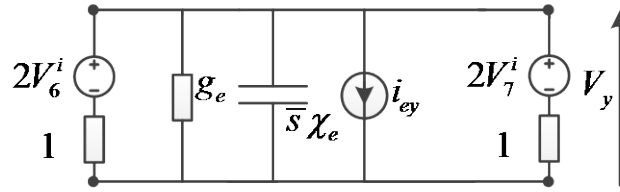
Fig. 2.5. Thevenin equivalent circuit for the shunt node.

A direct approach for the calculation of i_x and V_y utilizes the Thevenin's equivalent circuit at a load point of the transmission line induced with the right and left incident voltages (see Figs. 2.4 and 2.5). The open circuit voltage of a transmission line induced by (V^i), at a port load, is ($2V^i$). The equivalent impedance is the unity characteristic impedance of the transmission line (due to normalization). The solution of the proposed circuits is formulated as,

$$\frac{i_x}{i_x^{ex}} = t_{mxz} = \frac{2}{2 + r_m + \overline{s}\,\chi_m}, \quad i_x^{ex} = \left(V_7^i - V_6^i\right) - \frac{1}{2}V_{mx} \tag{2.11}$$

$$\frac{V_y}{V_y^{ex}} = t_{eyz} = \frac{2}{2 + g_e + \overline{s}\,\chi_e}, \quad V_y^{ex} = \left(V_7^i + V_6^i\right) - \frac{1}{2}i_{ey} \tag{2.12}$$

where t_{mxz} and t_{eyz} are magnetic and electric transmission coefficients utilized for direct calculation of the total voltage and current at each node. The total voltages and currents

are functions of the excitation currents and voltages (i_x^{ex}, V_y^{ex}), introduced by the incident voltage impulses combined with the free sources. The coefficients t_{mxz} and t_{eyz} have subscripts that denote the polarization (*mx*, *ey*) and the direction axis of change (*z*). This simplifies the derivation for the perfect matched layer materials that require field split for the Maxwell equations.

2.1.2 Z-Domain Representation of the TLM Solution

The $\bar{s}$ domain formulation is not directly compatible with the numerical discrete time-domain simulation. Convolution has to be performed in the time-domain. A simple yet powerful tool to evaluate the convolution is through *Z*-domain representation of the transmission coefficients in (2.11), and (2.12) [28]. Utilizing $z = e^{s\Delta t} = e^{\bar{s}}$ which can be approximated as $z = (1 + \bar{s}/2)/(1 - \bar{s}/2)$, the Laplace variable $\bar{s}$ can be substituted as

$$\bar{s} \approx 2\frac{1 - z^{-1}}{1 + z^{-1}} \tag{2.13}$$

The transformation (2.13) is substituted in (2.11) and (2.12) to obtain the following,

$$t_{mxz} = \frac{2}{2 + r_m + 2\left(\dfrac{1 - z^{-1}}{1 + z^{-1}}\right)\chi_m} \tag{2.14}$$

$$t_{eyz} = \frac{2}{2 + g_e + 2\left(\dfrac{1 - z^{-1}}{1 + z^{-1}}\right)\chi_e} \tag{2.15}$$

In order to calculate the total fields at each node inside the domain, we solve for the difference equations constructed from (2.14) and (2.15). Note that, the normalized

material parameters are general functions of z. For simplicity, we define extra storage per node to keep the history of the field values at previous instants, required for the calculation of the current instant. The number of extra storage depends on the dispersion function of the material properties.

For the simple case of non-dispersive material, all parameters are of constant values, and only one extra storage is required to keep the field history. From (2.14), for materials with constant magnetic properties, the total field i_x is calculated by the following scheme [28],

$$i_x = T_{mxz}\left(2i_x^{ex} + z^{-1}S_{mx}\right) \quad , \quad S_{mx} = 2i_x^{ex} + \kappa_{mxz}i_x \tag{2.16}$$

where S_{mx} is the magnetic field accumulator, T_{mxz} is the magnetic forward gain term [28], and κ_{mxz} is the feedback gain term. The gain terms are defined as [28]:

$$T_{mxz} = (2 + r_m + 2\chi_m)^{-1} \quad , \quad \kappa_{mxz} = -(2 + r_m - 2\chi_m) \tag{2.17}$$

Similar procedure can be applied to (2.15) to calculate V_y which is given by:

$$V_y = T_{eyz}\left(2V_y^{ex} + z^{-1}S_{ey}\right) \quad , \quad S_{ey} = 2V_y^{ex} + \kappa_{eyz}V_y \tag{2.18}$$

where S_{ey} is the electric field accumulator, T_{eyz} is the electric forward gain term [28], and κ_{eyz} is the feedback gain term. The gain terms are given by:

$$T_{eyz} = (2 + g_e + 2\chi_e)^{-1} \quad , \quad \kappa_{eyz} = -(2 + g_e - 2\chi_e) \tag{2.19}$$

The discussed update scheme in (2.16)-(2.19) is utilized at each node of the computational domain to calculate the electric and magnetic field normalized quantities

$$V_{eq} = 2(i_x + V_6^i - V_7^i)$$
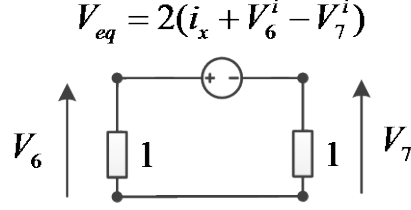
Fig. 2.6. Equivalent potential across the shunt node.

at each time instant k. For the TLM network, the incident impulses (V_6^i, V_7^i) are subject to reflections which are connected to the neighboring nodes. The reflected signals are calculated as

$$V_6^r = V_6 - V_6^i \quad , \quad V_7^r = V_7 - V_7^i \tag{2.20}$$

where V_6, V_7 are the total port voltages, and V_6^r, V_7^r are the reflected port voltages for port 6 and 7 respectively. The total port voltages are calculated, by means of superposition, from the circuits in Figs. 2.4 and 2.5, where i_x, and V_y are known. The total port voltages are calculated in terms of the node fields and incident voltages. An equivalent circuit is constructed (see Fig. 2.6) using the shunt node in Fig. 2.4. In Fig. 2.6, the equivalent potential between the transmission line ports is defined as V_{eq}. We calculate the superposition of the total voltage at each port from Figs. 2.5 and 2.6 as

$$
\begin{aligned}
V_6 &= V_y + (i_x + V_6^i - V_7^i) \\
V_7 &= V_y - (i_x + V_6^i - V_7^i)
\end{aligned}
\tag{2.21}
$$

From (2.20) and (2.21), the reflected voltages at each node are calculated as

$$
\begin{aligned}
V_6^r &= V_y + i_x - V_7^i \\
V_7^r &= V_y - i_x - V_6^i
\end{aligned}
\tag{2.22}
$$

The reflected voltage impulses calculated from (2.22) at an instant k are connected to the neighboring nodes to form incident impulses at instant $k+1$ [21]:

$$\begin{bmatrix} V_6^i \big|_{nz+1} \\ V_7^i \big|_{nz-1} \end{bmatrix}_{k+1} = \begin{bmatrix} V_7^r \big|_{nz} \\ V_6^r \big|_{nz} \end{bmatrix}_k \tag{2.23}$$

where the spatial index in the z direction is nz. The developed TLM scheme utilizes (2.11) and (2.12) to calculate the node excitation currents and voltages (i_x^{ex}, V_y^{ex}). The second step is to calculate the normalized fields at each node utilizing (2.16)-(2.19). The third step is to calculate the reflected voltage impulses as in (2.22). Finally, connection is done, as in (2.23), to calculate the updated incident voltage impulses at the next time step. The TLM scheme discussed in Section 2.1 can be extended to the three dimensional problem utilizing formulation based on the symmetrical condensed node (SCN) [21]. The development of the 3-D TLM method is a straight forward generalization of the proposed derivation. The 3D scheme is demonstrated briefly in Section 2.2. Similar derivation can be conducted for the modeling of perfect matched layer usually employed for domain termination (see Section 2.3).

2.2 3-D TRANSMISSION LINE MODELING

The development of the 3-D TLM is achieved by combining shunt and series nodes to model all possible polarizations governed by Maxwell equations. By means of superposition, we can build a set of 2-D shunt nodes for the calculation of normalized electric field for all polarizations. Similarly, 2-D series nodes are constructed for the normalized magnetic field calculations. Utilizing those combinations, a condensed node

30

for the 3-D modeling is constructed as in Fig. 2.7. In this 3-D case, a total number of 12 transmission line ports; $V = \begin{bmatrix} V_0^i & V_1^i & . & . & . & V_{11}^i \end{bmatrix}^T$ are formed.

For step-by-step explanation of the technique, first the modified node excitation voltages and currents are calculated. For example, similar to (2.12), the node excitation voltage for the y-polarized electric field (V_y^{ex}) is modified as [28]:

$$V_y^{ex} = \left(V_7^i + V_6^i + V_4^i + V_5^i \right) - \frac{1}{2} i_{ey} \tag{2.24}$$

where the modified formulation takes into consideration the field variation in x-z plane. Following the same procedure, the node excitation voltages and currents at each node inside the domain at each time instant is defined as:

$$F^{ex} = \begin{bmatrix} V_x^{ex} \\ V_y^{ex} \\ V_z^{ex} \\ i_x^{ex} \\ i_y^{ex} \\ i_z^{ex} \end{bmatrix} = \begin{bmatrix} V_0^i + V_1^i + V_2^i + V_3^i \\ V_4^i + V_5^i + V_6^i + V_7^i \\ V_8^i + V_9^i + V_{10}^i + V_{11}^i \\ V_7^i - V_6^i + V_8^i - V_9^i \\ V_0^i - V_1^i + V_{11}^i - V_{10}^i \\ V_3^i - V_2^i + V_4^i - V_5^i \end{bmatrix} - \frac{1}{2} \begin{bmatrix} i_{ex} \\ i_{ey} \\ i_{ez} \\ V_{mx} \\ V_{my} \\ V_{mz} \end{bmatrix} \tag{2.25}$$

where the node and time subscripts are omitted for clarity. Equation (2.25) is formulated in a concise matrix form as:

$$F_{j,k}^{ex} = R_{ex,j} V_{j,k} - \frac{1}{2} V_{j,k}^f \tag{2.26}$$

where at the computational node j and time instant k, $V_{j,k} \in R^{12}$ is the vector of incident voltage impulses, $F_{j,k}^{ex} \in R^6$ is the vector of node excitation voltages and currents, and
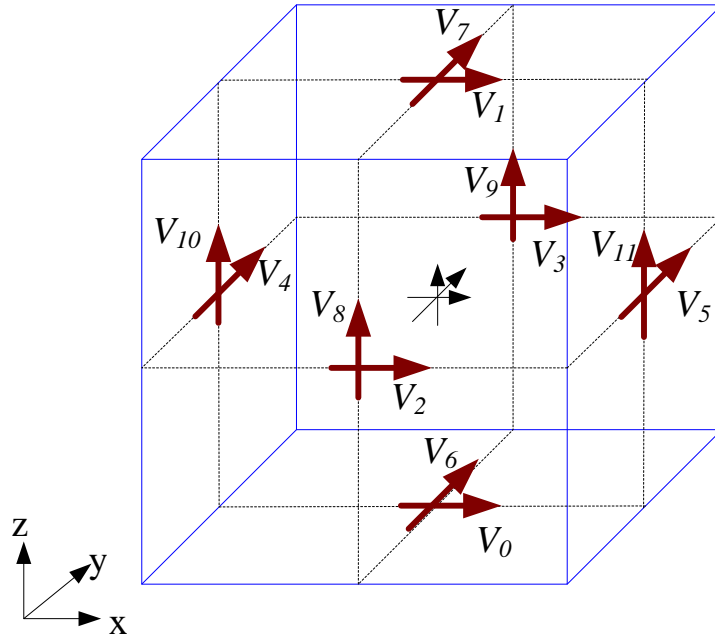
Fig. 2.7. The symmetrical condensed node (SCN) for the 3-D TLM.

$\boldsymbol{V}_{j,k}^{f} \in R^{6}$ is the vector of free sources. $\boldsymbol{R}_{ex,j} \in R^{6 \times 12}$ is the node excitation matrix whose elements belong to the set $\{0, -1, 1\}$.

The calculated node excitation voltages and currents (2.25) are utilized to calculate the normalized fields as [28]

$$\boldsymbol{F} = \begin{bmatrix} V_x \\ V_y \\ V_z \\ i_x \\ i_y \\ i_z \end{bmatrix} = \begin{bmatrix} t_{ex} & & & & & \\ & t_{ey} & & & & \\ & & t_{ez} & & & \\ & & & t_{mx} & & \\ & & & & t_{my} & \\ & & & & & t_{mz} \end{bmatrix} \begin{bmatrix} V_x^{ex} \\ V_y^{ex} \\ V_z^{ex} \\ i_x^{ex} \\ i_y^{ex} \\ i_z^{ex} \end{bmatrix} \tag{2.27}$$

where a transmission matrix is utilized for modeling a material of diagonal constitutive parameter. The transmission coefficients are calculated utilizing the corresponding

32

circuit model with the solution of the resultant equivalent circuit. In the 3-D case, the speed of the signal propagation in the transmission line link $\Delta l / \Delta t = 2c$ [20]. Electric and magnetic fields are mapped to electrical potential and currents as in (2.3). The free current and voltage densities are mapped according to (2.4). Utilizing the mapped circuit quantities (2.3), (2.4), the Thevenin's equivalent circuit can be constructed with the normalized conductivity $g_e = \sigma_e \Delta l \eta_0$ and normalized resistivity $r_m = \sigma_m \Delta l / \eta_0$. The transmission coefficient are formulated for example

$$t_{ex} = \frac{2}{4 + g_e + 2\overline{s}\chi_e} \tag{2.28}$$

and

$$t_{mx} = \frac{2}{4 + r_m + 2\overline{s}\chi_m} \tag{2.29}$$

Equation (2.27) in a matrix form is written as,

$$\boldsymbol{F}_{j,k} = \boldsymbol{T}_j \boldsymbol{F}_{j,k}^{ex} \tag{2.30}$$

where $\boldsymbol{F}_{j,k} \in R^6$ is the total normalized field at node j and time instant k and $\boldsymbol{T}_j \in R^{6\times6}$ is the node transmission matrix dependent on the local material constitutive parameters.

Utilizing the calculated normalized total fields, the reflected voltage impulses at each port for each node in the computational domain is calculated as

$$
\begin{bmatrix} V_0^r \\ V_1^r \\ V_2^r \\ V_3^r \end{bmatrix} = \begin{bmatrix} V_x - i_y - V_1^i \\ V_x + i_y - V_0^i \\ V_x + i_z - V_3^i \\ V_x - i_z - V_2^i \end{bmatrix} , \quad
\begin{bmatrix} V_4^r \\ V_5^r \\ V_6^r \\ V_7^r \end{bmatrix} = \begin{bmatrix} V_y - i_z - V_5^i \\ V_y + i_z - V_4^i \\ V_y + i_x - V_7^i \\ V_y - i_x - V_6^i \end{bmatrix} , \quad
\begin{bmatrix} V_8^r \\ V_9^r \\ V_{10}^r \\ V_{11}^r \end{bmatrix} = \begin{bmatrix} V_z - i_x - V_9^i \\ V_z + i_x - V_8^i \\ V_z + i_y - V_{11}^i \\ V_z - i_y - V_{10}^i \end{bmatrix} \tag{2.31}
$$
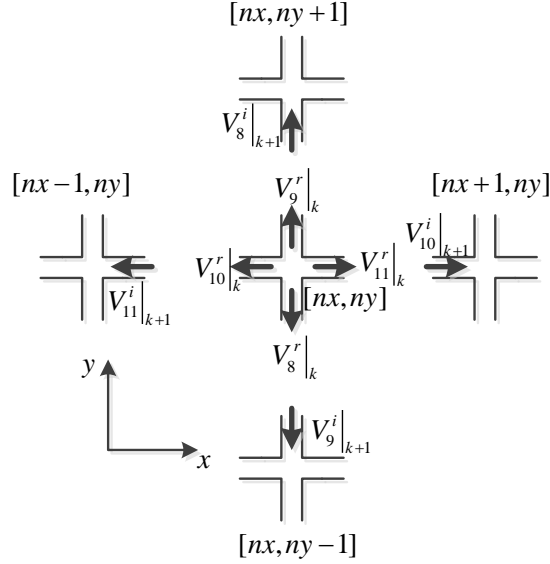
Fig. 2.8. The TLM connection process.

We define the vector of reflected voltage impulses at the node ports as $\boldsymbol{V}^r = \begin{bmatrix} V_0^r & V_1^r & . & . & . & V_{11}^r \end{bmatrix}^T$. A matrix form of (2.31) can thus be written as [28]

$$\boldsymbol{V}_{j,k}^r = \boldsymbol{R}_j \boldsymbol{F}_{j,k} - \boldsymbol{P} \boldsymbol{V}_{j,k} \tag{2.32}$$

where at the spatial node index j and time index k, $\boldsymbol{V}_{j,k}^r \in R^{12}$ is the vector of reflected voltages and $\boldsymbol{R}_j \in R^{12 \times 6}$ is the reflection matrix whose entries belong to the set $\{0, -1, 1\}$.

Finally, the reflected voltage impulses at each port at each time step k are connected to the neighboring ports to form the vector of impulse voltages at the next time step, $k+1$. In Fig. 2.8, the connection process for ports 8, 9, 10, 11 is demonstrated, where the spatial indices at the current node are nx, ny, nz. The update of the incident voltage impulses using the reflected ones is usually called the connection step and is performed as follows,

$$
\begin{bmatrix}
V_1^i\big|_{nx,ny,nz-1} \\
V_0^i\big|_{nx,ny,nz+1} \\
V_3^i\big|_{nx,ny-1,nz} \\
V_2^i\big|_{nx,ny+1,nz} \\
V_5^i\big|_{nx-1,ny,nz} \\
V_4^i\big|_{nx+1,ny,nz} \\
V_7^i\big|_{nx,ny,nz-1} \\
V_6^i\big|_{nx,ny,nz+1} \\
V_9^i\big|_{nx,ny-1,nz} \\
V_8^i\big|_{nx,ny+1,nz} \\
V_{11}^i\big|_{nx-1,ny,nz} \\
V_{10}^i\big|_{nx+1,ny,nz}
\end{bmatrix}_{k+1}
=
\begin{bmatrix}
V_0^r\big|_{nx,ny,nz} \\
V_1^r\big|_{nx,ny,nz} \\
V_2^r\big|_{nx,ny,nz} \\
V_3^r\big|_{nx,ny,nz} \\
V_4^r\big|_{nx,ny,nz} \\
V_5^r\big|_{nx,ny,nz} \\
V_6^r\big|_{nx,ny,nz} \\
V_7^r\big|_{nx,ny,nz} \\
V_8^r\big|_{nx,ny,nz} \\
V_9^r\big|_{nx,ny,nz} \\
V_{10}^r\big|_{nx,ny,nz} \\
V_{11}^r\big|_{nx,ny,nz}
\end{bmatrix}_{k}
\tag{2.33}
$$

The connection process applied to all links of the computational domain of size N is formulated as

$$
V_{k+1} = C V_k^r \tag{2.34}
$$

where V_k, $V_k^r \in R^{12N}$ are the vectors of all incident and reflected impulses respectively, for all nodes inside the computational domain at the kth time step. The matrix $C \in R^{12N \times 12N}$ is the overall TLM connection matrix utilized to perform the swapping operations on the reflected voltage impulses.

The TLM technique utilizes the update scheme (2.25)-(2.33) for the calculation of the normalized field quantities inside the computational domain at any time instant during the specified simulation time. This scheme is based on two distinct processes called

scattering and connection. Utilizing matrix formulations (2.26), (2.30), (2.32), and (2.34), the TLM scheme is formulated in a standard concise matrix formulation as follows,

$$V_{k+1} = C\left(RTR_{ex} - P\right)V_k + V_k^s \tag{2.35}$$

where the system factorized matrices, $R \in R^{12N \times 6N}, T \in R^{6N \times 6N}, R_{ex} \in R^{6N \times 12N}$, and $P \in R^{12N \times 12N}$, are block diagonal matrices whose diagonal blocks are the nodal matrices $R_j \in R^{12 \times 6}$, $T_j \in R^{6 \times 6}$, $R_{ex,j} \in R^{6 \times 12}$ and $P_j \in R^{12 \times 12}$, respectively, for $j=1\ 2\ \dots\ N$. The vector V_k^s is the source excitation at time step k. Equation (2.35) can be written in a more concise form as:

$$V_{k+1} = CSV_k + V_k^s \tag{2.36}$$

where $S \in R^{12N \times 12N}$ is a block diagonal matrix whose jth diagonal component is $S^j \in R^{12 \times 12}$, the scattering matrix of the jth node.

2.3   MODELING OF DISPERSIVE PLASMONIC MEDIA

The TLM scheme presented in Section 2.2 is general and can be extended to the modeling of the dispersive media by means of Z transform as demonstrated in (2.14)-(2.19). In this case, the transmission matrix defined in (2.27) is constructed from frequency dependent constitutive parameters (causal frequency dependence). The normalized electric and magnetic fields are calculated through the solution of a simple difference equation by means of extra storage that preserves the system history.

For modeling nano-plasmonic structures in the optical range, the dispersive behavior of metallic objects should be taken into account. The interaction between the

electron oscillations at the surface of metallic interface (surface plasmons) with the light, give rise to the surface plasmon polaritons (SPPs) wave, which can propagate along the metal surface. Dispersive Drude model is usually exploited to model the metal constitutive parameters in the optical range (plasma model). The metal is treated as a free electron gas of density (N_0) moves in the presence of the positive ion cores [33]. The electron undergoes damped oscillations in the presence of the electromagnetic radiation. The damping frequency is denoted as γ. The electric susceptibility for the metal in an SPP structure with the dispersion described by the Drude model [33], [34] is

$$\chi_e = \chi_\infty + \frac{\omega_p^2}{\omega(i\gamma - \omega)} \tag{2.37}$$

In (2.37), χ_∞ is the background frequency independent susceptibility of the model. ω_p is the bulk plasma frequency ($\omega_p = \sqrt{N_0 e^2 / \varepsilon_0}$) where e is the electron charge and ε_0 is the free space permittivity, ω is the angular frequency, and γ is the collision frequency. Equation (2.37) is derived for the field time dependence $\boldsymbol{E}(t) = \boldsymbol{E}_0 e^{j\omega t}$ of a wave propagating in the positive spatial co-ordinates [34].

The expression (2.37) may be transformed into the Laplace s domain and substituted in (2.28). Thus (2.28) is transformed into a time difference equation to calculate the vector $\boldsymbol{F}$ using the excitation vector $\boldsymbol{F}^{\text{ex}}$. An alternative approach for modeling the metal dispersion in SPP structures is to introduce dispersive conductivity using the relationship $\chi(\omega) = -\sqrt{-1}\,\sigma(\omega)/\varepsilon_0\omega$ [33], [34], where $\chi(\omega)$ is the frequency-dependent part of the metal susceptibility with χ_∞ excluded. Therefore, the

metal material is characterized as a non-magnetized plasma with constant susceptibility χ_∞ and a frequency dependent conductivity $\sigma(\omega)$. The frequency dependent conductivity in s form is given by [28]

$$\sigma_e(s) = \frac{\sigma_0}{1 + s\tau_c} \tag{2.38}$$

where $\tau_c = 1/\gamma$ is the collision time constant. The DC electric conductivity is $\sigma_0 = \omega_p^2 \varepsilon_0 \tau_c$. Our TLM realization is based on a dispersive equivalent conductivity approach. Transforming (2.38) to the Z-domain formulation utilizing the impulse invariant method, the normalized conductance is formulated as [28]

$$g_e(z) = \frac{g_{ec}(1 - \beta_0)}{1 - z^{-1}\beta_0} \tag{2.39}$$

where $g_{ec} = \sigma_0 \Delta l \eta_0$ is the normalized conductance and $\beta_0 = e^{-\Delta t/\tau_c}$. Equation (2.39) can be expanded as follows,

$$(1 + z^{-1})g_e(z) = g_{e0} + z^{-1}g_{e1}(z) \tag{2.40}$$

where $g_{e0} = g_{ec}(1 - \beta_0)$, $g_{e1} = \alpha/(1 - z^{-1}\beta_0)$ and $\alpha = g_{ec}(1 - \beta_0^2)$. Equation (2.40) is then substituted into the transmission matrix coefficients, e.g. (2.28), to construct a time-domain difference equation. For example, for the calculation of V_x at a certain computational node, the transmission parameter t_{ex} in (2.28) is calculated, using the plasmonic material model (2.40), as follows:

$$t_{ex} = \frac{V_x}{V_x^{ex}} = \frac{2(1 + z^{-1})}{4 + g_{e0} + 4\chi_\infty + z^{-1}(4 - 4\chi_\infty) + z^{-1}g_{e1}(z)} \tag{2.41}$$

where the transmission coefficient t_{ex} is transformed to the Z-domain representation using the bilinear transform (2.13). Equation (2.41) is frequency independent for the free space case ($\chi_\infty = 0$, $g_{e0} = 0$, $g_{e1} = 0$). No memory is required in this case to store past field values. For a material of finite frequency independent permittivity and conductivity, the previous field value needs to be stored. For the plasmonic materials, the field history for the previous two time steps is accumulated. This is due to the z^{-1} and z^{-2} terms in the transmission coefficients. The application of TLM to other dispersive materials is straightforward and is achieved with a number of extra storages dependent on the material model functions.

2.4   MODELING OF PERFECTLY MATCHED LAYER

The perfectly matched layer (PML), developed by Bérenger, is widely used with FDTD codes [35]. PML is based on the manipulation of Maxwell equations to allow for nonphysical contributions that lead to a finite computational domain. For the implementation of a PML at the boundary, in TLM, we utilize an adapted version of this approach.

The implementation of PML to the TLM computational domain can be achieved through different approaches. The first approach is to implement the PML through an attached FDTD layer [36]. This method requires an interpolation at the domain interface which may be a source of artificial spurious modes. It also adds the complexity of using two different numerical techniques for the same problem.

A second approach utilizes a modified TLM node suitable for the implementation of the PML for TLM [37]. The overhead of this approach is an increased memory storage, computational effort, and complexity. An extra 8 links are attached to each node for implementing the PML [37]. This approach, however, leads to a unified algorithm, which is more robust, accurate, and does not require any interpolation at the interface between different computational domains.

In this work, we utilize an optimized version of the PML based on the TLM approach presented in Section 2.2. It utilizes the same node for the computational domain and the PML. This PML realization does not require the definition of extra ports. However, extra storage will be required to account for the field splitting [30]. It is simple to implement with only a memory overhead due to the presence of extra field values. The calculation of the reflected waves (scattering) and new incident waves (connection) proceed as explained earlier.

According to the basic idea introduced by Bérenger, the TLM implementation [30] uses a modified set of normalized field quantities $\boldsymbol{F} = [\ V_{xz}\quad V_{xy}\quad V_{yx}\quad V_{yz}\quad V_{zy}\quad V_{zx}\quad i_{xz}\quad i_{xy}\quad i_{yx}\quad i_{yz}\quad i_{zy}\quad i_{zx}\ ]^T$. The vector of the node excitation fields $\boldsymbol{F}^{ex}$ is modified to $\boldsymbol{F}^{ex} = [\ V_{xz}^{ex}\quad V_{xy}^{ex}\quad V_{yx}^{ex}\quad V_{yz}^{ex}\quad V_{zy}^{ex}\quad V_{zx}^{ex}\quad i_{xz}^{ex}\quad i_{xy}^{ex}\quad i_{yx}^{ex}\quad i_{yz}^{ex}\quad i_{zy}^{ex}\quad i_{zx}^{ex}\ ]^T$. The calculations of both $\boldsymbol{F}^{ex}$ and $\boldsymbol{F}$ follow the same procedure as in (2.26) and (2.30) with modified $\boldsymbol{R}_{ex}$ and $\boldsymbol{T}$ matrices.

The evolution of the voltage and current signals inside the PML media is subject to similar scattering and connection processes, as in the non-split field regular TLM

technique. The scattering process is summarized as follows. The node excitation voltages and currents are calculated from the 12 ports incident voltages associated with the SCN [30] as

$$
\boldsymbol{F}^{ex} = \begin{bmatrix} V_{xz}^{ex} \\ V_{xy}^{ex} \\ V_{yx}^{ex} \\ V_{yz}^{ex} \\ V_{zy}^{ex} \\ V_{zx}^{ex} \\ i_{xz}^{ex} \\ i_{xy}^{ex} \\ i_{yx}^{ex} \\ i_{yz}^{ex} \\ i_{zy}^{ex} \\ i_{zx}^{ex} \end{bmatrix} = \begin{bmatrix} V_0^i + V_1^i \\ V_2^i + V_3^i \\ V_4^i + V_5^i \\ V_6^i + V_7^i \\ V_8^i + V_9^i \\ V_{10}^i + V_{11}^i \\ V_7^i - V_6^i \\ V_8^i - V_9^i \\ V_{11}^i - V_{10}^i \\ V_0^i - V_1^i \\ V_3^i - V_2^i \\ V_4^i - V_5^i \end{bmatrix} \tag{2.42}
$$

where the free sources terms are vanishes inside the PML domain. The above expression can be derived following the same procedure in Section 2.1 (see (2.11) and (2.12)). The normalized local split fields at each node are determined using,

$$
\begin{aligned}
V_{xz} &= t_{exz} V_{xz}^{ex}, & V_{xy} &= t_{exy} V_{xy}^{ex} \\
V_{yx} &= t_{eyx} V_{yx}^{ex}, & V_{yz} &= t_{eyz} V_{yz}^{ex} \\
V_{zy} &= t_{ezy} V_{zy}^{ex}, & V_{zx} &= t_{ezx} V_{zx}^{ex} \\
i_{xz} &= t_{mxz} i_{xz}^{ex}, & i_{xy} &= t_{mxy} i_{xy}^{ex} \\
i_{yx} &= t_{myx} i_{yx}^{ex}, & i_{yz} &= t_{myz} i_{yz}^{ex} \\
i_{zy} &= t_{mzy} i_{zy}^{ex}, & i_{zx} &= t_{mzx} i_{zx}^{ex}
\end{aligned} \tag{2.43}
$$

The real six field components can be calculated by adding the corresponding two field quantities as follows:

$$V_x = V_{xy} + V_{xz}, \quad V_y = V_{yx} + V_{yz}, \quad V_z = V_{zx} + V_{zy} \tag{2.44}$$

and

$$i_x = i_{xy} + i_{xz}, \quad i_y = i_{yx} + i_{yz}, \quad i_z = i_{zx} + i_{zy} \tag{2.45}$$

The reflected voltages and the connection processes (2.31), (2.33) are utilized to calculate the updated link voltage impulse.

For the calculation of the transmission matrix coefficients we map the PML constitutive parameters calculated as in [28] to the corresponding circuit parameters. The PML is an integral part of any computational domain for modeling photonic structures. It provides accurate truncation for infinite domains. To test our in-house simulator, we start by simulating a simple slab waveguide (see inset of Fig. 2.9). This waveguide is made of a cladding and a core layer with refractive index of 1.5 and 1.7, respectively. The width of the waveguide is $d = 0.8$ μm. This structure is excited with the fundamental mode. The excitation signal is a Gaussian-modulated sinusoid with a wavelength (λ) between 1.0 μm to 3.0 μm. The transmitted signal inside the waveguide is calculated using both the line-matching boundary condition [22] and the PML boundary condition. The results of this simple waveguide simulation are shown in Figs. 2.9 and 2.10. Fig. 2.9 shows a large time-domain reflection for the line-matching boundary condition. The transmission spectrum using the same boundary is highly distorted as shown in Fig. 2.10. The PML boundary provides more accurate results than the line-matching boundary especially for wideband excitations. Our PML implementation is employed in all subsequent examples. These examples are all conducted on an Intel® Xeon® Processor 5160 (3.0 GHz) platform.
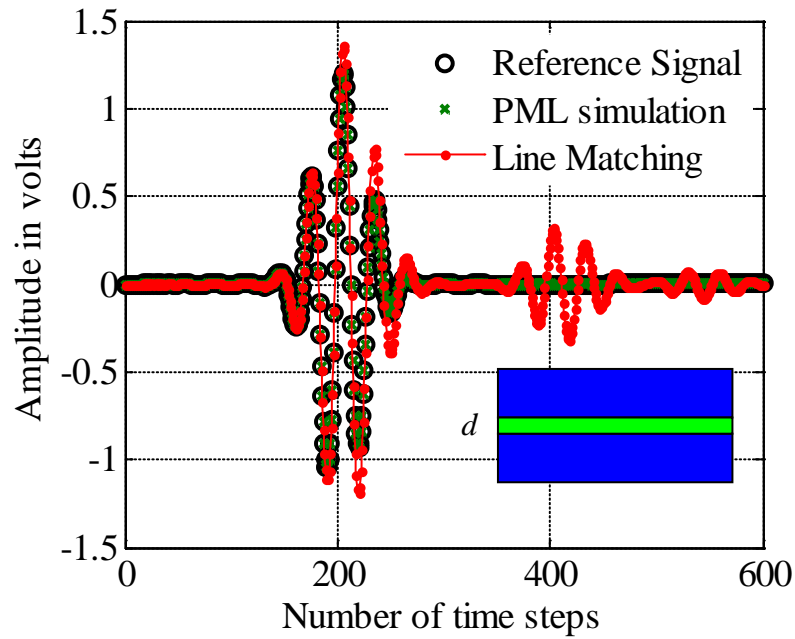
Fig. 2.9. The transmitted time-domain signal in a slab waveguide is compared for the two types of boundaries; PML boundary and line-matching boundary.
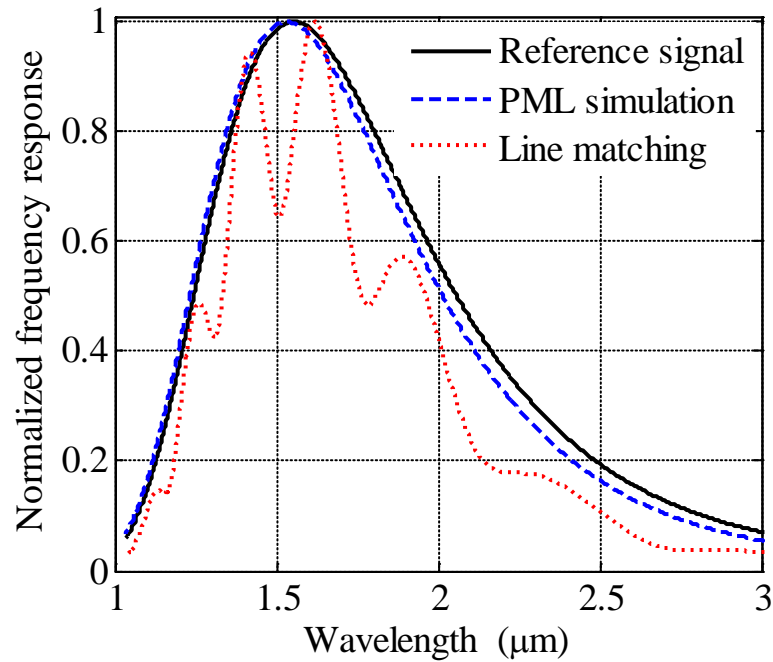
Fig. 2.10. The transmitted frequency-domain signal in a slab waveguide is compared for the two types of boundaries; PML boundary and line-matching boundary.

2.5 MODELING OF SUBWAVELENGTH NANO-PLASMONIC STRUCTURES

In this Section, we demonstrate the application of TLM to the modeling of plasmonic structures. We perform a wideband time-domain simulation for a number of structures using our in-house MATLAB-based TLM simulator. Our examples include surface plasmon polariton Bragg gratings, subwavelength beam focusing using surface dielectric gratings, improved focusing using surface metallic grooves, and focusing using nano-scale slit array. Our results are compared to the results available in the literature. We also utilize the TLM simulation to predict the dependence of the response on some device parameters (parametric study). Our examples are tested using both Gaussian-modulated sinusoidal excitations and impulse excitations in order to illustrate the stability of the TLM approach.

2.5.1 Surface Plasmon Bragg Grating

In this example, we model a metal-insulator-metal (MIM)-type waveguide with metallic grating (see Fig. 2.11). Using this grating, we can achieve Bragg filtering. This device is known as surface plasmon polariton waveguide Bragg grating (SPP-WBG) [38]. For wideband modeling of these devices, time-domain simulators are preferred. The parameters are chosen to be $W = 500.0$ nm, $W_1 = 100.0$ nm, $\Lambda = 660.0$ nm, and $L = 292.0$ nm [39]. The values of the last two parameters allow the Bragg condition to occur at a wavelength of 1550.0 nm. The number of grating pitches is set to 14. The thickness of the
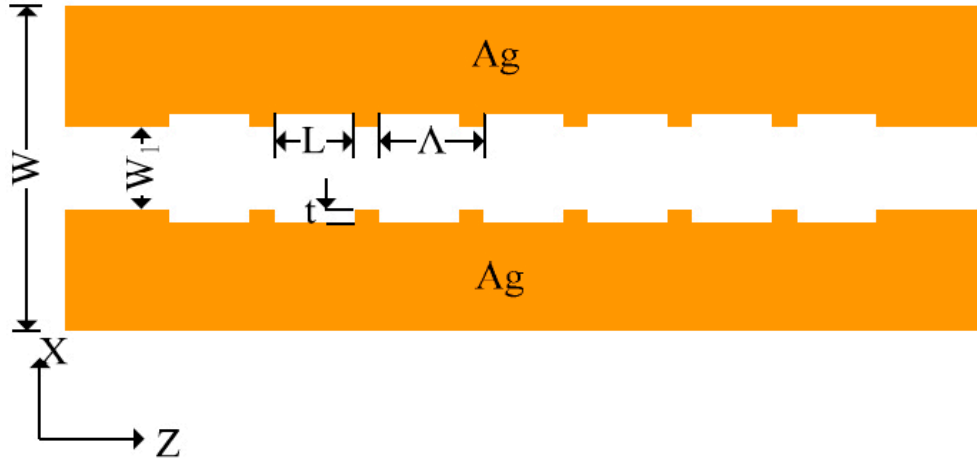
Fig. 2.11. The geometry of the SPP waveguide Bragg grating.

grating (*t*) is included as a parameter in order to evaluate its impact on the response. We set the minimum value of *t* to 25.0 nm. The metal is assumed to be silver with its permittivity given by the Drude model. The parameters of the model are $\varepsilon_\infty = \chi_\infty + 1 = 3.7$, $\hbar\omega_p = 9.1\text{eV}$, and $\hbar\gamma = 0.018\text{eV}$ [40]-[43], where $\hbar$ is the reduced Planck's constant. The dielectric layer is assumed air.

The SPP Bragg grating is simulated using a TLM space step of 10.0 nm for 30,000 time steps. The simulated structure has dimensions 0.4×13 μm which requires 40×1300 TLM nodes. For this large structure with a large number of time steps, the overall simulation time is about 90 minutes.

A time-domain impulse excitation is utilized in this example. The transmission spectrum is estimated, for the wavelength range 1.0 μm to 6.0 μm as shown in Fig. 2.12. The predicted center wavelength inside the band gap is 1550.0 nm. Both the center wavelength and the filter quality have good agreement to those reported in [39], [44]. The spectral response is asymmetric as in Fig. 2.12, which is consistent with the dispersive
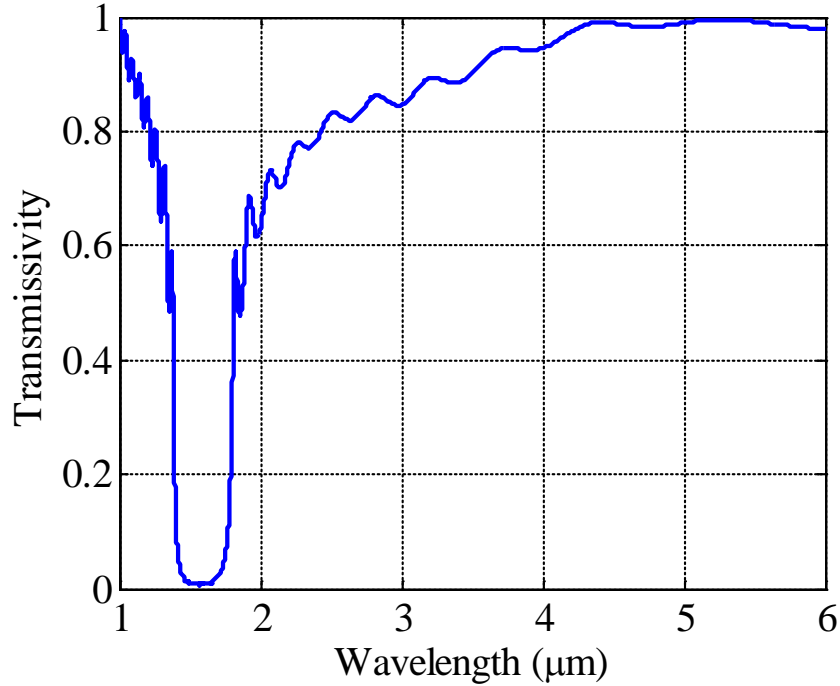
Fig. 2.12. The transmission response of the plasmonic Bragg grating whose operation wavelength is at 1.55 µm.

permittivity of the silver. The magnetic field distribution ($|H_y|$) inside the SPP-WBG is shown in Figs. 2.13 and 2.14, for incident wavelengths 1000.0 nm and 1550.0 nm, respectively. It is clear that the incident wave with a wavelength of 1000.0 nm, which lies outside the band gap, is transmitted. However, at 1550.0 nm, the incident wave is completely reflected.

For robust validation of our model, we estimate the impulse response due to different values of the grating thickness t. This is the first reported simulated impulse response of a photonic structure. This is the direct advantage of the TLM as a physics-based numerical technique. The transmission response is calculated for thicknesses

ranging from 25.0 nm to 155.0 nm as shown in Fig. 2.15. The grating thickness affects both the band gap and the performance of the device. As the thickness increases, the band gap increases with a significant shift in the mid wavelength and the transmitted energy decreases. The thickness increase also allows for a large propagation loss inside the grating, which leads to a degradation in the filter response as shown in Fig. 2.15.
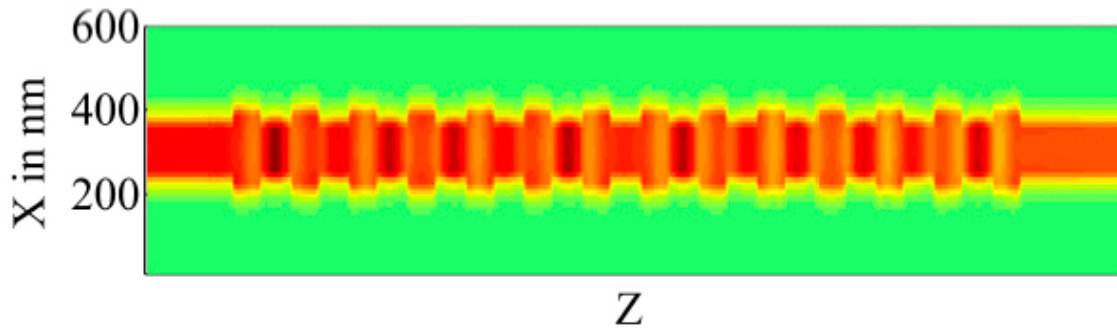
Fig. 2.13. The magnetic field distribution inside the plasmonic Bragg grating for an incident wavelength of 1000.0 nm.
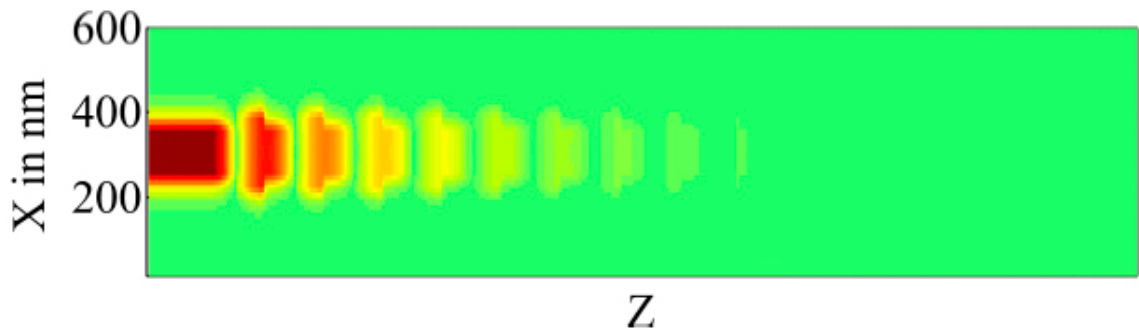
Fig. 2.14. The magnetic field distribution inside the plasmonic Bragg grating for an incident wavelength of 1550.0 nm.
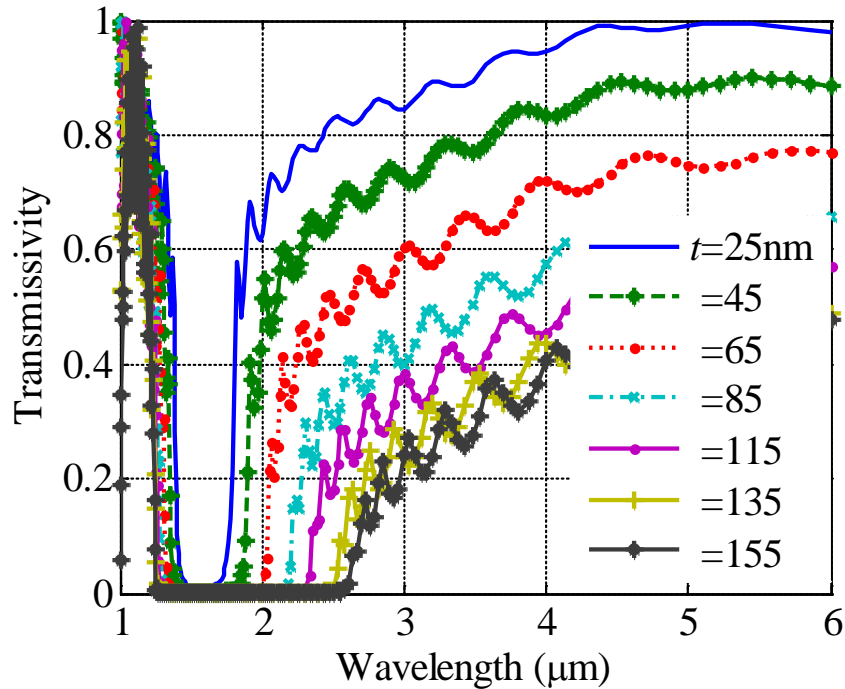
Fig. 2.15. The impulse response of the plasmonic Bragg grating for different grating thicknesses.

2.5.2 Sub-wavelength Beam Focusing Using Dielectric Surface Grating

In this example, we model a single subwavelength slit surrounded by chirped dielectric surface grating as shown in Fig. 2.16. By introducing a chirped dielectric grating on the metallic surface, the light is focused at a certain focal length that is dependent on the dielectric material and the grating period [45], [46]. This device can be used for focusing the light in nano-scale scanning optical microscopy. It consists of silver slab of thickness d with a slit of width a.
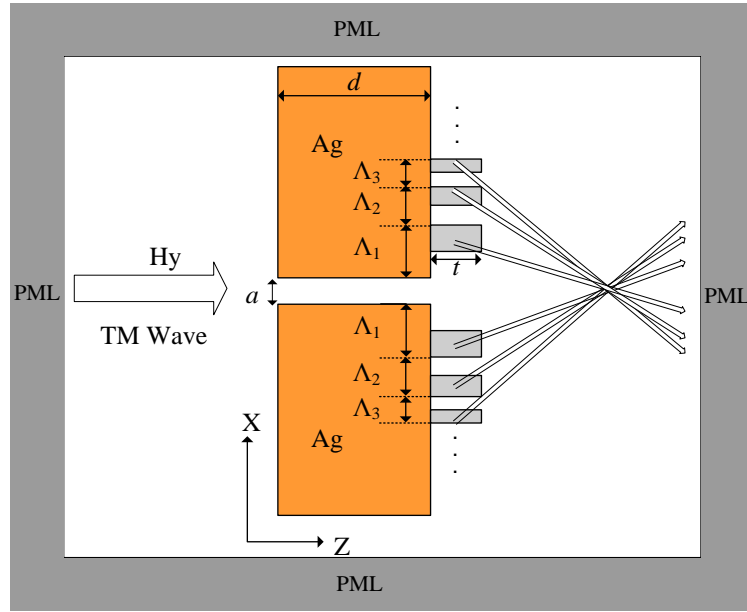
Fig. 2.16. The schematic of SPP beam focusing using aperture dielectric grating.

For the considered structure, we set d=1.0 μm, a=100.0 nm, and t=120.0 nm. The structure consists of 12 surface grating pitches at each side of the slit with a 0.5 fill factor. The periods of these grating are given by Λ= [327.0 294.0 272.0 258.0 249.0 242.0 238.0 234.0 231.0 229.0 228.0 226.0] nm which allows the focal point of an incident wave of wavelength 532.0 nm to be at 1.5 μm. The same silver dispersion model of Section 2.5.1 is utilized with dispersion parameters consistent with [47]. The dielectric grating material has a refractive index of 1.72.

The structure is simulated with a space step of 5.0 nm for 8000 time steps utilizing different types of excitation. The space step is small to match the contrast in the design dimensional parameters. The simulation is conducted for a large domain size to ensure that the focal point is located inside the computational domain. For a 7.0×10.0 μm
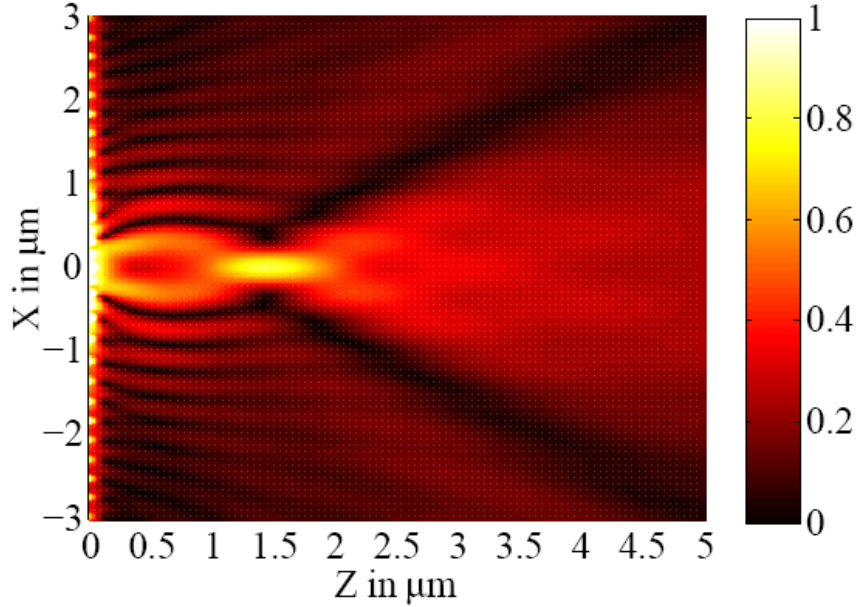
Fig. 2.17. The magnetic field distribution of the focused beam from subwavelength metallic slit in the presence of an aperture dielectric grating at an incidence wavelength of 532.0 nm.

structure, the computational domain includes 1400×2000 TLM nodes. The simulation time is approximately 300 minutes.

The field distribution ($|H_y|$) at an operating wavelength of 532.0 nm is shown in Fig. 2.17. The achieved focal point is 1.5 μm which is identical to that reported in [46] with the same full width at half maximum (FWHM=409.0 nm) as shown in Fig. 2.18.

In Fig. 2.19, the longitudinal intensity distribution ($|Hy|)^2$ for a selected set of wavelengths demonstrates the variation of the focal length. As can be seen, focusing is achieved at specific wavelengths from 500.0 nm to 600 nm according to the designed structure. Focusing is demonstrated by means of light intensity probing along the axis.
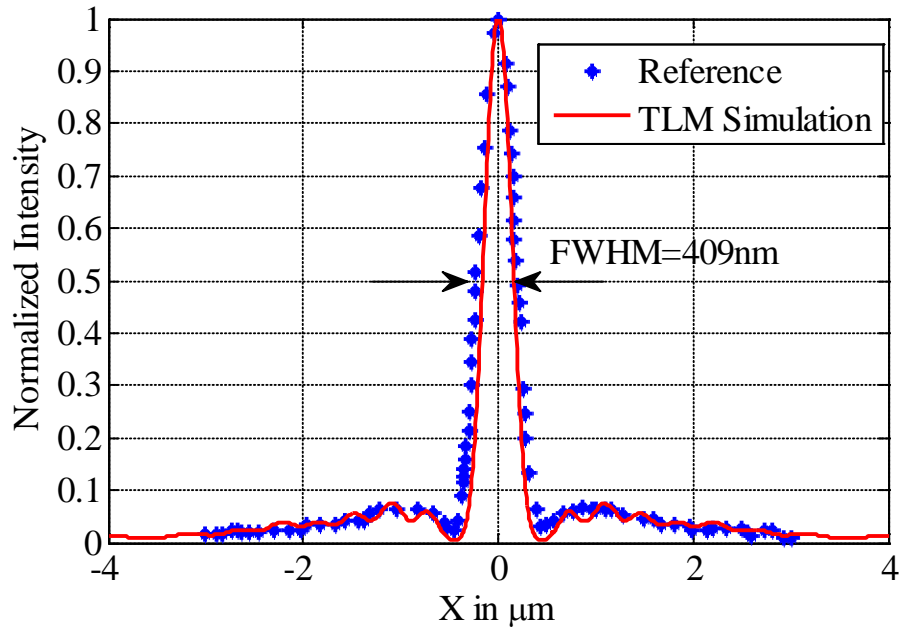
Fig. 2.18. The transverse intensity profile around the spot of the focused beam for the subwavelength metallic slit at an incidence wavelength of 532.0 nm.
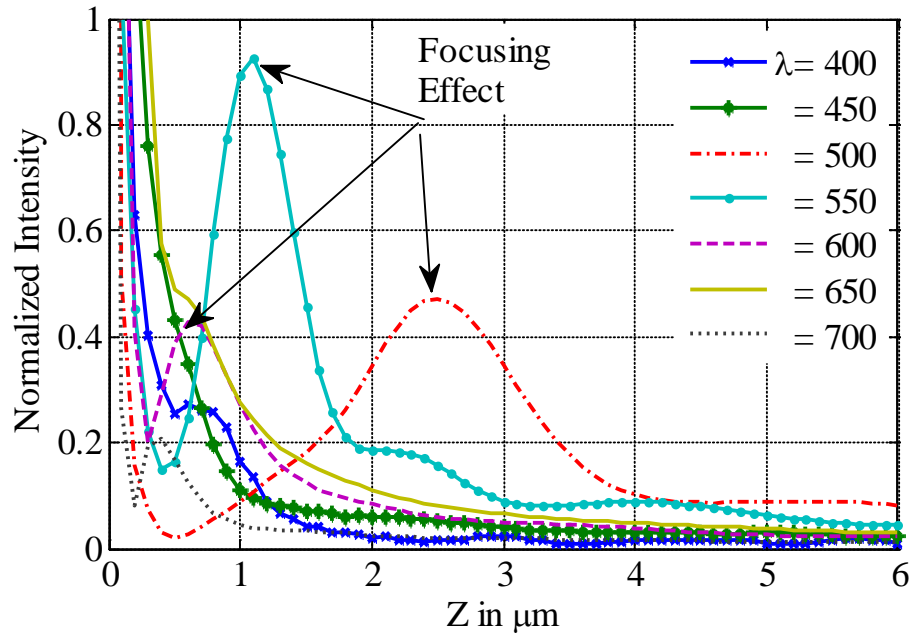
Fig. 2.19. The longitudinal intensity distribution for the subwavelength metallic slit surrounded by a chirped dielectric grating at a selected set of wavelengths.
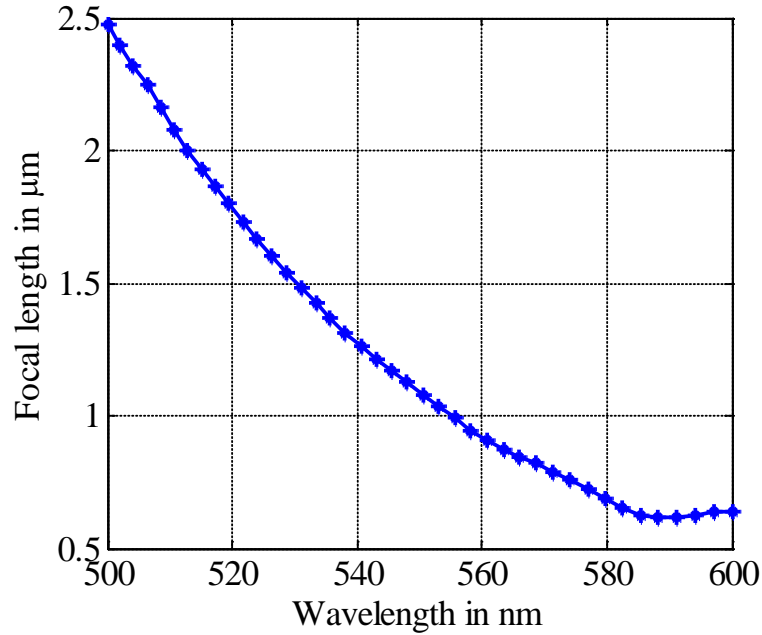
Fig. 2.20. The spectral distribution of the focal length for the lens structure of subwavelength metallic slit with chirped dielectric grating.

Utilizing the time-domain data calculated along the axis, the focal length is calculated for a wide spectral region (500.0 nm to 600.0 nm) as shown in Fig. 2.20. As the light wavelength increases, the focal point becomes closer to the slit.

2.5.3 Sub-wavelength Focusing Using Metallic Grooves

We consider the promising focusing structure shown in Fig. 2.21. It consists of a metallic slit surrounded with metallic grooves of constant depths [48]-[51]. These grooves allow for highly focused beam without any chirping. The main parameters are the slit width and groove period, depth, and width. The structure utilizes a gold film with a thickness of 400.0 nm. The film dielectric constant is characterized by the Drude model with parameters the ε_∞=9.0685, $\hbar\omega_p$=8.9269eV, and $\hbar\gamma$=0.076eV [40]-[42]. The
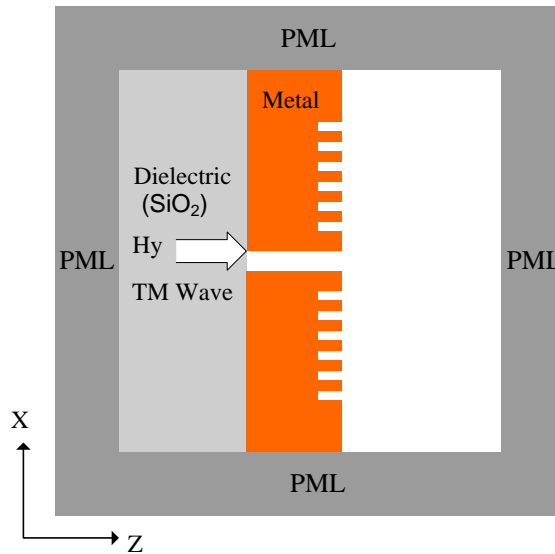
Fig. 2.21. The schematic of the focusing structure with metallic grooves.

dielectric layer is made of silicon dioxide (SiO_2) with a refractive index of 1.46. The slit width is 200.0 nm. The groove period, width, and depth are 380.0 nm, 60.0 nm and 40.0 nm, respectively. This structure provides focusing at wavelength of 650.0 nm with a focal point of 2.0 μm [49].

This structure is modeled using a computational domain with a space step of 10.0 nm for 8000 time steps. The computational effort for this simulation is less than the design in Section 3.2 because the grating is not chirped. For a 5×12 μm structure, the computational domain includes 500× 1200 TLM nodes. The simulation time is approximately 90 minutes.
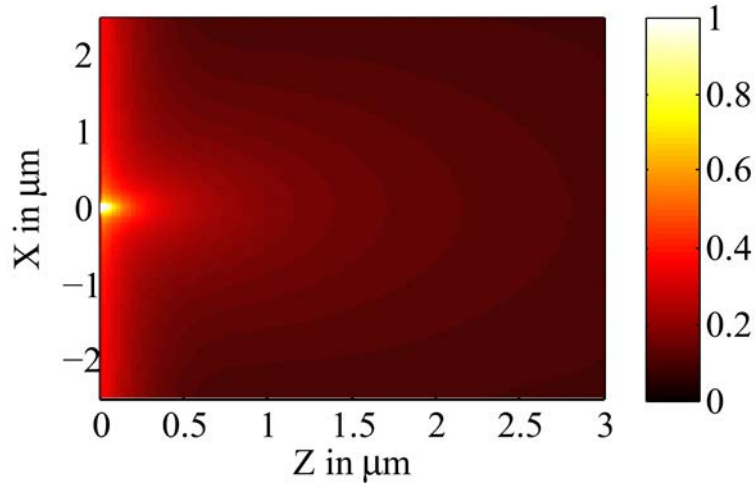
Fig. 2.22. The magnetic field distribution for the subwavelength slit without the grooves.
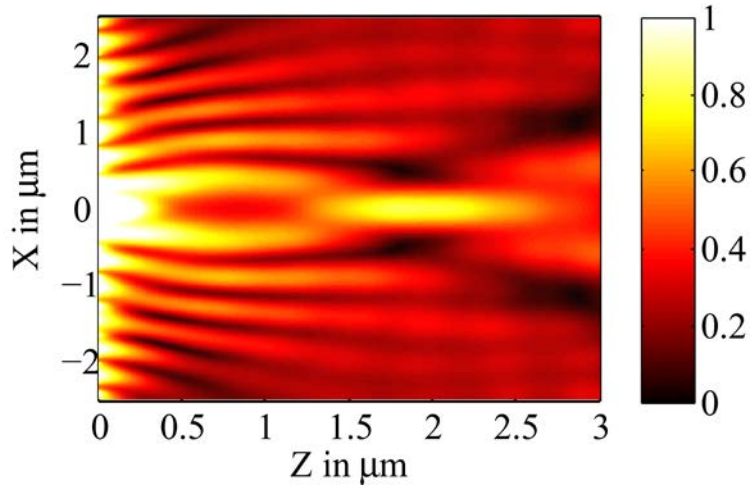
Fig. 2.23. The magnetic field distribution for the focusing structure with the grooves included.

The structure is excited with a wideband Gaussian-modulated sinusoidal signal (from 400.0 nm to 700.0 nm). For this example, we demonstrate focusing effect by estimating the change in the field distribution due to the introduction of surface metallic grooves. The field distribution ($|H_y|$) for the structure without metallic grooves is shown in Fig. 2.22. The field distribution of the focusing structure is shown in Fig. 2.23. Here,

light is focused at a focal length of 2.0 μm. In Fig. 2.24, the intensity distribution along the transverse direction at the focal point is compared to that obtained in [49]. The TLM simulation predicts a FWHM of 350.0 nm which is in good agreement with the reported data [49].

The TLM time-domain simulation is further exploited to predict the focusing behavior for different wavelengths. The lateral intensity distribution $(|H_y|)^2$ for a selected set of wavelengths is shown in Fig. 2.25. Focusing is achieved in the neighborhood of the wavelength 650.0 nm. For the wavelength range between 600.0 nm to 700.0 nm, the continuous focal length wavelength relation is shown in Fig. 2.26.
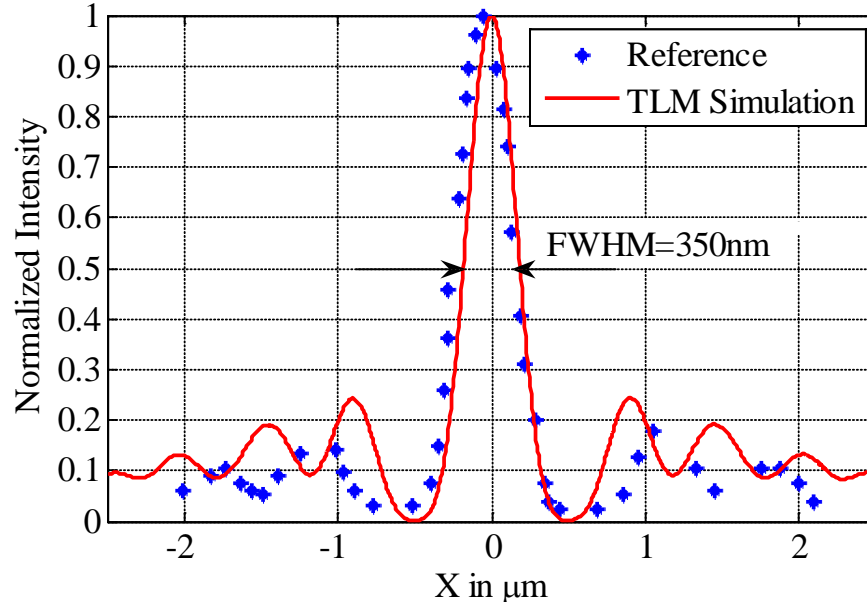
Fig. 2.24. The transverse intensity profile around the focusing spot for the subwavelength slit with metallic surface grooves.
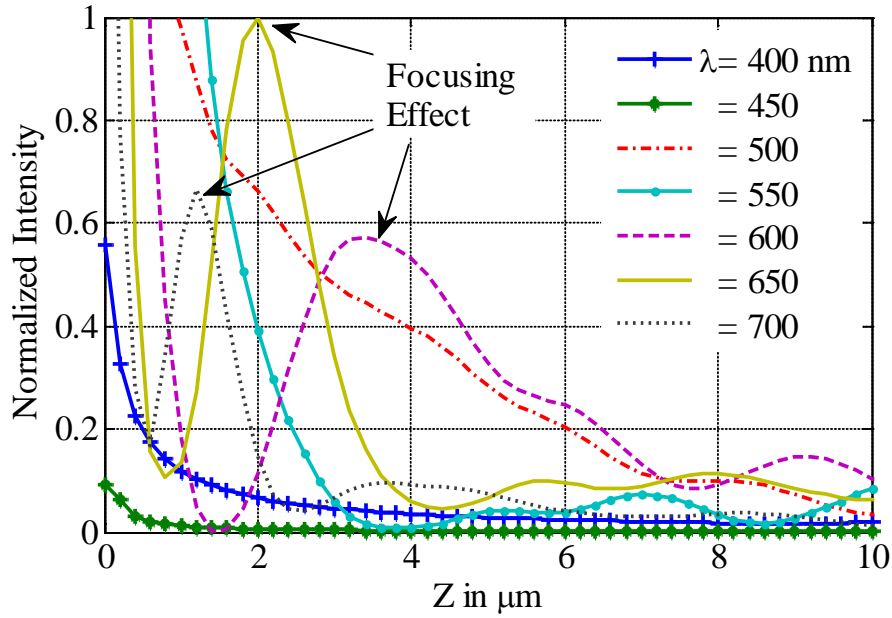
Fig. 2.25. The longitudinal intensity distribution for the subwavelength slit with metallic surface grooves at a selected set of wavelengths.
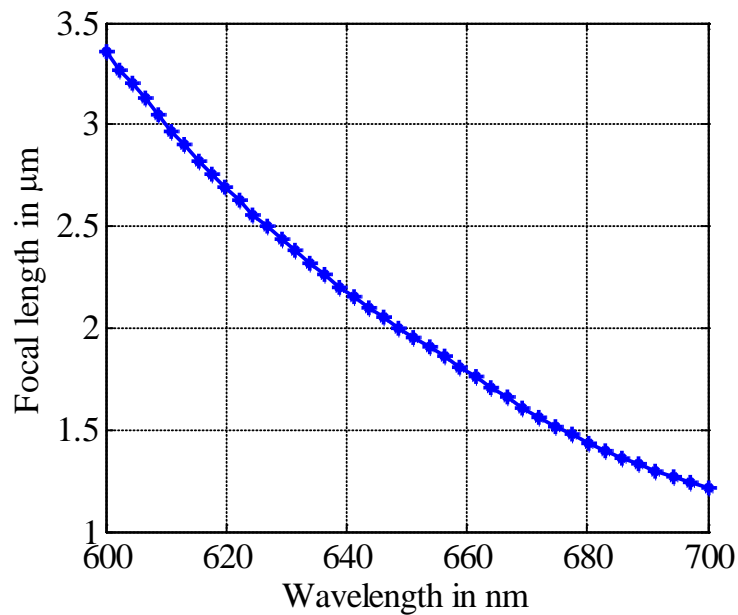
Fig. 2.26. The spectral distribution of the focal length for the subwavelength slit with metallic surface grooves.
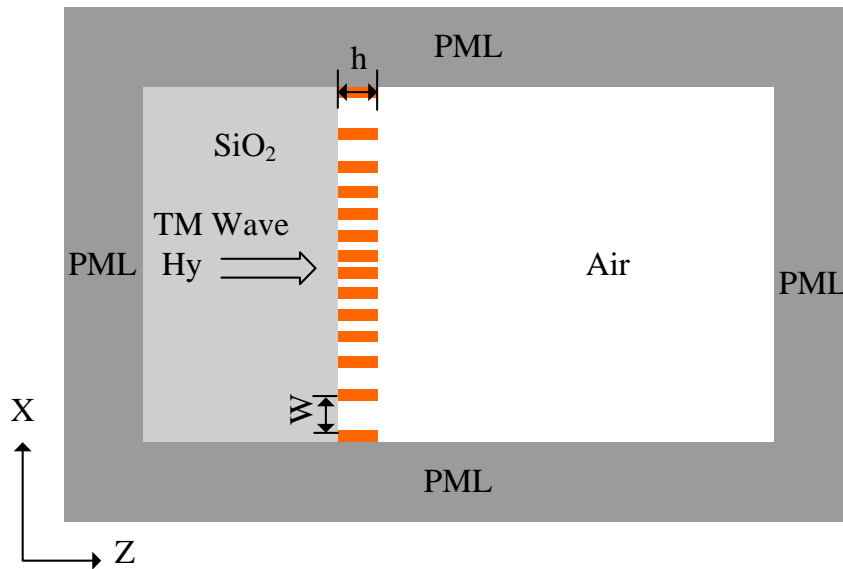
Fig. 2.27. The schematic of the planar slit array.

2.5.4 Slit Array in a Metallic Film

In this example, we model the nano-scale slit array shown in Fig. 2.27 using time-domain TLM. This structure has been utilized for angle compensation which enhances the efficiency of the off-axis pixels in solid state image sensors [52]. It also allows for beaming and focusing effects which can be utilized in optical microscopy [52]-[58].

The considered structure has a metal thickness h=400.0 nm. The slit widths are ranging from 80.0 nm in the middle to 150.0 nm at edges [53]. The dielectric constant of SiO_2 is 2.13. The metallic film is made of gold, which has the same parameters as in the previous example.
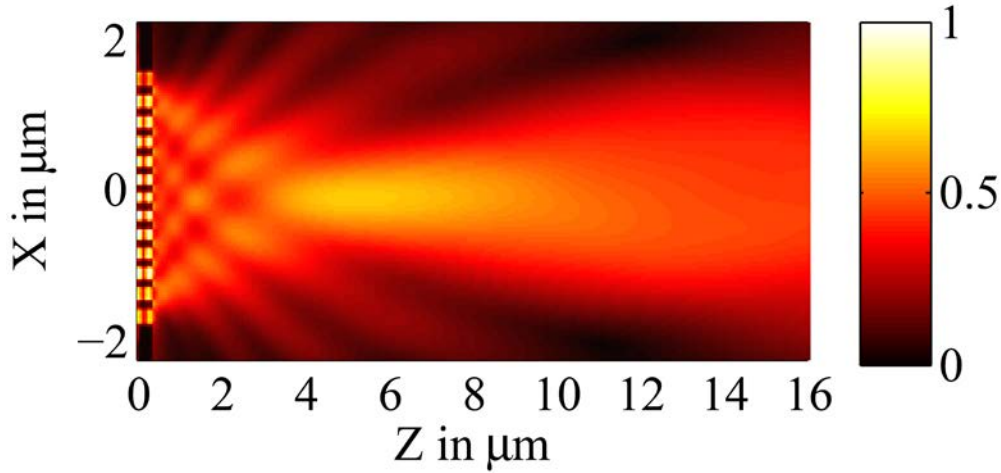
Fig. 2.28. The magnetic field distribution for the planar slit array.

We set the node dimension of the TLM domain to 10.0 nm for 8000 time steps. For the 5.0 μm ×16.0 μm structure, the computational domain includes 500× 1600 TLM nodes. The simulation time is approximately 100 minutes. The excitation exploits a wide band Gaussian-modulated sinusoid with wavelength ranging from 400.0 nm to 800.0 nm. In Fig. 2.28, the magnetic field distribution is shown for an incident wavelength of 637.0 nm. The achieved focal length is 5.3 μm which is identical to that reported experimentally [53]. The field distribution around the focal spot in the transverse direction is compared to the reported experimental result in Fig. 2.29. Both results have a good agreement.

From the conducted time-domain simulation, the focusing effect for different incidence wavelengths is investigated. Fig. 2.30 shows the longitudinal field distribution at the structure axis of the symmetry. The maximum field indicates the position of the
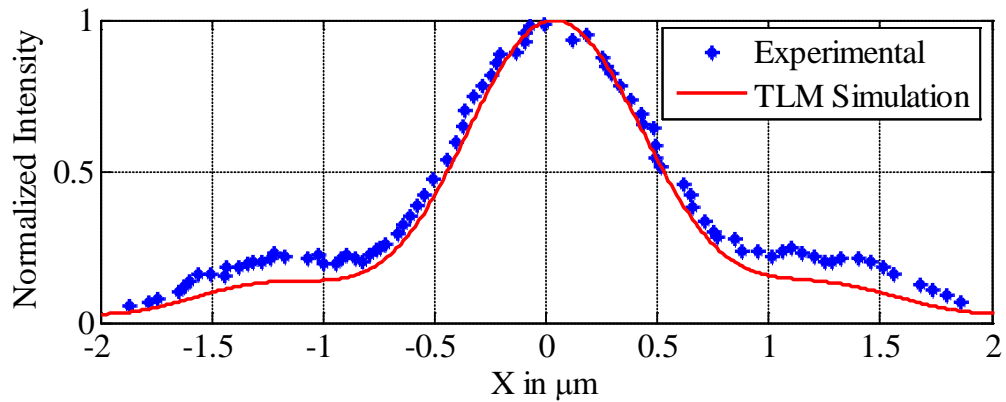
Fig. 2.29. The transverse intensity profile around the focal spot for the slit array.
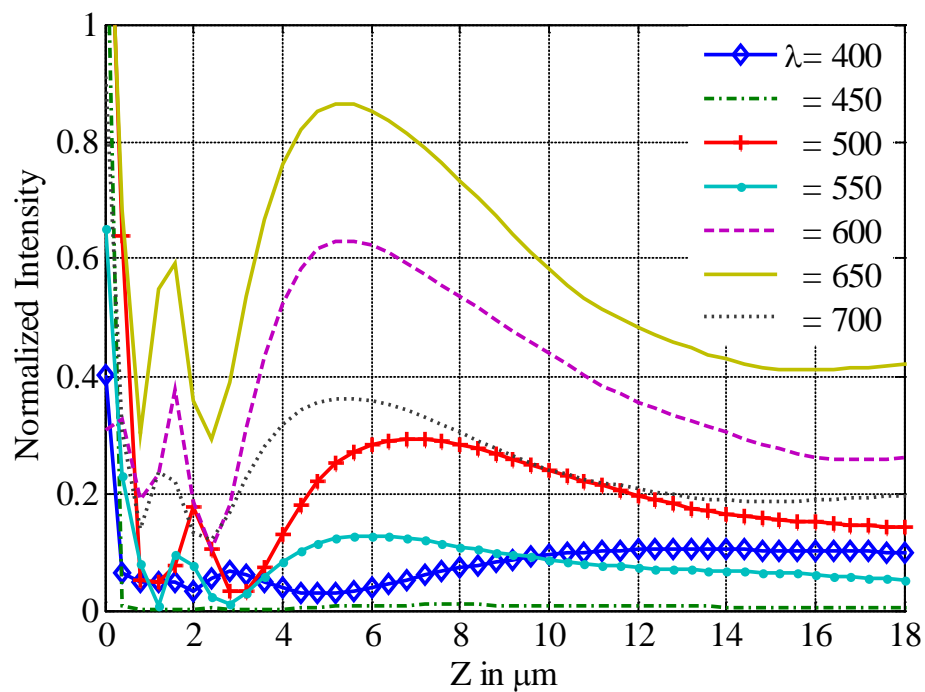
Fig. 2.30. The longitudinal intensity distribution for the planar slit array at a selected set of wavelengths.
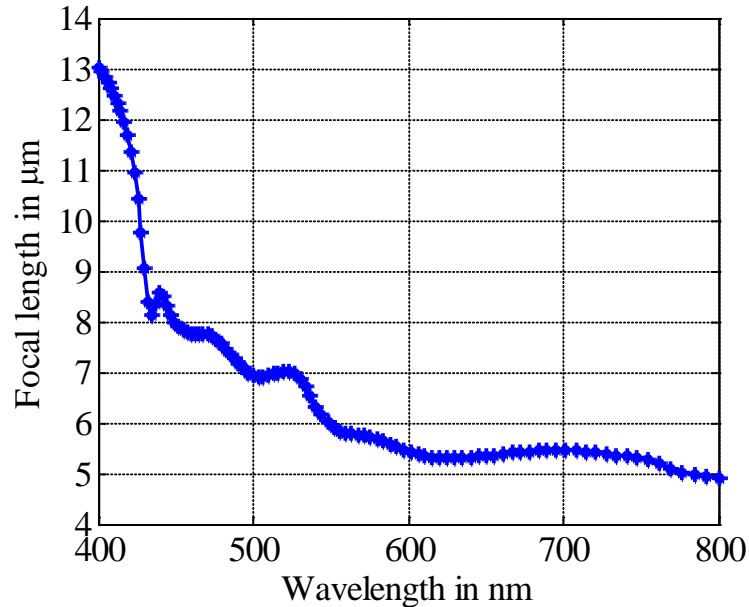
Fig. 2.31. The spectral distribution of the focal length of the planar slit array.

focal point. It is clear that focusing is achieved for all wavelengths at different focal lengths. The focusing effect for this structure is based on the interference pattern constructed from different waves coming out of the slits. The optical size of the lens determines the focal point. For an increased wavelength, the optical length is decreased leading to a scaled-down focal length. As the wavelength increases, the focal point becomes closer to the lens as shown in Fig. 2.31.

2.6 SUMMARY

We successfully demonstrated, for the first time, the application of the TLM method to the time-domain modeling of surface plasmon polaritons (SPPs) devices. A dispersive TLM node is utilized which allows for the modeling of any dispersion behaviour through simple difference equations. Wideband responses of various focusing

structures have been accurately modeled using impulse excitations or Gaussian modulated sinusoids. Our calculations match well the reported results in the literature.

2.7   REFERENCES

[1]   A. Yariv, "Coupled-mode theory for guided-wave optics," *IEEE J. Quantum Electron.,* vol. QE-9, pp. 919-933, 1973.

[2]   M. Yamada and K. Sakuda, "Analysis of almost-periodic distributed feedback slab waveguides via a fundamental matrix approach," *Appl. Opt.,* vol. 26, pp. 3474-3478, 1987.

[3]   K. A. Winick, "Effective-index method and coupled-mode theory for almost-periodic waveguide gratings: A comparison," *Appl. Opt*., vol. 31, pp. 757-764, 1992.

[4]   P. B. Catrysse and S. Fan, "Understanding the dispersion of coaxial plasmonic structures through a connection with the planar metal-insulator-metal geometry," *Appl. Phys. Lett*., vol. 94, p. 231111, 2009.

[5]   J. Henzie, J. Lee, H.M. Lee, W. Hasan, T.W. Odom, "Nanofabrication of Plasmonic Structures", *Annu. Rev. Phys. Chem*., vol. 60, pp. 147-165, 2008.

[6]   J. Melngailis, "Focused ion beam technology and applications," *J. Vac. Sci. Technol.,* vol. B5**,** pp. 469-495, 1987.

[7]   S. Aksu, A. A. Yanik, R. Adato, A. Altar, M. Huang, and H. Altug, "High-throughput nanofabrication of infrared plasmonic nanoantenna arrays for vibrational nanospectroscopy," *Nano Lett.* vol. 10, pp. 2511-2518, 2010.

[8] X. Li, *Optoelectronic devices: design, modeling, and simulation*. Cambridge University Press, New York, NY, USA, 2009.

[9] A. Taflove and S. C. Hagness, *Computational Electrodynamics: The Finite-Difference Time-Domain Method*, Third Edition, Artech House Publishers, Boston, 2005.

[10] G. V. Eleftheriades, O. Siddiqui, and A. Iyer, "Transmission line models for negative refractive index media and associated implementations without excess resonators," *IEEE Microwave Wireless Compon. Lett.*, vol. 13, pp. 53-55, 2003.

[11] A. J. Lowery, "New dynamic semiconductor laser model based on the transmission-line modeling method," *Proc. Inst. Elect. Eng.*, pt. J, vol. 134, pp. 281-289, 1987.

[12] P.B. Johns, and M. O'Brien, "Use of transmission-line modelling method to solve non-linear lumped networks", *Radio Electron.-Eng.*, vol. 50, pp. 59-70, 1980.

[13] S. Hui, K. FUNG, and C. Christopoulos, "Decoupled simulation of multistage power electronics systems using transmission-line links," *23rd Annu. IEEE Power Electronics Specialist Conference*, Toledo, Spain, 1992, vol. 3, pp. 1324-1330.

[14] L. Vietzorreck, F. Coccetti, V. Chtchekatourov, P. Russer, "Modeling of MEMS Capacitive switches by TLM," *2000 IEEE MTT-S International Microwave Symposium Digest*, vol. 2, Boston, MA, 2000, pp.1221-1223.

[15] C. Christopoulos and J. Herring, "The application of transmission-line modeling (TLM) to electromagnetic compatibility problems," *IEEE Trans. on Electromagnetic Compatibility*, vol. 35, pp. 185-191, 1993.

[16]   D. Vahldieck, "A hybrid drift-diffusion-TLM analysis of traveling-wave photodetectors," *IEEE Trans. Microwave Theory Tech.*, vol. 53, pp. 2700-2706, 2005.

[17]   D. D. Cogan, *Transmission line matrix (TLM) techniques for diffusion applications*, CRC Press, 1998.

[18]   De Cogan, Donard, William J. O'Connor, and Susan Pulko. *Transmission Line Matrix (TLM) in computational mechanics*. CRC Press, 2005.

[19]   P. B. Johns and R. L. Beurle, "Numerical solution of 2-dimensional scattering problems using a transmission-line matrix," *Proc. Inst. Elec. Eng.*, vol. 118, pp.1203-1208, 1971.

[20]   C. Christopoulos, *The Transmission-Line Modeling Method: TLM*, Wiley-IEEE Press, 1995.

[21]   P. B. Johns, "A symmetrical condensed node for the TLM method," *IEEE Trans. Microwave Theory Tech.*, vol. 35, pp. 370-377, 1987.

[22]   O. Jacquin, F. Ndagijimana, A. Cachard, and P. Benech, "Application of the TLM technique to integrated optic component modelling," *Int. J. of Numer. Model. : Electronic Networks, Devices and Fields*, vol. 14, pp. 95-105, 2001.

[23]   W. J. R. Hoefer, "The transmission-line matrix method –theory and applications," *IEEE Trans. Microwave Theory Tech.*, vol. MTTT-33, pp. 882-893, 1985.

[24]   P. B. Johns, "A simple, explicit and unconditionally stable numerical solution of the diffusion equation," *Int. J. Numer. Methods Eng.*, vol. 11, pp. 1307-1328, 1977.

[25] L. de Menezes and W. J. R. Hoefer, "Modeling frequency dependent dielectrics in TLM," *in IEEE Antennas Propagat.-S Symp. Dig*., 1994, pp. 1140-1143.

[26] L. de Menezes and W. J. R. Hoefer, "Modeling nonlinear dispersive media in 2-D-TLM," *in 24th European Microwave Conference Proc*., 1994, pp. 1739-1744.

[27] L. de Menezes and W. J. R. Hoefer, "Modeling of general constitutive relationships using SCN TLM," *IEEE Trans. Microwave Theory Tech.*, vol. 44, pp. 854-861, 1996.

[28] J. Paul, C. Christopoulos, and D. W. P. Thomas, "Generalized material models in TLM—Part I: Materials with frequency-dependent properties," *IEEE Trans. Antennas Propagat.*, vol. 47, pp. 1528-1534, 1999.

[29] J. Paul, C. Christopoulos, and D. W. P. Thomas, "Generalized material models in TLM—Part 2: Materials with anisotropic properties," *IEEE Trans. Antennas Propag*., vol. 47, pp. 1535-1542, 1999

[30] J. Paul, C. Christopoulos, and D.W.P. Thomas, "Perfectly matched layer for transmission line modelling (TLM) method," *Electronics Lett*., vol. 33, pp. 729-730, 1997.

[31] W. Greiner and J. Reinhardt, *Quantum Electrodynamics*, 4th ed., Berlin, Heidelberg: Springer Berlin Heidelberg, 2009.

[32] J. D. Jackson, *Classical Electrodynamics*, 3rd ed. New York: John Wiley, 1999.

[33] S. A. Maier, *Plasmonics: Fundamentals and Applications*, Springer, 2007.

[34]   R. J. Luebbers, F. Hunsberger, and K. S. Kunz, "A frequency-dependent finite-difference time-domain formulation for transient propagation in plasma," *IEEE Trans. Antennas Propagat.*, vol. 39, pp. 29-34, 1991.

[35]   J. P. Bérenger, "A perfectly matched layer for the absorption of electromagnetic waves," *J. Comput. Phys.*, vol. 114, pp. 185-200, 1994.

[36]   C. Eswarappa and W. Hoefer, "Implementation of Berenger absorbing boundary conditions in TLM by interfacing FDTD perfectly matched layers," *Electronics Lett.*, vol. 31, p. 1264, 1995.

[37]   S. Le Maguer, N. Peňa, and M. Ney, "Matched absorbing medium techniques for full-wave TLM simulation of microwave and millimeter-wave components," *Annals of Telecomm.*, vol. 53, pp. 115-129, 1998.

[38]   B. Wang and G. P. Wang, "Plasmon bragg reflectors and nanocavities on flat metallic surfaces," *Appl. Phys. Lett.*, vol. 87, p. 013107, 2005.

[39]   Z. Han, E. Forsberg, and S. He, "Surface plasmon Bragg gratings formed in metal-insulator-metal waveguides," *IEEE Photon. Tech. Lett.*, vol. 19, pp. 91-93, 2007.

[40]   C. Sönnichsen, *Plasmons in metal nanostructures*, Ph.D. dissertation, Ludwig-Maximilians-Universtät München, (München, 2001).

[41]   E. J. Zeman and G. C. Schatz, "An accurate electromagnetic theory study of surface enhancement factors for silver, gold, copper, lithium, sodium, aluminum, gallium, indium, zinc, and cadmium," *J. Phys. Chem.*, vol. 91, pp. 634-643, 1987.

[42]   P. B. Johnson and R. W. Christy, "Optical constants of the noble metals," *Phys. Rev. B*, vol. 6, pp. 4370-4379, 1972.

[43]   J. Park, H. Kim, and B. Lee, "High order plasmonic Bragg reflection in the metal-insulator-metal waveguide Bragg grating," *Opt. Express*, vol. 16, pp. 413-425, 2008.

[44]   A. Hosseini, H. Nejati, and Y. Massoud, "Modeling and design methodology for metal-insulator-metal plasmonic Bragg reflectors," *Opt. Express*, vol. 16, 1475-1480, 2008.

[45]   D. Z. Lin, C. Chang, Y. Chen, D. Yang, M. Lin, J. Yeh, J. Liu, C. Kuan, C. Yeh, and C. Lee, "Beaming light from a subwavelength metal slit surrounded by dielectric surface gratings," *Opt. Express*, vol. 14, pp. 3503-3511, 2006.

[46]   S. Kim, Y. Lim, H. Kim, J. Park, and B. Lee, "Optical beam focusing by a single subwavelength metal slit surrounded by chirped dielectric surface gratings," *Appl. Phys. Let*t., vol. 92, p. 013103, 2008.

[47]   E. D. Palik, *Handbook of optical constants of solids*. Academic Press, 1998.

[48]   F. J. Garcia-Vidal, L. Martin-Moreno, H. J. Lezec, and T. W. Ebbesen, "Focusing light with a single subwavelength aperture flanked by surface corrugations," *Appl. Phys. Lett.*, vol. 83, pp. 4500-4502, 2003.

[49]   B. Guo, Q. Gan, G. Song, J. Gao, and L. Chen, "Numerical study of a high-resolution far-field scanning optical microscope via a surface plasmon modulated light source," *J. Lightwave Technol.*, vol. 25, pp. 830-833, 2007.

[50] H. Shi, C. Du, and X. Luo, "Focal length modulation based on a metallic slit surrounded with grooves in curved depths," *Appl. Phys. Lett.*, vol. 91, p. 093111, 2007.

[51] B. Lee, S. Kim, H. Kim, and Y. Lim, "The use of plasmonics in light beaming and focusing," *Prog. in Quantum Electronics*, vol. 34, pp. 47-87, 2010.

[52] L. Verslegers, P. B. Catrysse, Z. Yu, and S. Fan, "Planar metallic nanoscale slit lenses for angle compensation," *Appl. Phys. Lett.*, vol. 95, p. 071112, 2009.

[53] L. Verslegers, P. B. Catrysse, Z. Yu, J. S. White, E. S. Barnard, M. L. Brongersma, and S. Fan, "Planar lenses based on nanoscale slit arrays in a metallic film," *Nano Lett.*, vol. 9, pp. 235-238, 2009.

[54] Z. Sun and H. K. Kim, "Refractive transmission of light and beam shaping with metallic nano-optic lenses," *Appl. Phys. Lett.*, vol. 85, pp. 642-644, 2004.

[55] H. Shi, C. Wang, C. Du, X. Luo, X. Dong, and H. Gao, "Beam manipulating by metallic nano-slits with variant widths," *Opt. Express*, vol. 13, pp. 6815-6820, 2005.

[56] D. Choi, Y. Lim, S. Roh, I. Lee, J. Jung, and B. Lee, "Optical beam focusing with a metal slit array arranged along a semicircular surface and its optimization with a genetic algorithm," *Appl. Opt.*, vol. 49, pp. A30-A35, 2010.

[57] J. Homola, S. S. Yee, and G. Gauglitz, "Surface plasmon resonance sensors: review," *Sens. Actuators B*, vol. 54, pp. 3-15, 1999.

[58] R. D. Harris and J. S. Wilkinson, "Waveguide surface plasmon resonance sensors," *Sens. Actuators B*, vol. 29, pp. 261-267, 1995.

3 MEMORY EFFICIENT TLM-BASED ADJOINT VARIABLE METHOD

In Chapter 2, we discuss the transmission line modeling (TLM) approach for the simulation of nano-plasmoic structures. Utilizing the self-consistent electric and magnetic field calculations, we model the structure to find its responses. The outcome of a time-domain simulation is a time sequence of all the electric and magnetic field polarizations at any spatial point. This data can be transformed to the frequency domain where the signal can be spectrally analyzed.

For design optimization of EM structures, the simulation has to be performed iteratively until an optimal objective value is reached [1]. The design parameters can be fine-tuned (optimized) to reach a good performance. However, tuning the design parameters does not generally provide an optimal design. The EM problem is thus formulated as an optimization problem at the response level [2]. The response is optimized by choosing the optimal design parameters (geometry and material properties). On the other hand, imaging and spectroscopy problems (inverse problems) require computationally efficient optimization approach to predict the structure parameters that lead to a given experimental response, [3] and [4]. The inverse problem is thus formulated as an optimization problem where the unknown structure parameters are predicted to minimize the deviation between the simulated and the experimental responses.

Sensitivity analysis resides at the heart of any optimization algorithm. It estimates how the objective function would change in response to slight changes (perturbations) in the design parameters [5]-[15]. Sensitivity calculation is an integral part of derivative-based optimization, where the vector of optimization parameters (p) is tuned according to the calculated derivatives [11]. Sensitivity is also utilized for tolerance and yield analysis.

Conventional approaches for sensitivity calculation introduces formidable extra computational cost. For the calculation of the sensitivity utilizing the finite difference approach at the response level, at least n extra simulations have to be performed, where n is the number of optimization parameters. These simulations are conducted for a structure with a perturbed design parameter p_i, where $i=1,2,\ldots,\ n$. The accurate central finite difference approach requires two extra simulations per each parameter. This leads to the execution of $2n$ extra simulations.

Adjoint variable method (AVM) represents the ultimate efficient modality for gradient or Jacobian calculations [12]-[25]. It estimates the sensitivity of the objective function with respect to all parameters using at most one extra simulation [14]. This can be contrasted with finite difference approaches where at least n extra simulations are required. The AVM approach has been successfully developed for both time and frequency domain modeling techniques, including the finite difference time-domain (FDTD) method [15], transmission line modeling (TLM) method [14], [17], method of moments (MOM) [18], and the finite element method (FEM) [8].

A self adjoint variable method (SAVM) is developed for sensitivity calculations of the frequency-dependent network parameters [22], [23]. Using this approach, the response and its sensitivities with respect to all design parameters are calculated without any extra simulations. Recently, the AVM algorithm has found early implementation in commercial softwares such as HFSS [24] and CST [25].

The development of the AVM approach for TLM-based solvers has been achieved in several stages. The AVM was first developed for 2D time-domain TLM problems with perfect conducting discontinuity where the shape of a metallic object is the optimizable design parameter [14]. An efficient mapping algorithm is developed in order to avoid the simulation of a perturbed adjoint structure. In this approach, only the perturbed transmission line links connected to the metallic object needs to be stored.

The AVM approach was then extended to include dielectric lossy materials [19]. An analytically accurate technique was developed to avoid any approximation for the required simulations. In this case, the impulses of all links inside the lossy dielectric discontinuities need to be stored in both the original and adjoint simulations at all time steps. The approach was also developed for problems that include dispersive boundaries [20] and for 3D problems [21]. A breakthrough self adjoint variable method (SAVM) is developed for a frequency dependent network parameters [22], [23]. Recently, the developed TLM-based AVM technique is utilized for sensitivity analysis of temporal fields [16].

TLM-based AVM for lossy dielectric discontinuities are memory intensive [19], [21]. The algorithm stores the incident impulses at all perturbed cells at all time steps for

both the original and adjoint simulations. For these problems, the perturbation is volumetric and thus, the entire discontinuity domain is perturbed. This presents a memory barrier for conducting TLM-based AVM approach for problems incorporating large perturbed discontinuities.

In this Chapter, we present a novel memory efficient implementation of the AVM algorithm with TLM. We show that the memory requirement is reduced to only 10% of that required for original TLM-based AVM algorithms [19], [21]. An elegant mathematical manipulation of the scattering matrices reduces the storage in the original domain simulation to 20% of that reported in earlier implementations. The memory storage of the adjoint simulation is completely avoided by estimating the sensitivities on the fly. This results in a net 90% reduction in the memory storage requirement for the algorithm. This chapter presents thorough explanation of the TLM-based AVM technique utilizing the memory efficient approach. The AVM memory requirements are demonstrated for both the 2D and 3D cases. The theory is supported by a number of general electromagnetic structures.

3.1 ADJOINT VARIABLE METHOD

Adjoint variable method is utilized to calculate the sensitivity of an objective function with respect to any optimization parameter. Exact sensitivity is obtained for analytic perturbation of the system equations. AVM utilizes a main simulation along with an adjoint simulation whose excitation is based on the objective function.

A general EM-based objective function is formulated as [14]

$$F = \int_0^{T_m} \int_\Omega \psi(\boldsymbol{p}, \boldsymbol{V}) d\Omega dt = \int_0^{T_m} \Psi(\boldsymbol{p}, \boldsymbol{V}) dt \qquad (3.1)$$

where Ω is the observation domain, $\boldsymbol{V}$ is the continuous vector of $\boldsymbol{V}_k$ and T_m is the simulation time. The vector $\boldsymbol{V}$ represents the simulation state variable. The discrete sequence $\boldsymbol{V}_k$ of the incident voltage impulses to all the TLM links, inside the computational domain, can be calculated according to (2.36) as follows

$$\boldsymbol{V}_{k+1} = \boldsymbol{CSV}_k + \boldsymbol{V}_k^s \qquad (3.2)$$

The sensitivity of F with respect to the ith parameter p_i can be calculated as

$$\frac{\partial F}{\partial p_i} = \frac{\partial^e F}{\partial p_i} + \int_0^{T_m} \left(\frac{\partial \Psi}{\partial \boldsymbol{V}}\right)^T \frac{\partial \boldsymbol{V}}{\partial p_i} dt \qquad (3.3)$$

where $\partial^e / \partial p_i$ denotes the explicit dependences and is a zero in most practical cases. The sensitivity can be calculated once $\partial \boldsymbol{V} / \partial p_i$ is obtained. Direct calculation of this quantity would require at least N extra simulations. An alternative AVM approach is utilized for the calculation of the integral in (3.3). This approach is based on the numerical technique system update equation (3.2) and can be explained as follows.

For a sufficiently small simulation time step (Δt), the vector of incident voltage impulses at a time step $k+1$ can be approximated as

$$\boldsymbol{V}_{k+1} = \boldsymbol{V}_k + \left(\frac{\partial \boldsymbol{V}}{\partial t}\right)_k \Delta t \qquad (3.4)$$

Utilizing (3.2), the time derivative of the incident voltage can be calculated as

$$\left(\frac{\partial \boldsymbol{V}}{\partial t}\right)_k = \frac{(\boldsymbol{CS} - \boldsymbol{I})}{\Delta t} \boldsymbol{V}_k + \frac{\boldsymbol{V}_k^s}{\Delta t} \qquad (3.5)$$

where I is the identity matrix. By defining the matrix $A = (CS - I)/\Delta t$, (3.5) at any time

instant k can be written as

$$\frac{\partial V}{\partial t} = AV + \frac{V^s}{\Delta t}$$

(3.6)

For sensitivity with respect to arbitrary parameter p_i, the derivative of (3.6) is calculated

as,

$$\frac{\partial^2 V}{\partial t \partial p_i} = \frac{\partial A}{\partial p_i} V + A \frac{\partial V}{\partial p_i}$$

(3.7)

Equation (3.7) is multiplied by the transpose of an arbitrary adjoint variable λ and

integrated over the simulation time $[0, T_m]$ to get

$$\int_0^{T_m} \lambda^T \left(\frac{\partial^2 V}{\partial t \partial p_i} - \frac{\partial A}{\partial p_i} V - A \frac{\partial V}{\partial p_i} \right) dt = 0$$

(3.8)

In (3.8), $\lambda^T \in R^{NL}$ where N is the number of computational nodes and L is the number of

links per each node. Equation (3.8) holds for an arbitrary adjoint variable and can be

applied to all the structure design parameters. We integrate (3.8) by parts [19]:

$$\lambda^T \frac{\partial V}{\partial p_i} \bigg|_0^{T_m} - \int_0^{T_m} \left(\frac{\partial \lambda^T}{\partial t} \frac{\partial V}{\partial p_i} + \lambda^T \frac{\partial A}{\partial p_i} V + \lambda^T A \frac{\partial V}{\partial p_i} \right) dt = 0$$

(3.9)

The vector V has a zero initial value independent of the optimization parameter p_i. The

adjoint variable can be arbitrary chosen to be of zero terminal condition, i.e. $\lambda(T_m) = 0$. It

follows that the first term in (3.9) vanishes. Equation (3.9) can be rewritten as:

$$\int_0^{T_m} \left(\frac{\partial \lambda^T}{\partial t} + \lambda^T A \right) \frac{\partial V}{\partial p_i} dt = -\int_0^{T_m} \left(\lambda^T \frac{\partial A}{\partial p_i} V \right) dt$$

(3.10)

From (3.3), using (3.10), we can construct the following system equation [14]:

74

$$\frac{\partial \boldsymbol{\lambda}^T}{\partial t} + \boldsymbol{\lambda}^T \boldsymbol{A} = \left(\frac{\partial \Psi}{\partial \boldsymbol{V}}\right)^T \tag{3.11}$$

which represents a possible choice for the adjoint variable calculation scheme. Equation (3.11) can be transposed, and the matrix $\boldsymbol{A}$ is substituted to get

$$\Delta t \frac{\partial \boldsymbol{\lambda}}{\partial t} + (\boldsymbol{S}^T \boldsymbol{C}^T - \boldsymbol{I})\boldsymbol{\lambda} = \Delta t \left(\frac{\partial \Psi}{\partial \boldsymbol{V}}\right) \tag{3.12}$$

Equation (3.12) can be reduced to the following update equation for the adjoint variable $\boldsymbol{\lambda}$,

$$\boldsymbol{\lambda}_{k-1} = (\boldsymbol{S}^T \boldsymbol{C}^T)\boldsymbol{\lambda}_k - \boldsymbol{\lambda}_k^s, \quad \boldsymbol{\lambda}(T_m) = \boldsymbol{0} \tag{3.13}$$

where $\boldsymbol{\lambda}_k^s = \Delta t \left(\partial \Psi / \partial \boldsymbol{V}\right)_{t=k\Delta t}$ is defined as the adjoint excitation.

Equation (3.13) is the adjoint update equation. It runs backward in time with a zero terminal condition. The excitation of the adjoint problem is derived from the objective function. By conducting the adjoint simulation, the value of the adjoint variable is calculated at every instant at any node inside the computational domain. Using (3.3), (3.10), and (3.11), the sensitivity of the objective function F with respect to a design parameter, p_i, is formulated as

$$\frac{\partial F}{\partial p_i} = \frac{\partial^e F}{\partial p_i} - \int_0^{T_m} \left(\boldsymbol{\lambda}^T \frac{\partial \boldsymbol{A}}{\partial p_i} \boldsymbol{V}\right) dt \tag{3.14}$$

which can be written in terms of the discrete values of the main and adjoint variables as

$$\frac{\partial F}{\partial p_i} = \frac{\partial^e F}{\partial p_i} - \Delta t \sum_{k=1}^{N_t} \boldsymbol{\lambda}_k^T \frac{\partial \boldsymbol{A}}{\partial p_i} \boldsymbol{V}_k \tag{3.15}$$

where the total simulation time $T_m = \Delta t N_t$. Equation (3.15) is utilized to calculate the AVM sensitivity by storing the main and adjoint fields that contribute to the summation. We notice that, the matrix $\partial A / \partial p_i$ contains few nonzero elements depending on the optimization parameter. Consequently, only the fields in the perturbation domain contribute to the calculation of the sensitivity.

For the derivation of the AVM theory, we did not use any approximation. The calculated sensitivity analyses are of analytical accuracy for the case of domain material perturbation. We note from (3.13), that the adjoint simulation does not require any perturbation of the original structure as it utilizes the same system matrix. One adjoint simulation is sufficient to calculate all the sensitivities. In the original simulation, we store the fields inside the perturbed domain according to the nonzero elements of the matrix $\partial A / \partial p_i$. Equation (3.15) is put in the more compact vector form:

$$\frac{\partial F}{\partial p_i} = -\sum_k \sum_j \boldsymbol{\lambda}_{j,k}^T \boldsymbol{\eta}_{j,k}^i \tag{3.16}$$

where the explicit derivative is zero in most practical cases. In (3.16), j denotes the node index. The vector of fields recorded in the main simulation at the jth node is defined as $\boldsymbol{\eta}_{j,k}^i = \Delta t \left(\partial A^j / \partial p_i \right) V_{j,k}$. The matrix $A^j \in R^{L \times L}$ is the nodal system matrix, and $V_{j,k}, \boldsymbol{\lambda}_{j,k} \in R^{L \times 1}$ are the vectors of all incident voltage impulses and adjoint impulses at the jth node.

From (3.16), we notice that all the voltage impulses at the TLM links, associated with each perturbed node inside the domain, has to be stored in both the original and

adjoint simulation. This extra storage is required at each time instant during the simulation. A total of $2 \times L \times N_p \times N_t$ extra storage is required, where *L* is the number of links per each node, and N_p is the number of perturbed nodes inside the domain. This storage may be formidable for volumetric large perturbation, which imposes a practical constraint on the size of the perturbation allowed by the AVM approach. Bulk photonic structures are electrically large. The TLM-based AVM theory in its current form is not of practical use for large photonic structures as a large memory overhead is required.

The TLM-based AVM is widely used for stub-loaded TLM techniques [14], [19]-[21]. These techniques are similar to that presented in Chapter 2, as they maintain the domain synchronization using a background air media introduced throughout the domain [26], [27]. The domain inhomogeneity is taken into consideration by introducing an extra stub to compensate the extra permittivity or permeability. The AVM approaches developed for stub-loaded technique requires the storage of all voltage impulses, at the TLM network ports, and the extra stubs as well [28]. For the modeling of lossy dielectric media with stub-loaded TLM, an extra stub is associated with each electric field polarization for a symmetrical condensed node. A total of 5 TLM ports per each node are needed for the 2D-TLM (see Fig. 3.1). For 3D-TLM case, 15 TLM ports are associated with each node.

In this Chapter, we introduce the impulse sampling technique for the efficient implementation of TLM-based AVM, for problems of lossy dielectric media. The total memory usage is reduced by 90% through an elegant mathematical manipulation that
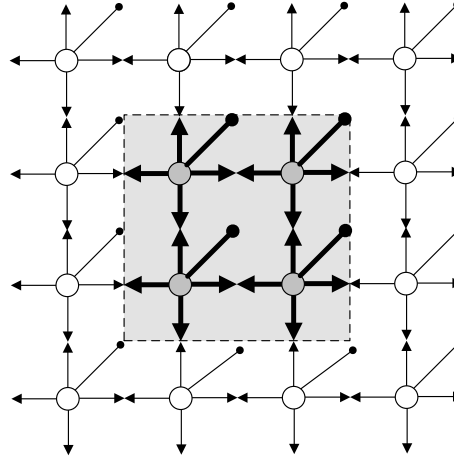
Fig. 3.1. Illustration of the link storage for the regular TLM based AVM. The arrowed bold links are the ones for which $\boldsymbol{\eta}_{j,k}^{i}$ has nonzero components for a perturbation in the material parameters in the shadowed region.

overcomes the redundant calculations in the original technique. There is no computational overhead associated with the memory saving. The proposed theory can be applied to bulk photonic structures with a large volumetric perturbation domain. The theory is applied to numerous microwave and photonic structures to ensure validity and accuracy.

3.2   IMPULSE SAMPLING METHOD

Enhancement of the memory requirement of TLM-based AVM can be achieved through careful manipulation of the system matrix $\boldsymbol{A} = (\boldsymbol{CS} \text{-} \boldsymbol{I})/\Delta t$ and its derivatives with respect to the designable parameters. From (2.35) and (2.36), the nodal scattering matrix $\boldsymbol{S}^{j}$ at each cell is expanded using two matrices as follows,

$$\boldsymbol{S}^{j} = \tilde{\boldsymbol{T}}^{j} - \boldsymbol{P}^{j} \tag{3.17}$$

where $\tilde{\boldsymbol{T}}^{\,j} = \boldsymbol{RTR}_{ex} \in R^{L \times L}$ is a parameter-dependent modified transmission matrix, denoted by $\tilde{\boldsymbol{T}}^{\,j}$, to avoid confusion with the field transmission matrix denoted by $\boldsymbol{T}$, defined as in (2.35). $\boldsymbol{P}^{\,j} \in R^{L \times L}$ is a constant matrix independent of the optimization variables. Due to the symmetry of link contributions for each cell, the matrix $\tilde{\boldsymbol{T}}^{\,j}$ can be divided into 3 sub-matrices each with identical rows (for 3D-TLM case). Each sub-matrix is associated with a distinct field polarization. The derivation of the impulse sampling scheme is generalized for the 2D and 3D cases in this section, while details of implementation for specific approaches are proposed in the following sections.

The AVM scheme calculated by (3.15), and (3.16) depends on the calculation of the voltage impulses at the links dependent on the optimization parameter using

$$\boldsymbol{\eta}_{j,k}^{i} = \boldsymbol{C}^{\,j} \frac{\partial \boldsymbol{S}^{\,j}}{\partial p_i} \boldsymbol{V}_{j,k} \tag{3.18}$$

where the connection matrix $\boldsymbol{C}$ represents a swapping operation that does not depend on the optimization parameter. We substitute by (3.17) in (3.18) to get

$$\boldsymbol{\eta}_{j,k}^{i} = \boldsymbol{C}^{\,j} \frac{\partial \tilde{\boldsymbol{T}}^{\,j}}{\partial p_i} \boldsymbol{V}_{j,k} \tag{3.19}$$

where $\partial \boldsymbol{P}^{\,j} / \partial p_i = 0$. It can be shown for both 2D and 3D-TLM approaches that the term $\left(\partial \tilde{\boldsymbol{T}}^{\,j} / \partial p_i \right) \boldsymbol{V}_{j,k}$ produces a vector of size L of identical row dependence on the material design parameters. For the 2D case we can calculate

$$\frac{\partial \tilde{\boldsymbol{T}}^{\,j}}{\partial p_i} \boldsymbol{V}_{j,k} = \zeta_{j,k}^{i} \boldsymbol{f}_p \tag{3.20}$$

where $\zeta_{j,k}^{i}$ is a scalar quantity to be stored for each cell affected by the optimization

parameter p_i, and $\boldsymbol{f}_p \in R^L$ is a time independent analytic function of the local material

properties only. The vector $\boldsymbol{f}_p$ is not stored during the original or adjoint simulations as it

is calculated analytically as a function of the material property of the local cell. In most

practical cases $\boldsymbol{f}_p$ are constant throughout the entire perturbation domain. However, each

entry of the produced vector are linked to a different cell due to application of the

connection matrix as in (3.19). The subsequent connection process can be avoided by

defining a modified adjoint variable vector

$$\tilde{\boldsymbol{\lambda}}_k^T = \boldsymbol{\lambda}_k^T \boldsymbol{C} \tag{3.21}$$

Equations (3.21) and (3.17) are substituted in (3.15) to get

$$\frac{\partial F}{\partial p_i} = \frac{\partial^e F}{\partial p_i} - \sum_{k=1}^{N_t} \tilde{\boldsymbol{\lambda}}_k^T \frac{\partial \tilde{\boldsymbol{T}}}{\partial p_i} \boldsymbol{V}_k \tag{3.22}$$

where $\boldsymbol{A}$ is substituted with the connection and factorized scattering matrices. Equation

(3.22) can be put in concise simpler formulation as

$$\frac{\partial F}{\partial p_i} = -\sum_k \sum_j \zeta_{j,k}^{i} (\tilde{\boldsymbol{\lambda}}_{j,k}^T \boldsymbol{f}_p) \tag{3.23}$$

From (3.23), the AVM sensitivity is calculated by storing one impulse per each

node inside the perturbed domain (see Fig. 3.2). The memory requirement is thus reduced

by 80% for the original simulation compared to the stub-loaded 2D-TLM that requires

the storage of 5 links per each cell. Equation (3.23) can be further simplified to

$$\frac{\partial F}{\partial p_i} = -\sum_k \sum_j \zeta_{j,k}^{i} \mu_{j,k} \tag{3.24}$$
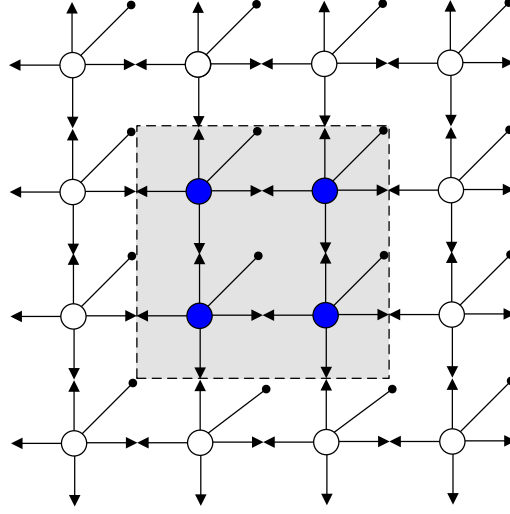
Fig. 3.2. Illustration of the storage for the impulse sampling AVM approach. The colored circled nodes are the ones for which $\partial \tilde{T} / \partial p_i$ has nonzero components for a perturbation in the material parameters in the shadowed region.

where $\mu_{j,k} = \boldsymbol{\lambda}_{j,k}^{T} \boldsymbol{f}_{p}$. From (3.24), we can calculate the sensitivity on the fly, without any extra storage, during the adjoint simulation. The vector summation in (3.16) is thus converted to a scalar summation in (3.24). This approach has been successfully applied for both 2D and 3D TLM problems. We achieve a maximum memory requirement of 10% of that utilized earlier [19], [28]. Notice that, while (3.24) uses a simple sum of scalars; the original equation (3.16) uses a sum of vector products. This implies more saving in the computational time of the algorithm.

3.2.1 Impulse Sampling for 2D-TLM Case

In this section, we provide implementation details of the impulse sampling scheme for the 2D-TLM case. The application of the impulse sampling to the stub-loaded TLM approach is straightforward and is demonstrated in detail in our work [29]-[32]. However,

in this dissertation, we provide the reader an AVM formulation based on the TLM scheme in Chapter 2.

The TLM update scheme, for the 2D shunt node, follows similar procedure to the introduced in Chapter 2. For the numerical TMy mode, there are four ports $V = \begin{bmatrix} V_4^i & V_5^i & V_6^i & V_7^i \end{bmatrix}$ associated with each node. We calculate the node excitation voltage as in (2.24),

$$V_y^{ex} = \left(V_7^i + V_6^i + V_4^i + V_5^i \right) \tag{3.25}$$

where the free source excitation term is assumed zero in the perturbation domain. The normalized field calculated as in (2.27), utilizing the Z-domain representation,

$$V_y = \frac{2V_y^{ex}}{4 + g_e + 4\left(\dfrac{1 - z^{-1}}{1 + z^{-1}} \right)\chi_e} \tag{3.26}$$

The difference equation (3.26) is solved, similar to (2.18), and (2.19), to get

$$V_y = T_{ey}\left(2V_y^{ex} + z^{-1}S_{ey} \right) \quad , \quad S_{ey} = 2V_y^{ex} + k_{ey}V_y \tag{3.27}$$

where S_{ey} is the field accumulator, T_{ey} is the forward gain term [33], and κ_{ey} is the feedback gain term. The gain terms are defined as

$$T_{ey} = (4 + g_e + 4\chi_e)^{-1} \quad , \quad \kappa_{ey} = -(4 + g_e - 4\chi_e) \tag{3.28}$$

The reflected voltage impulses at the four ports

$$V^r = V_y I - V \tag{3.29}$$

where I is the identity matrix. We utilize (3.25), (3.27), and (3.29) to construct the scattering matrix as follows:

$$\begin{bmatrix} V_j^r \\ S_{ey,j} \end{bmatrix} = S^j \begin{bmatrix} V_j \\ z^{-1}S_{ey,j} \end{bmatrix} \tag{3.30}$$

where $S^j \in R^{5\times5}$, is the real valued nodal scattering matrix, constructed for the update of the link (port) voltage impulses and the extra storage associated with the node. This is similar to the stub-loaded TLM technique where the scattering matrix is of the same size. The scattering matrix S^j is factorized as follows,

$$S^j = \tilde{T}^j - I \tag{3.31}$$

where

$$\tilde{T}^j = T_{ey} \begin{pmatrix} 1 \\ 1 \\ 1 \\ 1 \\ 1/T_{ey} + \kappa_{ey} \end{pmatrix} (2 \quad 2 \quad 2 \quad 2 \quad 1) \tag{3.32}$$

Taking the derivative of the scattering matrix with respect to the material properties and multiplying it by the vector constructed from incident voltage impulse and the extra storage S_{ey}, one gets

$$\frac{\partial \tilde{T}^j}{\partial p_i} \begin{bmatrix} V_j \\ S_{ey} \end{bmatrix} = \frac{\partial T_{ey}}{\partial p_i} \left(2V_y^{ex} + z^{-1}S_{ey}\right) \begin{bmatrix} 1 \\ 1 \\ 1 \\ 1 \\ \kappa_{ey} + T_{ey}\left(\dfrac{\partial \kappa_{ey}/\partial p_i}{\partial T_{ey}/\partial p_i}\right) \end{bmatrix} \tag{3.33}$$

Equation (3.33) can be in the form of (3.20) by defining

$$\zeta_y^i = \frac{\partial T_{ey}}{\partial p_i}\left(2V_y^{ex} + z^{-1}S_{ey}\right) \tag{3.34}$$

and

$$\boldsymbol{f}_{y,pi} = \begin{bmatrix} 1 \\ 1 \\ 1 \\ 1 \\ \kappa_{ey} + T_{ey}\left(\dfrac{\partial \kappa_{ey}/\partial p_i}{\partial T_{ey}/\partial p_i}\right) \end{bmatrix} \tag{3.35}$$

where ζ_y^i is denoted with the subscript y as it is based on links contributing to the y polarized electric field. The time and space subscripts k and j are omitted for clarity. Equation (3.34) and (3.35) are substituted in (3.23) towards the calculation of the AVM sensitivity.

The impulse sampling adjoint technique has been applied to the TLM scheme introduced in Chapter 2. However, the application is not limited to a specific TLM scheme as equivalence can be proved between them [29]. The numerical examples that illustrate the accuracy and efficiency of the technique are provided in Section 3.3.

3.2.2 Impulse Sampling AVM for 3D-TLM

The development of the impulse sampling approach for the 3D case follows similar procedure as utilized in the 2D case. The scattering matrix is factorized and the derivatives are simplified. For the 3D case, original stub-loaded algorithms with the SCN utilizes 15 TLM ports to model a lossy dielectric media. We apply our impulse sampling to achieve similar memory saving to the case of 2D. Using the impulse sampling, we

store three nodal voltage values corresponding to the three possible electric field polarizations. This is achieved through factorization of the overall scattering matrix.

For the 3D case, the scattering matrix can be reordered and factorized similar to (3.17), where the modified transmission matrix $\tilde{T}^j$ is defined as

$$\tilde{T}^j = \begin{bmatrix} \tilde{T}^j_x & & \\ & \tilde{T}^j_y & \\ & & \tilde{T}^j_z \end{bmatrix} \tag{3.36}$$

where $\tilde{T}^j \in R^{15 \times 15}$ is a block diagonal matrix whose elements are $\tilde{T}^j_x$, $\tilde{T}^j_y$, and $\tilde{T}^j_z \in R^{5 \times 5}$ constructed in a similar way as (3.32). The AVM calculation requires the derivative of the modified transmission matrix $\tilde{T}^j$ multiplied by the vector of voltage impulses and the extra storage defined as

$$X_{j,k} = \begin{bmatrix} V_0^i & V_1^i & V_2^i & V_3^i & S_{ex} & V_4^i & V_5^i & V_6^i & V_7^i & S_{ey} & V_8^i & V_9^i & V_{10}^i & V_{11}^i & S_{ez} \end{bmatrix}_{j,k} \tag{3.37}$$

From (3.36), we calculate

$$\frac{\partial \tilde{T}^j}{\partial p_i} X_j = \begin{bmatrix} \zeta^i_{x,j,k} f_{x,pi} \\ \zeta^i_{y,j,k} f_{y,pi} \\ \zeta^i_{z,j,k} f_{z,pi} \end{bmatrix} \tag{3.38}$$

where $\zeta^i_{x,j,k}$, $\zeta^i_{y,j,k}$, and $\zeta^i_{z,j,k}$ are dependent on the total fields calculated in the original simulation and are calculated as:

$$\zeta^i_{x,j,k} = \frac{\partial T_{ex}}{\partial p_i} \left(2V^{ex}_{x,j,k} + z^{-1} S_{ex,j,k} \right)$$

$$\zeta^i_{y,j,k} = \frac{\partial T_{ey}}{\partial p_i} \left(2V^{ex}_{y,j,k} + z^{-1} S_{ey,j,k} \right) \tag{3.39}$$

$$\zeta^i_{z,j,k} = \frac{\partial T_{ez}}{\partial p_i} \left(2V^{ex}_{z,j,k} + z^{-1} S_{ez,j,k} \right)$$

In (3.38), $f_{x,pi}$, $f_{y,pi}$, and $f_{z,pi} \in R^{5\times5}$ are vector quantities of analytical dependence on the material properties of the perturbation domain. Similar to (3.35), we get

$$
f_{x,pi} = \begin{bmatrix} 1 \\ 1 \\ 1 \\ 1 \\ \kappa_{ex} + T_{ex}\left(\dfrac{\partial \kappa_{ex} / \partial p_i}{\partial T_{ex} / \partial p_i} \right) \end{bmatrix}, \quad
f_{z,pi} = \begin{bmatrix} 1 \\ 1 \\ 1 \\ 1 \\ \kappa_{ez} + T_{ez}\left(\dfrac{\partial \kappa_{ez} / \partial p_i}{\partial T_{ez} / \partial p_i} \right) \end{bmatrix}
\tag{3.40}
$$

From (3.38)-(3.40), we see that only three values are to be stored at each cell for each time step. This reduces the storage required for the original impulses by 80%. The vector of the adjoint variables $\lambda_{j,k}$ is also split into three sub vectors based on the three polarizations associated with the problem. Using simple additive mathematical operations, the three vector quantities are replaced by three scalar ones. By substitution from (3.38) into (3.22), the AVM sensitivities are calculated using [30]:

$$
\frac{\partial F}{\partial p_i} = -\sum_k \sum_j \left(\zeta^i_{x,j,k} \mu^i_{x,j,k} + \zeta^i_{y,j,k} \mu^i_{y,j,k} + \zeta^i_{z,j,k} \mu^i_{z,j,k} \right)
\tag{3.41}
$$

where $\mu^i_{x,j,k}$, $\mu^i_{y,j,k}$, and $\mu^i_{z,j,k}$ are quantities derivable from the adjoint variables. Using (3.41), we calculate the sensitivities on the fly, without any extra storage, during the adjoint simulation. The vector summation in (3.16) has been converted to the scalar summation (3.41). This implies more saving in the computational time of the algorithm. This approach has been successfully applied to 3D TLM. We achieve a maximum memory requirement of 10% of that is utilized in [21], [28].

From the thorough explanation of the 3D case, we notice that the memory reduction eliminates redundancy due to the symmetric contribution of the background network. The four ports contributing to the calculation of the sensitivity are summed together as in (3.25). For the case of magnetic material with magnetic susceptibility, a direct extension to our work would require another three extra storages based on the normalized current equation, see (2.27), contribution to the derivatives calculated. A brief derivation of the case of magnetic material suggests the definition of similar impulses based on the normalized current calculation equation. For example, the 1D update scheme of i_x at any computational cell using the node excitation term i_x^{ex} is shown in (2.16), and (2.17). The 3D update equation is very similar. However, four links are contributing to the current instead of two. The 3D update equation is formulated as

$$i_x = T_{mx}\left(2i_x^{ex} + z^{-1}S_{mx}\right) \quad , \quad S_{mx} = 2i_x^{ex} + k_{mx}i_x \tag{3.42}$$

where S_{mx} is the magnetic field accumulator, T_{mx} is the magnetic forward gain term [33], and κ_{mx} is the feedback gain term. The gain terms are defined as [33]

$$T_{mx} = (4 + r_m + 4\chi_m)^{-1} \quad , \quad \kappa_{mx} = -(4 + r_m - 4\chi_m) \tag{3.43}$$

Following similar procedure to the dielectric material case, we calculate the impulses

$$\zeta_x^{i,m} = \frac{\partial T_{mx}}{\partial p_i}\left(2i_x^{ex} + z^{-1}S_{mx}\right)$$

$$\zeta_y^{i,m} = \frac{\partial T_{my}}{\partial p_i}\left(2i_y^{ex} + z^{-1}S_{my}\right) \tag{3.44}$$

$$\zeta_z^{i,m} = \frac{\partial T_{mz}}{\partial p_i}\left(2i_z^{ex} + z^{-1}S_{mz}\right)$$

Comparing (3.44) to (3.39), the magnetic AVM impulses are defined as ζ_{mx}^i, ζ_{my}^i, and ζ_{mz}^i where the j, k subscripts are omitted. The adjoint variables can be manipulated using simple additive and factorization operations. The AVM sensitivity is calculated as

$$\frac{\partial F}{\partial p_i} = -\sum_k \sum_j \left(\zeta_{x,j,k}^i \mu_{x,j,k}^i + \zeta_{y,j,k}^i \mu_{y,j,k}^i + \zeta_{z,j,k}^i \mu_{z,j,k}^i + \zeta_{x,j,k}^{i,m} \mu_{x,j,k}^{i,m} + \zeta_{y,j,k}^{i,m} \mu_{y,j,k}^{i,m} + \zeta_{z,j,k}^{i,m} \mu_{z,j,k}^{i,m} \right) (3.45)$$

where $\mu_{x,j,k}^{i,m}$, $\mu_{y,j,k}^{i,m}$, and $\mu_{z,j,k}^{i,m}$ are quantities derivable from the adjoint variables.

3.3 NUMERICAL VALIDATION

In order to validate the impulse sampling approach, we perform AVM sensitivity analyses for 2D and 3D problems. We utilize the self adjoint formulation [23] for efficient estimation of the sensitivity of the scattering parameters of a dielectric resonator antenna (DRA). The results are identical to that obtained using the accurate and expensive central finite difference applied at the response level.

The Impulse sampling is applied to structures operating in both the microwave and optical regimes. We demonstrate the accuracy and efficiency of our approach in the optical frequency range through the calculation of sensitivity analysis of loaded slot waveguide [31]. The approach is then applied to an expensive grating structure with large number of design parameters [31], [34]. The memory usage is compared to conventional AVM approaches.

3.3.1   Dielectric Loaded Parallel Plate Waveguide

Our approach is first demonstrated through sensitivity calculations of the scattering parameters of a partially filled parallel plate waveguide (see inset of Fig. 3.3). Analytical results are available for this example [35].

The parallel plate waveguide has a length of 80.0 mm and a width a=20.0 mm. The width of the dielectric slab is D=20.0 mm. The relative permittivity of the slab is ε_r=20.0 and the conductivity is σ= 0.7508 S/m. The 2D computational domain is discretized using a spatial resolution Δl=0.25 mm. The structure is excited using a plane wave excitation of a Gaussian modulated signal centered at f=4.0 GHz with a bandwidth of 3.0 GHz.

For this problem, the vector of designable parameters is $\boldsymbol{p}$=$[\varepsilon_r \quad \sigma \quad D]^T$. The calculation of the sensitivities with respect to the material parameters ε_r and σ requires the storage of the parameter $\zeta^i_{y,j,k}$ at every cell inside the dielectric. For the shape parameter D, only the voltage impulses for the cells at the interface between air and dielectric inside the dielectric are stored.

The sensitivities of the $|S_{11}|$ parameter with respect to the material and shape parameters are calculated and compared to both exact analytical results and finite difference approximation (see Figs. 3.3-3.5). Our AVM calculations are accurate as compared to the exact results. The central finite difference (CFD) calculations require two separate simulations per parameter for each sensitivity calculation.
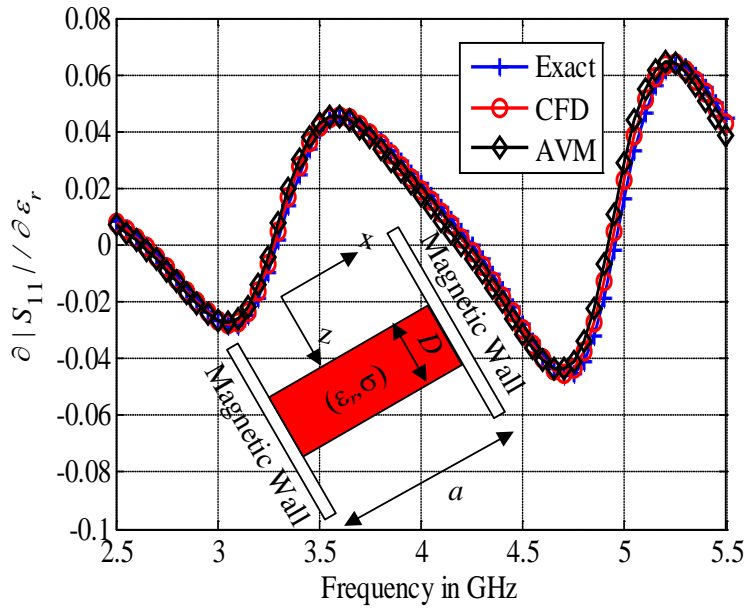
Fig. 3.3. The sensitivity of $|S_{11}|$ with respect to the dielectric constant of the slab (ε_r) using AVM, finite difference approximations, and exact analytical sensitivity.
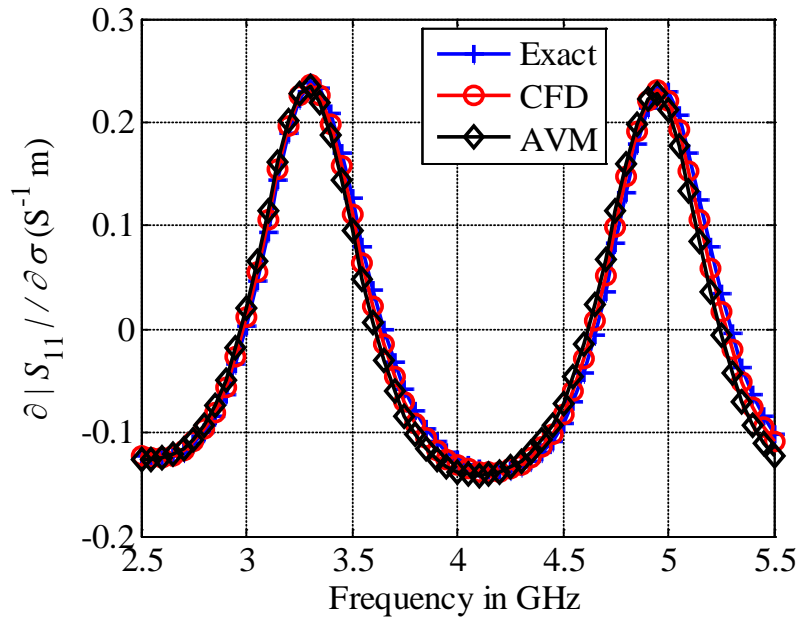
Fig. 3.4. The sensitivity of $|S11|$ with respect to the conductivity of the slab (σ) using AVM, finite difference approximations, and exact analytical sensitivity.
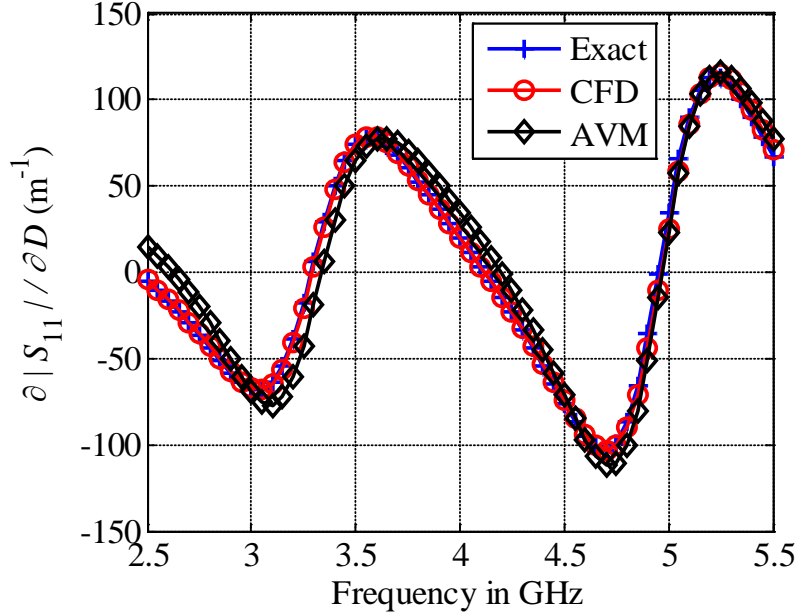
Fig. 3.5. The sensitivity of $|S_{11}|$ with respect to the slab width (D) using AVM, finite difference approximations, and exact analytical sensitivity.

Further illustration of the technique is through the calculation of the sensitivity of a time-domain objective function with respect to the slab parameters. The utilized objective function is the energy function:

$$F(\boldsymbol{p},\boldsymbol{V}) = \Delta t \sum_{k=1}^{N_t} \sum_{i=1}^{N_x} E_{y,k}^2(i, N_z) \tag{3.46}$$

where N_x is the number of cells in the x direction, N_z is the size of the computational domain along the z direction, and N_t is the number of time steps. In (3.46), $E_{y,k}$ is the value of the electric field at the kth time step. The objective function (3.46) is a measure of the energy delivered to the output port.
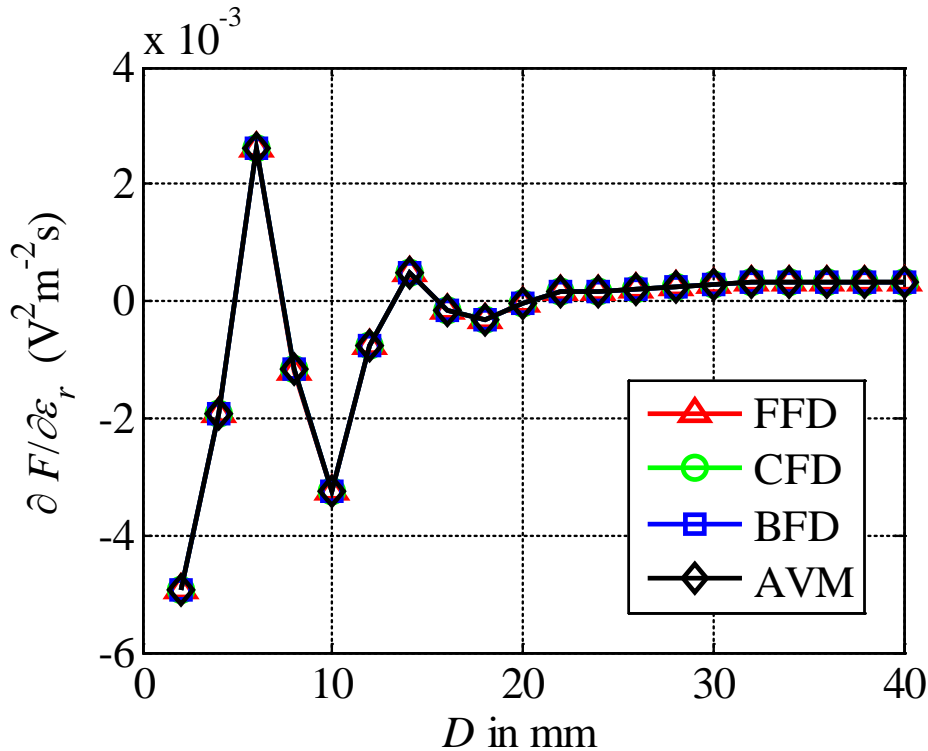
Fig. 3.6. The energy function sensitivity with respect to ε_r for the 2D partially filled waveguide at $\varepsilon_r=20$, $\sigma=0.7508$ S/m with $\Delta l=0.25$ mm, for different values of D using finite difference approaches and AVM.

The AVM sensitivities are estimated, for different dielectric widths, as shown in Figs. 3.6-3.8. The results are compared to the forward, central, and backward finite difference (FFD, CFD, and BFD, respectively). The central finite difference approach requires 6 additional complete simulations for the calculation of the sensitivities with respect to the three parameters. However, AVM approaches require only one extra simulation. For the dielectric loaded waveguide, the problem is simulated for $N_t=10,000$. The number of the perturbed cells is dependent on the size of the dielectric. For the original formulation, the memory storage in the main and adjoint simulation is 2.56 Gigabytes per simulation.
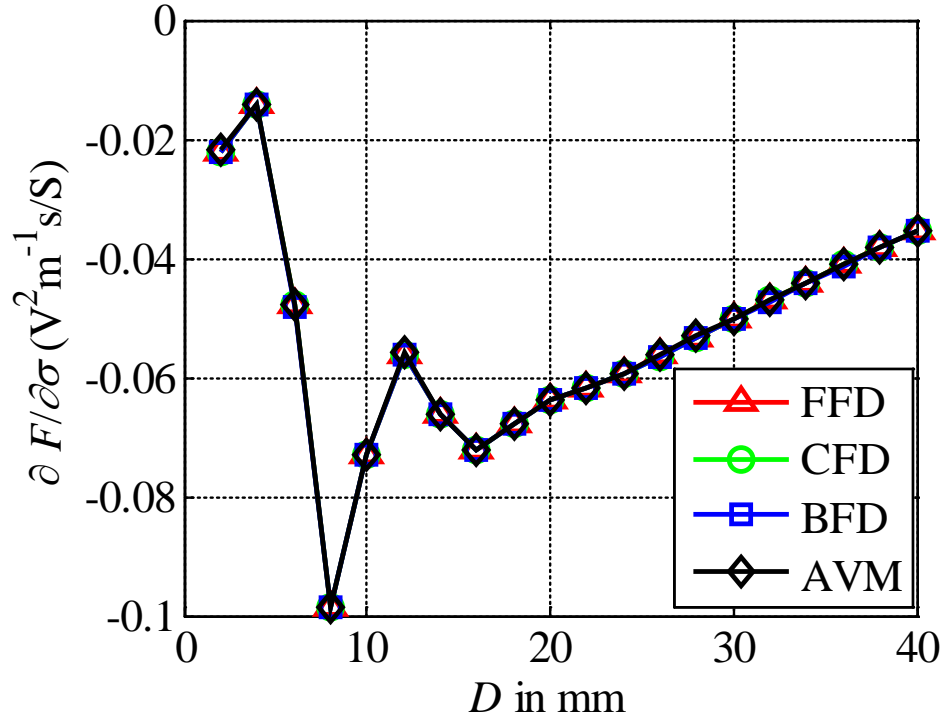
Fig. 3.7. The energy function sensitivity with respect to σ for the partially filled waveguide at ε_r=20, σ=0.708 S/m with Δl=0.25 mm for different values of D using finite difference approaches and AVM.

In this example, 80×160 is the number of perturbed cells due to the change of the material parameters. The total memory requirement is 5.12 Gigabytes. Using the new AVM formulation, we store only 512 Megabytes in the original simulation. According to the newly formulated AVM calculation (3.24), with the calculation of the parameter $\zeta_{y,j,k}^{i}$, the sensitivity $\partial F / \partial p_i$ is calculated on the fly without extra storage in the adjoint problem.
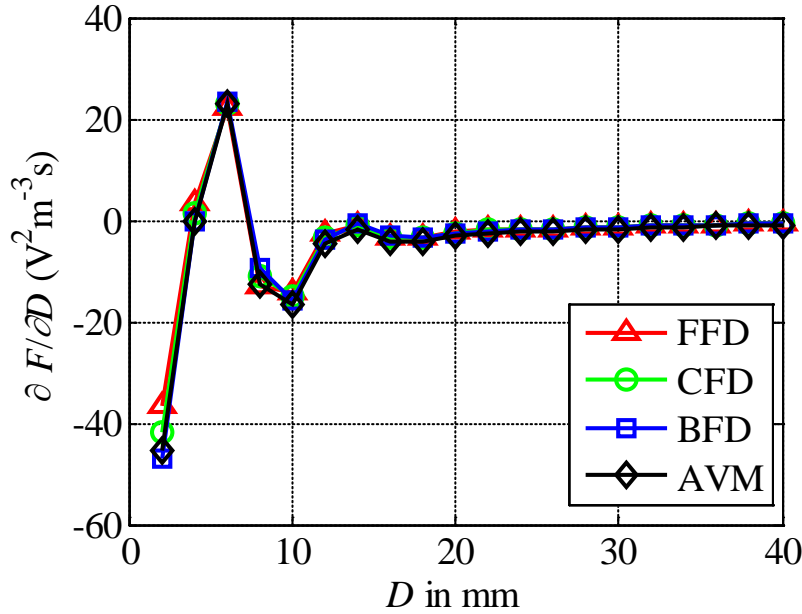
Fig. 3.8. The energy function sensitivity with respect to D for the partially filled waveguide at ε_r=20, σ=0.708 S/m with Δl=0.25 mm, for different values of D using finite difference approaches and AVM.

3.3.2 A 3D Discontinuity

In this example, a dielectric discontinuity is introduced inside the waveguide structure shown in Fig. 3.9. The parallel plate waveguide has a width a=20.0 mm, a height b=20.0 mm, and a length L=80.0 mm. The dielectric discontinuity has ε_r=1.5 and dimensions h=7.0mm and w=11.0 mm. The sensitivity is calculated for different lengths of the discontinuity d. The 3D computational domain is discretized using spatial resolution Δl=1.0 mm. The structure is excited using a plane wave excitation of a Gaussian modulated signal centered at f=3.0 GHz.

The utilized objective function is a measure of the transmitted energy and is given by:
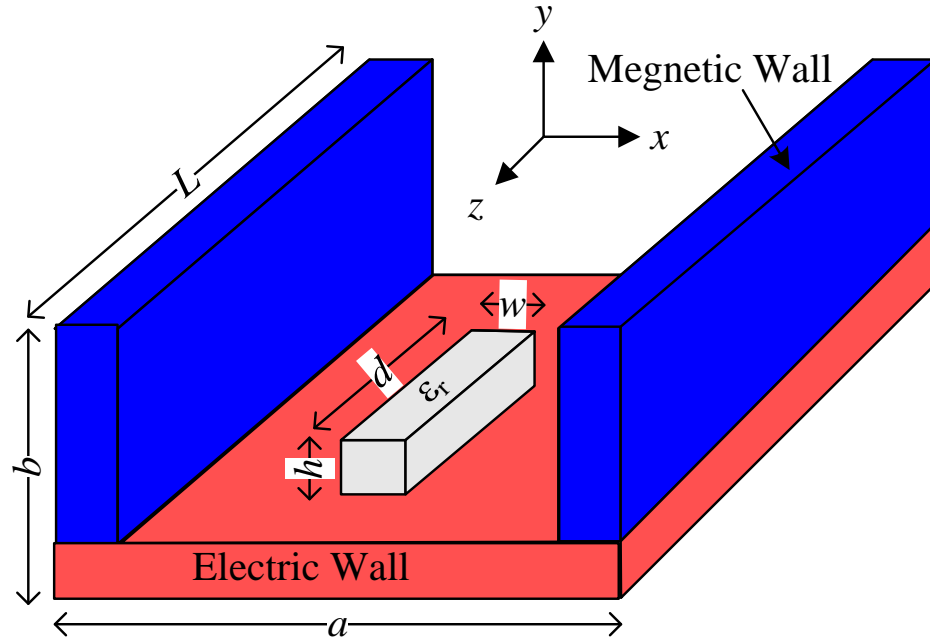
Fig. 3.9. A dielectric discontinuity is introduced inside the waveguide.

$$F(\boldsymbol{p},\boldsymbol{V}) = \Delta t \sum_{k=1}^{N_t} \sum_{j=1}^{N_y} \sum_{i=1}^{N_x} V_{6,k}^2(i,j,N_z) \qquad (3.47)$$

where N_t is the number of the simulation time instants, N_y and N_z are the numbers of computational cells in the y and z direction respectively. For this problem, the vector of designable parameters is $\boldsymbol{p}=[\varepsilon_r \quad w \quad d \quad h]^T$.

In this 3D problem, due to memory efficiency of our algorithm, we can extend the regular AVM to the central AVM (CAVM) [36]. For CAVM calculation, we calculate the sensitivities with respect to the shape parameters by perturbing the scattering matrix in both the forward and backward directions. While the work in [36] exploited the frequency domain TLM, extension to the time-domain TLM is straightforward. Although negligible computational overhead is required, more accurate results are achieved [36].

All sensitivities are calculated using both the CAVM and three finite difference techniques; backward finite difference (BFD), central finite difference (CFD), and forward finite difference (FFD). In Figs. 3.10-3.13, the sensitivity calculations using CAVM is shown to have good match with the finite difference approximations. The CAVM requires only one extra adjoint simulation.

The memory requirement for sensitivity estimation using the original TLM-based AVM approach can be calculated using the perturbation dimensions and all the numerical parameters. For a discontinuity with dimensions of $7\Delta l \times 11\Delta l \times 34\Delta l$, the memory requirement for both the original and adjoint simulation is approximately 4.8 Gigabytes. Utilizing our memory efficient approach only 480 Megabytes are required for the AVM calculations.
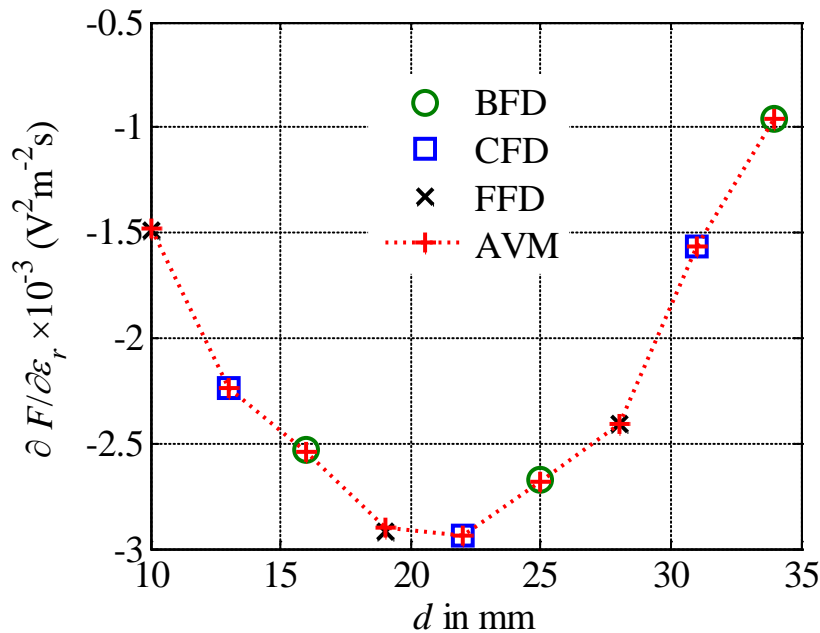
Fig. 3.10. The objective function sensitivity with respect to ε_r of the discontinuity inside the 3D waveguide at $\varepsilon_r=1.5$ with $\Delta l=1.0$ mm, for different values of d using finite difference approximations and AVM.
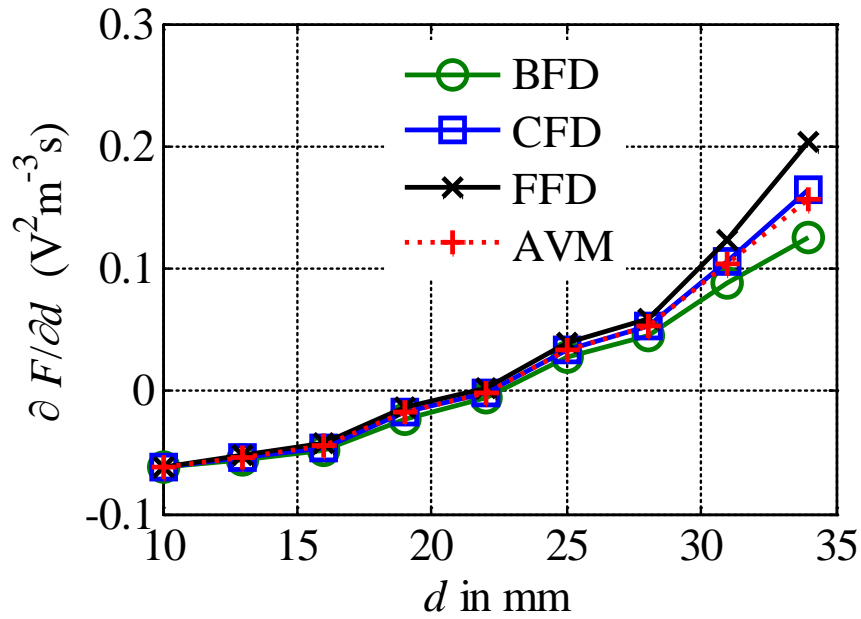
Fig. 3.11. The objective function sensitivity with respect to d of the discontinuity inside the 3D waveguide at ε_r=1.5 with Δl=1.0 mm, for different values of d using finite difference approximations and AVM.
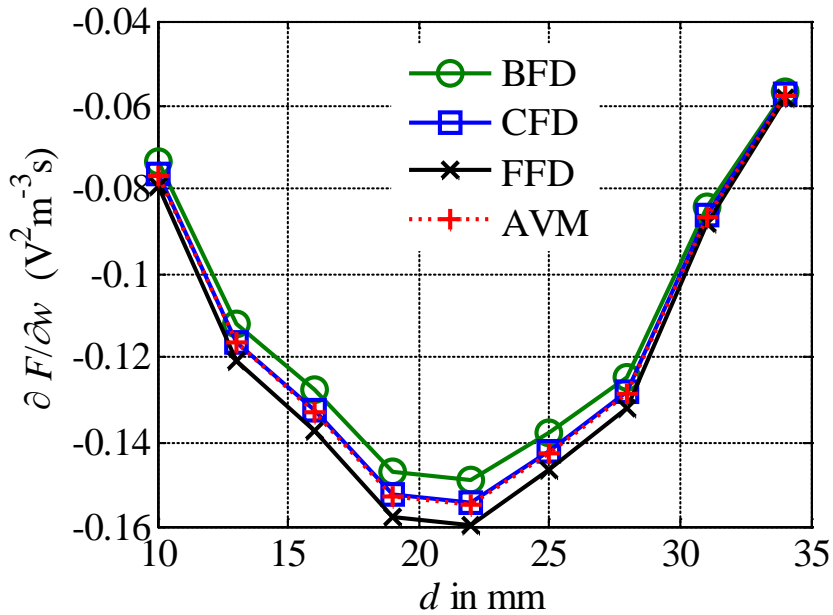
Fig. 3.12. The objective function sensitivity with respect to w of the discontinuity inside the 3D waveguide at ε_r=1.5 with Δl=1.0 mm, for different values of d using finite difference approximations and AVM.
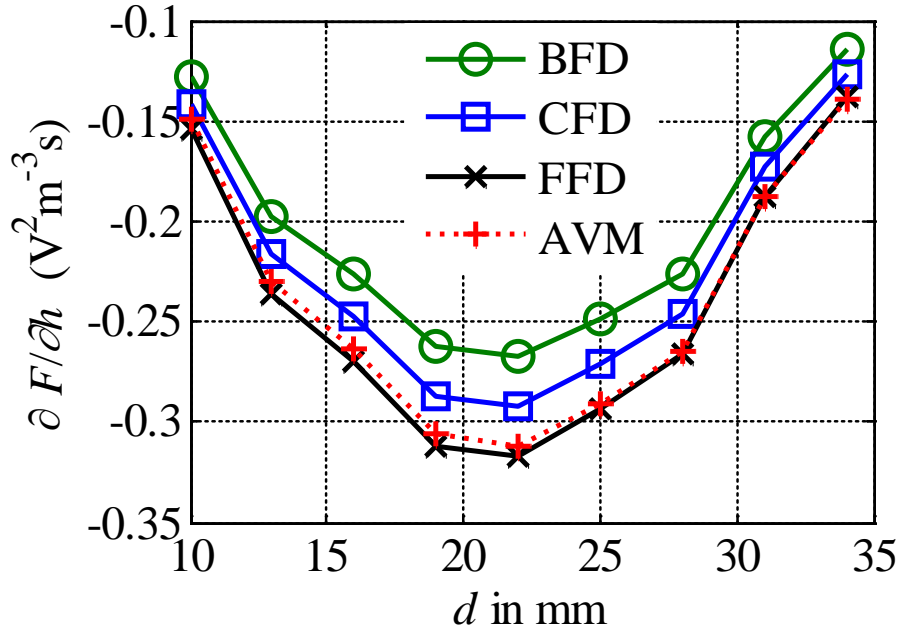
Fig. 3.13. The objective function sensitivity with respect to *h* of the discontinuity inside the 3D waveguide at ε_r=1.5 with Δl=1.0 mm, for different values of *d* using finite difference and AVM.

3.3.3 Dielectric Resonator Antenna

We also illustrate our memory efficient approach through sensitivity analysis of the multi-segment dielectric resonator antenna (DRA) shown in Fig. 3.14. An inset of high permittivity dielectric material is included for feed matching as discussed in [37].

In this problem we estimate the sensitivities of the frequency domain objective function $|S_{11}|$. The self-adjoint algorithm is utilized leading to the calculation of the scattering parameters and its sensitivity for all the design parameters without performing any extra simulations. The design parameters are the relative permittivity of the antenna (ε_r), the dielectric permittivity of the inset (ε_i), and the dimensions (*w*, *d*, *h*, *t*).
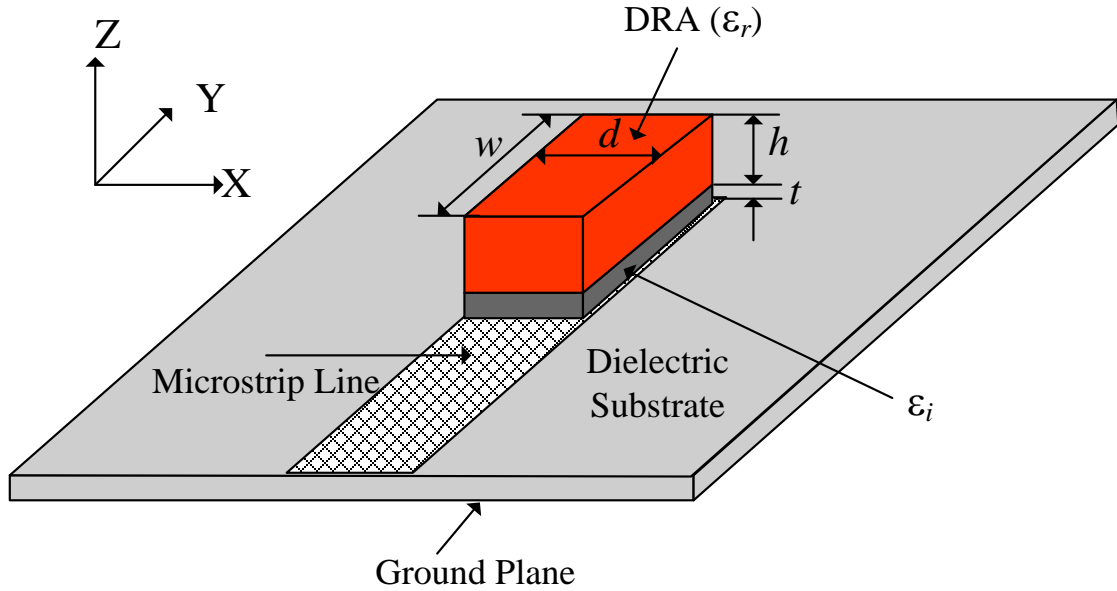
Fig. 3.14. The multisegment dielectric resonator antenna.

The studied structure is a wide band antenna operating around a center frequency of 16.0 GHz with a relative bandwidth of approximately 20% [37]. The DRA is fed by a 50 Ω microstrip line of (width=1.9 mm) over a dielectric substrate of relative permittivity ε_{sub}=3.0, and thickness h_{sub}=0.762 mm. The DRA is designed of a material with ε_r=10.0, and dimensions w=7.875 mm, d=2.0 mm, and h=3.175 mm. A dielectric inset is included to allow for wide band impedance matching. It is made from a ceramic of relative permittivity ε_i=20.0 and thickness t=0.6 mm.

The structure is simulated using our in-house TLM code in order to estimate the return loss (S_{11}) and its sensitivities using our memory efficient technique. The utilized spatial step size is Δl=0.2 mm. The sensitivities of the return loss with respect to DRA and inset material properties are shown in Figs. 3.15 and 3.16. Shown in Figs. 3.17-3.20,

are the sensitivities of the return loss with respect to the dimensional parameters. The AVM results are in good agreement with finite difference results.

For the studied design parameters (ε_r, ε_i, w, d, h, t), the central finite difference approach requires twelve extra simulations for sensitivity calculations. The regular AVM technique for TLM requires a large memory overhead. For the DRA example a domain of size $10\Delta l \times 19\Delta l \times 39\Delta l$ is perturbed. The simulation requires 20,000 time instants to accurately calculate the wideband scattering parameters. The overall memory overhead for regular AVM technique is 16.5 Gigabytes. Our memory efficient AVM technique requires only 1.65 Gigabytes memory overhead. This order of magnitude reduction allows for the sensitivity calculation of 10 times larger perturbations.
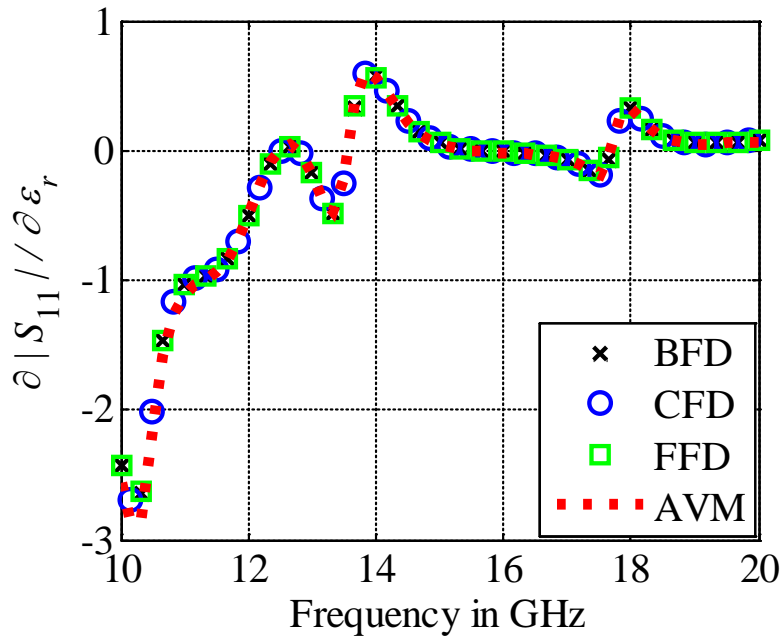
Fig. 3.15. The return loss sensitivity with respect to the dielectric constant of the DRA (ε_r) with Δl=0.2 mm using finite difference approximations and AVM.
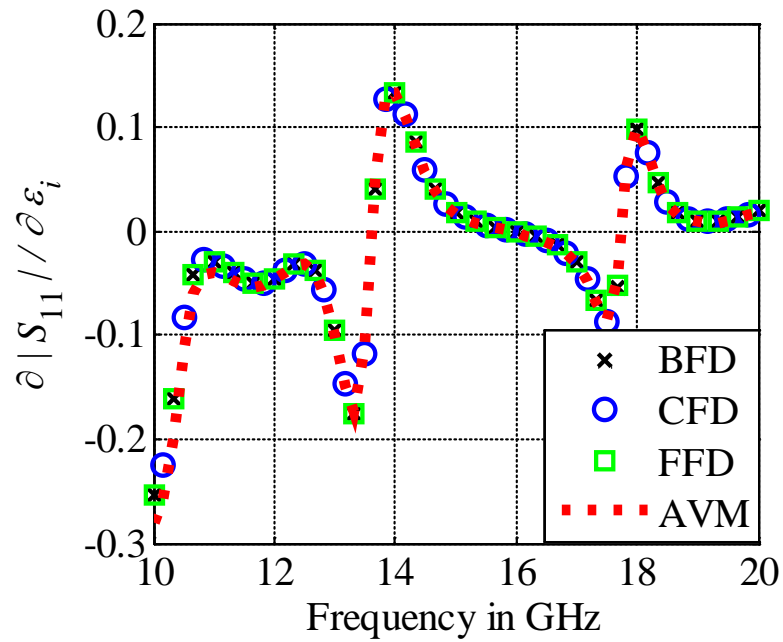
Fig. 3.16. The return loss sensitivity with respect to the dielectric constant of the inset (ε_i) with Δl=0.2 mm using finite difference approximations and AVM.
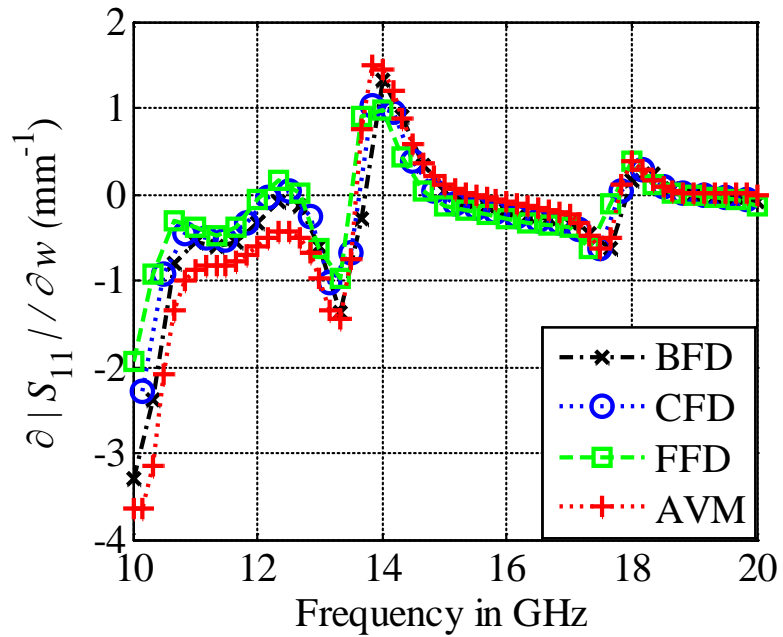
Fig. 3.17. The return loss sensitivity with respect to the dimension (w) of the DRA with Δl=0.2 mm using finite difference approximations and AVM.
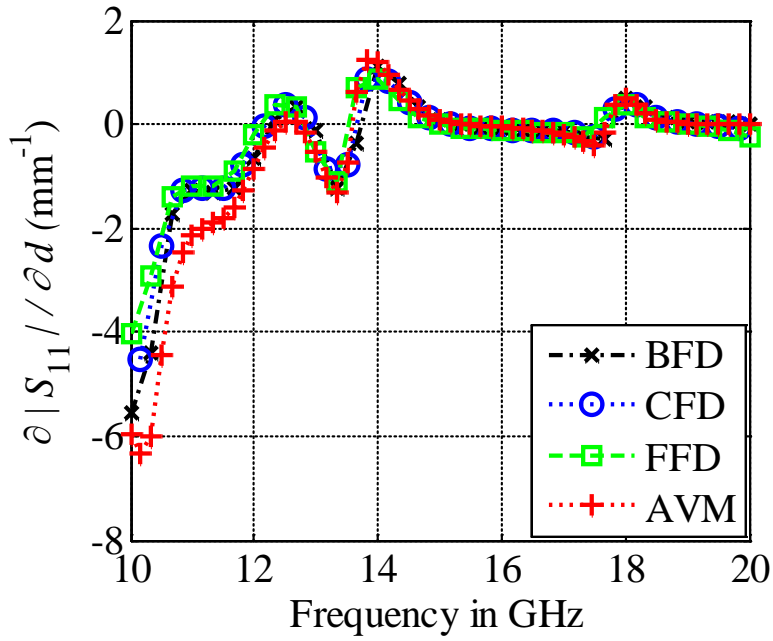
Fig. 3.18. The return loss sensitivity with respect to the dimensions (*d*) of the DRA with Δl =0.2 mm using finite difference approximations and AVM.
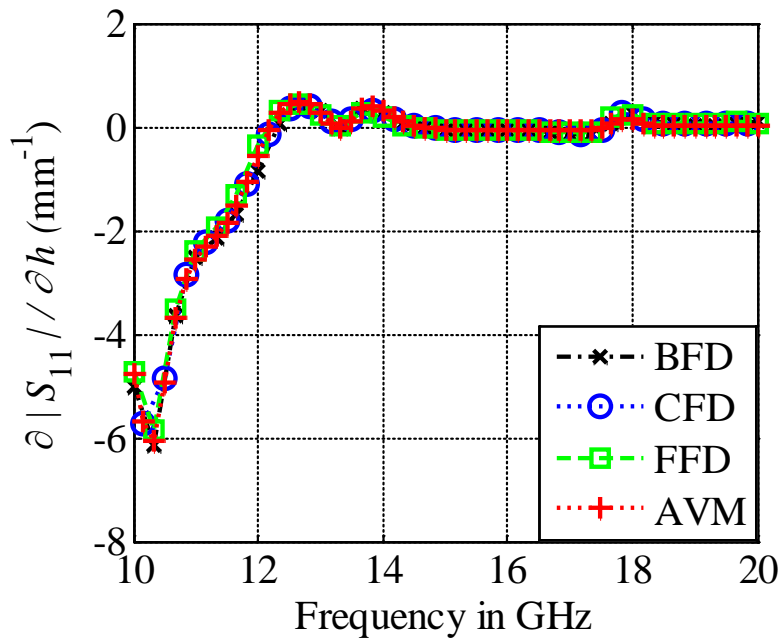
Fig. 3.19. The return loss sensitivity with respect to the DRA height (*h*) with Δl=0.2 mm using finite difference approximations and AVM.
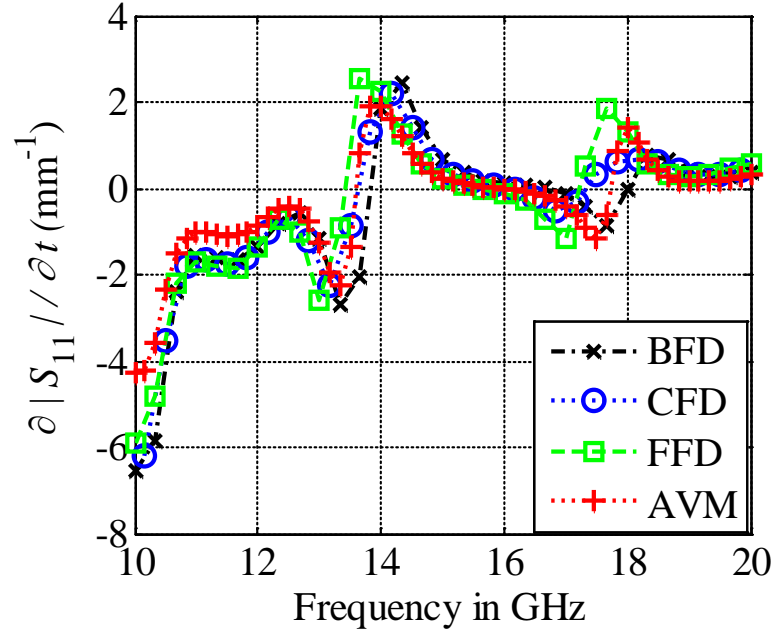
Fig. 3.20. The return loss sensitivity with respect to the inset thickness (*t*) with Δ*l*=0.2 mm using finite difference approximations and AVM.

3.3.4 Slot Waveguide

In this section, a benchmark photonic structure is used to validate the impulse sampling approach in the optical regime. In this example, we calculate the sensitivity of the scattering parameter S_{21} of a slot waveguide loaded with a dielectric discontinuity. The configuration, in Fig. 3.21, is preferred for sensing applications, where a material of unknown characteristics is explored in the low index core of the slot waveguide. The sensitivity analysis can be utilized for efficient estimation of the dielectric parameters. For this numerical example, the optimization parameters are the material and shape properties of the dielectric post.
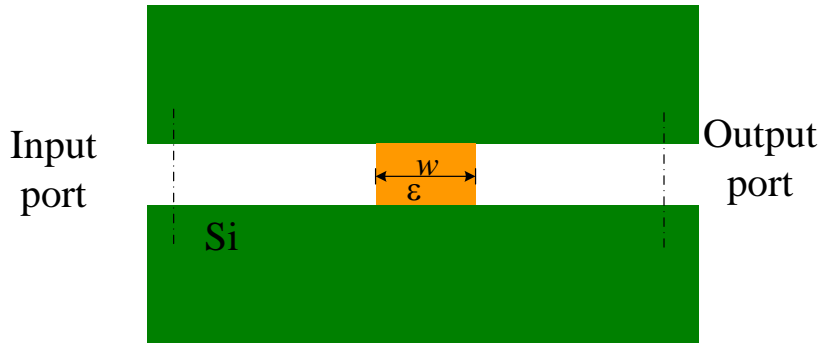
Fig. 3.21. The configuration of loaded slot waveguide.

The slot width is 50.0 nm while the dielectric post is of width of 600 nm. The simulation and sensitivity analysis are conducted using our in house TLM software with a cell size of 2.0 nm. A wideband Gaussian excitation is utilized (from 1.0 μm to 3.0 μm). The sensitivities of the scattering parameter $|S_{21}|$, with respect to the dielectric post permittivity and thickness, are shown in Figs. 3.22 and 3.23, respectively. The results match well the expensive central finite difference (CFD). The memory requirement for a dielectric perturbation (size of 300 cells) is 120 Megabytes utilizing the original AVM approach. The memory requirement is reduced to 12 Megabytes using our approach.

3.3.5 Slot Waveguide Bragg Gratings

The proposed approach is also applied to the structure of a slot waveguide Bragg gratings [34]. In Fig. 3.24, the studied structure has 7 grating periods. The gratings are assumed to be of general geometrical (width and thickness) and material properties. All the grating parameters are designed to achieve a target spectral response. In this case, the number of parameters is 42 shape and material parameters. The vector of optimization
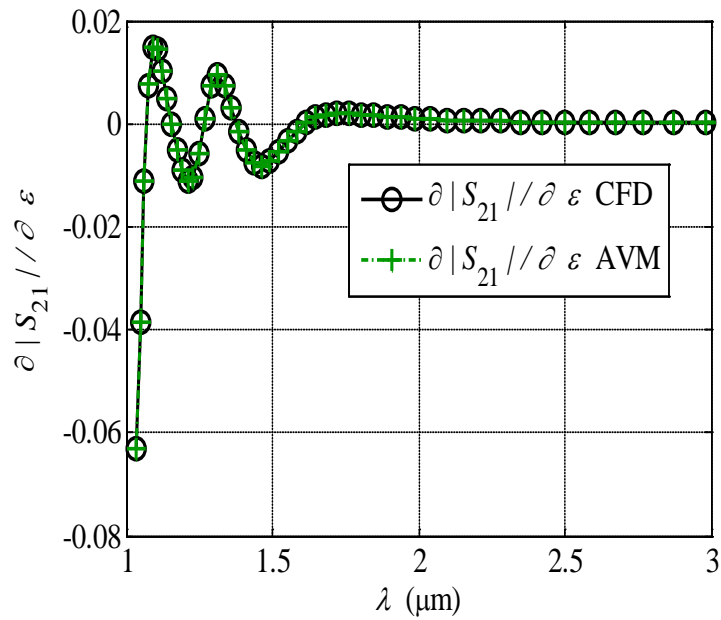
Fig. 3.22. Sensitivity of the scattering parameter $|S_{21}|$ with respect to the dielectric post permittivity utilizing memory efficient AVM is compared to the accurate CFD.
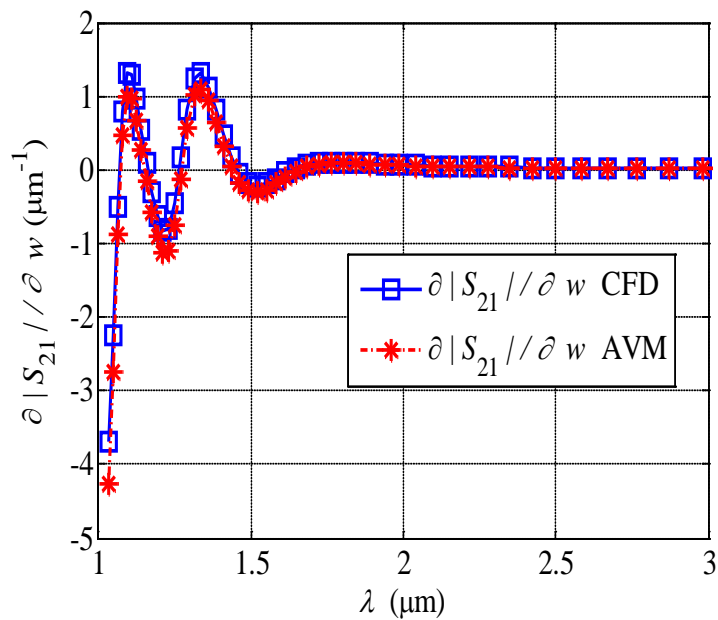
Fig. 3.23. Sensitivity of the scattering parameter $|S_{21}|$ with respect to the dielectric width (w) utilizing AVM approach is compared to the CFD.

parameters $p = \begin{bmatrix} \varepsilon_1 & w_1 & t_1 & \varepsilon_2 & w_2 & t_2 & ... & \varepsilon_{14} & w_{14} & t_{14} \end{bmatrix}^T$, where the subscripts indicate the grating index. The finite difference approaches require at least 42 extra simulations to calculate the sensitivity with respect to all the gratings parameters.

Our memory efficient approach is utilized without any extra simulation exploiting the self adjoint scheme [21], [22]. For 10.0 nm cell size, extra memory storage of 150 Megabytes is required. The conventional AVM approach requires 1.5 Gigabytes. Sensitivity with respect to 42 shape and material parameters are calculated. Here, we show the sensitivity with respect to the gratings indexed 5 and 9. The sensitivity of $|S_{11}|$ with respect to selected parameters is demonstrated (see Figs. 3.25-3.28). The results show excellent match with the expensive CFD approach.
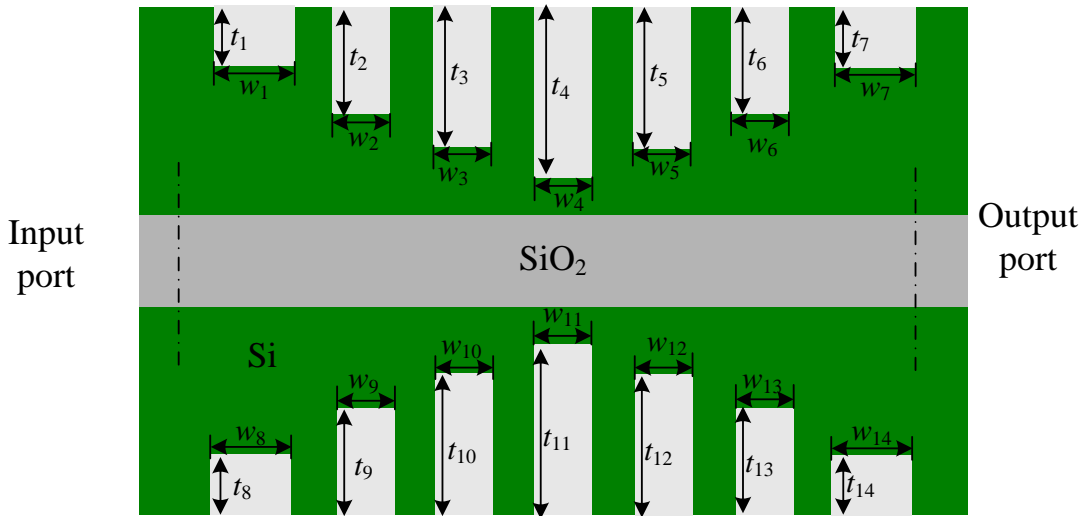
Fig. 3.24. The structure of the slot waveguide Bragg gratings.
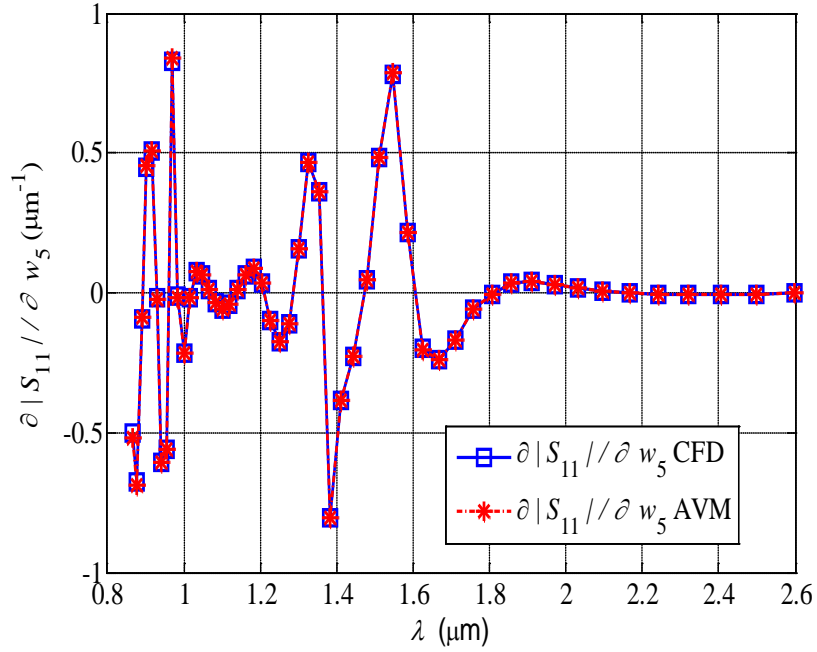
Fig. 3.25. The sensitivity of $|S_{11}|$ of the slot Bragg gratings with respect to the shape parameter w_5 using memory efficient AVM is compared to the accurate CFD.
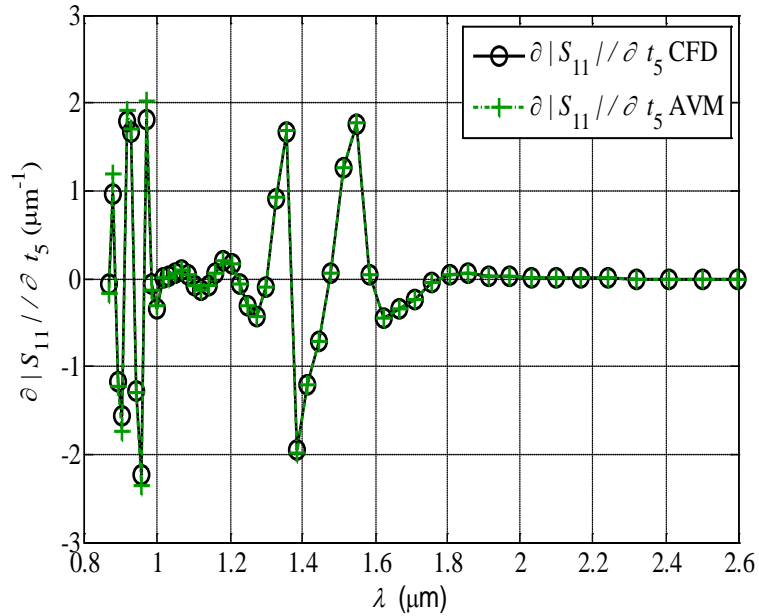
Fig. 3.26. The sensitivity of $|S_{11}|$ of the slot Bragg gratings with respect to the shape parameter t_5 using memory efficient AVM is compared to the accurate CFD.
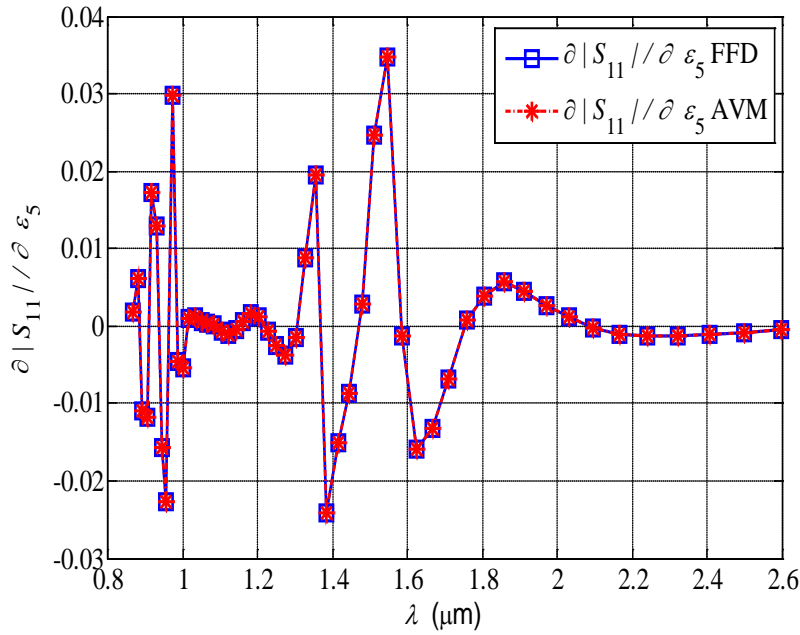
Fig. 3.27. The sensitivity of $|S_{11}|$ of the slot Bragg gratings with respect to the material parameter ε_5 using memory efficient AVM is compared to the accurate CFD.
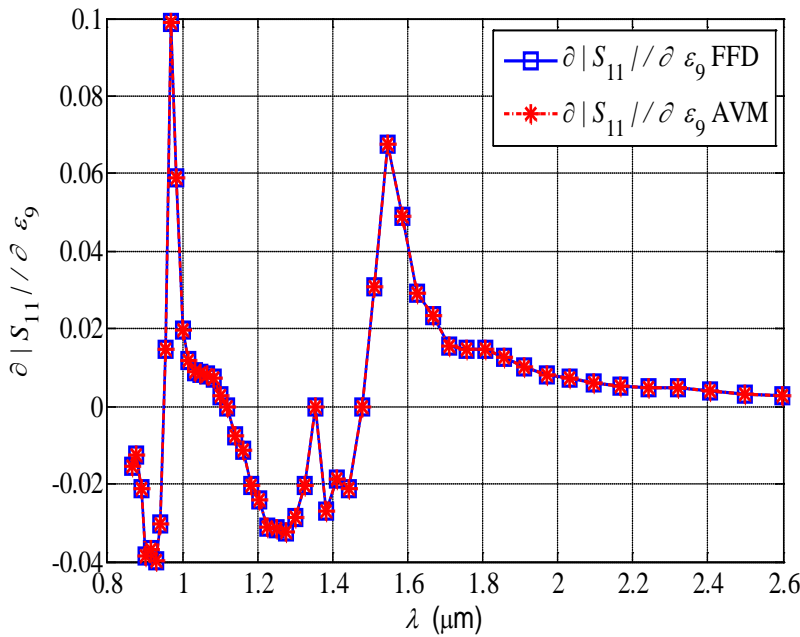
Fig. 3.28. The sensitivity of $|S_{11}|$ of the slot Bragg gratings with respect to the material parameter ε_9 using memory efficient AVM is compared to the accurate CFD.

3.4 SUMMARY

We propose an efficient approach for TLM-based AVM sensitivity analysis. The elegant manipulation of the scattering and connection matrices, utilizing symmetry properties and re-ordering the calculation procedure, allow for optimal memory usage. We modified the definition of the adjoint variable by applying a constant connection matrix. In this work, we present the ultimate memory reduction for adjoint simulation which is zero additional memory usage. The technique is proposed to regular stub-loaded TLM and the *Z*-domain general formulation.

3.5 REFERENCES

[1]   J. W. Bandler, Q. S. Cheng, S. A. Dakroury, A. S. Mohamed, M. H. Bakr, K.Madsen, and J. Sondergaard, "Space mapping: The state of the art," *IEEE Trans. Microwave Theory Tech*., vol. 52, pp. 337-361, 2004.

[2]   P. Garcia and J. P. Webb, "Optimization of planar devices by the finite element method," *IEEE Trans. Microwave Theory Tech*., vol. 38, pp. 48-53, 1990.

[3]   M. Gustafsson and S. He, "An optimization approach to two-dimensional time domain electromagnetic inverse problems," *Radio Sci*., vol. 35, pp. 525-536, 2000.

[4]   N. Joachimowicz, C. Pichot, and J. P. Hugonin, "Inverse scattering: An iterative numerical method for electromagnetic imaging," *IEEE Trans. Antennas Propag*., vol. 39, pp. 1742-1753, 1991.

[5]   E. J. Haug, K. K. Choi, and V. Komkov, *Design Sensitivity Analysis of Structural Systems*. Orlando, FL: Academic, 1986.

[6]   H. Akel and J. P. Webb, "Design sensitivities for scattering-matrix calculation with tetrahedral edge elements," *IEEE Trans. Magn.,* vol. 36, pp. 1043-1046, 2000.

[7]   J. P. Webb, "Design sensitivities using high-order tetrahedral vector elements," *IEEE Trans. Magn.,* vol. 37, pp. 3600-3603, 2001.

[8]   J. P. Webb, "Design sensitivity of frequency response in 3-D finite-element analysis of microwave devices," *IEEE Trans. Magn.*, vol. 38, pp. 1109-1112, 2002.

[9]   G. Iuculano, V. A. Monaco, and P. Tiberio, "Network sensitivities in terms of scattering parameters," *Electron. Lett.*, vol. 7, pp. 53-55, 1971.

[10]   J. W. Bandler, Q.-J. Zhang, and R. M. Biernacki, "A unified theory for frequency domain simulation and sensitivity analysis of linear and nonlinear circuits," *IEEE Trans. Microwave Theory Tech.*, vol. 36, pp. 1661-1669, 1988.

[11]   Y. Chung, C. Cheon, I. Park, and S. Hahn, "Optimal shape design of microwave device using FDTD and design sensitivity analysis," *IEEE Trans. Microwave Theory Tech.*, vol. 48, pp. 2289-2296, 2000.

[12]   Y. Chung, J. Ryu, C. Cheon, I. Park, and S. Hahn, "Optimal design method for microwave device using time domain method and design sensitivity analysis— Part I: FETD case," *IEEE Trans. Magn.,* vol. 37, pp. 3289-3293, 2001.

[13]   Y. Chung, C. Cheon, I. Park, and S. Hahn, "Optimal design method for microwave device using time domain method and design sensitivity analysis—Part II: FDTD case," *IEEE Trans. Magn.,* vol. 37, pp. 3255-3259, 2001.

[14]   M. H. Bakr and N. K. Nikolova, "An adjoint variable method for time-domain transmission line modeling with fixed structured grids," *IEEE Trans. Microwave Theory Tech.*, vol. 52, pp. 554-559, 2004

[15]   N. K. Nikolova, H. W. Tam, and M. H. Bakr, "Sensitivity analysis with the FDTD method on structured grids," *IEEE Trans. Microwave Theory Tech.*, vol. 52, pp. 1207-1216, 2004

[16]   M. H. Bakr, P. Zhao, and N. K. Nikolova, "Adjoint first order sensitivities of transient responses and their applications in the solution of inverse problems," *IEEE Trans. Antennas Propag*., vol. 57, pp. 2137-2146, 2009.

[17]   M. H. Bakr and N. K. Georgieva, "An adjoint variable method for frequency domain TLM problems with conducting boundaries," *IEEE Microwave wireless Comp. Lett.*, vol. 13, pp. 408-410, 2003.

[18]   N. K. Georgieva, S. Glavic, M. H. Bakr, and J. W. Bandler, "Feasible adjoint sensitivity technique for EM design optimization," *IEEE Trans. Microwave Theory Tech*., vol. 50, pp. 2751-2758, 2002.

[19]   P. A. W. Basl, M. H. Bakr, and N. K. Nikolova, "Efficient estimation of adjoint sensitivities in TLM with dielectric discontinuities," *IEEE Microwave and Wireless Comp. Lett.*, vol. 15, pp. 89-91, 2005.

[20]   M. H. Bakr and N. K. Nikolova,"An adjoint variable method for time-domain TLM with wide-band Johns matrix boundaries," *IEEE Trans. Microwave Theory Tech.*, vol. 52, pp. 678-685, 2004.

[21]   P. A. W. Basl, M. H. Bakr, and N. K. Nikolova, "An AVM technique for 3D TLM with symmetric condensed nodes," *IEEE Microwave and Wireless Comp. Lett.*, vol. 15, pp. 618-620, 2005.

[22]   M. H. Bakr, N. K. Nikolova, and P. A. W. Basl, "Self-Adjoint S-Parameter Sensitivities for Lossless Homogeneous TLM Problems," *International Journal of Numerical Modeling: Electronic Networks, Devices and Fields*, vol. 18, pp. 441-455, 2005.

[23]   P. A. W. Basl, M. H. Bakr, and N. K. Nikolova, "Theory of self-adjoint S-parameter sensitivities for lossless nonhomogeneous transmission-line modeling problems," *IET Microwave Antennas Propag.*, vol. 2, pp. 211-220, 2008.

[24]   N. Appannagaari, R. Edlinger, and B. Gray, "Optimetrics: Parametrics and Optimization Using Ansoft HFSS," *Microwave Journal*, Nov. 1999. [Online]. Available: http://www.ansoft.com/news/articles/MWJ.11.99.pdf. [Accessed 20 Jan. 2013].

[25]   Press Release, "Sensitivity analysis and adapted optimization strategies for CST MICROWAVE STUDIO transient solver," May 2010. [Online]. Available: http://www.cst.com/Content/News/Documents/2010_5_TimeDomain2011_web.pdf. [Accessed 20 Jan. 2013]

[26]   C. Christopoulos, *The Transmission-Line Modeling Method: TLM*, Wiley-IEEE Press, 1995.

[27]   P. B. Johns, "A symmetrical condensed node for the TLM method," *IEEE Trans. Microwave Theory Tech.*, vol. 35, pp. 370-377, 1987.

[28]   P. A. W. Basl, *An adjoint variable method for time-domain transmission line modeling*. Ph.D. dissertation, McMaster University, Hamilton, Ontario, Canada (Hamilton, 2007).

[29]   O. S. Ahmed, M. H. Bakr, and X. Li, "A memory-efficient implementation of TLM-based adjoint sensitivity analysis," *IEEE Trans. Antennas and Propag.*, vol. 60, pp. 2122-2125, 2012.

[30]   O. S. Ahmed, M. H. Bakr, and X. Li, "Memory efficient adjoint sensitivity analysis exploiting 3D time domain transmission line modeling," *2012 IEEE MTT-S International Microwave Symposium Digest*, Montreal 2012.

[31]   O. S. Ahmed, M. H. Bakr, M. A. Swillam, and X. Li, "Efficient sensitivity analysis of photonic structures with transmission line modeling," in *Proc. SPIE*, vol. 8412, Photonics North 2012, 841213, Montreal 2012.

[32]   O. S. Ahmed, M. H. Bakr, X. Li, "Efficient formulation for TLM-based adjoint sensitivity analysis," *The 28th International Review of Progress in Applied Computational Electromagnetics* (ACES), Columbus, Ohio 2012.

[33]   J. Paul, C. Christopoulos, and D. W. P. Thomas, "Generalized material models in TLM—Part I: Materials with frequency-dependent properties," *IEEE Trans. Antennas Propagat.*, vol. 47, pp. 1528-1534, 1999.

[34]   J. Mu, H. Zhang, and W.-P. Huang, "A theoretical investigation of slot waveguide Bragg gratings," *IEEE J. Quantum Electron*., vol. 44, pp. 622-62, 2008.

[35]   H. Haus, *Waves and Fields in Optoelectronics*. Englewood Cliffs, NJ: Prentice-Hall, ch. 3, 1984.

[36]   S. Ali, N. Nikolova, and M. Bakr, "Central adjoint variable method for sensitivity analysis with structured grid electromagnetic solvers," *IEEE Trans. on Magnetics*, vol. 40, pp. 1969-1971, 2004.

[37]   A. Petosa, N. Simons, R. Siushansian, A. Ittipiboon, and M. Cuhaci, "Design and analysis of multisegment dielectric resonator antennas," *IEEE Trans. Antennas Propag*., vol. 48, pp. 738-742, 2000.

4 ADJOINT VARIABLE METHOD FOR MATERIALS WITH DISPERSIVE CONSTITUTIVE PARAMETERS

In this chapter, we present the time-domain Adjoint Variable Method (AVM) algorithm for materials with dispersive constitutive parameters. We develop our algorithm based on the transmission line modeling (TLM) techniques for electromagnetic problems. The developed theory is based on the *Z*-domain representation of the dispersive materials, which can model arbitrary dispersive behavior. We develop a formulation similar to the original AVM theory for non-dispersive materials. The theory has been successfully applied to problems with dispersive materials modeled by the Drude, Debye, and Lorentz models.

4.1 INTRODUCTION

Computer Aided Design (CAD) tools are often utilized for design optimization [1]-[4]. Different optimization techniques can be utilized to satisfy the design specifications. Gradient-based algorithms are a subset of these techniques. They require accurate calculation of the response sensitivities with respect to the optimization parameters [1]-[6]. The computation of these derivatives can be costly though using finite difference approaches. The Adjoint Variable Method (AVM) is proposed for efficient sensitivity

analysis of high frequency structures [7]-[11]. It provides an efficient approach for Jacobian estimations [10], [11]. Using at most one extra simulation, the sensitivities relative to all parameters regardless of their number are estimated.

The AVM approach has been successfully developed for both time and frequency domain modeling techniques [11]-[17]. A self adjoint variable method (SAVM) was also developed for sensitivity calculations of the frequency-dependent network parameters [18], [19]. Recently, the AVM algorithm was implemented in commercial softwares such as HFSS [20] and CST [21].

One major limitation of the existing time-domain AVM approaches is that they do not take into consideration the frequency dependence of the constitutive parameters. However, materials with highly dispersive characteristics are used in wideband applications, e.g. [22]. These dispersive models are needed to accurately model the complete electromagnetic spectrum [23]-[25]. Recent developments in biological material interaction with electromagnetic waves also require accurate dispersive modeling of the biological materials [25].

In this chapter, we present the first AVM technique for dispersive materials with time-domain TLM. The Z-domain representation of the material properties with causal functions is exploited in deriving this approach. Using careful mathematical manipulations, we prove that the new technique is similar to the well-established existing techniques for non-dispersive materials. The new technique requires only one extra simulation to estimate the sensitivities of the response of interest over the whole frequency band for all parameters regardless of their number. Our approach is illustrated

through various examples with different dispersion models. Numerical results are shown for problems with materials modeled by the Drude, Debye, and Lorentz models. We estimate the sensitivies of energy functions and scattering parameters with respect to the parameters of dispersive discontinuities.

This chapter is organized as follows; The TLM technique for modeling dispersive materials is reviewed in Section 4.2. In Section 4.3, we present the theory of adjoint variable method for the generalized TLM formulation. Section 4.4 applies the theory presented in Section 4.4 to different dispersive models. Numerical results are provided in Section 4.5, where a number of examples illustrate both the accuracy of our theory and its compatibility with earlier approaches. Section 4.6 is dedicated to the discussion of the algorithm extension to the other time-domain numerical techniques. Our work is concluded in Section 4.7.

4.2   TLM APPROACH FOR DISPERSIVE MATERIALS

The theory of time-domain TLM utilizing the Symmetrical Condensed Node (SCN) is well established [26]-[30]. Considerable efforts have been dedicated to the adaptation of the technique to general materials. Frequency dependent, non-isotropic, and nonlinear materials have been successfully modeled using TLM [29]-[33]. The integration of the computational domain to a compatible TLM Perfectly Matched Layer (PML) for domain truncation has been reported [30]. Recently, TLM has been successfully utilized for the modeling of nano-plasmonic structures [34]. Advanced numerical techniques and optimization approaches have been incorporated for TLM- based simulations [35]-[37].
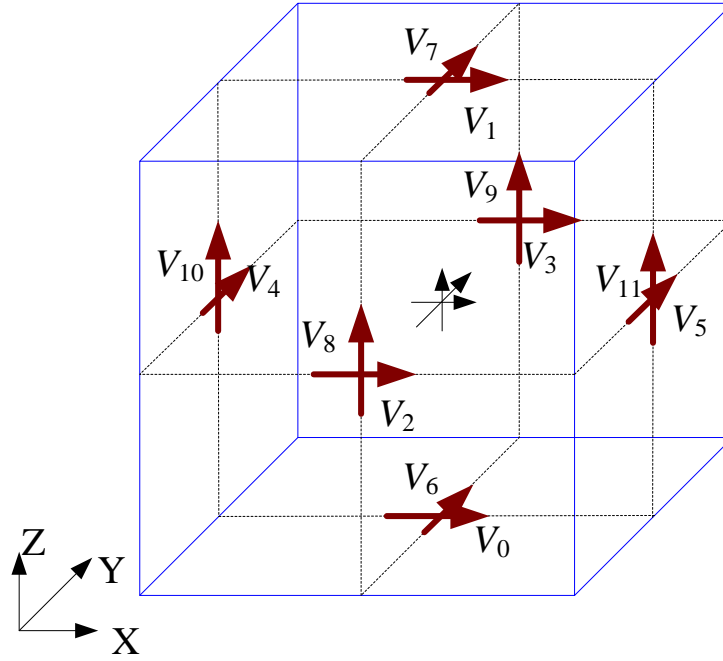
Fig. 4.1. The symmetric condensed node (SCN).

The TLM formulation, utilized here, is based on the symmetrical condensed node (SCN) [27]. The computational domain is modeled using a network of transmission lines (see Fig. 4.1). The time evolution of the port voltages follows:

$$V_{k+1} = C\left(RTR_{ex} - P\right)V_k + V_k^s \qquad (4.1)$$

where $V_k \in R^{12N}$ is the vector of all the port voltages in the computational domain of N cells at a time step k. The vector of incident voltages of the jth node (a subset of V_k) is defined as $V_{j,k}$. The vector V_k^s is the source excitation at time step k. In (4.1), the system factorized matrices $R \in R^{12N \times 6N}, T \in R^{6N \times 6N}, R_{ex} \in R^{6N \times 12N}$, and $P \in R^{12N \times 12N}$ are block diagonal matrices whose diagonal blocks are the nodal matrices $R_j \in R^{12 \times 6}$, $T_j \in R^{6 \times 6}$, $R_{ex,j} \in R^{6 \times 12}$ and $P_j \in R^{12 \times 12}$, respectively, for j=1 2 … N. The elements of R_j, $R_{ex,j}$ and P_j

118

are from the set {0, -1, 1} [31]. $C \in R^{12N \times 12N}$ is the total TLM link connection matrix. For a general dispersive material, the elements of the nodal matrix T_j are material and frequency dependent [31] and are given by:

$$T_j = \begin{bmatrix} t_{ex} & & & & & \\ & t_{ey} & & & \mathbf{0} & \\ & & t_{ez} & & & \\ & & & -t_{mx} & & \\ & \mathbf{0} & & & -t_{my} & \\ & & & & & -t_{mz} \end{bmatrix}_j ,$$

(4.2)

where, for example:

$$t_{ex} = \frac{2}{(4 + g_{ex} + 2\overline{s}\,\chi_{ex})} \;,\; t_{mx} = \frac{2}{(4 + r_{mx} + 2\overline{s}\,\chi_{mx})} .$$

(4.3)

The parameters χ_e, χ_m, g_e, and r_m are the electrical susceptibility, magnetic susceptibility, normalized electric conductivity, and normalized magnetic resistivity, respectively. $\overline{s}$ is the normalized frequency parameter $\overline{s} = s / \Delta t$, where $s = \sqrt{-1}\,\omega$ and Δt is the time step.

The calculation of (4.1) requires the transformation of the parameters in T_j into the corresponding Z-domain representation. The frequency operator in (4.3) is replaced by the time shift operator z utilizing a bilinear transformation [31]. The intermediate voltages and currents are given by [31]:

$$\begin{aligned} F &= \begin{bmatrix} V_x & V_y & V_z & i_x & i_y & i_z \end{bmatrix}^T \\ &= T_j F^{ex} = T_j R_{ex,j} V_{j,k} \end{aligned}$$

(4.4)

where, $\boldsymbol{F}^{ex}$, the vector of excitation is defined as $\boldsymbol{F}^{ex} = \begin{bmatrix} V_x^{ex} & V_y^{ex} & V_z^{ex} & i_x^{ex} & i_y^{ex} & i_z^{ex} \end{bmatrix}^T$.

$\boldsymbol{F}$ is directly mapped to the electric and magnetic fields inside the cell (j). In (4.4), the subscripts j and k are dropped from the defined intermediate variables $\boldsymbol{F}$ and $\boldsymbol{F}^{ex}$.

4.3 AVM APPROACH FOR THE GENERALIZED TLM FORMULATION

We formulate in this Section a generalized Adjoint Variable Method (AVM) that applies to both dispersive and non-dispersive materials utilizing the TLM formulation given by (4.1)-(4.4). We show that using only one adjoint simulation, the sensitivities of a given objective function with respect to all parameters are obtained regardless of their number.

Without loss of generality, we consider the solution of (4.4) for only the x polarization ($V_x = t_{ex} V_x^{ex}$). Utilizing the Z-domain representation, equation (4.4) for the x polarization can be written as:

$$\left[4 + g_{ex}(z) + 4\left(\frac{1-z^{-1}}{1+z^{-1}}\right)\chi_{ex}(z) \right] V_x = 2V_x^{ex} \tag{4.5}$$

In (4.5), all the constitutive parameters are transformed to the corresponding Z-domain and can be expanded using partial fractions to get [31]:

$$(1+z^{-1})g_{ex}(z) = g_{e0} + z^{-1}(g_{e1} + \tilde{g}_e(z)) \tag{4.6}$$

$$(1-z^{-1})\chi_{ex}(z) = \chi_{e0} - z^{-1}(\chi_{e1} + \tilde{\chi}_e(z)) \tag{4.7}$$

where g_{e0}, g_{e1}, χ_{e0}, χ_{e1} are constant expansion coefficients and $\tilde{g}_e(z)$, $\tilde{\chi}_e(z)$ are the expansion functions. Direct substitution of (4.6) and (4.7) in (4.5) leads to

$$V_x = T_e (2V_x^{ex} + z^{-1}S^{ex}),$$ (4.8)

where the transmission coefficient $T_e = (4 + g_{e0} + 4\chi_{e0})^{-1}$. In (4.8), S^{ex} is a voltage back storage defined as

$$S^{ex} = 2V_x^{ex} + \kappa_e V_x - \tilde{g}_e(z)V_x + 4\tilde{\chi}_e(z)V_x$$ (4.9)

where $\kappa_e = -(4 + g_{e1} - 4\chi_{e1})$. For a material of nondispersive properties, $\tilde{g}_e(z) = 0$, $\tilde{\chi}_e(z) = 0$, $g_{e1} = g_{e0} = g_e$, and $\chi_{e1} = \chi_{e0} = \chi_e$. In this case, only one back storage S^{ex} is required per cell for the x polarization. The same applies to the y and z polarizations. Equations (4.8) and (4.9) can be cast in the form:

$$\begin{bmatrix} V_x \\ S^{ex} \end{bmatrix} = T_e \begin{bmatrix} 2 & 1 \\ 2/T_e + 2\kappa_e & \kappa_e \end{bmatrix} \begin{bmatrix} V_x^{ex} \\ z^{-1}S^{ex} \end{bmatrix}$$ (4.10)

A general formulation for all polarizations is given by:

$$\begin{bmatrix} F \\ S^e \end{bmatrix} = U_j \begin{bmatrix} F^{ex} \\ z^{-1}S^e \end{bmatrix} = \begin{bmatrix} U_{11}(p) & U_{12}(p) \\ U_{21}(p) & U_{22}(p) \end{bmatrix} \begin{bmatrix} F^{ex} \\ z^{-1}S^e \end{bmatrix}$$ (4.11)

where S^e is the vector of all the required back storage in the computational domain at the time step k for the jth cell. In (4.11), the subscripts j and k are dropped for brevity. $U_j \in R^{(6+m) \times (6+m)}$ is a real valued frequency independent transmission matrix calculated as in (4.10), where m is the number of required back storage per node in the computational domain.

Equation (4.11) holds for arbitrary number of back storages depending on the order of the dispersion model of the material. The system update scheme utilizing (4.1), (4.4) and (4.11) is thus given by:

$$X_{k+1} = Q\left(WUW_{ex} - J\right)X_k + X_k^s \tag{4.12}$$

where X_k is a vector of all the voltage impulses at all ports and the associated extra storage. It is constructed from the nodal vectors $X_{j,k}$, $\forall j$. The matrix U is a block diagonal matrix constructed from U_j in (4.11). The matrices Q, W, W_{ex}, and J are block diagonal whose jth diagonal blocks are defined as:

$$Q_j = \begin{pmatrix} C_j & 0 \\ 0 & I_{m \times m} \end{pmatrix}, \quad W_j = \begin{pmatrix} R_j & 0 \\ 0 & I_{m \times m} \end{pmatrix},$$
$$W_{ex,j} = \begin{pmatrix} R_{ex,j} & 0 \\ 0 & I_{m \times m} \end{pmatrix}, \quad J_j = \begin{pmatrix} P_j & 0 \\ 0 & 0_{m \times m} \end{pmatrix} \tag{4.13}$$

The modified excitation vector X_k^s is constructed from V_k^s with zeros in the entries corresponding to the extra storage components. Equation (4.12) can be formulated in a standard update scheme given by:

$$X_{k+1} = QSX_k + X_k^s \tag{4.14}$$

where $S = \left(WUW_{ex} - J\right)$, $S \in R^{(12+m)N \times (12+m)N}$. Q represents the connection matrix. Notice that, in reality the large matrices Q and S are never actually constructed. All operations are carried out node by node. The system (4.14) casts the TLM iterations with arbitrary dispersion profiles in a form similar to the dispersion-free case.

The system update equation (4.14) is utilized for the AVM sensitivity calculation of a general objective function, F, of the form:

$$F = \int_{0}^{T_m} G(\boldsymbol{p}, \boldsymbol{X}) dt \, . \tag{4.15}$$

Utilizing the formulation (4.14) and following a similar derivation to that in [13], the sensitivities of the objective function (4.15) with respect to the ith parameter p_i, $\forall i$, is given by:

$$\frac{\partial F}{\partial p_i} = -\Delta t \sum_{j} \sum_{k} \boldsymbol{\lambda}_{j,k}^{T} \boldsymbol{Q}_{j} \boldsymbol{\eta}_{j,k}^{i} \tag{4.16}$$

where $\boldsymbol{\eta}_{j,k}^{i} = \left(\partial \boldsymbol{S}_{j}(\boldsymbol{p}) / \partial p_i \right) \boldsymbol{X}_{j,k}$. The summation (4.16) is carried out over all cells affected by the ith parameter over all time steps. The vector $\boldsymbol{\lambda}_{j,k}$ is the nodal adjoint variable calculated using the backward running simulation

$$\begin{aligned} \boldsymbol{\lambda}_{k-1} &= \boldsymbol{S}^{T} \boldsymbol{Q}^{T} \boldsymbol{\lambda}_{k} - \boldsymbol{\lambda}_{k}^{s} \\ &= \left(\boldsymbol{W} \boldsymbol{U}^{T} \boldsymbol{W}_{ex} - \boldsymbol{J} \right) \boldsymbol{Q}^{T} \boldsymbol{\lambda}_{k} - \boldsymbol{\lambda}_{k}^{s}, \quad \boldsymbol{\lambda}(T_m) = \boldsymbol{0} \end{aligned} \tag{4.17}$$

The adjoint variable $\boldsymbol{\lambda}_{j,k}$ represents all the TLM link impulses at a cell j and a time step k. The adjoint excitation in (4.17) is $\boldsymbol{\lambda}_{k}^{s} = (\partial G / \partial \boldsymbol{X})_{t=k\Delta t}$. The backward running adjoint problem (4.17) has zero terminal conditions. Its matrices are the transpose of those in the original system (4.12). In (4.17), symmetry properties of the involved matrices were utilized. It can be shown that the matrix $\boldsymbol{J}$ is symmetric and $\boldsymbol{W}^{T} = \boldsymbol{W}_{ex}$.

Similar to (4.4), intermediate voltages and currents are utilized for the adjoint simulation,

$$\begin{aligned} \boldsymbol{F}^{\lambda} &= \begin{bmatrix} V_{x}^{\lambda} & V_{y}^{\lambda} & V_{z}^{\lambda} & i_{x}^{\lambda} & i_{y}^{\lambda} & i_{z}^{\lambda} \end{bmatrix}^{T} \\ &= \boldsymbol{T}_{j} \boldsymbol{F}^{ex,\lambda} = \boldsymbol{T}_{j} \boldsymbol{R}_{ex,j} \boldsymbol{\lambda}_{j,k} \end{aligned} \tag{4.18}$$

where the superscript λ denotes adjoint variables. Utilizing (4.10), the adjoint system (4.17) can be built using

$$\begin{bmatrix} V_x^{\lambda} \\ S^{ex,\lambda} \end{bmatrix} = T_e \begin{bmatrix} 2 & 2/T_e + 2\kappa_e \\ 1 & \kappa_e \end{bmatrix} \begin{bmatrix} V_x^{ex,\lambda} \\ zS^{ex,\lambda} \end{bmatrix} \tag{4.19}$$

where $S^{ex,\lambda}$ is the adjoint extra storage required during the adjoint simulation. The z parameter is included to indicate the calculation sequence of the adjoint extra storage for a backward running simulation. The calculation of the adjoint variables $\lambda_{j,k}$ utilizing the transposed transmission matrix in (4.19) follows the TLM update scheme (4.17).

Utilizing (4.4) and (4.11), a compact formula for the parameter $\eta_{j,k}^i$ is

$$\eta_{j,k}^i = W_j \begin{bmatrix} \dfrac{\partial U_{11}}{\partial p_i} F^{ex} + \dfrac{\partial U_{12}}{\partial p_i} z^{-1} S^e \\ \dfrac{\partial U_{21}}{\partial p_i} F^{ex} + \dfrac{\partial U_{22}}{\partial p_i} z^{-1} S^e \end{bmatrix} = W_j \begin{bmatrix} \zeta^F \\ \zeta^s \end{bmatrix} \tag{4.20}$$

where $\zeta^F \in R^6$ and $\zeta^s \in R^m$ are simplified quantities utilized for the calculation of the parameter $\eta_{j,k}^i$. For the non-dispersive case, $m=1$. In this case, the x-components of these parameters are calculated as

$$\zeta_x^F = \frac{\partial T_e}{\partial p_i}(2V_x^{ex} + z^{-1}S^{ex})$$
$$\zeta^{sex} = \frac{\partial \kappa_e}{\partial p_i}V_x + \kappa_e \zeta_x^F \tag{4.21}$$

where the cell index j is dropped for brevity. Similar expressions apply for the non-dispersive case in other polarizations.

4.4   AVM FOR DISPERSIVE MATERIALS

In this Section, the adjoint theory presented by (4.5)-(4.17), (4.20) is applied to some of the commonly used dispersive models such as the Drude, Debye and Lorentz models. More details are provided to bridge the gap between the theory and implementation. For simplicity, the formulation is proposed for only one electric field polarization, the *x*-polarization. Similar expressions can be derived for the other two polarizations.

4.4.1   AVM for the Drude Model

Different materials in the microwave and photonic ranges are modeled by the Drude model [38]-[40]. For this model, the material conductivity in the frequency domain can be expressed as in [41]:

$$\sigma_e(s) = \frac{\sigma_0}{1 + s\tau_c} \tag{4.22}$$

where τ_c is the collision time constant. The DC electric conductivity is $\sigma_0 = \omega_p^2 \varepsilon_0 \tau_c$ with ε_0 denoting the vacuum permittivity. The Z-domain normalized conductivity function is calculated utilizing the impulse invariant method as [31]

$$g_e(z) = \frac{g_{ec}(1 - \beta_c)}{1 - z^{-1}\beta_c} \tag{4.23}$$

where $\beta_c = e^{-\Delta t / \tau_c}$ and Δt is the time step. The normalized conductivity (4.23) is expanded as [31]:

$$(1 + z^{-1})g_e(z) = g_{ec}(1 - \beta_c) + z^{-1}\frac{g_{ec}(1 - \beta_c^2)}{1 - z^{-1}\beta_c} \tag{4.24}$$

Comparing (4.6) and (4.24), the material dependent coefficients are $g_{e0}=g_{ec}(1-\beta_c)$, $g_{e1}=0$, and $\tilde{g}_e(z) = \alpha_c / (1 - z^{-1}\beta_c)$, where $\alpha_c = g_{ec}(1 - \beta_c^2)$. The TLM scheme in (4.8) and (4.9) is modified according to the dispersion model. Because this dispersive model is first order in z^{-1}, only one extra accumulator S^{ec} is utilized for each polarization. In this case, the TLM scheme utilizing the matrix formulation, (4.10), is

$$\begin{bmatrix} V_x \\ S^{ec} \\ S^{ex} \end{bmatrix} = T_e \begin{bmatrix} 2 & 0 & 1 \\ -2\alpha_c & \beta_c/T_e & -\alpha_c \\ 2/T_e + 2(\kappa_e - \alpha_c) & \beta_c/T_e & \kappa_e - \alpha_c \end{bmatrix} \begin{bmatrix} V_x^{ex} \\ z^{-1}S^{ec} \\ z^{-1}S^{ex} \end{bmatrix} \qquad (4.25)$$

where $T_e = (4 + g_{e0} + 4\chi_{e\infty})^{-1}$, $\kappa_e = -(4 - 4\chi_{e\infty})$ and $\chi_{e\infty}$ is the material susceptibility.

For the Drude material, the original field storage ζ^F and ζ^s in (4.20) are given by:

$$\zeta_x^F = \frac{\partial T_e}{\partial p_i}(2V_x^{ex} + z^{-1}S^{ex})$$

$$\zeta^{sec} = -\frac{\partial \alpha_c}{\partial p_i}V_x - \alpha_c\zeta_x^F + \frac{\partial \beta_c}{\partial p_i}z^{-1}S^{ec} \qquad (4.26)$$

$$\zeta^{sex} = \frac{\partial \kappa_e}{\partial p_i}V_x + \kappa_e\zeta_x^F + \zeta^{sec}$$

The adjoint system corresponding to (4.25) is given by:

$$\begin{bmatrix} V_x^\lambda \\ S^{ec,\lambda} \\ S^{ex,\lambda} \end{bmatrix} = T_e \begin{bmatrix} 2 & -2\alpha_c & 2/T_e + 2(\kappa_e - \alpha_c) \\ 0 & \beta_c/T_e & \beta_c/T_e \\ 1 & -\alpha_c & \kappa_e - \alpha_c \end{bmatrix} \begin{bmatrix} V_x^{ex,\lambda} \\ zS^{ec,\lambda} \\ zS^{ex,\lambda} \end{bmatrix} \qquad (4.27)$$

Once the temporal original fields components are determined by (4.26) and the temporal adjoint variables are determined by (4.27), the adjoint sensitivities are estimated using (4.16).

4.4.2   AVM for the Debye Model

Dispersion behavior of biological tissues in the microwave range follows the Debye model [42]. The material susceptibility for a Debye dielectric in the frequency domain can be expressed as [43]

$$\chi_e(s) = \chi_{e\infty} + \frac{\Delta\chi_e}{1 + s\tau_e} \tag{4.28}$$

where τ_e is the dielectric relaxation time, $\chi_{e\infty}$ is the high frequency susceptibility, and $\Delta\chi_e$ is the difference between DC and high frequency dielectric susceptibility. Similar to the Drude model, we utilize the dispersive z-representation:

$$\chi_e(z) = \chi_{e\infty} + \frac{\Delta\chi_e(1-\beta_e)}{1 - z^{-1}\beta_e} \tag{4.29}$$

where $\beta_e = e^{-\Delta t/\tau_e}$. The susceptibility can be expanded as in (4.7) to get the modified scheme for a Debye material. The TLM coefficients in (4.7) are thus given by [31]:

$$\chi_{e0} = \chi_{e\infty} + \Delta\chi_e(1-\beta_e), \ \chi_{e1} = \chi_{e\infty}$$
$$\tilde{\chi}_e(z) = \frac{\alpha_e/4}{(1 - z^{-1}\beta_e)} \tag{4.30}$$

where $\alpha_e = \Delta\chi_e(1-\beta_e)^2$. Because this dispersive model is first order in z^{-1}, the TLM scheme in (4.8) and (4.9) is applied with only one additional accumulator S^{ed} per polarization. The nodal TLM equation is thus given by:

$$\begin{bmatrix} V_x \\ S^{ed} \\ S^{ex} \end{bmatrix} = T_e \begin{bmatrix} 2 & 0 & 1 \\ 2\alpha_e & \beta_e/T_e & \alpha_e \\ 2/T_e + 2(\kappa_e + \alpha_e) & \beta_e/T_e & \kappa_e + \alpha_e \end{bmatrix} \begin{bmatrix} V_x^{ex} \\ z^{-1}S^{ed} \\ z^{-1}S^{ex} \end{bmatrix} \tag{4.31}$$

For this dispersion model, the original field storage ζ^F and ζ^s utilized in (4.20) are given by:

$$\zeta_x^F = \frac{\partial T_e}{\partial p_i}(2V_x^{ex} + z^{-1}S^{ex})$$

$$\zeta^{sed} = \frac{\partial \alpha_e}{\partial p_i}V_x + \alpha_e\zeta_x^F + \frac{\partial \beta_e}{\partial p_i}z^{-1}S^{ed} \qquad (4.32)$$

$$\zeta^{sex} = \frac{\partial \kappa_e}{\partial p_i}V_x + \kappa_e\zeta_x^F + \zeta^{sed}$$

Using (4.31), the adjoint simulation can be shown to have the form:

$$\begin{bmatrix} V_x^\lambda \\ S^{ed,\lambda} \\ S^{ex,\lambda} \end{bmatrix} = T_e \begin{bmatrix} 2 & 2\alpha_e & 2/T_e + 2(\kappa_e + \alpha_e) \\ 0 & \beta_e/T_e & \beta_e/T_e \\ 1 & \alpha_e & \kappa_e + \alpha_e \end{bmatrix} \begin{bmatrix} V_x^{ex,\lambda} \\ zS^{ed,\lambda} \\ zS^{ex,\lambda} \end{bmatrix} \qquad (4.33)$$

Once (4.32) and (4.33) are available at all time steps for all perturbed cells, the sensitivities with respect to all parameters are estimated using (4.16).

4.4.3   AVM for the Lorentz Model

The Lorentz model is utilized to describe the dispersion behavior of dielectric materials whose electrons and ions are treated as natural oscillators [44]. Different organic materials in the microwave and terahertz frequency ranges are modeled by the Lorentz model [45]. The material susceptibility for a Lorentz dielectric in the frequency domain can be expressed as [31], [46]:

$$\chi_e(s) = \chi_{e\infty} + \frac{\Delta\chi_e\omega_0^2}{s^2 + s2\delta + \omega_0^2} \qquad (4.34)$$

where δ is the damping frequency and ω_0 is the resonant frequency. Equation (4.34) can be reformulated in the z-domain as follows [31]:

$$\chi_e(z) = \chi_{e\infty} + \frac{\Delta\chi_e(1 - 2A_e + A_e^2 + B_e^2)z^{-1}}{1 - z^{-1}2A_e + z^{-2}(A_e^2 + B_e^2)} \tag{4.35}$$

where $\beta = \sqrt{\omega_0^2 - \delta^2}$, $A_e = e^{-\delta\Delta t}\cos(\beta\Delta t)$ and $B_e = e^{-\delta\Delta t}\sin(\beta\Delta t)$. The expression in (4.35) can be simplified to

$$\chi_e(z) = \chi_{e\infty} + \frac{K_1 z^{-1}}{1 - z^{-1}a_1 - z^{-2}a_2} \tag{4.36}$$

where $K_1 = \Delta\chi_e(1 - 2A_e + A_e^2 + B_e^2)$, $a_1 = 2A_e$, and $a_2 = -(A_e^2 + B_e^2)$. By comparing (4.36) with (4.7), we have

$$\chi_{e0} = \chi_{e1} = \chi_{e\infty}$$
$$\tilde{\chi}_e(z) = \frac{b_1/4 + z^{-1}b_2/4}{1 - z^{-1}a_1 - z^{-2}a_2} \tag{4.37}$$

where $b_1 = -4K_1$ and $b_2 = 4K_1$. Substituting (4.37) in (4.9), it is obvious that three back-storages per cell (S^{L1}, S^{L2} and S^{ex}) are required to account for the z^{-2} terms. The modified real valued transmission matrix is thus given by:

$$\begin{bmatrix} V_x \\ S^{L1} \\ S^{L2} \\ S^{ex} \end{bmatrix} = T_e \begin{pmatrix} 2 & 0 & 0 & 1 \\ 2 & a_1/T_e & a_2/T_e & 1 \\ 0 & 1/T_e & 0 & 0 \\ 2\kappa_e' & b'/T_e & b_1 a_2/T_e & \kappa_e' - 1/T_e \end{pmatrix} \begin{bmatrix} V_x^{ex} \\ z^{-1}S^{L1} \\ z^{-1}S^{L2} \\ z^{-1}S^{ex} \end{bmatrix} \tag{4.38}$$

where

$$\kappa_e' = \kappa_e + 1/T_e + b_1, \quad b' = b_2 + b_1 a_1 \tag{4.39}$$

For AVM calculations, the *x*-polarization components of ζ^F and ζ^s utilized in (4.20) are given by:

$$\zeta_x^F = \frac{\partial T_e}{\partial p_i}(2V_x^{ex} + z^{-1}S^{ex})$$

$$\zeta^{SL1} = \zeta_{x,k}^F + z^{-1}\left(\frac{\partial a_1}{\partial p_i}S^{L1} + \frac{\partial a_2}{\partial p_i}S^{L2}\right)$$

$$\zeta^{SL2} = 0 \qquad (4.40)$$

$$\zeta^{ex} = \frac{\partial \kappa_e}{\partial p_i}V_x + \kappa_e\zeta_x^F + b_1\zeta^{SL1} + b_2\zeta^{SL2} + z^{-1}\left(\frac{\partial b_1}{\partial p_i}S^{L1} + \frac{\partial b_2}{\partial p_i}S^{L2}\right)$$

For the construction of the adjoint scheme, we utilize (4.38). By transposing the transmission matrix in (4.38), the adjoint simulation has the form:

$$\begin{bmatrix} V_x^{\lambda} \\ S^{L1,\lambda} \\ S^{L2,\lambda} \\ S^{ex,\lambda} \end{bmatrix} = T_e \begin{pmatrix} 2 & 2 & 0 & 2\kappa_e' \\ 0 & a_1/T_e & 1/T_e & (b_2+b_1a_1)/T_e \\ 0 & a_2/T_e & 0 & b_1a_2/T \\ 1 & 1 & 0 & \kappa_e'-1/T_e \end{pmatrix} \begin{bmatrix} V_x^{ex,\lambda} \\ zS^{L1,\lambda} \\ zS^{L2,\lambda} \\ zS^{ex,\lambda} \end{bmatrix} \qquad (4.41)$$

Utilizing (4.40) and (4.41), we can calculate (4.17) and (4.20) for the calculation of AVM dispersive sensitivity.

4.5 NUMERICAL RESULTS

In this Section, we perform AVM-based sensitivity analyses of problems with dispersive materials. We apply our technique to non-magnetized plasma, Debye material, and air-Lorentz material interface. The adjoint sensitivities are shown to be identical to the sensitivities obtained using the accurate and computationally intensive central finite difference (CFD) applied at the response level. All the simulations are conducted on an Intel® Xeon® Processor 5160 (3.0 GHz), (16.0 GB of RAM) platform.
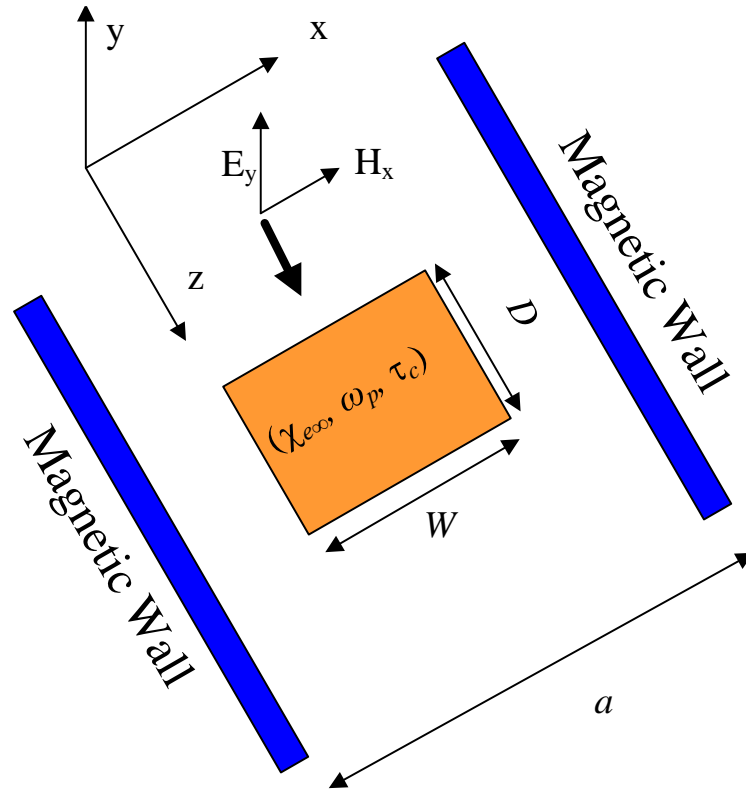
Fig. 4.2. A parallel plate waveguide with a plasma discontinuity.

4.5.1 Plasma Discontinuity

In this example, a plasma discontinuity is introduced inside a parallel plate waveguide (see Fig. 4.2). Similar setup is commonly utilized for parameter extraction problems where the discontinuity parameters are unknown. By calculating sensitivities of the scattered energy with respect to the material and shape properties, accurate characterization of the discontinuity can be achieved [47] .

The waveguide has a 5.0 mm width and is excited with a broadband Gaussian excitation (with E_y polarization), a center frequency of 50.0 GHz, and bandwidth of 60.0 GHz. The plasma discontinuity has a width W=2.0 mm. The model parameters for this

material are ω_p=28.7 GHz, τ_c=50.0 ps and $\chi_{e\infty}$=1 [41]. The length of the discontinuity D is chosen as a parameter that changes from 1.0 cm to 3.0 cm. The cell size of the TLM computational domain Δl=0.1 mm.

The objective function for this example is the transmitted energy to an output port P_o which is given by:

$$F = \Delta t \sum_{k=1}^{N_t} \sum_{i=1}^{N_x} E_y^2(i, P_o) \Big|_k \qquad (4.42)$$

where N_t is the total number of time instants at which the structure is simulated. N_x is the number of cells in the transverse direction of the output port.

The adjoint sensitivities are calculated with respect to the material and shape parameters $\boldsymbol{p}$=[χ β_c g_{ec} D W]^T. The sensitivities are calculated using the dispersive AVM approach and compared to the accurate central finite difference (CFD) approach. In Figs. 4.3-4.5, the sensitivities are calculated with respect to $\chi_{e\infty}$, β_c, and g_{ec} for different plasma lengths. The sensitivities with respect to the shape parameters are shown in Fig. 4.6. The AVM results match well the expensive central finite difference. For 51 different plasma lengths, the CFD requires 510 extra simulations (2 per parameter). However, utilizing AVM approach only 51 extra simulations are required. The total time required for sensitivity calculations, utilizing the CFD approach $\approx$13.6 hours. However, utilizing the AVM approach, only 2.3 hours are required for sensitivity calculations at all different slab widths.
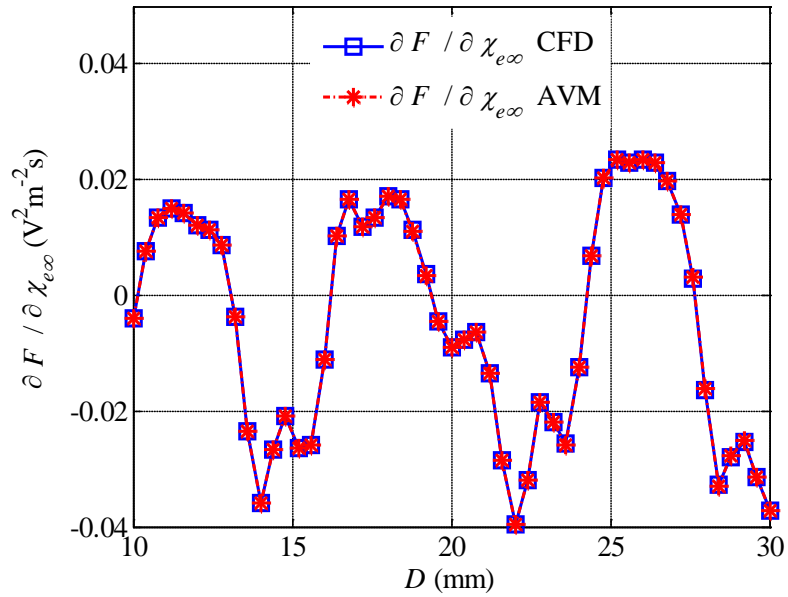
Fig. 4.3. The adjoint sensitivity of the transmitted energy for the plasma discontinuity example with respect to the material parameters ($\chi_{e\infty}$) as compared to the accurate finite difference results.
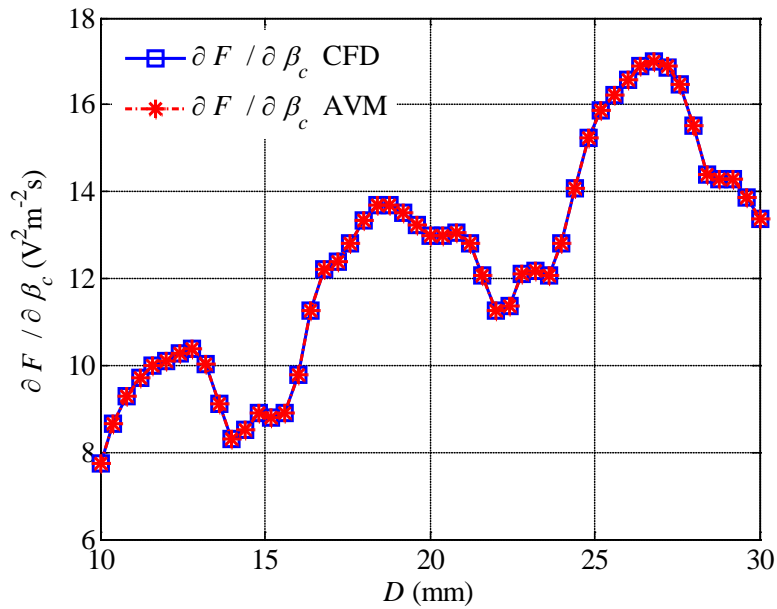
Fig. 4.4. The adjoint sensitivity of the transmitted energy for the plasma discontinuity example with respect to (β_c) as compared to the accurate finite difference results.

133
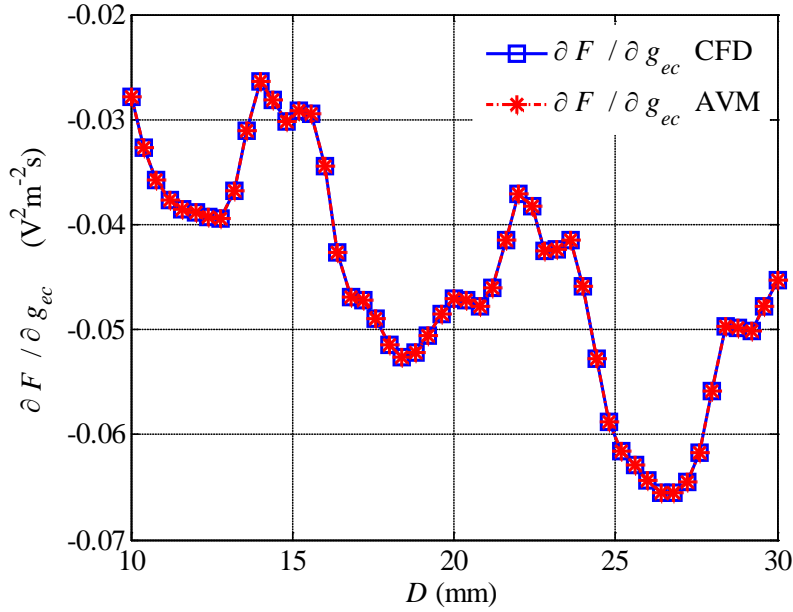
Fig. 4.5. The adjoint sensitivity of the transmitted energy for the plasma discontinuity example with respect to the material parameters g_{ec} as compared to the accurate finite difference results.
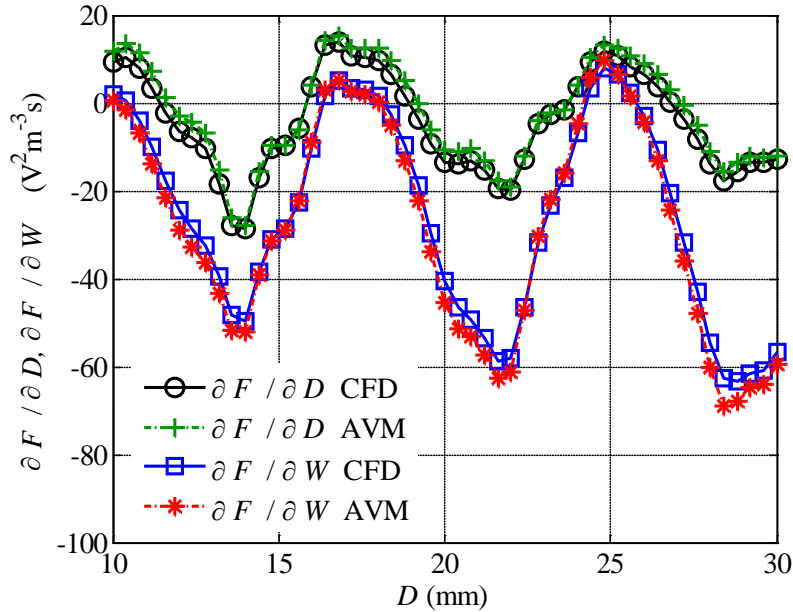
Fig. 4.6. The adjoint sensitivities of the transmitted energy for the plasma discontinuity example with respect to the length D and width W as compared to the accurate finite difference results.
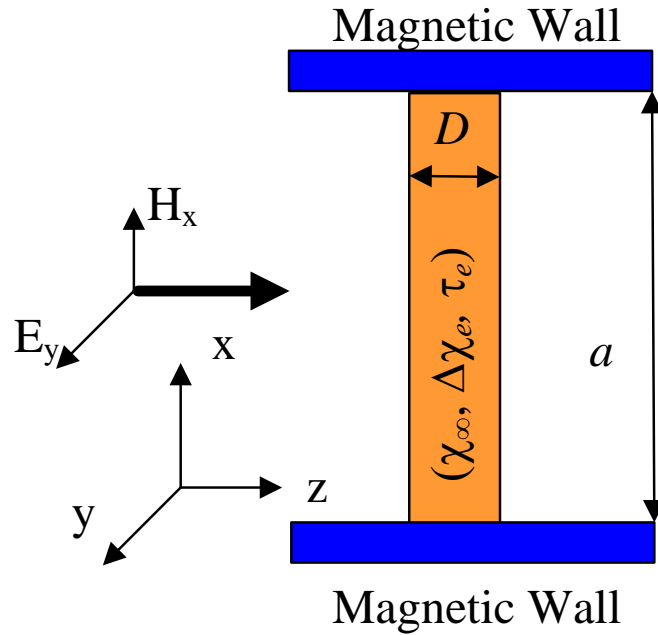
Fig. 4.7. A parallel plate waveguide loaded by a Debye material.

4.5.2 Debye Slab

In this example, a parallel plate waveguide (a=1.0 cm) is loaded by a Debye material (see Fig. 4.7). The objective function for this example is the total energy at the input port P_{input}. We calculate the sensitivities of the objective function with respect to dispersion and shape parameters $\boldsymbol{p} = [\chi_{e\infty} \ \Delta\chi_e \ \beta_e \ g_e \ D]^T$. The utilized Debye material has the parameters $\chi_{e\infty}$=1.8, $\Delta\chi_e$=79.2, and τ_e=9.4 ps [23] with a normalized conductivity g_e=0.1. The waveguide is excited by a y-polarized wave. A wideband Gaussian signal of 20.0 GHz bandwidth centered around 30.0 GHz is utilized. For accurate modeling, a discretization of Δl=0.2 mm is utilized.

The energy objective function in (4.42) can be utilized by calculating the energy at the input port. Fig. 4.8 shows the sensitivities of the objective function with respect to the

model parameters $\chi_{e\infty}$ and $\Delta\chi_e$ for different slab widths D. Figures 4.9 and 4.10 show the sensitivities with respect to the normalized parameter β_e, the normalized conductivity $g_{e,}$ and the slab width D as compared to the CFD. Good match is observed. AVM calculations require approximately 0.8 hours, while the CFD approach requires 4.7 hours.
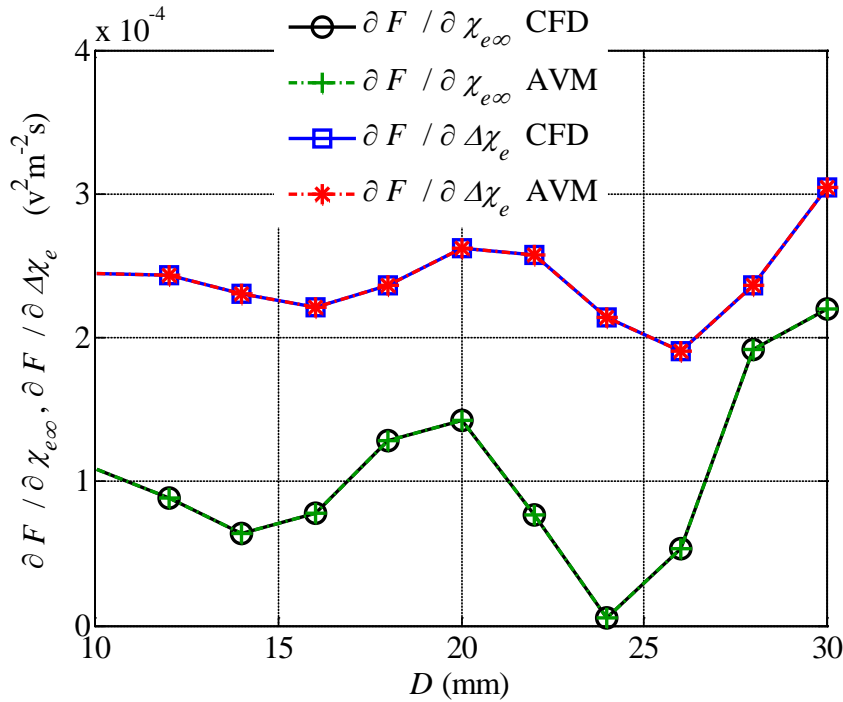
Fig. 4.8. The adjoint sensitivities of the total energy at the input port for the Debye slab with respect to the material parameters $\chi_{e\infty}$ and $\Delta\chi_e$ as compared to the accurate finite difference results.
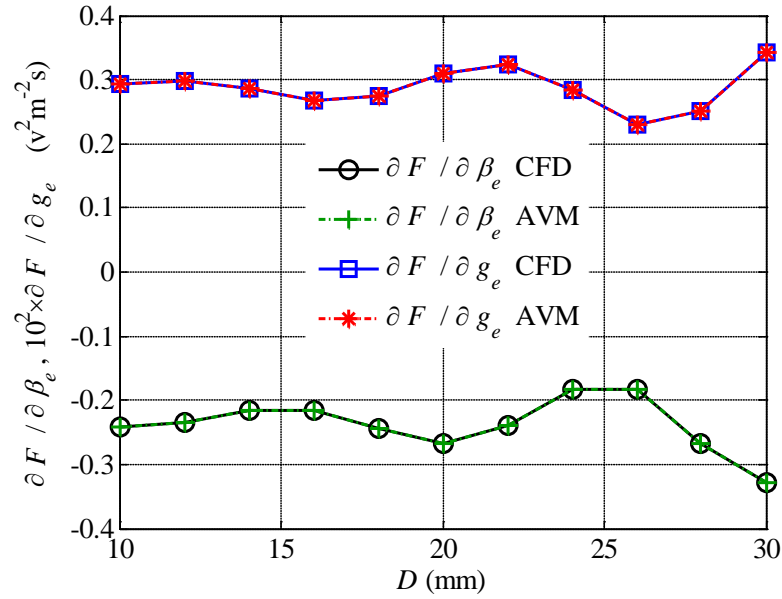
Fig. 4.9. The adjoint sensitivities of the total energy at the input port for the Debye slab with respect to the material parameters β_e and g_e as compared to the accurate finite difference results.
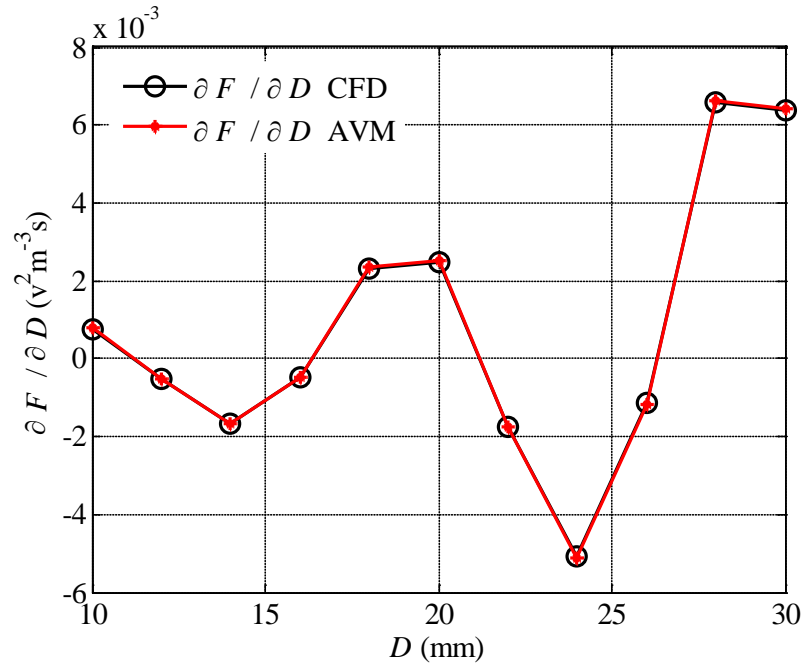
Fig. 4.10. The adjoint sensitivity of the total energy at the input port for the Debye slab with respect to the shape parameters D as compared to the accurate finite difference results.
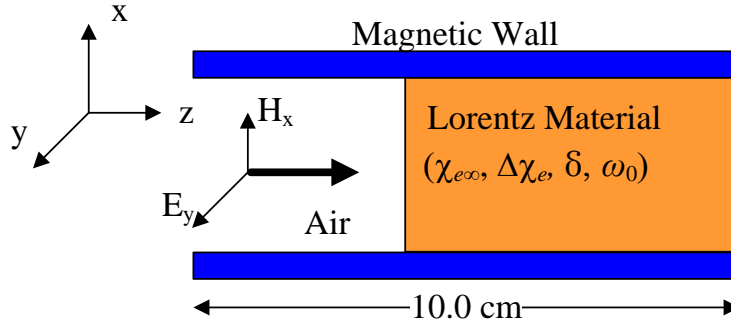
Fig. 4.11. An air/Lorentz interface.

4.5.3 Lorentz Interface

This example considers an interface between a Lorentzian material and air as shown in Fig. 4.11. The objective function is the total energy at the input port. The sensitivities with respect to the dispersive parameters $\chi_{e\infty}$, $\Delta\chi_e$, δ, and ω_0 are calculated utilizing the developed AVM theory. The model parameters (δ and ω_0) have values nine orders of magnitude higher than the values of $\chi_{e\infty}$ and $\Delta\chi_e$. For rigorous gradient-based optimization, those parameters are scaled to have the same order of magnitude. In (4.35), another normalized parameters (A_e and B_e) which are functions of (δ and ω_0) are defined. We calculate the sensitivities for both the original model parameters (δ and ω_0) and the defined normalized parameters (A_e and B_e) using the dispersive AVM approach.

The utilized air/Lorentz interface has the parameters $\chi_{e\infty}$=0.5, $\Delta\chi_e$=1.5, ω_0=20.0 GHz and δ=0.1ω_0 [48]. For accurate calculation of the objective function and its sensitivities, a discretization of Δl=0.1 mm is used. The total length of the computational domain is 10.0 cm. The excitation (with E_y polarization) is a wide band Gaussian signal with a central frequency of 60.0 GHz and a bandwidth of 118.0 GHz.
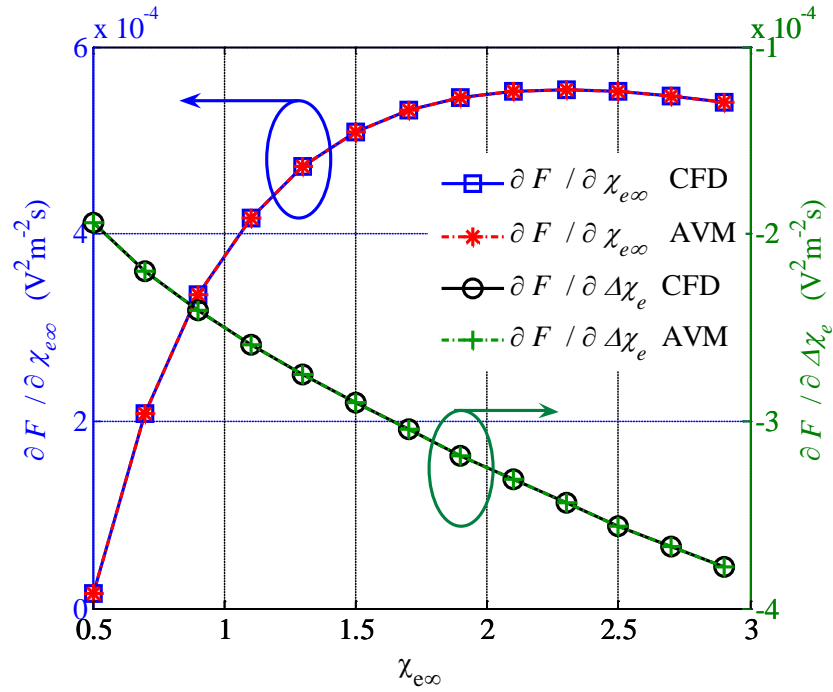
Fig. 4.12. The adjoint sensitivities of the total energy at the input port for the air/Lorentz interface with respect to the parameters $\chi_{e\infty}$ and $\Delta\chi_e$ as compared to the accurate finite difference results.

The sensitivities of total input power, see (4.42), with respect to the Lorentz model parameters are calculated at 13 different values of the material high frequency susceptibility ($\chi_{e\infty}$). The results are shown in Figs. 4.12 and 4.13. The sensitivities with respect to the normalized parameters A_e and B_e are also shown in Fig. 4.14. Good match with the CFD approximation is achieved for all sensitivities. The total execution time utilizing the AVM approach is 15 minutes for all 13 different values of $\chi_{e\infty}$. Using CFD, the total execution time is 75 minutes.
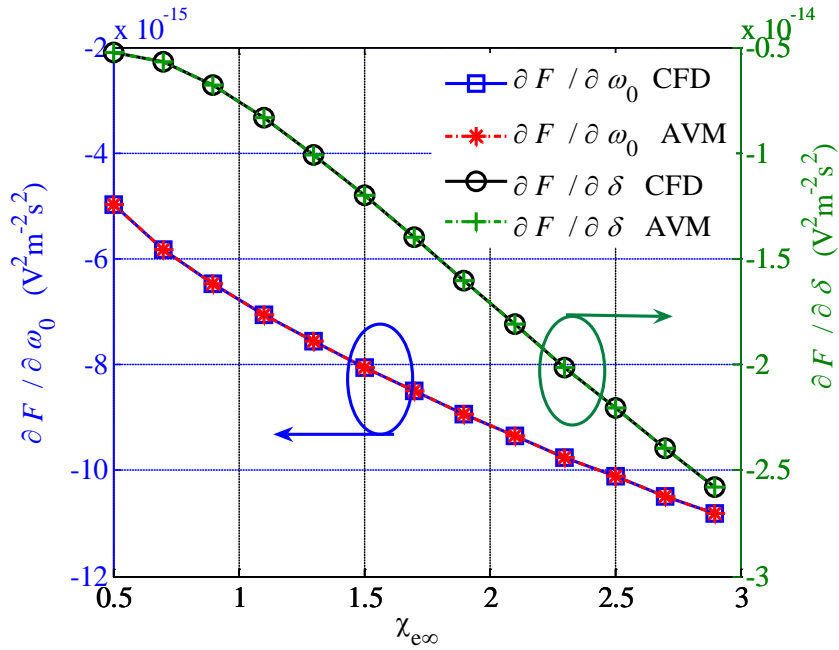
Fig. 4.13. The adjoint sensitivities of the total energy at the input port for the air/Lorentz interface with respect to the parameters ω_0 and δ as compared to the accurate central finite difference results.
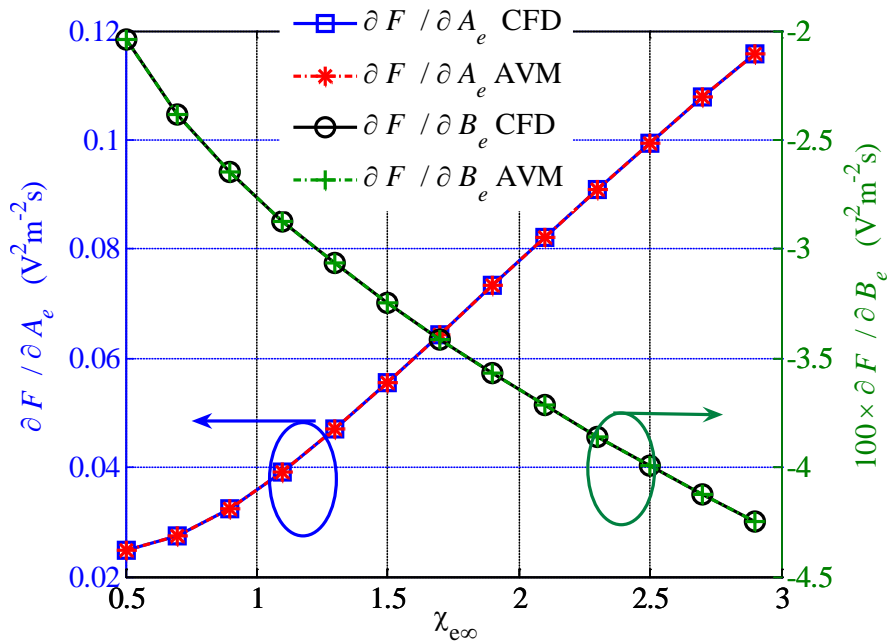
Fig. 4.14. The adjoint sensitivities the total energy at the input port for the air/Lorentz interface with respect to the numerical parameters A_e and B_e as compared to the accurate central finite difference results.
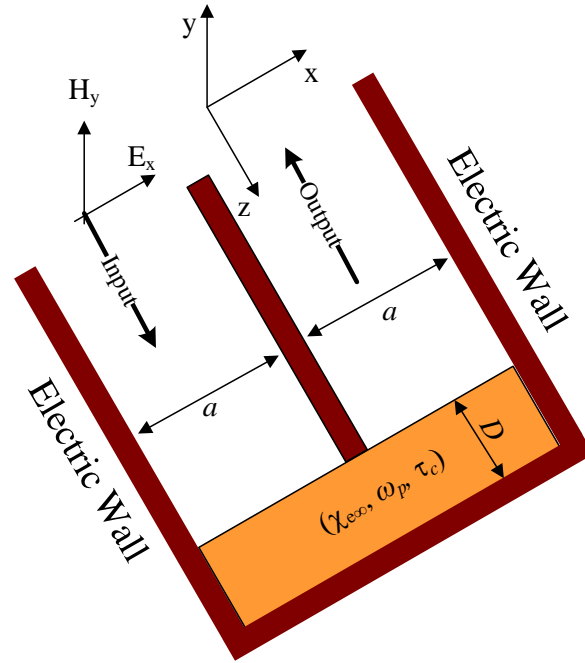
Fig. 4.15. A structure of 180° bend filled with a metamaterial slab.

4.5.4 Tunneling Through a Metamaterial Plasmonic Slab

Artificial materials (metamaterials) have been proposed for extraordinary functionality that could not be achieved using regular materials [49]. The Drude model has been verified to accurately model metamaterials [38]-[39].

In this example, we calculate the sensitivities of the scattering parameters for a recently proposed 180° reflection-less bend [40] (see Fig. 4.15). The wave is coupled from a parallel plate waveguide of width a to another by introducing a slab of metamaterial of width D and parameters ω_p, τ_c, and $\chi_{e\infty}$. The complete absorption at abrupt bends occurs at specific wavelength where the total permittivity vanishes [40] (see Fig. 4.16). The device performance is governed by the sensitivity information of the reflectivity $|S_{11}|$ due to the change in both the dispersion properties and dimension.
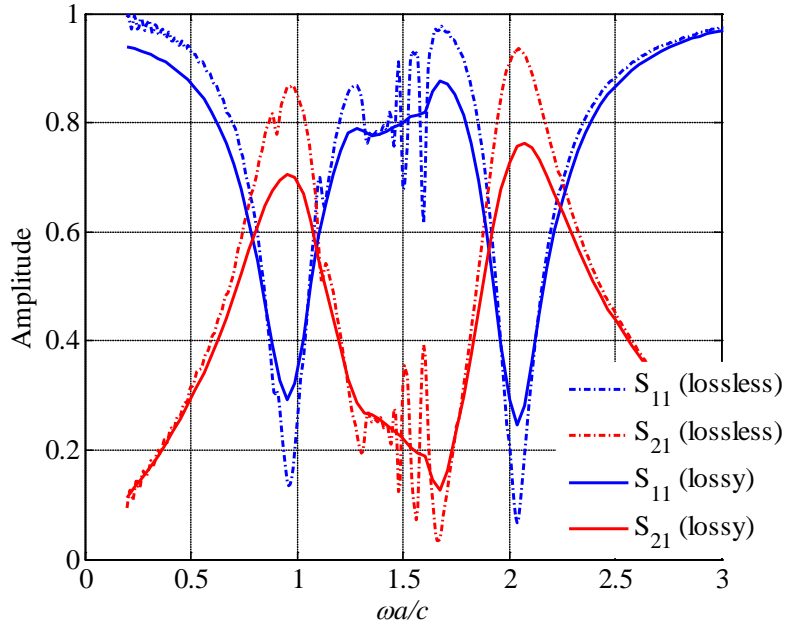
Fig. 4.16. The scattering parameters of the 180° bend for both cases of lossless and lossy metamaterial slab as compared to the case without the slab.

The metametrial slab has a width $D = 0.1a$, high frequency susceptibility $\chi_{e\infty} = 0$, and plasma frequency $\omega_p = 2c/a$ where c is the speed of light. The slab is considered for both the lossless ($1/\tau_c \approx 0$) and the lossy case ($1/\tau_c \approx 0.05\omega_p$). The structure is excited with a wide band Gaussian signal (with E_x polarization) around the frequency ω_0 where $\omega_0 = 2c/a$ (for $a=0.2$mm, $\omega_0 = 3.0$ THZ). For accurate modeling of the thin metamaterial layer, a space step of $\Delta l = 0.01a$ is chosen.

For the lossless case, the sensitivities of $|S_{11}|$ are calculated with respect to the model and shape parameters of the metamaterial slab (see Figs. 4.17-4.20). In Fig. 4.17, the adjoint sensitivity with respect to $\chi_{e\infty}$ is compared to the forward finite difference approach (FFD) as central finite differences cannot be estimated for $\chi_{e\infty} = 0$.
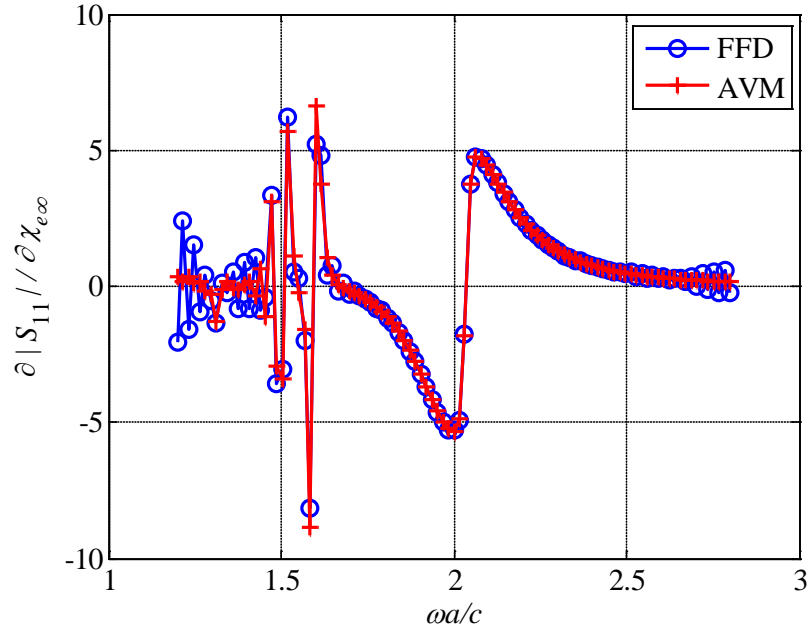
Fig. 4.17. The sensitivity of $|S_{11}|$ with respect to $\chi_{e\infty}$ for the lossless metamaterial slab example.

Figures 4.18-4.20 show the adjoint sensitivities with respect to all other parameters. Good match with the central finite difference (CFD) is observed for the non-oscillatory region ($\omega \geq \omega_p$). For the oscillatory region ($\omega \leq \omega_p$), the real part of the permittivity is negative. The calculation of the sensitivity analysis suffers from inaccuracies due to the field singularity [40]. The results of AVM sensitivity are of the same order of the CFD.

In the finite loss case, the sensitivities with respect to the material properties and shape properties are shown in Figs. 4.21-4.24. The AVM sensitivities match well the accurate finite difference results. The total execution time for sensitivity calculations using AVM is 20 minutes while 40 minutes are required utilizing the CFD approach. The CFD execution time scales linearly with the number of parameters and thus the difference

between the two execution times. In Fig. 4.24, an expected deviation of the sensitivity results shows at low frequency due to the field singularities around the metallic plate.
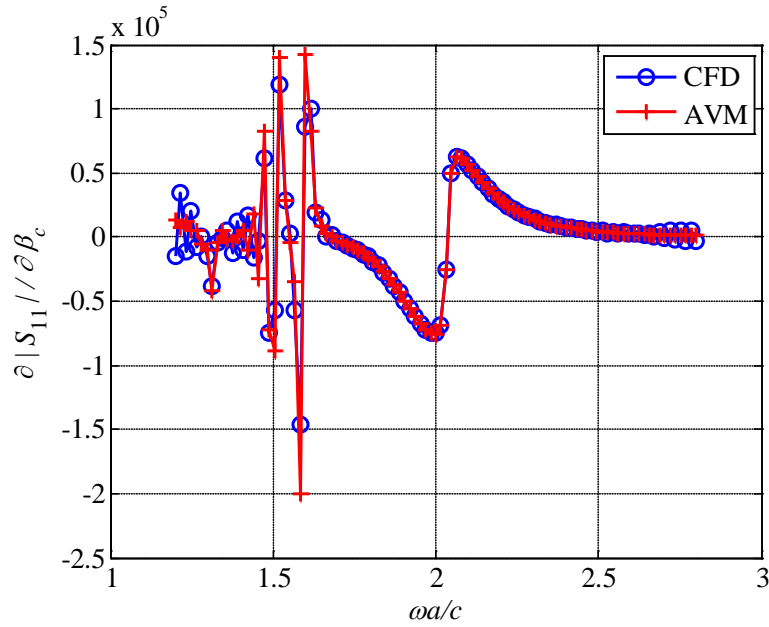
Fig. 4.18. The sensitivity of $|S_{11}|$ with respect to the normalized parameter β_c for lossless metamaterial slab example.
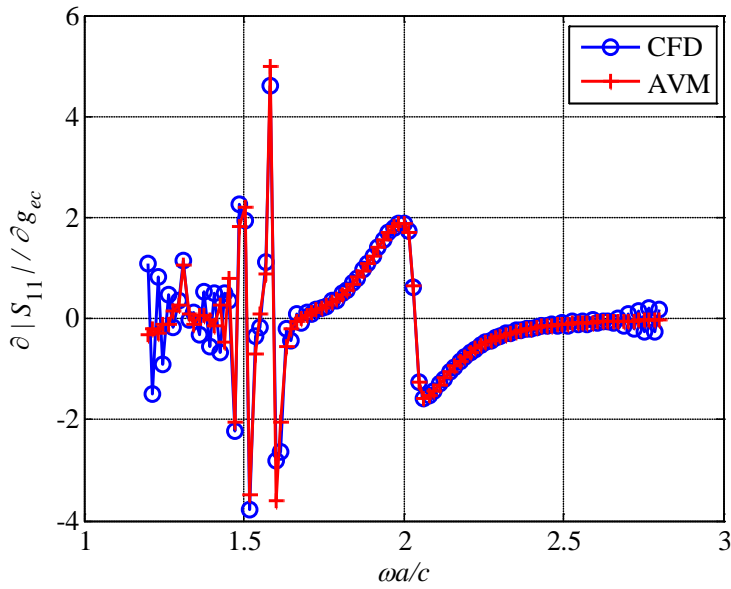
Fig. 4.19. The sensitivity of $|S_{11}|$ with respect to the normalized parameter g_{ec} for the lossless metamaterial slab example.
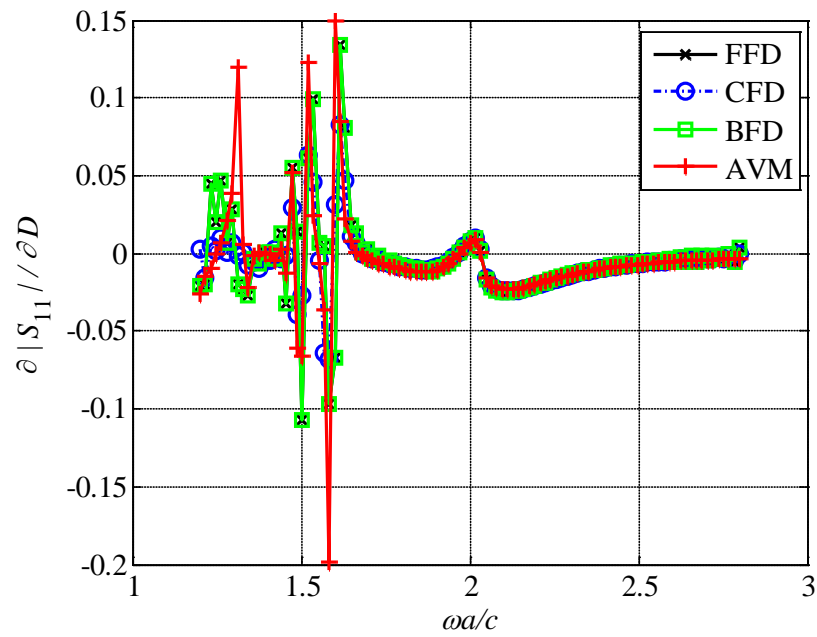
Fig. 4.20. The sensitivity of $|S_{11}|$ with respect to the shape parameter D for the lossless metamaterial slab example.
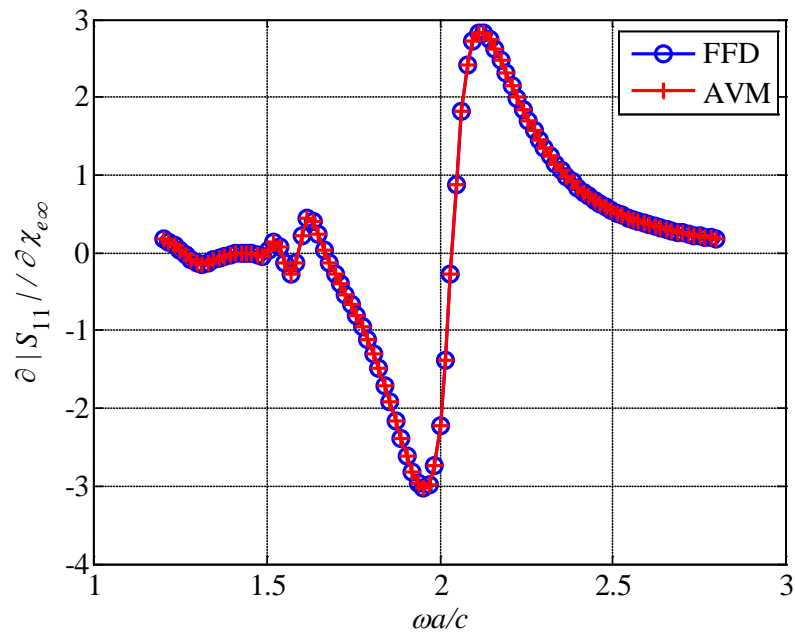
Fig. 4.21. The sensitivity of $|S_{11}|$ with respect $\chi_{e\infty}$ for the lossy metamaterial slab example.
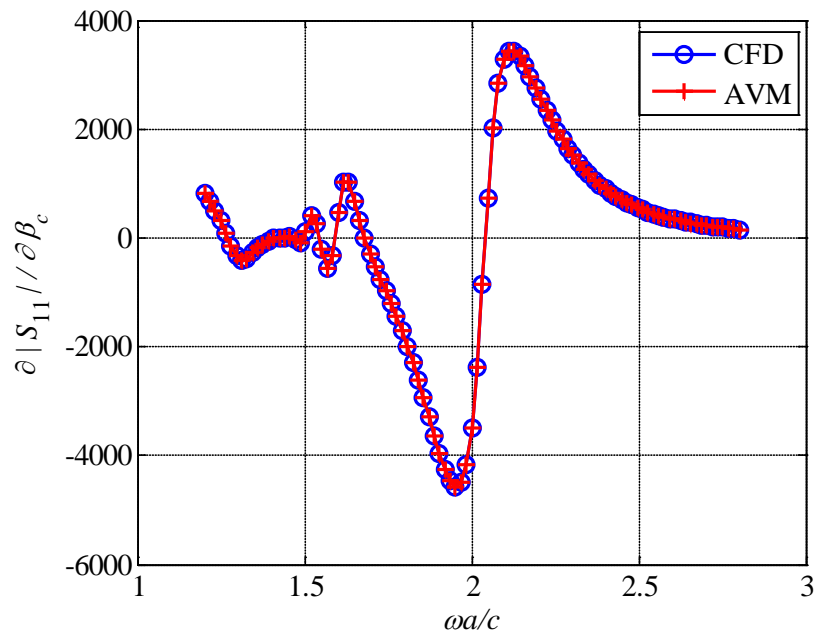
Fig. 4.22. The sensitivity of $|S_{11}|$ with respect to the normalized parameter β_c for the lossy metamaterial slab example.
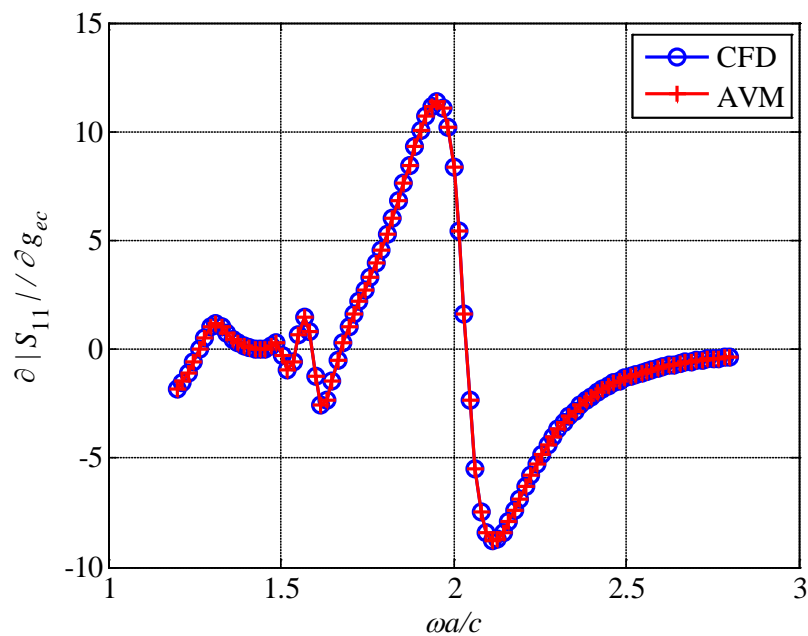
Fig. 4.23. The sensitivity of $|S_{11}|$ with respect to the normalized parameter g_{ec} for the lossy metamaterial.
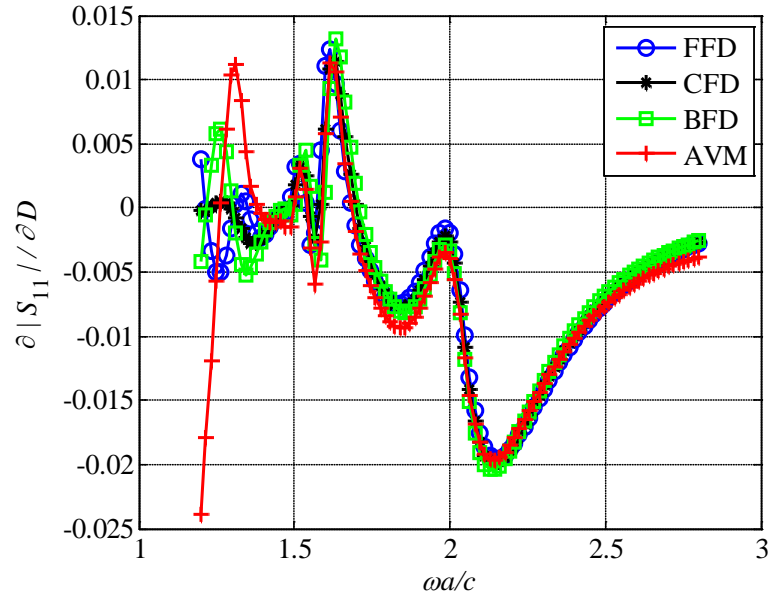
Fig. 4.24. The sensitivity of $|S_{11}|$ with respect to the shape parameter D for the lossy metamaterial slab example.

4.5.5 Teeth Shaped Plasmonic Resonator

The developed AVM is applied to several plasmonic structures. The first order Drude model is utilized to model the metal. The dispersive approach is demonstrated through the teeth shaped plasmonic resonator [50] shown in Fig. 4.25. The teeth widths (w_i) are set to 50.0 nm where the teeth thicknesses are t_1=50.0 nm, $t_2 = t_6$ =100.0 nm, $t_3 = t_5$ =150.0 nm and t_4=260.0 nm. The structure is illuminated by a wide band signal of bandwidth 2.0 μm (0.5μm to 2.5μm). The vector of design parameters is p=[w_1 t_1 w_2 t_2 ... w_6 t_6]. The sensitivity of the scattering parameter $|S_{11}|$ with respect to the optimization parameters (shape properties) are illustrated in Fig. 4.26-4.28, where the AVM results are compared to the expensive finite difference approach. Good agreement between the

147

expensive central finite difference (CFD) and dispersive AVM results is achieved except for the sensitivity with respect to the parameter w_1 over a certain frequency band.

By also examining the forward finite difference (FFD) and backward (BFD) results with respect to w_1, it is obvious from their difference that the objective function is highly nonlinear with respect to this parameter which explains the difference between AVM and CFD. These results are illustrated in Fig. 4.29. For this example, while AVM calculate the sensitivity using at most one extra simulation, the central difference utilizes 24 extra simulations to calculate the sensitivity with respect to the 12 design parameters.
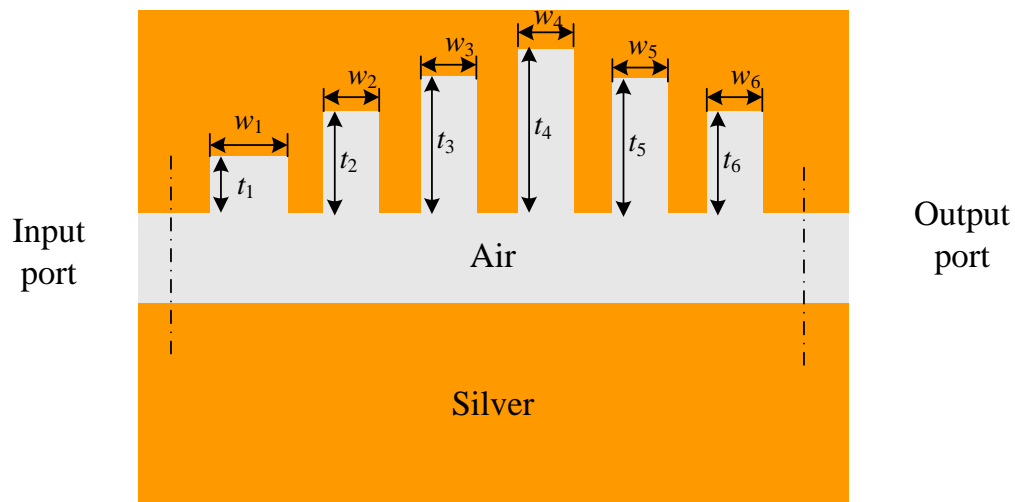
Fig. 4.25. The teeth-shaped plasmonic resonator.
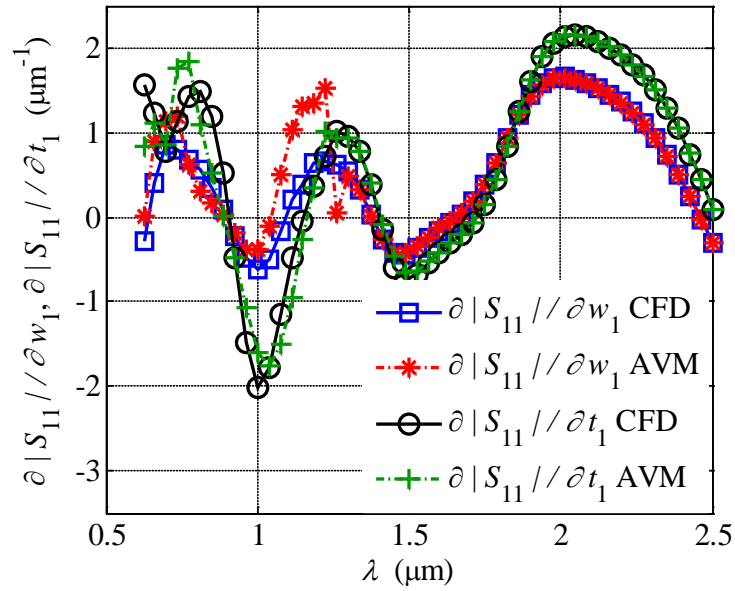
Fig. 4.26. Sensitivity of the scattering parameter $|S_{11}|$ to the shape parameters, w_1, and t_1, using AVM is compared to the expensive central finite difference approach.
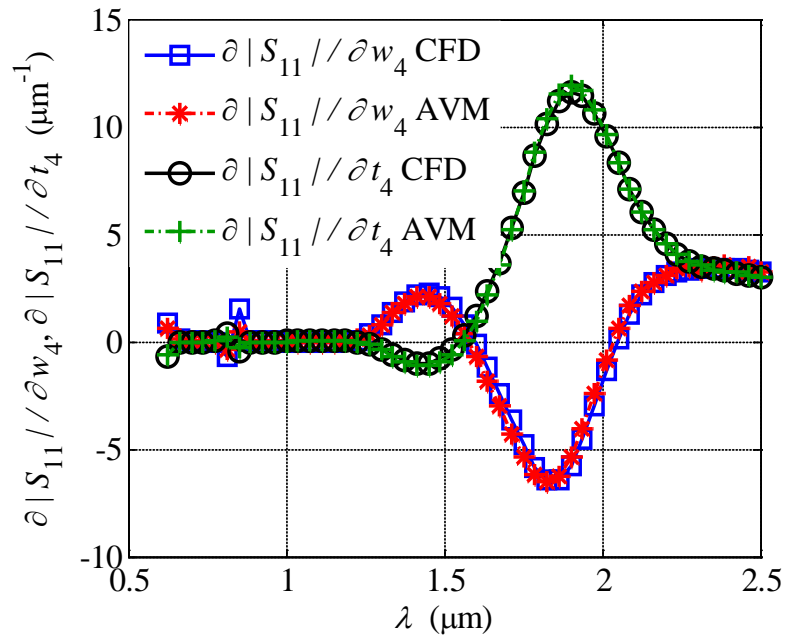
Fig. 4.27. Sensitivity of the scattering parameter $|S_{11}|$ to the shape parameters, w_4, and t_4, using AVM is compared to the expensive finite central difference approach.
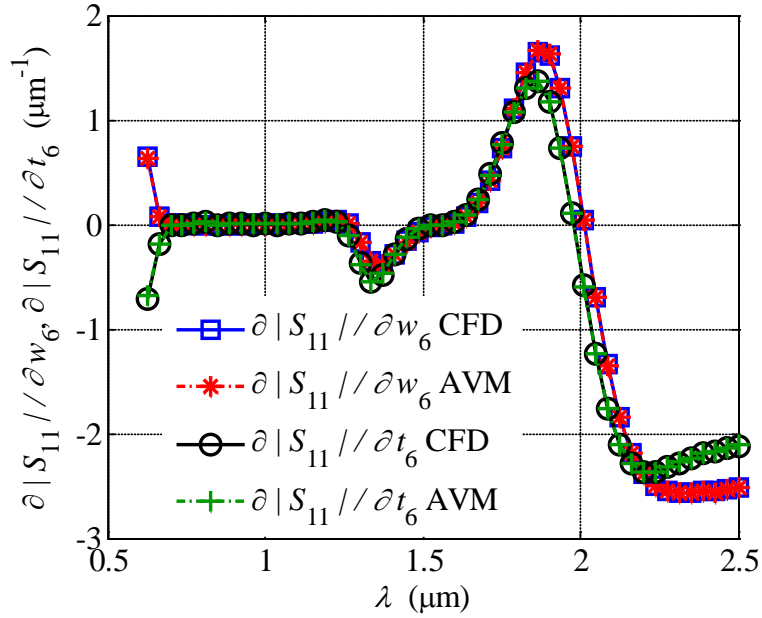
Fig. 4.28. Sensitivity of the scattering parameter $|S_{11}|$ to the shape parameters, w_6, and t_6, using AVM is compared to the expensive central finite difference approach.
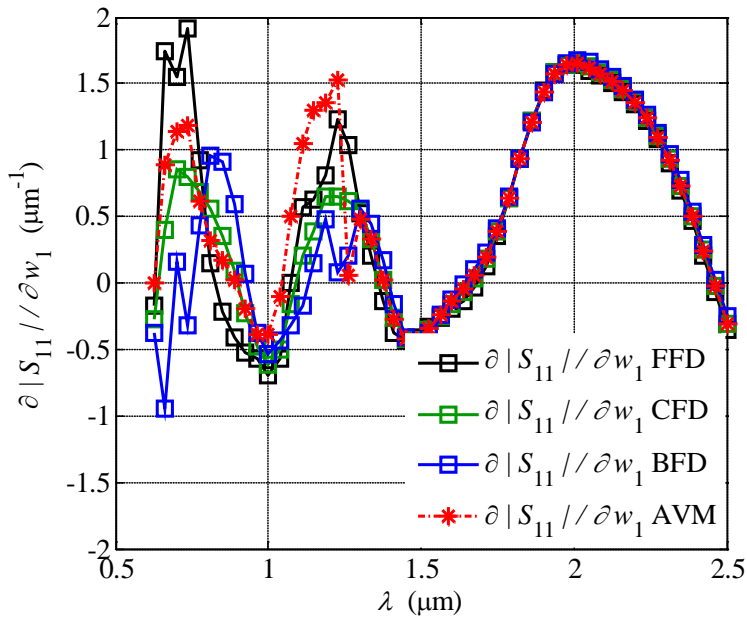
Fig. 4.29. Sensitivity calculation of the scattering parameter $|S_{11}|$ to w_1 using FFD, CFD, BFD, and AVM.
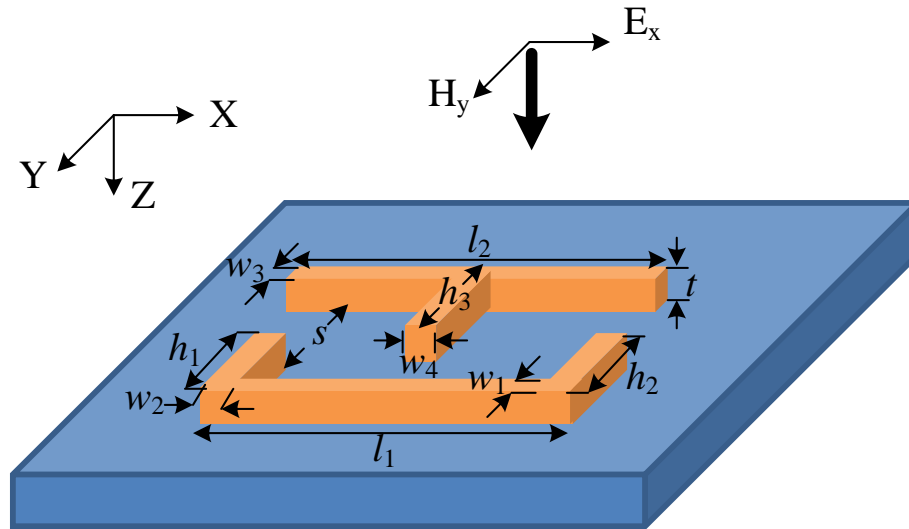
Fig. 4.30. Schematic of the gold nano-plasmonic resonating antenna.

4.5.6 Sensitivity of 3D Plasmonic Resonator Antenna

In this example a multiband plasmonic resonator antenna (UT shaped) is studied [51] (see Fig. 4.30). Plasmonic metamaterials provide unique light manipulation capabilities. Utilizing inherent resonant properties of plasmonic materials, light is guided and focused at a subwavelength range.

The UT shaped gold nano-structures are utilized to create plasmonic metamaterials by introducing a two dimensional array of the structure. The design of such a multi-resonant structure requires proper choice of the geometrical parameters.

The sensitivities of the UT nano-structure is calculated utilizing adjoint variable method. They are compared to the accurate expensive central difference approach. The structure is perturbed at every side plane. This enables us to calculate sensitivity with respect to all possible geometrical changes.
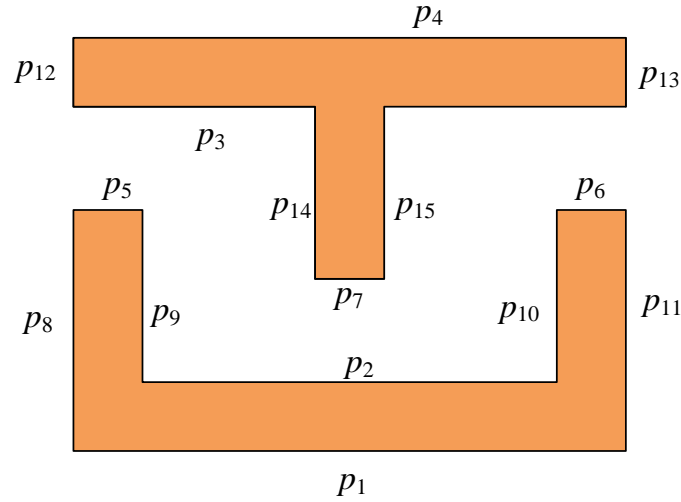
Fig. 4.31. Top view of the gold nano-structure. All different perturbation planes are shown.

Fig. 4.31 shows the top view of the structure. 15 different geometrical planes are shown and denoted by (p_1 p_2 ... p_{15}). By perturbing the structure in the Z direction another parameter is also included (p_{16}). The sensitivities of the scattering parameter $|S_{11}|$ are calculated with respect to all possible perturbations.

The modeled nano-structure has the geometrical parameters $l_1 = l_2 = 800.0$ nm, $h_1 = h_2 = h_3 = 400.0$ nm, $w_1 = w_2 = w_3 = w_4 = s = 100.0$ nm, and $t=60.0$ nm [51]. The Drude model is utilized for the gold material. A silicon dioxide substrate of refractive index of 1.46 is utilized. The structure is excited with a wideband Gaussian signal of center frequency 80 THz and a bandwidth 120 THz. Plane wave propagating in the Z direction is utilized with x-polarized field excitation. Magnetic walls are included in the X and Y terminations and absorbing boundary is introduced for domain truncation in the Z direction. The simulation is conducted on an Intel® Xeon® Processor 5160 (3.0 GHz), (16.0 GB of RAM) platform.
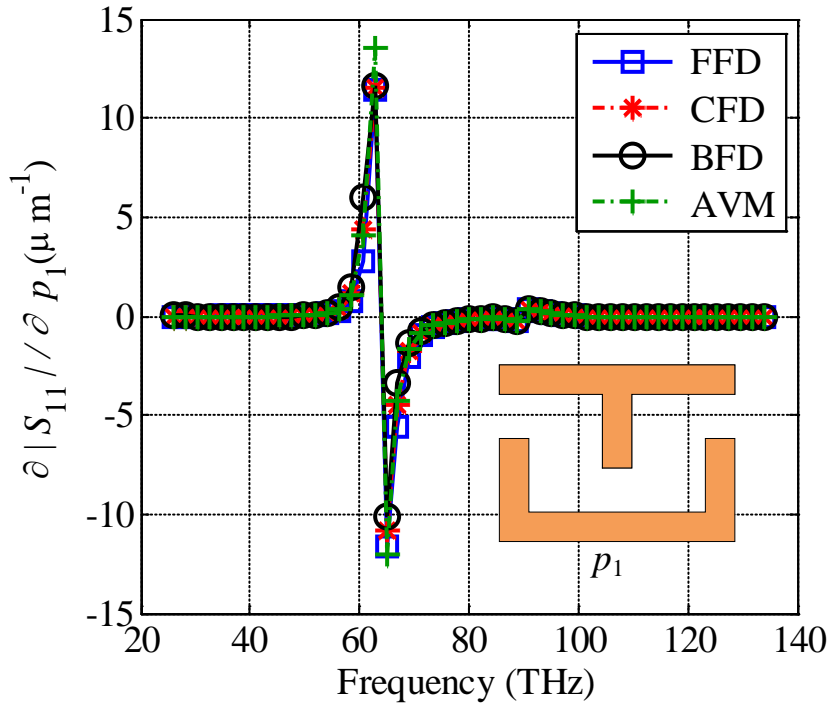
Fig. 4.32. Adjoint sensitivity analysis of $|S_{11}|$ for the 3D plasmonic resonator antenna relative to p_1.

Because of space limitation, only a subset of the adjoint sensitivity analysis results is shown in Figs. 4.32-4.35. The AVM results are compared to finite difference approaches. The AVM matches well the expensive central finite difference results. A total of 2 simulations are required for AVM calculation (overall calculation time ≈ 1.5 hours). For central difference calculations a total of 33 simulations are required (overall calculation time ≈12.0 hours).

(a)

(b)
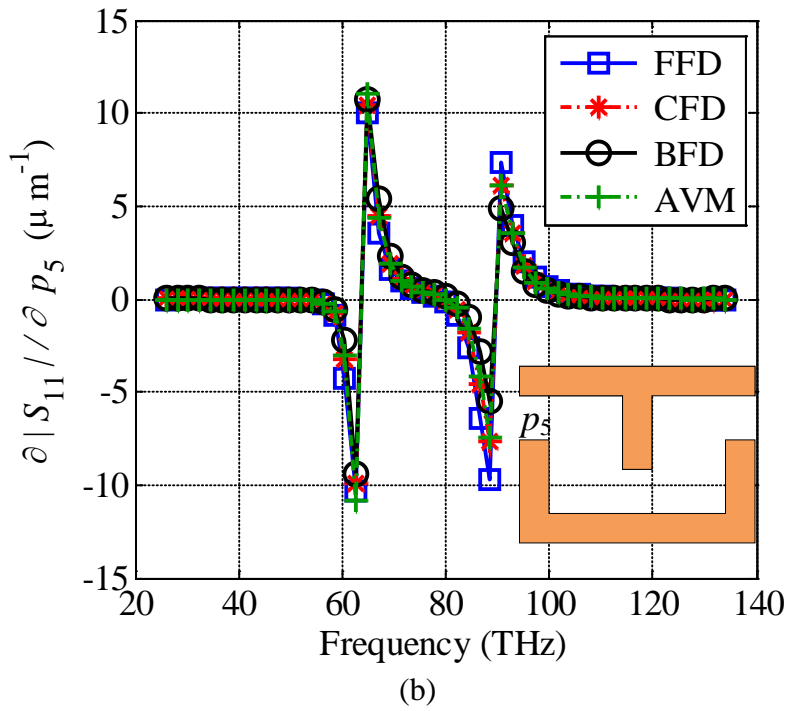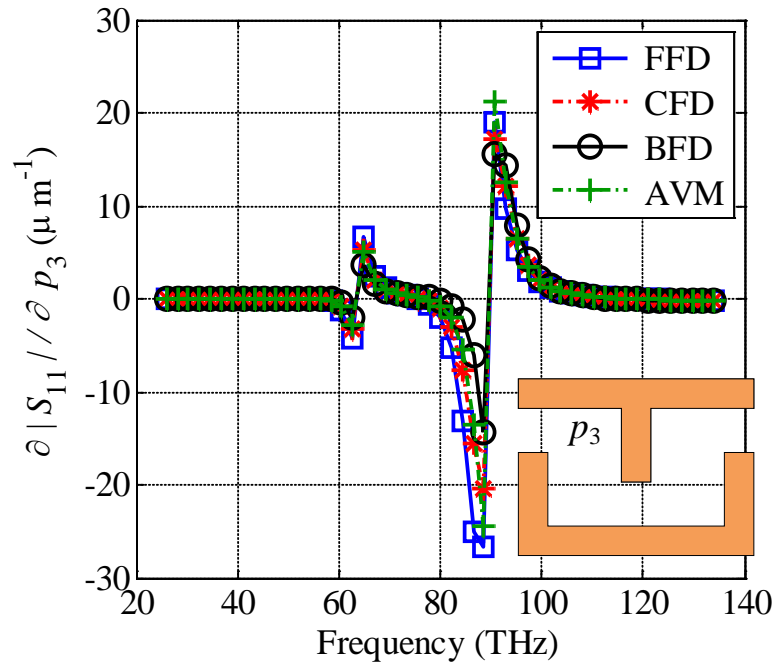
Fig. 4.33. Adjoint sensitivity analysis of $|S_{11}|$ for the 3D plasmonic resonator antenna; a) sensitivity relative to p_3, and b) sensitivity relative to p_5.
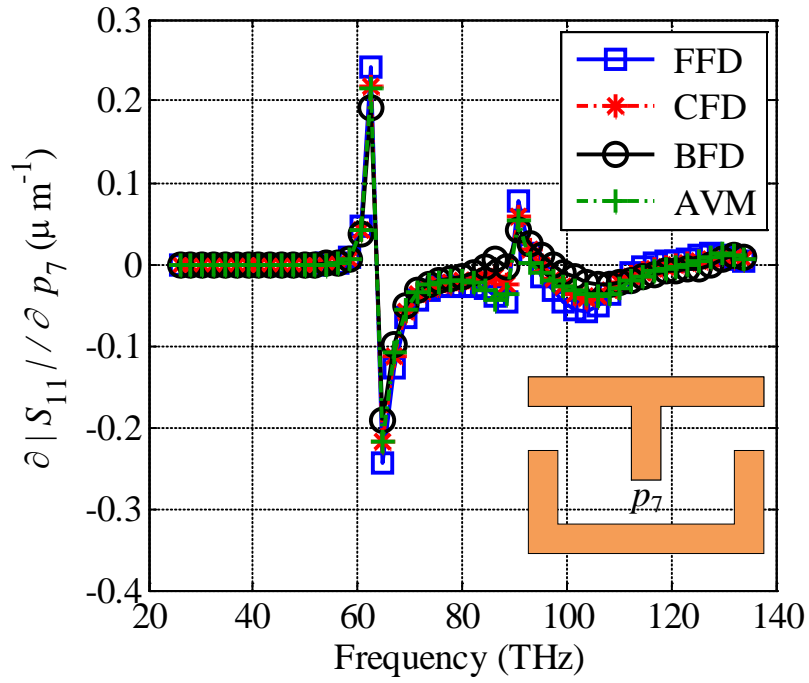
(a)
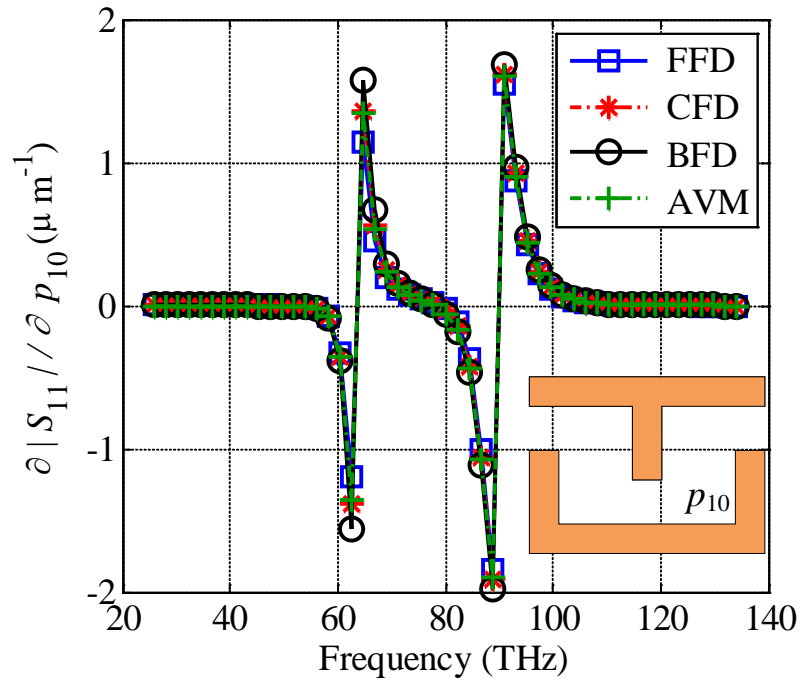
(b)

Fig. 4.34. Adjoint sensitivity analysis of $|S_{11}|$ for the 3D plasmonic resonator antenna; a) sensitivity relative to p_7, and b) sensitivity relative to p_{10}.

(a)

(b)
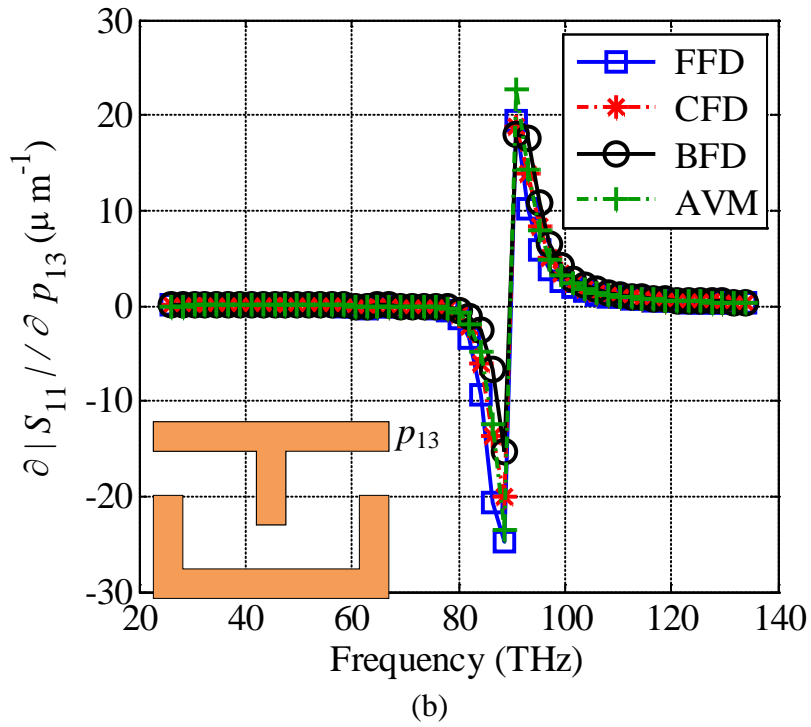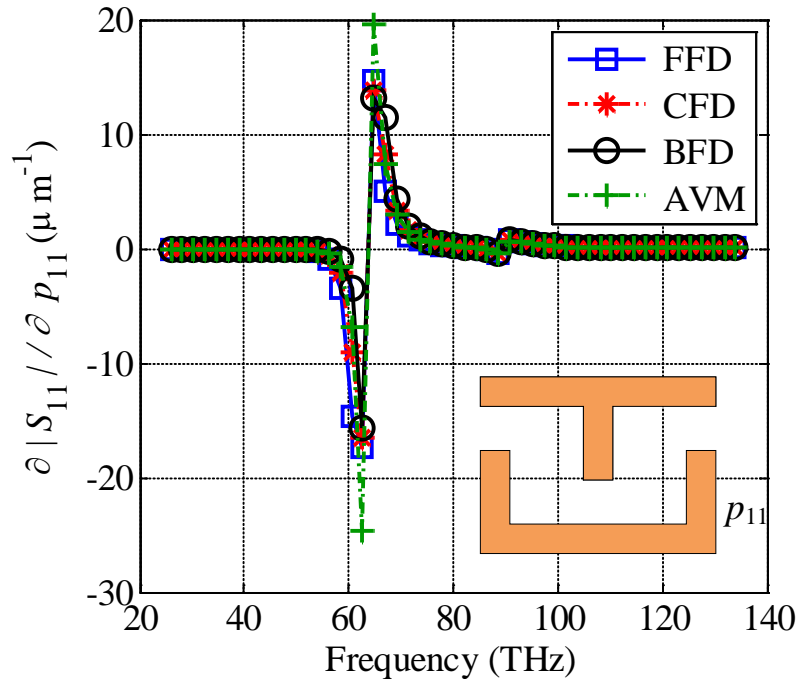
Fig. 4.35. Adjoint sensitivity analysis of $|S_{11}|$ for the 3D plasmonic resonator antenna; a) sensitivity relative to p_{11}, and b) sensitivity relative to p_{13}.

4.6 DISCUSSION

The presented approach can be extended to other time-domain modeling techniques such as the FETD (finite element time-domain) and FDTD (finite difference time-domain). Numerical differences between these approaches and the TLM method have to be taken into account. The algorithm has to be modified to take into consideration the system history. Extra storage state variables have to be defined [52] . The size of extra storage will be dependent on the dimensionality of the problem and the order of the dispersion model as well.

For the FDTD case, the linear matrix formulation [11] should be modified. A new system is formulated to link the field state variables (E_x, E_y, E_z) to the system storage variables. The FDTD-based algorithm will require the calculation of the derivatives of the system matrix during the main simulation. Proper transformation of the dispersive original problem is required to construct the adjoint simulation. The original and adjoint state variables are utilized to formulate an AVM expression similar to those provided in (4.19) and (4.20).

4.7 CONCLUSION

We introduce a novel theory for wideband AVM sensitivity analysis for dispersive materials. The theory can be extended to different fields other than electromagnetics. It has been successfully applied to Drude, Debye, and Lorentz materials.

We utilized the dispersive AVM for the calculation of sensitivities with respect to both the material and shape properties of a dispersive media. Our results are compared to

the accurate and expensive finite difference approaches; perfect match is achieved. The theory has been applied for basic test examples and for recently introduced structures of special model parameters and promising functionality. The advantage of AVM is also demonstrated through adjoint sensitivity analysis of a complex 3D nano-structure.

4.8 REFERENCES

[1]   K. C. Gupta, R. Garg, and R. Chadha, *Computer-Aided Design of Microwave Circuits*. Dedham, MA: Artech House, 1981.

[2]   H. Lee and T. Itoh, "A systematic optimum design of waveguide-to-microstrip transition," *IEEE Trans. Microwave Theory Tech.*, vol. 45, pp. 803-809, 1997.

[3]   H. Akel and J. P. Webb, "Design sensitivities for scattering-matrix calculation with tetrahedral edge elements," *IEEE Trans. Magn.,* vol. 36, pp. 1043-1046, 2000.

[4]   J. P. Webb, "Design sensitivities using high-order tetrahedral vector elements," *IEEE Trans. Magn.,* vol. 37, pp. 3600-3603, 2001.

[5]   G. Iuculano, V. A. Monaco, and P. Tiberio, "Network sensitivities in terms of scattering parameters," *Electron. Lett.*, vol. 7, pp. 53-55, 1971.

[6]   J. W. Bandler, Q.-J. Zhang, and R. M. Biernacki, "A unified theory for frequency-domain simulation and sensitivity analysis of linear and nonlinear circuits," *IEEE Trans. Microwave Theory Tech.*, vol. 36, pp. 1661-1669, 1988.

[7]   Y. Chung, C. Cheon, I. Park, and S. Hahn, "Optimal shape design of microwave device using FDTD and design sensitivity analysis," *IEEE Trans. Microwave Theory Tech.*, vol. 48, pp. 2289-2296, 2000.

[8]   Y. Chung, J. Ryu, C. Cheon, I. Park, and S. Hahn, "Optimal design method for microwave device using time domain method and design sensitivity analysis—Part I: FETD case," *IEEE Trans. Magn.,* vol. 37, pp. 3289-3293, 2001.

[9]   Y. Chung, C. Cheon, I. Park, and S. Hahn, "Optimal design method for microwave device using time domain method and design sensitivity analysis—Part II: FDTD case," *IEEE Trans. Magn.,* vol. 37, pp. 3255-3259, 2001.

[10]   M. H. Bakr and N. K. Nikolova, "An adjoint variable method for time-domain transmission line modeling with fixed structured grids," *IEEE Trans. Microwave Theory Tech.*, vol. 52, pp. 554-559, 2004.

[11]   N. K. Nikolova, H. W. Tam, and M. H. Bakr, "Sensitivity analysis with the FDTD method on structured grids," *IEEE Trans. Microwave Theory Tech.*, vol. 52, pp. 1207-1216, 2004.

[12]   M. H. Bakr, P. Zhao, and N. K. Nikolova, "Adjoint first order sensitivities of transient responses and their applications in the solution of inverse problems," *IEEE Trans. Antennas Propag.*, vol. 57, pp. 2137-2146, 2009.

[13]   M. H. Bakr and N. K. Georgieva, "An adjoint variable method for frequency domain TLM problems with conducting boundaries," *IEEE Microwave wireless Comp. Lett.*, vol. 13, pp. 408-410, 2003.

[14] N. K. Georgieva, S. Glavic, M. H. Bakr, and J.W. Bandler, "Feasible adjoint sensitivity technique for EM design optimization," *IEEE Trans. Microwave Theory Tech.*, vol. 50, pp. 2751-2758, 2002.

[15] J. P. Webb, "Design sensitivity of frequency response in 3-D finite-element analysis of microwave devices," *IEEE Trans. Magn.*, vol. 38, pp. 1109-1112, 2002.

[16] P. A. W. Basl, M. H. Bakr, and N. K. Nikolova, "Efficient estimation of sensitivities in TLM with dielectric discontinuities," *IEEE Microwave and Wireless Components Lett.* vol. 15, pp. 89-91, 2005.

[17] P. A. W. Basl, M. H. Bakr, and N. K. Nikolova, "An AVM technique for 3D TLM with symmetric condensed nodes," *IEEE Microwave and Wireless Components Lett.* vol. 15, pp. 618-620, 2005.

[18] M. H. Bakr, N. K. Nikolova, and P. A. W. Basl, "Self-Adjoint S-Parameter Sensitivities for Lossless Homogeneous TLM Problems," *International Journal of Numerical Modeling: Electronic Networks, Devices and Fields*, vol. 18, pp. 441-455, 2005.

[19] P. A. W. Basl, M. H. Bakr, and N. K. Nikolova, "Theory of self-adjoint S-parameter sensitivities for lossless nonhomogeneous transmission-line modeling problems," *IET Microwave Antennas Propag.*, vol. 2, pp. 211-220, 2008.

[20] N. Appannagaari, R. Edlinger, and B. Gray, "Optimetrics: Parametrics and Optimization Using Ansoft HFSS," *Microwave Journal*, Nov. 1999. [Online].

Available: http://www.ansoft.com/news/articles/MWJ.11.99.pdf. [Accessed 20 Jan. 2013].

[21]   Press Release, "Sensitivity analysis and adapted optimization strategies for CST MICROWAVE STUDIO transient solver," May 2010. [Online]. Available: http://www.cst.com/Content/News/Documents/2010_5_TimeDomain2011_web.pdf. [Accessed 20 Jan. 2013].

[22]   A. V. Chebykin, A. A. Orlov, A. V. Vozianova, S. I. Maslovski,Yu. S. Kivshar, and P. A. Belov, "Nonlocal effective medium model for multilayered metal-dielectric metamaterials," *Phys. Rev. B*, vol. 84, pp. 115438, 2011.

[23]   R. J. Luebbers, F. P. Hunsberger, K. S. Kunz, R. B. Standler, and M. Schneider, "A frequency-dependent finite-difference time-domain formulation for dispersive materials," *IEEE Trans. Electromagn. Compat*., vol. 32, pp. 222-227, 1990.

[24]   D. Jiao and J.-M. Jin "Time-domain finite-element modeling of dispersive media,*" IEEE Microwave and Wireless Components Lett*., vol. 11, pp. 220-222, 2001.

[25]   E. Fear, S. C. Hagness, P. Meaney, M. Okoniewski, and M. Stuchly, "Enhancing breast tumor detection with near-field imaging,*"IEEE Microwave Mag*., vol. 3, pp.48-56, 2002.

[26]   W. J. R. Hoefer, "The transmission-line matrix method –theory and applications," *IEEE Trans. Microwave Theory Tech*., vol. MTTT-33, pp. 882-893, 1985.

[27]   P. B. Johns, "A symmetrical condensed node for the TLM method," *IEEE Trans. Microwave Theory Tech*., vol. MTTT-35, pp. 370-377, 1987.

[28]   V. Trenkic, C. Christopoulos, and T.M. Benson, "New symmetrical super-condensed node for the TLM method," *Electron. Lett.*, vol. 30, pp. 329-330, 1994.

[29]   L. de Menezes and W. J. R. Hoefer, "Modeling of general constitutive relationships using SCN TLM," *IEEE Trans. Microwave Theory Tech.*, vol. 44, pp. 854-861, 1996.

[30]   J. Paul, C. Christopoulos, and D. W. P. Thomas, "Perfectly matched layer for transmission line modelling (TLM) method," *Electron. Lett.* vol. 33, pp. 729-730, 1997.

[31]   J. Paul, C. Christopoulos, and D. W. P. Thomas, "Generalized material models in TLM—Part 1: Materials with frequency-dependent properties," *IEEE Trans. Antennas Propag.*, vol. 47, pp. 1528-1534, 1999.

[32]   J. Paul, C. Christopoulos, and D. W. P. Thomas, "Generalized material models in TLM—Part 2: Materials with anisotropic properties," *IEEE Trans. Antennas Propag.*, vol. 47, pp. 1535-1542, 1999.

[33]   J. Paul, C. Christopoulos, and D. W. P. Thomas, "Generalized material models in TLM—Part 2: Materials with nonlinear properties," *IEEE Trans. Antennas Propag.*, vol. 50, pp. 997-1004, 2002.

[34]   O. S. Ahmed, M. A. Swillam, M. H. Bakr, and Xun Li, "Modeling and design of nano-plasmonic structures using transmission line modeling," *Opt. Express*, vol. 18, pp. 21784-21797, 2010.

[35]   P. SO, "Exploit the parallel paradigm," *IEEE Microwave Mag.*, vol. 11, pp.79-85, 2010.

[36] F. Rossi and P. P. M. So, "Hardware accelerated symmetric condensed node TLM procedure for NVIDIA graphics processing units," *IEEE Antennas Propag. Soc. Int. Symp.* (APSURSI'09), pp. 1-4, 2009.

[37] A. G. Radwan, M. H. Bakr, and N. K. Nikolova, "Transient adjoint sensitivities for discontinuities with Gaussian material distribution," *J. Progress in Electromagnetic Research* (PIER) B, vol. 27, pp. 1-19, 2011.

[38] J. B. Pendry, "Negative Refraction Makes a Perfect Lens," *Phys. Rev. Lett.*, vol. 85, pp. 3966-3969, 2000.

[39] R. W. Ziolkowski and E. Heyman, "Wave propagation in media having negative permittivity and permeability," *Phys. Rev. E*, vol. 64, p. 056625, 2001.

[40] M. G. Silveirinha and N. Engheta, "Tunneling of electromagnetic energy through subwavelength channels and bends using ε-near-zero materials," *Phys. Rev. Lett.*, vol. 97, p. 157403, 2006.

[41] R. J. Luebbers, F. Hunsberger, and K. S. Kunz, "A frequency -dependent finite-difference time-domain formulation for transient propagation in plasma," *IEEE Trans. Antennas Propag.*, vol. 39, pp. 29-34, 1991.

[42] S. Gabriel, R. W. Lau, and C. Gabriel, "The dielectric properties of biological tissues—III: Parametric models for the dielectric spectrum of tissues," *Phys. Medicine and Biology*, vol. 41, pp. 2271-2293, 1996.

[43] A. von Hippel. *Dielectrics and Waves.* The M.I.T. Press, 1954.

[44] C. F. Bohren and D. R. Huffman, *Absorption and Scattering of Light by Small Particles.* Wiley, New York, 1983, Ch. 9.

[45]   B. M. Fischer, M. Walther, and P. Jepsen, "Far-infrared vibrational modes of DNA components studied by terahertz time domain spectroscopy," *Phys. Med. Biol.*, vol. 47, pp. 3807-3814, 2002.

[46]   R. Siushansian and J. LoVetri, "A comparison of numerical techniques for modeling electromagnetic dispersive media," *IEEE Microwave Guided Wave Lett.*, vol. 5, pp. 426-428, 1995.

[47]   O. S. Ahmed, M. A. Swillam, M. H. Bakr, and X. Li, "Efficient optimization approach for accurate parameter extraction with terahertz time-domain spectroscopy," *IEEE J. of Lightwave Technol.*, vol. 28, pp. 1685-1692, 2010.

[48]   D. F. Kelley and R. J. Luebbers, "Piecewise linear recursive convolution for dispersive media using FDTD," *IEEE Trans. Antennas Propagat.*, vol. 44, pp. 792-797, 1996.

[49]   C. Caloz and T. Itoh, *Electromagnetic Metamaterials, Transmission Line Theory and Microwave Applications*. New York: Wiley, 2005.

[50]   X. -S. Lin and X. -G. Huang, "Tooth-shaped plasmonic waveguide filters with nanometeric sizes," *Opt. Lett*. vol. 33, pp. 2874-2876, 2008.

[51]   A. E. Cetin, M. Turkmen, S. Aksu, and H. Altug, "Nanoparticle-based metamaterials as multiband plasmonic resonator antennas," *IEEE Trans. On Nanotech.,* vol. 11, pp. 208–212, 2012.

[52]   D. M. Sullivan, "Frequency-dependent FDTD methods using Z transforms," *IEEE Trans. Antennas Propagat*., vol. 40, pp. 1223–1230, 1992.

5 TERAHERTZ TIME-DOMAIN SPECTROSCOPY

In Chapters 5 and 6, we introduce analytical optimization approaches for both inverse problems and design optimization. In both cases simple analytical models can be utilized throughout the optimization procedure. Efficient optimization algorithms are developed to overcome the high non-linearity in the original problem. Thus, optimal solution can be reached, accurately, and efficiently.

In this chapter, we propose an original approach for efficient terahertz time-domain spectroscopy. It enables the extraction of the material complex refractive index. We exploit the dispersive dielectric models for accurate parameter extraction of a sample of unknown thickness. This approach allows for simultaneously estimating the parameters and fitting them to one of the common material dispersive models, in the terahertz frequency range. Our approach has been successfully illustrated through a number of examples that include the characterization carbon nano-tubes and doped semiconductors.

5.1 INTRODUCTION

Terahertz time-domain spectroscopy (THz-TDS) is a technique for material parameter extraction in the terahertz frequency range, 0.1-10 THz. Using this approach, the material sample is illuminated by a single ultra-wideband pulse. The transmitted field is recorded, and compared to the transmitted field in the absence of the sample. Fourier

transform is then applied to the recorded data. The complex transmission coefficient of the sample is the ratio of the Fourier transforms of the recorded data with and without the sample [1], [2]. The experimental data of the sample transmission coefficient is then compared and fitted to a valid analytical model, which depends on the complex refractive index of the material under study. The outcome of that fitting is an estimation of the material refractive index.

The parameter extraction problem is usually formulated as an optimization problem where the optimization variable is the complex refractive index of the material. The utilized objective function is a measure of the deviation of the simulated transmission coefficient from the experimental results [1]. This technique is used to study a material sample of a sufficient known thickness, where the parameter extraction problem is solved at each frequency. The major limitation of this algorithm is the requirement of prior knowledge of the sample thickness. The mechanical uncertainty in the measured sample thickness limits the estimation of the material refractive index [1]-[3]. This uncertainty is investigated in [2]-[4], where the optimization problem is solved for all possible values of the material thickness. A certain criterion is then applied on the estimated refractive index in order to choose the accurate material thickness.

This chapter introduces a new approach for solving the parameter extraction problem in the terahertz frequency regime. Our new approach is based on adopting a parameterized dispersive model of the material under investigation. This model is utilized to estimate the complex refractive index of the material $\tilde{n}(\omega)$ as a function of frequency, ω, without testing all possible values of the sample thickness, l. Our approach takes into

account the uncertainty in the thickness of the sample under study. Different materials are tested using this approach. The solution of the utilized optimization problem is accelerated by estimating both the first order derivatives (gradient) and second order derivatives (Hessian) of the objective function and supplying them to the optimizer. Our approach is demonstrated to be accurate and robust for the calculation of the optical parameters of materials of unknown thickness.

The chapter is organized as follows; a review of existing techniques is provided in Section 5.2. In Sections 5.3, the new approach for efficiently solving the parameter extraction problem is explained. The application of this approach to a number of parameter extraction examples is provided in Section 5.4. In these examples, we utilize our approach to characterize the carbon nano-tubes working in THz regime. It is also utilized to model the doped semiconductors that are capable of propagating surface plasmon wave in the THz frequency range. Finally, the summary is provided in Section 5.5.

5.2 EXISTING APPROACHES

Previous approaches utilize a frequency-dependent transfer function, which is the ratio of the transmitted field to the incident field. An analytical model for this transfer function is achieved by assuming that: the sample under test is a dielectric slab, the scattering at the surface is negligible, and that light is incident normal to the interface [5]. The transmission coefficient of the first transmitted pulse under these assumptions is

related to the complex refractive index ($\tilde{n}(\omega)$) and the sample thickness (l) by the following formula [2]:

$$T_{\text{theory}}(\omega) = \frac{4\tilde{n}}{(\tilde{n}+1)^2} \times \exp(-i(\tilde{n}-1)\omega l / c), \tag{5.1}$$

where $\tilde{n}(\omega) = n(\omega) - ik(\omega)$, n is the refractive index, k is the extinction coefficient which represents absorption losses, and c is the velocity of light. Equation (5.1) is extended to the general case of the pth echo through the formula [2]:

$$T_p(\omega) = \frac{4\tilde{n}(\tilde{n}-1)^{2p}}{(\tilde{n}+1)^{2p+2}} \times [\exp(-i\tilde{n}\omega l / c)]^{2p+1} \exp(i\omega l / c). \tag{5.2}$$

Over the last decade, several algorithms were presented for accurate material parameter extraction in the terahertz range. All of these algorithms utilize the analytical model introduced in (5.1) and (5.2). They attempt to minimize the difference between the experimental and analytical data for both the amplitude and the phase. The errors in the magnitude and phase are given by:

$$\delta A(\omega) = |T_{\text{theory}}| - |T_{\text{exp}}|, \tag{5.3}$$

$$\delta\phi(\omega) = \angle T_{\text{theory}} - \angle T_{\text{exp}}. \tag{5.4}$$

where T_{theory} is the transfer function estimated from the analytical model in (5.1), and T_{exp} is the measured transmission coefficient. The objective function utilized in the parameter extraction problem can be written as [4]:

$$f(n(\omega), k(\omega)) = |\delta A(n(\omega), k(\omega))| + \zeta |\delta\phi(n(\omega), k(\omega))|, \tag{5.5}$$

where ζ is a regularization parameter. The optimization function in (5.5) is minimized at each frequency sample. If the number of frequency samples is m, we then need to solve m nonlinear optimization problems each of 2 parameters $n(\omega)$ and $k(\omega)$. This approach assumes that the sample thickness is known.

The mechanical uncertainty of the sample thickness, l, introduces a major inaccuracy of the extracted results [2], [3]. It causes the extracted parameters to be oscillatory with frequency. The approach reported in [2] compares the calculated parameter data produced from different echoes at every simulated sample thickness [2]. The best value of l is the one that minimizes the variance between the estimated parameters. The approach reported in [3] utilizes a total variation method. The transfer function is calculated as a sum of different transmitted echoes. The accuracy measure in the thickness calculation is the smoothness of the estimated parameters. All previous techniques [1]-[4] utilize small thickness uncertainty to limit the required number of optimization problems. These techniques neglect experimental noise effects.

5.3   MODEL BASED OPTIMIZATION APPROACH

Our technique utilizes a formulation of the objective function which is based on the magnitude and the phase of the transfer function. Different formulations can lead to different optimization functions. However, we only consider the following two well behaved formulations [1]-[3]:

$$g(\omega) = \delta M^2(\omega) + \zeta \delta \phi^2(\omega), \tag{5.6}$$

$$h(\omega) = \delta A^2(\omega) + \zeta \delta \phi^2(\omega), \tag{5.7}$$

where

$$\delta M(\omega) = \ln\left(\left|T_{\text{theory}}(\omega)\right| / \left|T_{\text{exp}}(\omega)\right|\right), \tag{5.8}$$

$$\delta\phi(\omega) = \angle T_{\text{theory}}(\omega) - \angle T_{\text{exp}}(\omega), \tag{5.9}$$

$$\delta A(\omega) = \left|T_{\text{theory}}(\omega)\right| - \left|T_{\text{exp}}(\omega)\right|, \tag{5.10}$$

and ζ is a regularization factor [6].

Both formulations in (5.6) and (5.7) lead to the same global solution. However, the phase information should be manipulated in order to remove its periodicity. The objective function which is based on the logarithm, provides larger penalty on the error function without any scaling mechanism [6]. This justifies why the function g is preferred than h.

Our approach is based on reformulating the problem as a certain function of the whole set of frequency points $\mathbf{n} = [\ n(\omega_1)\ \ n(\omega_2)\ \ ...\ n(\omega_m)]$, and $\mathbf{k} = [\ k(\omega_1)\ \ k(\omega_2)\ \ ...\ k(\omega_m)]$. Instead of minimizing the objective function g in (5.6) at each frequency, we minimize a norm of the vector of error functions at all frequencies. From (5.6), we can write the problem as follows:

$$\begin{aligned} \min_{\mathbf{n,k}} \quad & \delta\mathbf{M}^T\delta\mathbf{M} + \zeta\delta\boldsymbol{\phi}^T\delta\boldsymbol{\phi} \\ \text{subject to} \quad & \mathbf{n} \succeq 1, \quad \mathbf{n} \in R^m \\ & \mathbf{k} \succeq 0, \quad \mathbf{k} \in R^m \end{aligned} \tag{5.11}$$

where $\delta\mathbf{M}, \delta\boldsymbol{\phi} \in R^m$.

The proposed formulation in (5.11) leads to accurate parameter estimation of $\mathbf{n}$ and $\mathbf{k}$ when l is precisely known. If l is unknown, the number of unknowns becomes more than the available information. For m frequency samples, the number of unknowns is

2*m*+1. The available 2*m* pieces of information are the amplitude and the phase of the transfer function *T*. This may lead to inaccurate parameter estimation as mentioned earlier.

To overcome this problem, we utilize a model-based parameter extraction approach. Here, the dependence of the material parameters on frequency is assumed to follow a certain material model. In this case, the number of optimization variables is reduced and no prior thickness information is required. The parameter extraction and interpolation of the results are done simultaneously. This approach is robust against experimental noise sources as will be demonstrated later.

This parameter-based optimization is utilized, for the first time, for spectroscopy purposes of a sample of uncertainty in the thickness. For example, various materials can be modeled by the standard Debye model [7]-[10],

$$\epsilon(\omega) = \epsilon_\infty + \frac{\Delta\epsilon}{1 + (i\omega\tau)}. \tag{5.12}$$

In this case, the optimization variables are ϵ_∞, $\Delta\epsilon$, τ, and l. Here, $\Delta\epsilon = \epsilon_s - \epsilon_\infty$, where ϵ_s and ϵ_∞ are the static and infinite frequency dielectric constant, respectively. τ is the dipole relaxation time of the sample. The parameter extraction problem is thus reformulated as:

$$
\begin{aligned}
\min_{\mathbf{x}} \quad & \delta\mathbf{M}^T \delta\mathbf{M} + \zeta \delta\boldsymbol{\phi}^T \delta\boldsymbol{\phi} \\
\text{subject to} \quad & \epsilon_\infty \geq 1 \\
& \Delta\epsilon \geq 0 \\
& \tau \geq 0 \\
& l_{lower} \leq l \leq l_{upper}
\end{aligned}
\tag{5.13}
$$

where $\mathbf{x} = [\epsilon_\infty \quad \Delta\epsilon \quad \tau \quad l\,]^T$ and $\epsilon_\infty, \;\Delta\epsilon, \;\tau, \;l \in R$. We thus simultaneously solve for both the model parameters and the unknown sample thickness.

The formulation (5.13) enables accurate results for a non-convex optimization problem with no restrictions on the initial values of the parameters. The upper and lower bounds of the parameters are set to assure physical realization of the optimal parameters. For efficient solution of the problem, the analytical gradient of the objective function is calculated and supplied to the optimization algorithm [11]. The same approach presented by (5.13) can also be directly applied to materials following other dispersive models such as the Cole-Cole model [7], [10], the Lorentz model [12], [13], or the Drude model [14]-[16].

5.4 NUMERICAL RESULTS

Both the formulation (5.11) and the model-based formulation in (5.13) are used for the parameter estimation problem. Formulation (5.11) is used for the parameter extraction of a sample with a known thickness *l*. The model-based formulation is used for the parameter extraction of samples of unknown thickness. Different types of materials are tested.

Before illustrating the model-based case, we first demonstrate that our approach have very good accuracy for arbitrary frequency-dependent material parameters with known thickness. For this purpose, we consider a sample made of Plywood [10]. The refractive index *n* and the extinction coefficient *k* are estimated over a frequency range from 0.01 THz to 1.5 THz. Optimization is carried out for *m*= 300. The initial starting

points for **n** and **k** are chosen arbitrarily. The lower and upper bounds are set according to (5.11). The gradient and Hessian of the objective function are calculated analytically to allow the solver to use a sequential quadratic programming algorithm [11].

In Fig. 5.1, the estimated data for n and k are compared to the reference data for the plywood material [10]. Good agreement is achieved between both sets of data. The relative error in each parameter p is defined as:

$$e_p(j) = \frac{\left| p_{\text{est}}(j) - p_{\text{ref}}(j) \right|}{p_{\text{ref}}(j)}, \qquad (5.14)$$

where j denotes the frequency sample, p_{est} is the estimated parameter value, and p_{ref} is the reference value of the parameter p. The relative errors in both n and k are plotted versus frequency in Fig. 5.2.

In order to illustrate the model-based approach, we apply it for materials that are characterized by Debye, Cole-Cole, Lorentz, and Drude dispersive models. To test the reliability of the approach, noise is added to the reference data of n and k. We assume a uniformly distributed random noise with zero mean. The noise strength is different for each example. Although this noise complicates the estimation procedure, our approach successfully retrieves the original model parameters.
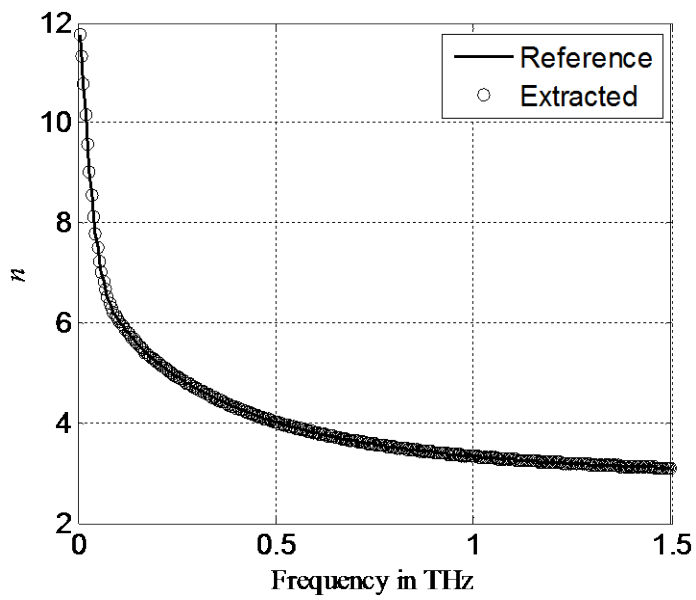
(a)
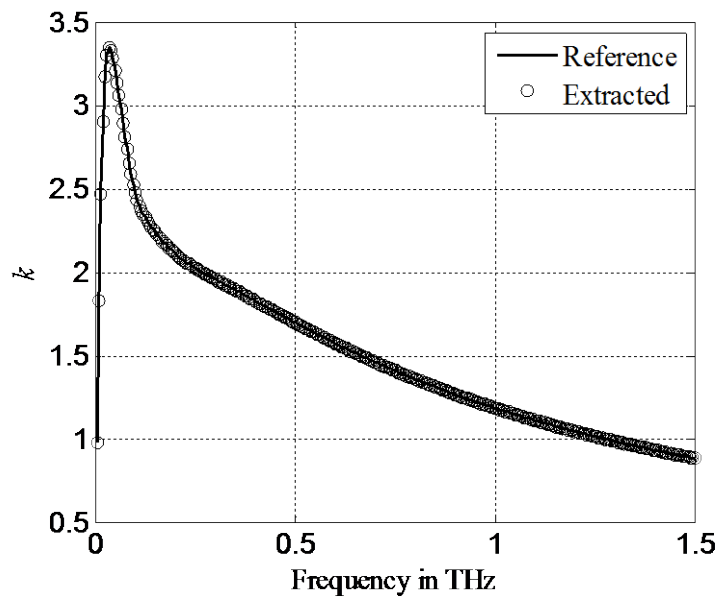
(b)

Fig. 5.1. A comparison between the estimated and reference parameters (n, k) for Plywood; (a) the estimated refractive index (n) and (b) the estimated extinction coefficient (k).
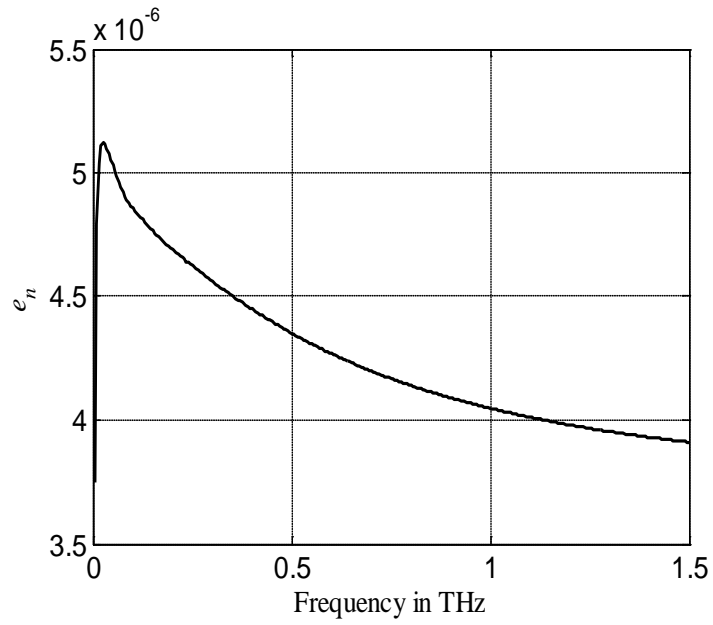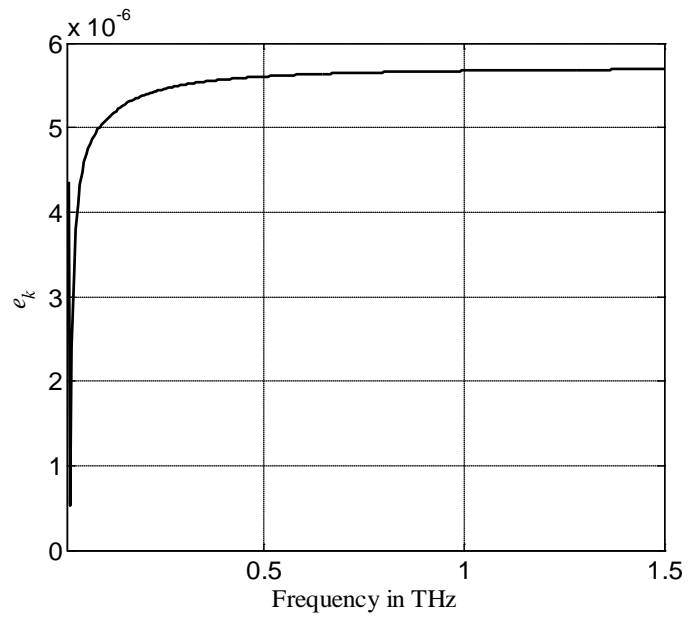
Fig. 5.2. The relative error in the estimated parameters (n, k) for Plywood as defined by (5.14); (a) the estimated refractive index (n) and (b) the estimated extinction coefficient (k).
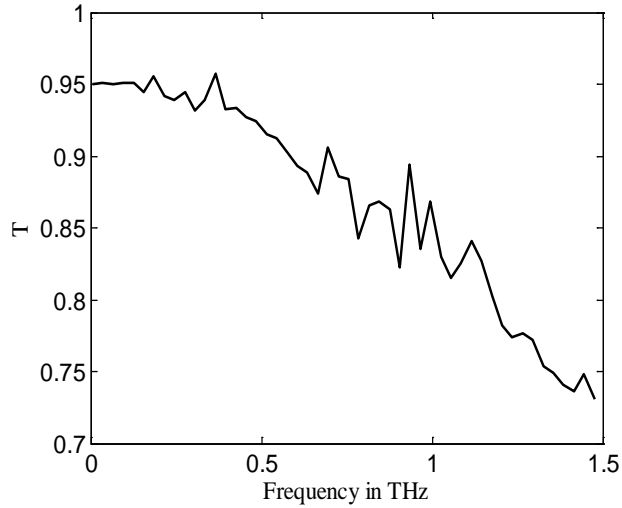
Fig. 5.3. The noisy transfer function of the fullerene (C_{60}) sample.

5.4.1 Debye Model

The Debye model is used to extract the parameters of a high density polyethylene mixed with fullerene (C_{60}) (8.36%). Experimental data and reference parameters are available in [7]. Using (5.13), the model parameters ϵ_∞, $\Delta\epsilon$, τ, and the material thickness, l, are the optimization variables. The noise strength is 5×10^{-3}. The noisy transfer function of the sample is shown in Fig. 5.3. The reference sample thickness is set to 10.0 μm. Although the mechanical uncertainty in the sample thickness is around 1% [17], we utilize a large uncertainty in the sample thickness (10%) to illustrate that our algorithm works for materials with large thickness uncertainty.

The dispersion profile of the C_{60} over the frequency range from 0.01 to 1.5 THz is estimated. This range is sampled every 0.03 THz. The comparison between the reference optical parameters and the estimated ones is shown in Fig. 5.4. Our technique is able to estimate the original non-noisy optical parameters with a good accuracy. The estimated

thickness of the sample can be considered as a figure of merit of the approach accuracy. For this example, the estimated sample thickness is 9.999 μm, with a percentage error of 0.001%.

(a)

(b)
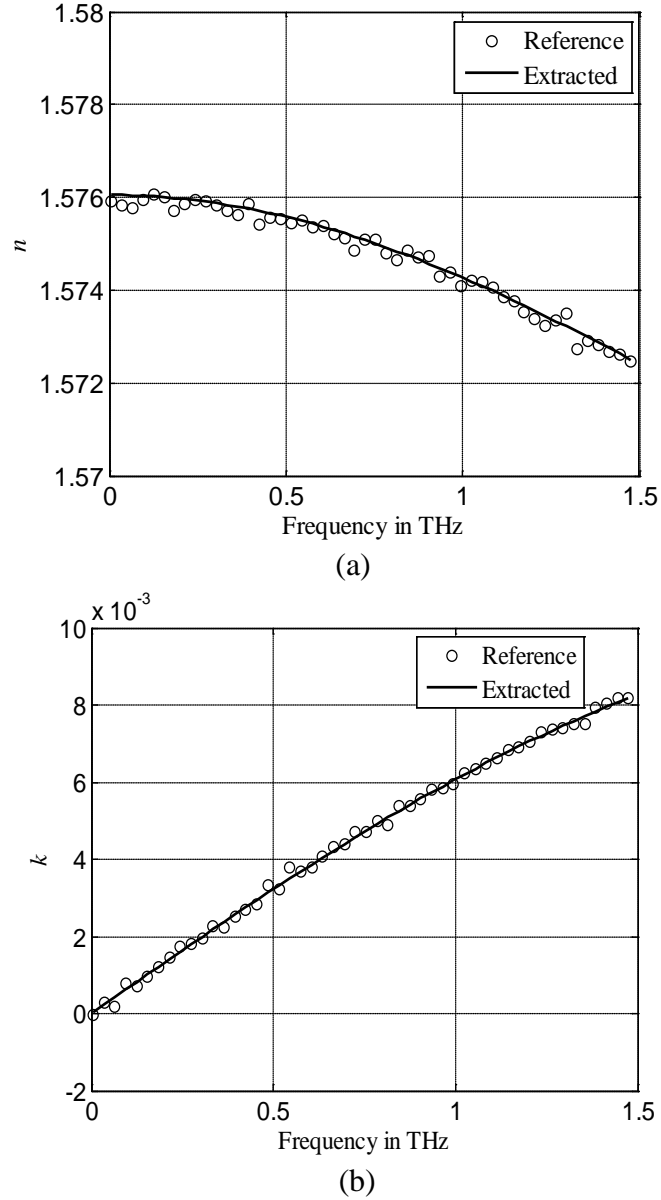
Fig. 5.4. The estimated n and k of the fullerene (C_{60}) sample compared to the reference data over the frequency range from 0.01 to 1.5 THz; (a) the estimated refractive index (n) and (b) the estimated extinction coefficient (k).

5.4.2 Cole-Cole Model

The Cole-Cole model is a generic material model that can be used for a wide variety of materials [7], [10]. The dispersion relation according to the Cole-Cole model is [10]:

$$\epsilon(\omega) = \epsilon_\infty + \frac{\Delta\epsilon}{1+(i\omega\tau)^\alpha} + \frac{\sigma}{i\epsilon_0\omega}. \tag{5.15}$$

where α is an empirical parameter, σ is the material conductivity, and ϵ_0 is the air permittivity. The parameters α and σ are included as optimization variables in (5.13), with the constraints $0 \le \alpha \le 1$ and $\sigma \ge 0$. The model is applied to extract the parameters of a high-density polyethylene mixed with multi-wall carbon nano-tubes (MWNT) and carbon black (CB), respectively. The experimental values of n and k are already available in [7]. Random noise of strength 10^{-2} is added to account for experimental errors.

In this problem, the model parameters ϵ_∞, $\Delta\epsilon$, τ, α and σ of the Cole-Cole model and the material thickness, l, are unknown. The exact value of l is 0.1 mm with a 10% uncertainty. The initial values of the variables are chosen to be the lower bound of all parameters. Different initial points are also tested and they all lead to the same optimal point. The percentage error in the estimated sample thickness is 1% for the (MWNT) case and 0.75% for the CB case. The dispersion profiles of the (MWNT) and CB mixtures are calculated over the frequency range from 0.01 to 1.5 THz. The comparisons between the reference data and the estimated profiles are shown in Figs. 5.5 and 5.6.

(a)

(b)
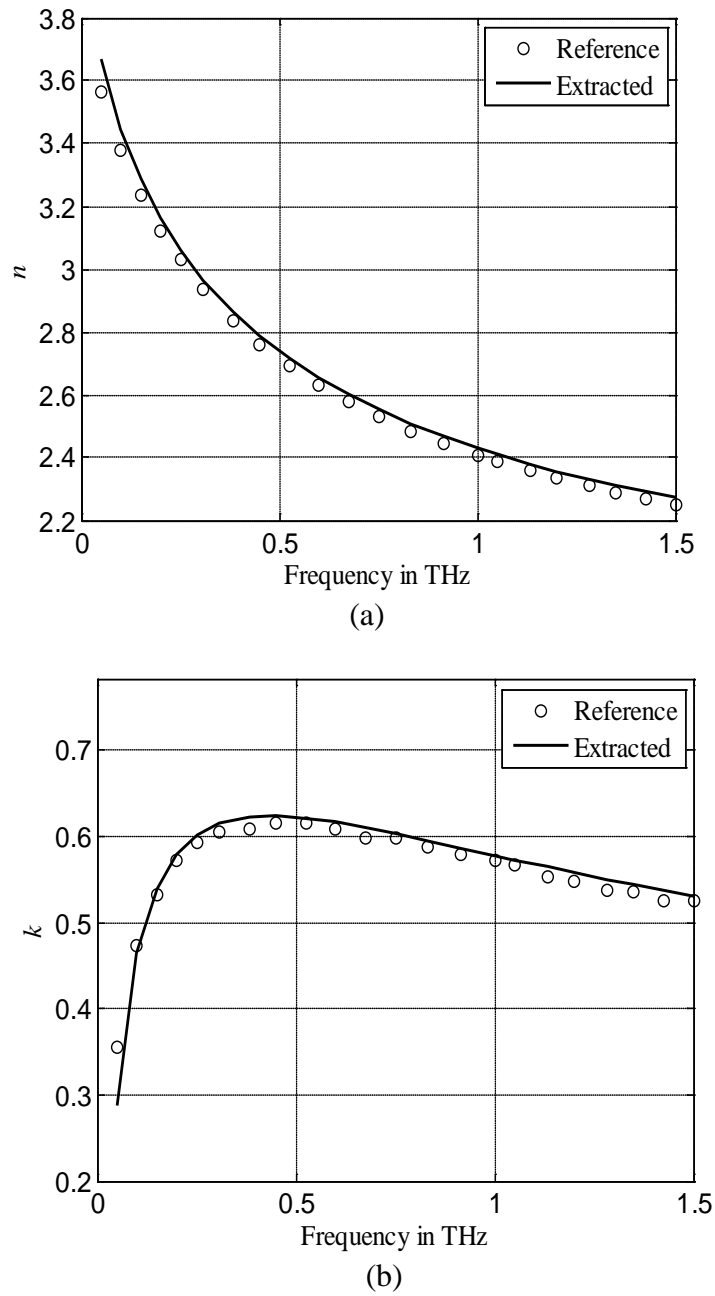
Fig. 5.5. The estimated *n* and *k* compared to the reference data of the MWNT mixture over the frequency range from 0.01 to 1.5 THz; (a) the estimated refractive index (*n*) and (b) the estimated extinction coefficient (*k*).
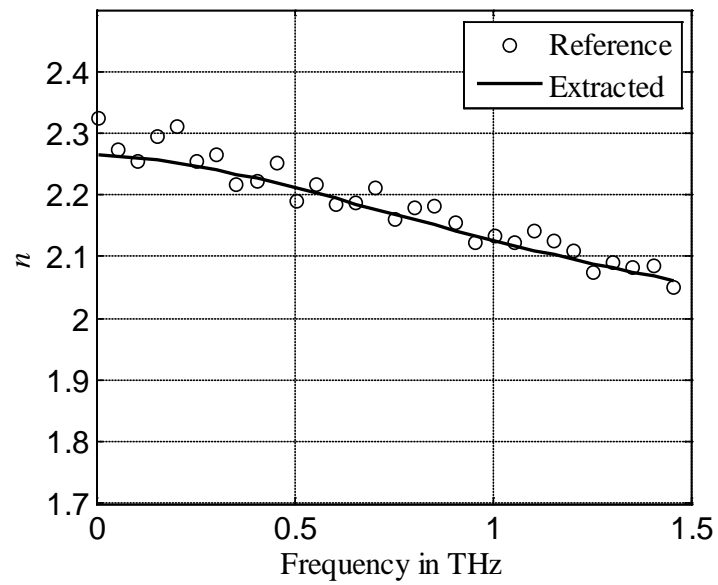
(a)
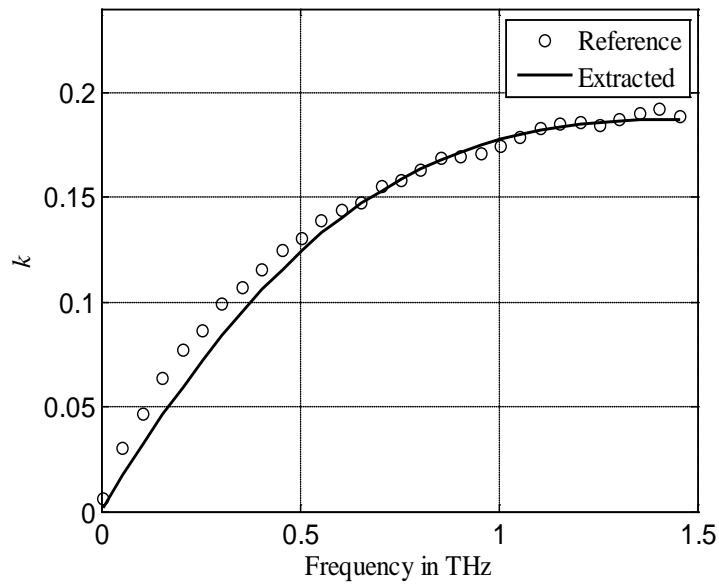
(b)

Fig. 5.6. The estimated *n* and *k* compared to the reference data of the CB mixture over the frequency range from 0.01 to 1.5 THz; (a) the estimated refractive index (*n*) and (b) the estimated extinction coefficient (*k*).

5.4.3 Lorentz Model

In the THz regime, biological materials can be modeled by the standard Lorentz model [12], [13]:

$$\epsilon(\omega) = \epsilon_{\infty} + \frac{S\omega_0^2}{(\omega_0^2 - \omega^2) - i\Gamma\omega}, \tag{5.16}$$

where ϵ_{∞} is the frequency independent permittivity, ω_0 is the center frequency, S is the oscillator strength, and Γ is the oscillation damping factor. Here, the optimization variables are ϵ_{∞}, ω_0, S, Γ and the sample thickness l.

In Fig. 5.7, the parameter extraction procedure is applied to naphthalene. Naphthalene can be modeled by a Lorentz model using one oscillator term [13]. Noise is added to the reference data obtained from [13] in order to account for experimental non-idealities. The noise strength is 10^{-2}. The dispersion profile of the naphthalene is estimated over the frequency range from 0.1 to 2.5 THz. The error in the sample thickness estimation is about 1%.
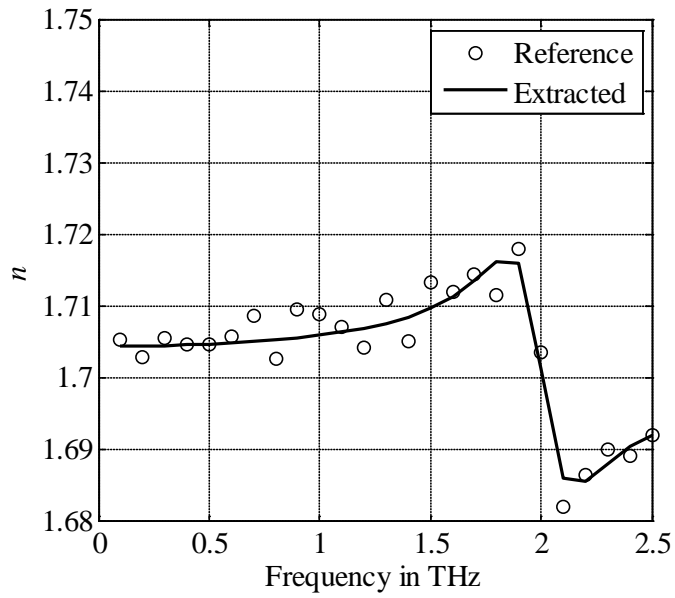
(a)
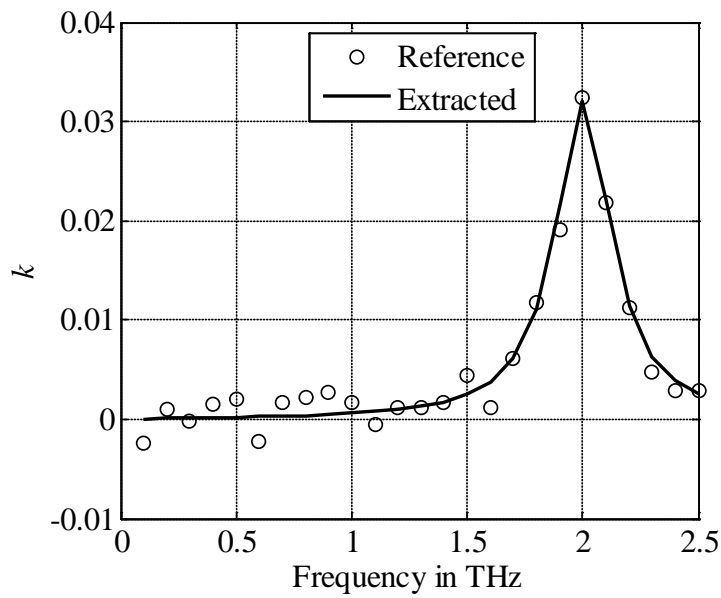
(b)

Fig. 5.7. estimated *n* and *k* compared to the reference data of the naphthalene over the frequency range from 0.1 to 2.5 THz; (a) the estimated refractive index (*n*) and (b) the estimated extinction coefficient (*k*).

5.4.4 Drude Model

We also apply our approach to semiconductor materials modeled using the Drude model [14], [15]. The dispersion of these semiconductor materials is significant at the high frequency range. The parameter extraction problem for the Drude materials utilizes the following dispersion relation [16]:

$$\epsilon(\omega) = \epsilon_\infty - \frac{\omega_p^2}{\omega(\omega + i\Gamma)}, \tag{5.17}$$

where ϵ_∞ is the frequency-independent part of the dielectric constant and Γ is the damping rate. ω_p is the plasma angular frequency defined by $\omega_p{}^2 = Ne^2 / \epsilon_0 m$, where N is the number density of the semiconductor carriers, e is the electronic charge, and m is the effective carrier mass. The variables of the optimization problem are ϵ_∞, ω_p, Γ and the sample thickness l.

Our approach is applied to extract the parameters of a 0.92 Ω cm P-type silicon and 1.15 Ω cm N-type silicon. The reference values of the optical parameters for these materials are available in [15]. The error in the estimated value of the sample thickness is 0.09% and 0.1% for the P-type and N-type (silicon) materials, respectively.

The dispersion profiles of the both materials are estimated over the frequency range from 0.1 to 2 THz. In Figs. 5.8 and 5.9, the estimated values of the optical parameters are compared to the reference values. Good agreement is achieved.
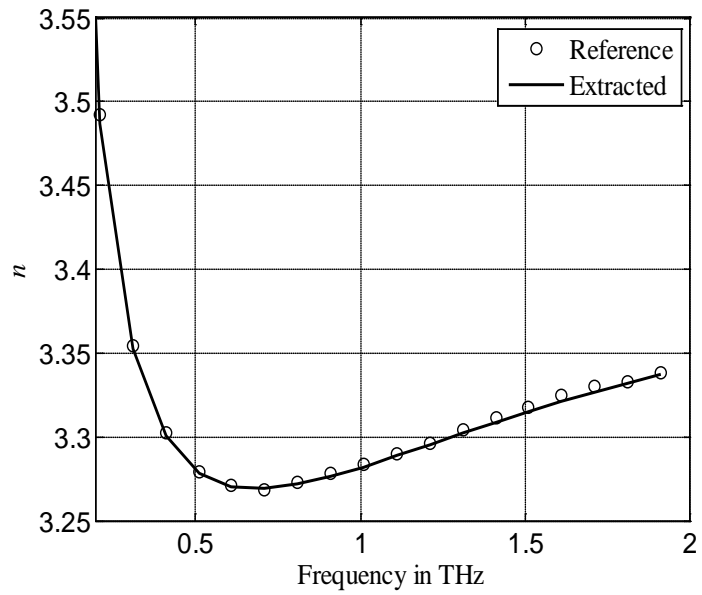
(a)
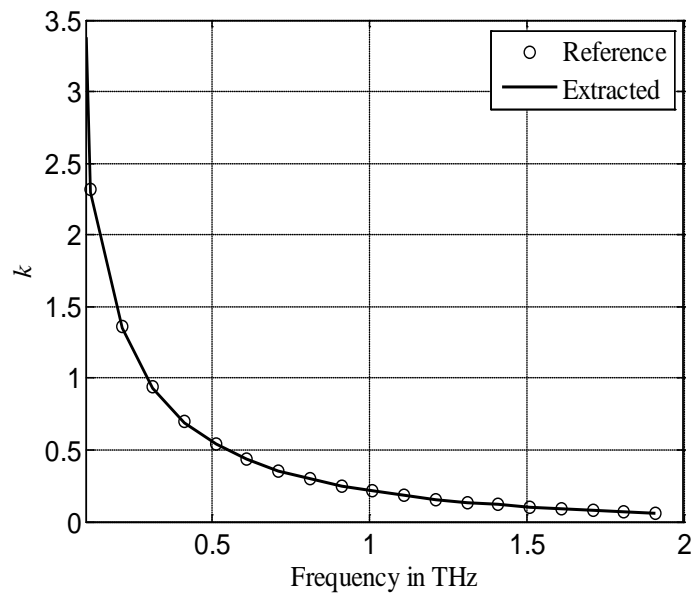
(b)

Fig. 5.8. The estimated *n* and *k* compared to the reference data of the *P*-type Si material over the frequency range from 0.1 to 2 THz; (a) the estimated refractive index (*n*) and (b) The estimated extinction coefficient (*k*).
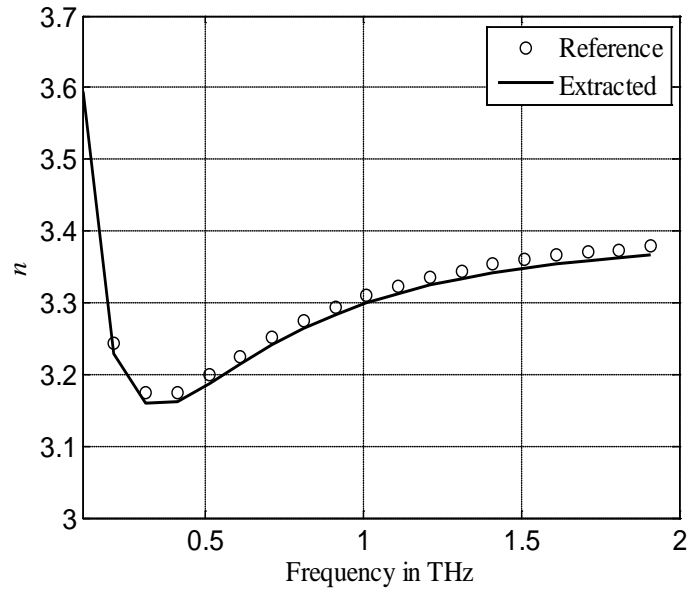
(a)
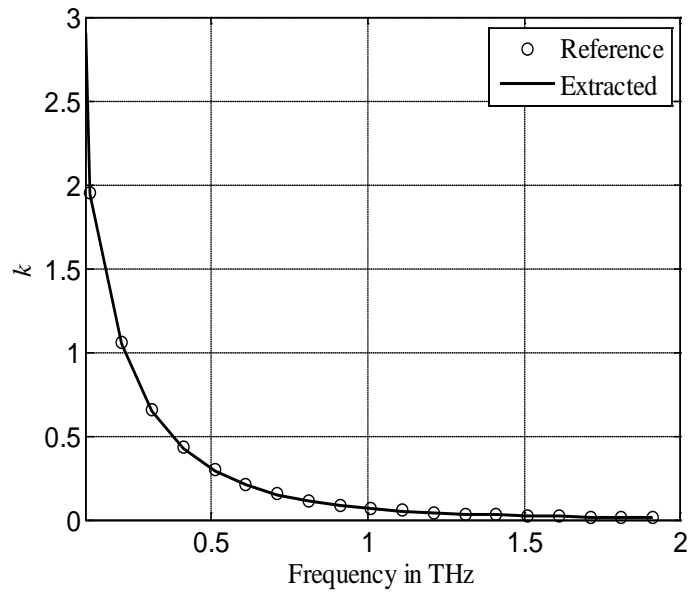
(b)

Fig. 5.9. The estimated *n* and *k* compared to the reference data of the *N*-type Si material over the frequency range from 0.1 to 2 THz; (a) the estimated refractive index (*n*) and (b) the estimated extinction coefficient (*k*).

5.4.5   Spectroscopy of Surface Plasmon Polaritons in Doped Semiconductors

Surface plasmon wave has been recently demonstrated in the THz regime using doped semiconductors [18]. In [18], the parameters of the Drude model have been calculated for different doping levels of different semiconductors with known thickness, exhibiting negative permittivity in the THz frequency range.

In this example, we utilize our approach not only to obtain the unknown material parameters of the doped semiconductor, but also to precisely estimate the doping level at which the semiconductor has negative permittivity. This is the level that allows for propagation of surface plasmon waves. For this purpose, a sample of GaN of thickness 1.0 μm is utilized for illustration. We exploit a wide range of sample thickness uncertainties ranging from 0.1% to 10%. The noise is compensated using a noise compensation mechanism [19].

For efficient application of our algorithm, both the reflection and transmission coefficients are utilized. The extracted parameters are then utilized to estimate the doping level of each sample by using the approach reported in [18]. As shown in Fig. 5.10, the results have very good agreement with the reference data given in [18]. The relative error in the estimated thickness is 10^{-6} %. The estimated and reference values of ϵ_{real} for different doping levels of GaN are shown in Fig. 5.10. The values of ϵ_{real} are estimated over the range of 0.1 to 7.0 THz with a sample rate of 0.2 THz.
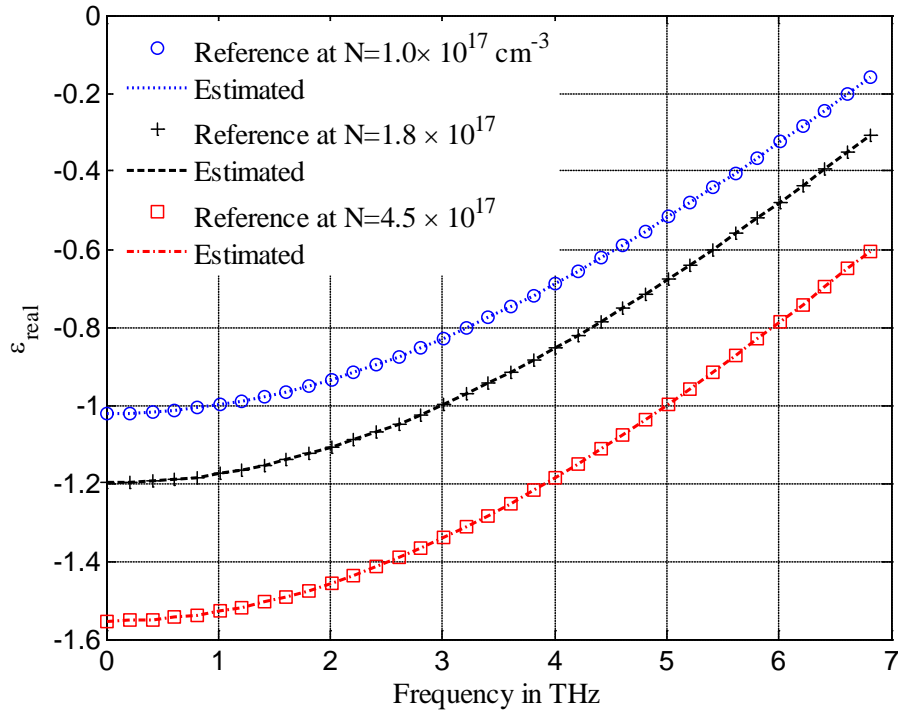
Fig. 5.10. The estimated ϵ_{real} as compared to the reference data of the *N*-doped GaN over the frequency range from 0.1 to 7 THz.

5.5 SUMMARY

A novel approach is applied for efficient parameter extraction in terahertz time-domain spectroscopy. This approach is based on the material theoretical dispersive models in the terahertz regime. A new formulation of the parameter extraction problem of a dielectric slab problem is developed. The sample thickness is included as an optimization variable, which allows us to apply our algorithm for samples of unknown thickness. Our new technique accurately recovers the unknown sample thickness. The algorithm not only estimates the optical parameters, but also fit them to one of the

standard dispersive material models. Our approach is successfully illustrated through a number of numerical examples.

In previous examples, we consider the sample thickness uncertainty and noise effects simultaneously. Previous algorithms avoided this scenario [1]-[5]. Our approach, however, has good accuracy for data contaminated with large noise. Our approach is also more efficient than those demonstrated previously as our problem is only solved once to calculate all the constitutive parameters and the dimensions of the structure, directly without any iterative technique, that consumes more memory and more computational time. Moreover, if noise compensation methods are exploited as given in [19], our approach can achieve challenging thickness estimation accuracy, with up to 10^{-6} % sample uncertainty.

5.6 REFERENCES

[1]   L. Duvillaret, F. Garet, and J. Coutaz, "A reliable method for extraction of material parameters in terahertz time-domain spectroscopy," *IEEE J. Sel. Topics Quantum Electron*., vol. 2, pp. 739-746, 1996.

[2]   L. Duvillaret, F. Garet, and J. L. Coutaz, "Highly precise determination of optical constants and sample thickness in terahertz Time-Domain spectroscopy," *Appl. Opt*., vol. 38, pp. 409-415, 1999.

[3]   T. D. Dorney, R. G. Baraniuk, and D. M. Mittleman, "Material parameter estimation with terahertz time-domain spectroscopy," *J. Opt. Soc. Am. A*, vol. 18, pp. 1562-1571, 2001.

[4]   I. Pupeza, R. Wilk, and M. Koch, "Highly accurate optical material parameter determination with THz time-domain spectroscopy," *Opt. Express*, vol. 15, pp. 4335-4350, 2007.

[5]   W. Withayachumnankul, G. Png, X. Yin, S. Atakaramians, I. Jones, H. Lin, S. Y. Ung, J. Balakrishnan, B. Ng, B. Ferguson, S. Mickan, B. Fischer, and D. Abbott, "T-Ray sensing and imaging," in *Proc. Of IEEE*, vol. 95, pp. 1528-1558, 2007.

[6]   S. Boyd and L. Vandenberghe, *Convex Optimization*. New York: Cambridge, 2004, ch. 6.

[7]   X. Chen, M. Ma, T. Ji, S. Wu, and Z. Zhu, "Optical properties of carbon materials in THz region," *in Proc. of Joint 32nd International Conference on Infrared and Millimeter Waves, and the 15th International Conference on Terahertz Electronics*. IRMMW-THz. 2007, pp. 550-552.

[8]   D. Mittleman, *Sensing with Terahertz Radiation*. London: Springer, 2003, pp. 39–43

[9]   H. Frolich, *Theory of dielectrics: Dielectric constant and dielectric loss*. USA: Clarendon P, 1958, pp. 98–103

[10]   W. Zhu, C. Li, G. Zhang, and G. Fang, "The calculation of dielectric dispersive models in THz range with GA," *Microwave and Opt. Tech. Lett*., vol. 49, pp. 2540-2545, 2007.

[11]   P. T. Boggs and J. W. Tolle, "Sequential quadratic programming," *Acta Numerica*, vol. 4, pp. 1-51, 1995.

[12]   M. M. Nazarov, A. P. Shkurinov, E. A. Kuleshov, V. V. Tuchin, "Terahertz time-domain spectroscopy of biological tissues," *Quantum Electron.*, vol. 38, pp. 647-654, 2008.

[13]   J. Han, H. Xu, Z. Zhu, X. Yu, W. Li, "Terahertz spectroscopy of naphthalene, α-naphthol, β-naphthol, biphenyl and anthracene," *Chem. Phys. Lett.*, vol. 392, pp. 348-351, 2004.

[14]   D. Grischkowsky, S. Keiding, M. van Exter, and Ch. Fattinger, "Far-infrared time-domain spectroscopy with terahertz beams of dielectrics and semiconductors," *J. Opt. Soc. Am. B*, vol. **7**, pp. 2006-2015, 1990.

[15]   M. van Exter and D. Grischkowsky, "Optical and electronic properties of doped silicon from 0.1 to 2 THz," *Appl. Phys. Lett.*, vol. 56, pp. 1694-1696, 1990.

[16]   S. A. Maier. *Plasmonics: Fundamentals and Applications*, Springer, 2007.

[17]   W. Withayachumnankul, B. M. Fischer, H. Lin, and D. Abott, "Uncertainty in terahertz time-domain spectroscopy measurement," *J. Opt. Soc. Am. B*, vol. 25, pp. 1059-1072, 2008.

[18]   B. D. Kong, V. N. Sokolov, K. W. Kim, and R. J. Trew, "Terahertz emission mediated by surface Plasmon polaritons in doped semiconductors with surface grating," *J. Appl. Phys.*, vol. 103, pp. 056101-3, 2008.

[19]   L. Duvillaret, F. Garet, and J. Coutaz, "Influence of noise on the characterization of materials by terahertz time-domain spectroscopy," *J. Opt. Soc. Am. B*, vol. 17, pp. 452-461, 2000.

6 CONVEX APPROACHES FOR DESIGN OPTIMIZATION OF COUPLED MICROCAVITIES

In this chapter, we present simple and efficient approaches for filter design at optical frequencies using large number of coupled microcavities. The design problem is formulated as an optimization problem with a unique global solution. Various efficient filter designs are obtained at both the drop and through ports. Our approaches are illustrated through a number of examples.

6.1 INTRODUCTION

Multiple coupled microcavities have been widely utilized for optical communication systems [1]-[9]. For wavelength division multiplexing (WDM) techniques, optimal filter design is mandatory and flat responses are ultimately required [3]. Higher order coupled microcavities have been proposed as promising candidates for optical filtering. The dispersion analysis of large chain of microcavities has been recently introduced [5]. The application of multiple coupled microcavities can be extended to optical signal processing and routing. Systematic and rigorous design procedures are essential to obtain the required filter response especially with large number of microcavities.

The design of coupled resonators is usually done through the coupling parameters [10]-[19]. These parameters have a direct effect on the achievable transfer function of the filter. Once the coupling coefficient for each stage is determined, the geometrical specifications for each resonator are adjusted [11]. The design theory of coupled microcavities has been originally developed for microwave filters [20]-[22]. In the last decade, this work was extended to the design of optical filters [11] using Bragg gratings and ring resonators. In [11], [12], the design procedure utilizes a transmission line equivalent network. Distributed capacitances and inductances are utilized to build a filter prototype which is mapped to the corresponding equivalent resonator design [21]. The method is used successfully for the design of Chebyshev-based filters [11]. Other filter types can be readily designed using different cascading configurations [12]. This design approach is limited to narrow band responses [21]. It is also based on add drop filters, where the output is only at the drop port of the coupled structure. Other approaches are developed for the optimal placement of zeros and poles of the filter transfer function [23] and [24]. These approaches are intended for the design of parallel and series coupled ring resonators [24]. They utilize resonators of equal coupling parameters to overcome the complexity of the design. Using these approaches, tapering of the coupling parameters is done intuitively [24]. This intuitive tuning is successful for a small set of cascaded series or parallel ring resonators. For higher order filters, optimal responses are not guaranteed.

We discuss in this chapter two simple structured optimization methods for the design optimization of coupled microcavities. Though these techniques are simple, they can design filters with tens of coupled microcavities in few seconds. These techniques are

based on adopting simplified transfer functions that transform the nonlinear optimization problem of highly coupled parameters to a linear optimization problem with a global solution. In the first technique [25], the microcavity coupling parameters are assumed to vary around known mean values. A perturbation theory is developed to propose a design optimization problem in the perturbation parameters. By dumping the higher order perturbation terms, we ignore the effect of multiple reflections among the rings introduced by the small adjustment of the coupling coefficients. This is a first order accurate approach as it takes into account only multiple reflections introduced by the zero order terms. The design problem is then formulated as a linear least square design problem. This linear least square problem has a unique solution that can be obtained in few seconds for tens of design parameters [26]. This can be contrasted with other approaches that converge to a local solution [14]-[16].

Another efficient approach for filter design using a large number of cascaded microcavities is based on linear phase filter (LPF) approximation [27]. An approximate objective function is exploited to solve the design as a linear program (LP) problem.This allows for fast and efficient solution of large scale problems. In addition, no initial design is required. The LP solver can find a feasible starting point by solving an initial feasibility problem. The computational time is less than one second for structures that contains up to 150 coupled microcavities.

In this chapter, the theory of cascaded series rings is summarized. We provide the development of convex optimization approaches for coupled resonators. Our approaches are supported with design examples.
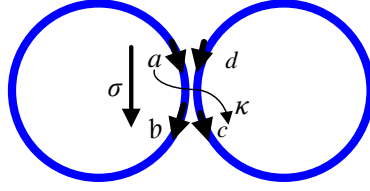
Fig. 6.1. The field coupling at the interface of two coupled ring resonators.

6.2 THEORY OF COUPLED MICROCAVITIES

Complex ring configurations contain multiple ring-to-ring coupling stages. Each stage incorporates a directional coupler approximation. A single stage coupling is shown in Fig. 6.1, where a, b, c, and d are the field values at the interfaces. The quantities σ and κ represent the through and cross-port field coupling parameters, respectively. The relationship between the fields can be summarized using the scattering matrix [28]:

$$\begin{bmatrix} b \\ c \end{bmatrix} = \begin{bmatrix} -\sigma & j\kappa \\ j\kappa & -\sigma \end{bmatrix} \begin{bmatrix} a \\ d \end{bmatrix} \tag{6.1}$$

For the series-connected ring resonators shown in Fig. 6.2, the a and b fields at the ith stage are related to the fields at the next stage through the relationship:

$$\begin{bmatrix} a_i \\ b_i \end{bmatrix} = T_i \begin{bmatrix} a_{i+1} \\ b_{i+1} \end{bmatrix} \tag{6.2}$$

where [28]

$$T_i = \frac{1}{j\kappa_i} \begin{bmatrix} e^{\frac{j\gamma}{2}} & \sigma_i e^{-\frac{j\gamma}{2}} \\ -\sigma_i e^{\frac{j\gamma}{2}} & -e^{-\frac{j\gamma}{2}} \end{bmatrix}. \tag{6.3}$$

Here, $\gamma=\theta-j\alpha$ is the complex propagation factor inside curved structures. θ is the phase factor due to the propagation inside the ring and is given by:
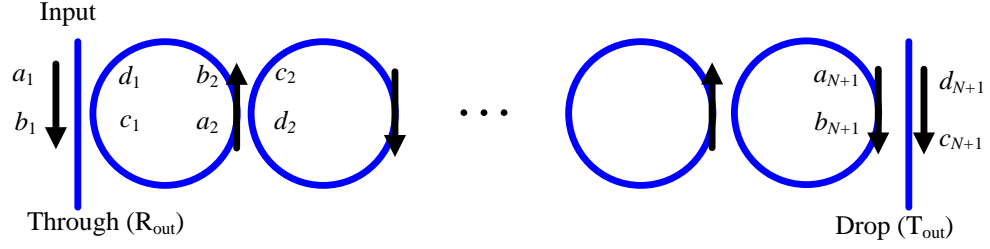
Fig. 6.2. The structure of N ring resonators connected in series.

$$\theta = n_{eff}\, \frac{2\pi f}{c} L_c ,$$ (6.4)

where f is the light frequency, n_{eff} is the real part effective waveguide index, and L_c is the cavity length of the resonator. The parameter α is the field attenuation coefficient.

For N resonator stages, the total transfer matrix is given by:

$$\begin{bmatrix} a_1 \\ b_1 \end{bmatrix} = T \begin{bmatrix} a_{N+1} \\ b_{N+1} \end{bmatrix},$$ (6.5)

where

$$T = T_1 T_2 \dots T_N = \begin{bmatrix} T_{11} & T_{12} \\ T_{21} & T_{22} \end{bmatrix}.$$ (6.6)

Every transmission matrix T_i is unimodular and the total transmission matrix T is also a unimodular matrix that satisfies $T_{22} = T_{11}^{*}$ and $T_{12} = T_{21}^{*}$.

The coupling parameters between the Nth ring and the output waveguide are σ_{N+1} and κ_{N+1}. Utilizing $b_{N+1} = -\sigma_{N+1} a_{N+1}$, the transfer function for the through port (reflectivity) $R_{out} = b_1/a_1$ is given by:

$$R_{\text{out}} = \frac{T_{21} - \sigma_{N+1}T_{22}}{T_{11} - \sigma_{N+1}T_{12}}. \tag{6.7}$$

Utilizing $c_{N+1} = j\kappa_{N+1}a_{N+1}$, the transfer function for the drop port (transmissivity) defined as c_{N+1}/a_1 is given by:

$$T_{\text{out}} = \frac{j\kappa_{N+1}}{T_{11} - \sigma_{N+1}T_{12}}. \tag{6.8}$$

The calculated transfer functions in (6.7) and (6.8) are utilized for analyzing coupled resonators of known ring coupling parameters at every stage σ_i, κ_i, $\forall i$.

The design of ring resonator filters is based on transforming the transfer functions for both the through and drop ports to their corresponding Z-domain responses [24]. This is accomplished by utilizing $z^{-1} = e^{-j\theta}$, where z^{-1} includes only the phase factor. All the transfer matrices are thus z-dependent and both R_{out} and T_{out} are transformed to the Z-domain:

$$R_{\text{out}}(z) = \frac{B(z)}{A(z)} = \frac{\sum_{n=0}^{N} p_n z^{-n}}{1 + \sum_{m=1}^{M} q_m z^{-m}}, \quad T_{\text{out}}(z) = \frac{z^{-N/2} e^{-N\alpha L_c/2} \prod_{i=1}^{N+1} j\kappa_i}{A(z)} \tag{6.9}$$

The calculated transfer function has the same form of the response of a linear discrete system [6]. All coefficients p_n and q_m are dependent on the ring coupling parameters (σ_i, κ_i) for all rings. They are also dependent on the cavity loss parameter defined as $\tau = e^{-\alpha L_c}$. Those coupling parameters are optimized to achieve the target filter response represented by a certain numerator and denominator polynomials. Control of the waveguide to ring and ring-to-ring scattering parameters allows a high degree of freedom

to achieve different targeted filter responses. Both the through and drop ports can be utilized to achieve the desired filter response.

6.3 DESIGN OPTIMIZATION BASED ON THE PERTURBATION APPROACH

We develop a new simple formulation utilizing the perturbation theory to reduce the complexity of the filter transfer function. For global optimization of cascaded series rings filters, robust optimization techniques can be incorporated to provide optimal filter designs. The proposed technique assumes that the required design has certain known mean coupling parameters. By calculating the optimal perturbations from these parameters, the overall coupling coefficients are modified to achieve the targeted filter response. Our approach takes into consideration unavoidable losses that are inherent in curved structures.

We illustrate our approach for the case of three series ring resonators. By using (6.7) and (6.8), we calculate the transfer functions of both the through and drop ports as follows:

$$
\begin{aligned}
B(z) = \Big(& \sigma_1 - (\sigma_2 + \sigma_1\sigma_2\sigma_3 + \sigma_1\sigma_3\sigma_4)\tau z^{-1} \\
& + (\sigma_3 + \sigma_2\sigma_3\sigma_4 + \sigma_1\sigma_2\sigma_4)\tau^2 z^{-2} - \sigma_4\tau^3 z^{-3} \Big)
\end{aligned}
\tag{6.10}
$$

and

$$
\begin{aligned}
A(z) = 1 & - (\sigma_1\sigma_2 + \sigma_2\sigma_3 + \sigma_3\sigma_4)\tau z^{-1} \\
& + (\sigma_1\sigma_2\sigma_3\sigma_4 + \sigma_1\sigma_3 + \sigma_2\sigma_4)\tau^2 z^{-2} - \sigma_1\sigma_4\tau^3 z^{-3}.
\end{aligned}
\tag{6.11}
$$

We further assume that each coupling coefficient is perturbed around a given mean value

$\bar{\sigma}_i$:

$$\sigma_i = \bar{\sigma}_i + \delta\sigma_i \quad i = 1, 2, ..., 4. \tag{6.12}$$

Substituting from (6.12) in both (6.10) and (6.11), the polynomials A and B are of fourth

order dependence on the individual perturbations $\delta\sigma_i$, $\forall i$. Assuming small perturbations

$\boldsymbol{\delta\sigma} = [\ \delta\sigma_1 \ \delta\sigma_2 \ \delta\sigma_3 \ \delta\sigma_4]^T$, higher order terms can be neglected. By dumping the higher

order perturbation terms, we ignore the effect of multiple reflections among the rings

introduced by the small adjustment of the parameters σ. This is a first order accurate

approach as it takes into account only multiple reflections introduced by the zero order

terms $\bar{\sigma}_i$. For N cascaded coupled resonators, a linear approximation of the polynomials

$B(z)$ and $A(z)$ dependence on the perturbed through port coupling $\boldsymbol{\delta\sigma}$ can thus be

formulated. In this case we have :

$$\begin{aligned} p_n &= \left(c_n + \boldsymbol{h}_n^T \boldsymbol{\delta\sigma}\right) \quad n = 0, 1, ..., N \\ q_m &= \left(d_m + \boldsymbol{g}_m^T \boldsymbol{\delta\sigma}\right) \quad m = 1, 2, ..., M \end{aligned} \tag{6.13}$$

In (6.13), c_n and d_m are the zero order terms in $\boldsymbol{\delta\sigma}$ that can be calculated by substituting

with $\bar{\sigma}_i$ in (6.9), respectively. The coefficients of the first order terms in $\boldsymbol{\delta\sigma}$ are

represented by $\boldsymbol{h}_i$ and $\boldsymbol{g}_i$, both are polynomials in $\bar{\sigma}_i$.

In order to achieve a filter response with a specific z-dependence, we match the

ring filter coefficients (p, q) to the targeted filter coefficients (b, a). The following system

of linear equations is thus constructed:

$$\boldsymbol{y} = \begin{bmatrix} \boldsymbol{b} - \boldsymbol{c} \\ \boldsymbol{a} \text{ - } \boldsymbol{d} \end{bmatrix} = \boldsymbol{A}\boldsymbol{\delta\sigma}, \tag{6.14}$$

where

$$\boldsymbol{c} = [c_0 \ c_1 \ ... \ c_N], \quad \boldsymbol{d} = [d_1 \ d_2 \ ... \ d_N], \tag{6.15}$$

and

$$\boldsymbol{A}^T = \left[\boldsymbol{h}_0 \ \boldsymbol{h}_1 \ ... \boldsymbol{h}_N \ \boldsymbol{g}_1 \ \boldsymbol{g}_2 \ \cdots \boldsymbol{g}_N \right]. \tag{6.16}$$

In (6.14), $\boldsymbol{b}$ and $\boldsymbol{a}$ are the vectors of the numerator and denominator polynomials of the target filter transfer function (6.9). The solution of the linear system of equation in (6.14) produces the optimal $\boldsymbol{\delta\sigma}$ that satisfies the target filter transfer function.

The system of linear equations (6.14) is overdetermined. However, a least squares solution will lead to the optimal perturbation parameters. The design problem can thus be cast as a constrained optimization problem with a quadratic objective function over linear constraints:

$$\begin{aligned} \min_{\boldsymbol{\delta\sigma}} \quad & \left\| \boldsymbol{A}\boldsymbol{\delta\sigma} - \boldsymbol{y} \right\|_p^2 \\ & 0 \le \delta\sigma_i + \bar{\sigma}_i \le 1 \\ & \left| \delta\sigma_i \right| \le \zeta \qquad i = 1, 2, ..., N+1 \end{aligned} \tag{6.17}$$

In (6.17), the first constraint is placed to ensure the total through coupling parameter less than unity. The second constraint imposes a trust region for the perturbation model. The parameter ζ is the maximum allowable perturbation in the coupling parameters.

The formulation in (6.17) can be solved using the L_1-norm, the L_2-norm, or the L_∞-norm. For the case of L_∞-norm, the problem is transformed into the minimization of the maximum of the deviation. In this case, (6.17) is equivalent to:

$$\min_{\delta\boldsymbol{\sigma}} \quad \Gamma^2$$

$$\left| \boldsymbol{a}_j^T \delta\boldsymbol{\sigma} - y_j \right| \le \Gamma \quad j = 1, 2, ..2N + 1$$

$$0 \le \delta\sigma_i + \bar{\sigma}_i \le 1$$

$$\left| \delta\sigma_i \right| \le \zeta \qquad i = 1, 2, ..., N + 1$$

$$(6.18)$$

where $\boldsymbol{a}_j^T$ is the jth row of the matrix $\boldsymbol{A}$. This problem is convex and leads to a unique optimal design [26].

For lossy structures, the total loss of the ring modifies the optimization problem constraints. This can be taken into consideration by a direct modification of the system coefficients in (6.13). The same system of equations is solved to get the perturbation in the coupling coefficients in the presence of the losses.

Our formulation can be contrasted with other conventional nonlinear least square problems. These approaches have complex dependence on parameters. They are computationally expensive and their solution is not globally optimal.

The perturbation technique is verified through the design of third, fifth and tenth order optical filters using series connected ring resonators. We carry out optimization for both lossless and lossy structures. The optimization algorithm achieves the required response efficiently within the trusted perturbation region [25]. Our algorithm is also applied to a set of lossy structures to predict the change in the achievable design with a loss increase [25].

6.3.1 Third Order Ring Resonator Filter

For the design of a third order filter, the target filter is commonly represented by the corresponding zero-pole relationship [24]. For this example, the target filter response

has three zeros at $z = \exp(j148\pi/180)$, $z = \exp(j\pi)$, and $z = \exp(j212\pi/180)$, and three poles at $z = 0.6\exp(j50\pi/180)$, $z = 0.7$, and $z = 0.6\exp(j315\pi/180)$. The response of the filter is Chebyshev type II filter, with both a flat pass band response and a high selectivity.

We utilize our algorithm to optimize the coupling parameters in order to design a filter with the optimal match to the target response. The mean waveguide to ring through coupling is set to 0.5 and the mean ring to ring through coupling is set to 0.8. The ring is assumed to be of negligible losses. The achievable optimized filter (see Fig. 6.3) has a feasible value ring to ring through coupling coefficients (σ_2, σ_3) of 0.83, and a ring to waveguide through coupling (σ_1, σ_4) of 0.48. The target response cannot be ideally achieved by three ring resonators. However, our proposed approach provides systematically the best achievable response that can be provided by the three rings. For more idealized responses, higher order rings should be utilized. The response of the ring resonators at the drop port is also shown in Fig. 6.4.

6.3.2 Fifth Order Ring Resonator Filter

The fifth order drop filter proposed in [8] can be optimized to match a desired IIR filter of different pass band, stop band, and stop band reduction. For an achievable ideal response, we apply our technique to the design of a filter whose response can be achieved using ring resonator based filters [25].
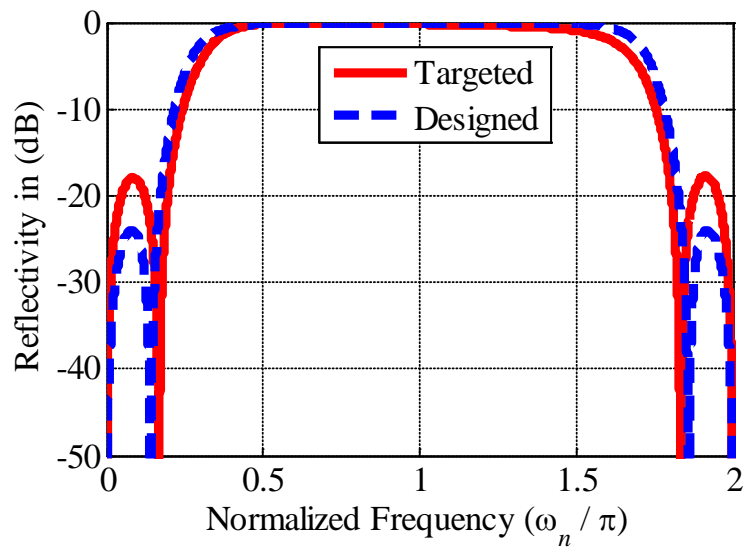
Fig. 6.3. The achieved third order filter response as compared to the targeted response [25].
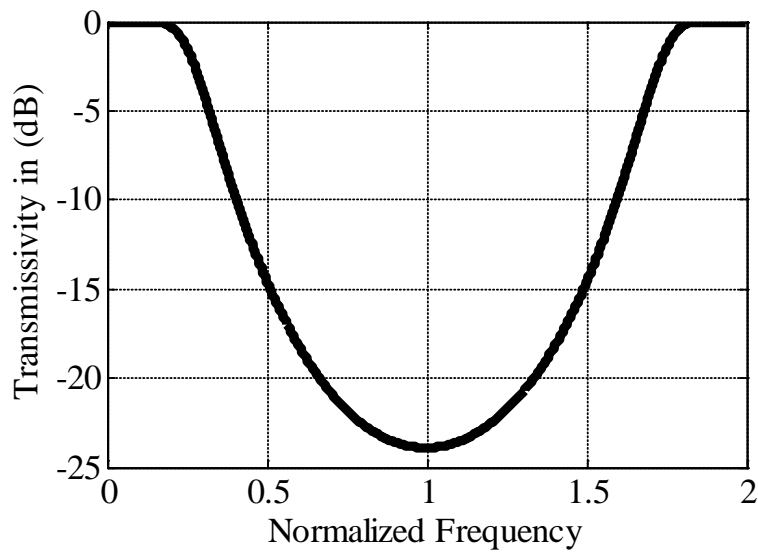
Fig. 6.4. The designed cascaded ring response at the drop port (transmissivity) [25].

For this filter, the pass band occupies approximately one seventh of the free spectral range. The pass band ripples are less than 0.4 dB, and the stop band rejection is more than 40 dB. The targeted transfer function has the form,

$$T_{\text{target}}(z) = \frac{0.002z^{-5/2}}{1 - 4.23z^{-1} + 7.33z^{-2} - 6.51z^{-3} + 2.96z^{-4} - 0.55z^{-5}} \qquad (6.19)$$

In order to achieve this transfer function using ring resonators, we assume a known waveguide to ring through coupling coefficient of 0.7416 [8]. The ring-to-ring mean through coupling is assumed to be 0.9. This value is an acceptable approximation for the required filter response from the drop port. This assures the validity of our algorithm for a high value of the mean through coupling coefficient.

Our algorithm is applied to extract the vector of perturbation in the through coupling parameters ($\delta\sigma$). The convexity of the optimization problem yields a unique solution regardless of the initial starting point. The application of our technique results in a perfect match with the target filter as shown in Fig. 6.5. The optimal coupling perturbations $\delta\sigma = [0.0602\ 0.0753\ 0.0753\ 0.0602]^T$ result in a symmetric structure. The ring resonator drop port transfer function is as follows:

$$T_{\text{designed}}(z) = \frac{0.0017z^{-5/2}}{1 - 4.25z^{-1} + 7.39z^{-2} - 6.57z^{-3} + 2.97z^{-4} - 0.55z^{-5}}. \qquad (6.20)$$

The resulting transfer function (6.20) is close to (6.19) which reflects the reliability of the technique to achieve a target filter response of arbitrary feasible coefficients. The response of the ring resonators at the through port (reflectivity) is shown in Fig. 6.6.
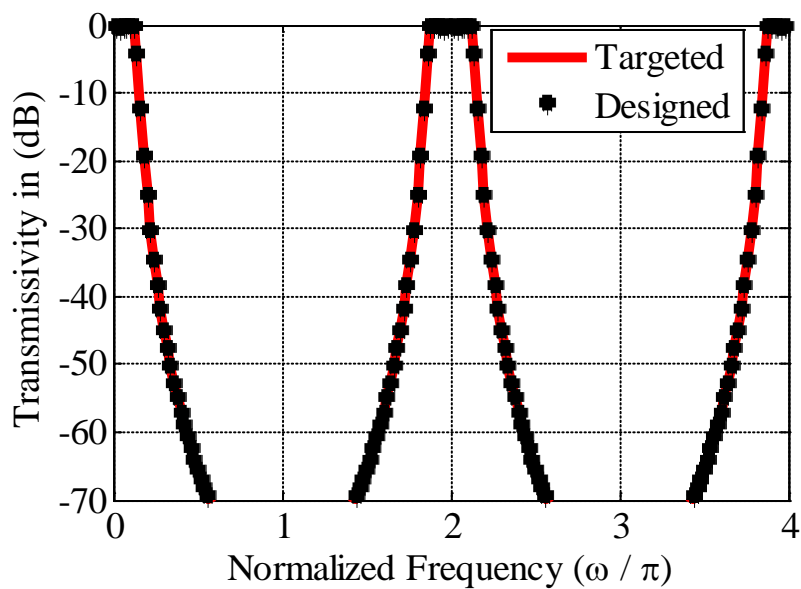
Fig. 6.5. The achieved fifth order filter response as compared to a targeted fifth order filter proposed in [8].
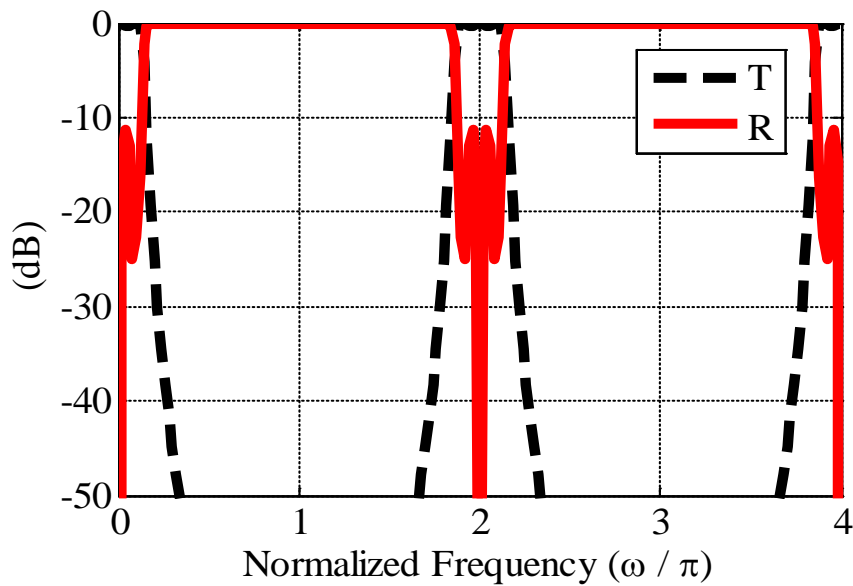
Fig. 6.6. The responses at the through port (R) and the drop port (T) for the five cascaded ring resonators [25].

6.3.3   Tenth Order Ring Resonator Filter

For tenth order dropping filters, our technique is also utilized to design a number of ten series connected rings [25]. For this example, the targeted filter has small pass band ripples with an increased normalized bandwidth and improved steep filter pass band to stop band transition. The targeted filter design is proposed using matlab digital filter design functions [29]. Our technique is then utilized to determine the best rings coupling parameters to achieve the target design.

The target filter is a Chebyshev type I filter of bandwidth of one third of the free spectral range with minimal pass band ripples. The (cheby1) matlab function [29] is utilized with ripple parameters of 0.001 and normalized band width of 0.33. The target vector of the denominator polynomial coefficients is $a=$ [1.0000 −5.2448 13.8635 −23.6303 28.3988 −24.9452   16.1369 −7.5663 2.4561 −0.4980 0.0479]^T.

For this problem, the number of optimization parameters is 11 representing the through coupling coefficient σ_i for all the stages. Equation (6.18) is utilized with average couplings $\bar{\sigma}=$[0.25 0.5 0.75 0.75 0.75 0.75 0.75 0.75 0.75 0.5 0.25]^T. The perturbation trust region size ζ is set to 0.1. The optimal set of coupling is found to be $\sigma=$ [0.227 0.5624 0.8328 0.8414 0.843 0.8433 0.843 0.8414 0.8328 0.5624 0.227]^T. The achieved response and the target response are shown in Fig. 6.7. Good match is achieved between the two responses. The response of the ring resonators at the through port (reflectivity) compared to the response at the drop port (transmissivity) is shown in Fig. 6.8. Figure 6.9 shows the optimized coupling coefficients utilizing the perturbation approach.
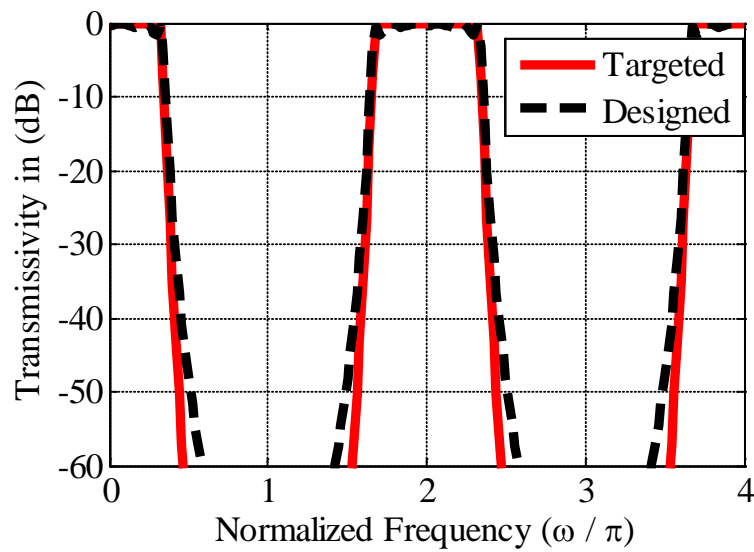
Fig. 6.7. The achieved tenth order filter response as compared to the target response [25].
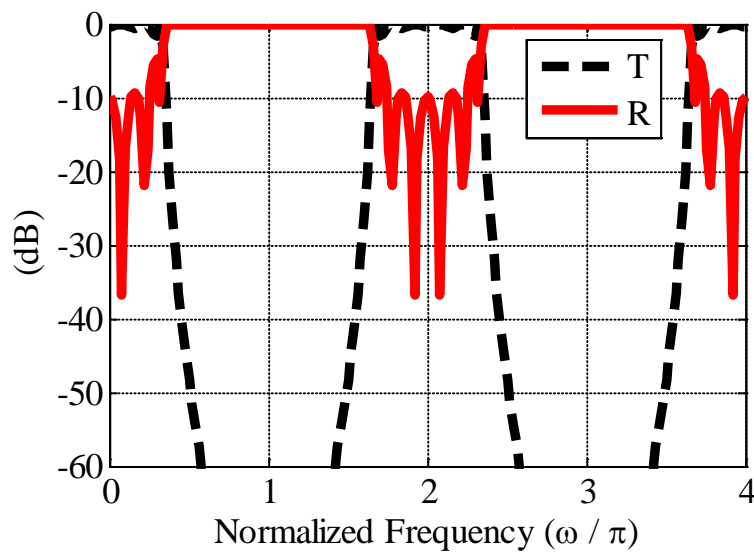
Fig. 6.8. The responses at the through port (R) and the drop port (T) for the ten cascaded ring resonators [25].
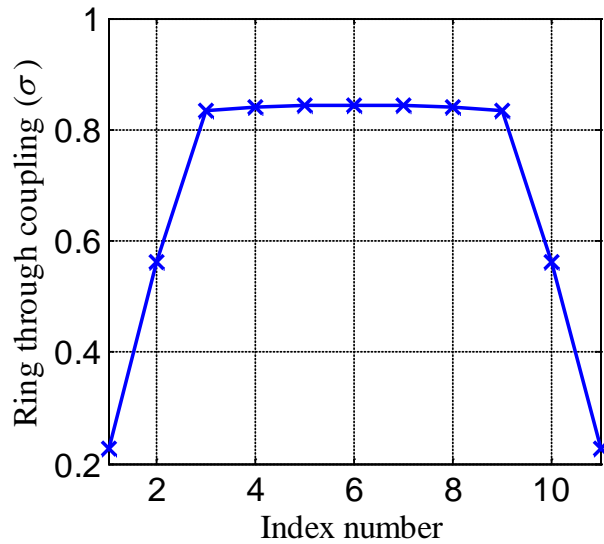
Fig. 6.9. The coupling coefficients for the optimized tenth order optical filter utilizing the perturbation approach.

6.3.4 Fifth Order Lossy Filter

In order to illustrate the accuracy and correctness of the proposed approach, we compare our results to that in [11]. We design the target filter in [11] utilizing both cases ideal and lossy coupled ring resonators [25]. In [11], a fifth order filter is utilized to achieve a highly selective filter with a bandwidth of 20% of the free spectral range and maximum pass band flatness. Utilizing the method in [11], the achievable design has ring through coupling parameters $\boldsymbol{\sigma} = [0.4186 \quad 0.821 \quad 0.909 \quad 0.909 \quad 0.821 \quad 0.4186]^T$. The target vector of the polynomial coefficients in (6.9) is calculated as $\boldsymbol{a} = [1 \quad -3.0083 \quad 4.0132 \quad -2.8776 \quad 1.0944 \quad -0.1753]$.

We utilize our approach for the design of the same target filter. The average couplings $\bar{\boldsymbol{\sigma}} = [0.45\ 0.85\ 0.85\ 0.85\ 0.85\ 0.45]^T$ are utilized. The perturbation trust region size ζ is set to 0.2. The optimal set of coupling are calculated to be $\boldsymbol{\sigma} = [0.421\ 0.808$

0.917 0.917 0.808 0.421$]^T$ utilizing lossless coupled ring resonators. The designed

polynomial coefficients are $a = [1 \quad -3.0053 \quad 4.0 \quad -2.8652 \quad 1.0939 \quad -0.1776]$. Fig.

6.10 shows the filter response utilizing our approach. It has a good agreement with the

target filter. The ability of our perturbation algorithm to predict the optimal design is best

illustrated in Fig. 6.11. The optimal coupling coefficients for the lossless case have a very

good match with the results in [11].

To further illustrate the universality of our approach, we design the same ideal

target filter utilizing lossy ring resonators with a power loss factor (1-τ^2) of 9.8%.
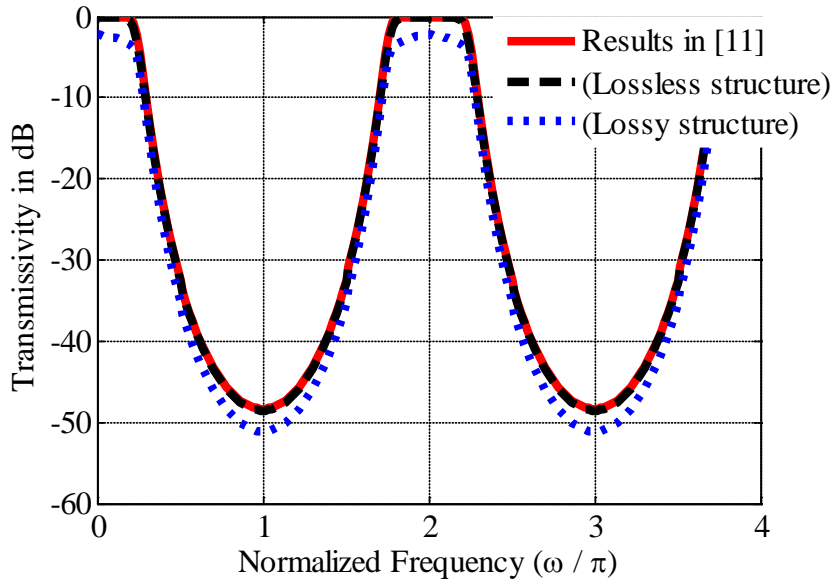
Fig. 6.10. The achieved fifth order filter response utilizing the perturbation approach for both lossless and lossy structures as compared to [11].
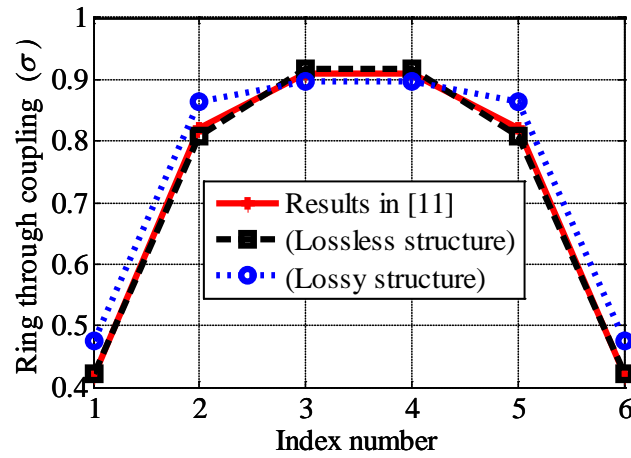
Fig. 6.11. The optimal coupling coefficients for the optimized filter for both lossless and lossy case as compared to the coefficients predicted in [11].

Utilizing our approach, the same filter response can be achieved except for magnitude scaling due to losses. In Fig. 6.10, the optimal filter design utilizing the lossy structure is compared to the ideal one. The dominant optimal coupling coefficients for the lossy case are larger than the ideal case as shown in Fig. 6.11 [25].

6.4   LINEAR PHASE FILTER REALIZATION

For highly coupled microcavities, the through port coupling for each coupling stage ($|\sigma_i|\leq1$) is usually small. This allows for physically neglecting the higher order coupling between the microcavities, as their amplitudes are proportional to $\sigma_i\sigma_{i+1}$. Notice that by neglecting the higher order coupling terms, the polynomial $A(z)$ in (6.9) becomes unity. For low loss coupled microcavities, the recursive formula for the reflectivity at the ith stage is calculated as

$$R_i = \sigma_i - z^{-1}R_{i+1} \tag{6.21}$$

This approximates the response to

209

$$\tilde{R}_{\text{out}}(z) = \sum_{n=0}^{N} b_n z^{-n} \tag{6.22}$$

For symmetric coupled microcavities, the through coupling coefficients are symmetric around the middle coefficient. This is a practical assumption which allows for having a linear phase filter response [30]. The symmetry assumption implies that

$$\sigma_i = \sigma_{N+2-i}, \quad i = 1, 2, ..., N+1 \tag{6.23}$$

The total through port coupling can be represented in terms of the normalized angular frequency (θ) as

$$\tilde{R}_{\text{out}}(\theta) = e^{-j(N\theta/2)}[2\sigma_1 \cos(N\theta/2) - 2\sigma_2 \cos((N/2-1)\theta) + \cdots + \sigma_{N/2+1}e^{j\pi N/2}] \tag{6.24}$$

From (6.24), the through port transfer function can be represented as $\tilde{R}_{\text{out}}(\theta) = e^{-j(N\theta/2)}R'_{\text{out}}(\theta)$ where $R'_{\text{out}}(\theta)$ is a real and periodic even function. It is thus sufficient to only consider $\theta \in [0, \pi]$. The linear phase approximation of the phase response (wrapped) in the case of 10 microcavities is shown in Fig. 6.12.

The developed approximate transfer function is a linear phase filter formulation [27]. It transforms the design procedure into a convex optimization problem whose solution can be estimated efficiently and accurately for large number of coupled microcavities. The general formulation of the problem is

$$
\begin{aligned}
\min_{\sigma} \quad & \max_{\theta \in [\omega_s, \pi]} \left| R'_{\text{out}}(\theta) \right| \\
\text{subject to} \quad & \left| R'_{\text{out}}(\theta) \right| \leq \zeta, \qquad \theta \in \left[0, \omega_p\right] \\
& \delta_1 \leq \sigma_i \leq \delta_2 \qquad \forall i
\end{aligned}
\tag{6.25}
$$

In (6.25), ω_s is the normalized stop band angular frequency, ω_p is the normalized pass band angular frequency, and ζ is the pass band ripples. The design parameters are the
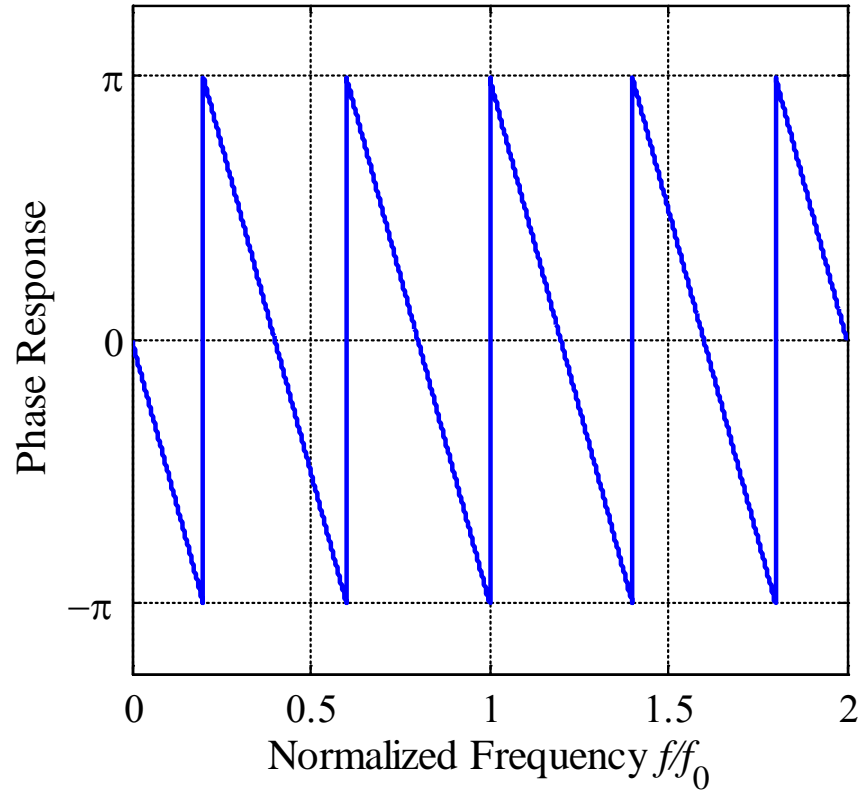
Fig. 6.12. The linear phase of the approximate transfer function, is illustrated for the case of 10 microcavities.

through coupling coefficients $\boldsymbol{\sigma} = [\sigma_1 \; \sigma_2 \cdots \sigma_{N+1}]^T$. In (6.25), the last constraint is added to ensure the physical realization of the designable coupling coefficients.

The proposed technique is exploited in filter design problems. For this purpose, the interior point-based solver, SeDuMi, is used for solving the linear programming problem [31]. One of advantages of this solver is the ability to find a feasible starting point. Thus, there is no need to supply an initial design which is considered as a significant advantage especially for problems with large number of microcavities.

For the first example, a filter response with minimum ripples in the passband is obtained. The number of microcavities is 36. The pass band is 1.0 f_o around the central frequency f_o. The response of the through and drop port is given in Fig. 6.13. The length of the cavity L_c is taken to be one quarter of the central wavelength. For the second example, the length of the cavity is taken to be half the central wavelength. Thus, the response is switched from band pass filter to band stop filter in the through port and vice versa in the drop port. The number of microcavities in this example is 30. The response in the through port has a rejection band of 0.4 f_o centered around f_o. This band has a flat response in the drop port as shown in Fig. 6.14.

For the third example, a design of 150 rings is obtained for a flat response over 0.2 f_o and sharp roll off over .01 f_o from each side of the transmission band as shown Fig. 6.15. The computation time of this example is 1.2 sec. However, solving the non convex minimax problem [30], the computational time for this example is 1.5×10^5 sec for a starting point in the middle of the feasible domain. This comparison is performed on a 2.2 GHz dual core processor computer with 2.0 GB of RAM. The optimized values of σ for all examples are given in Fig. 6.16.
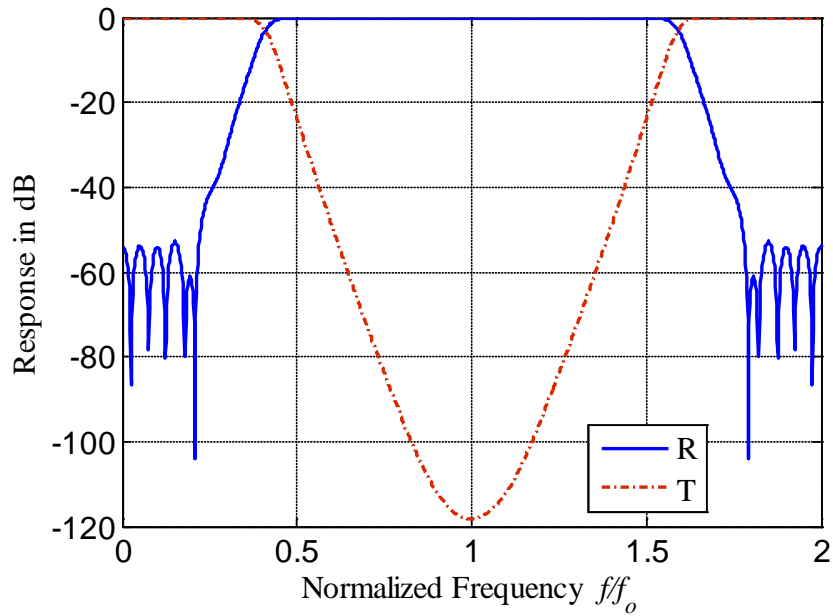
Fig. 6.13. The drop and through response of the optimized structure with 36 microcavities.
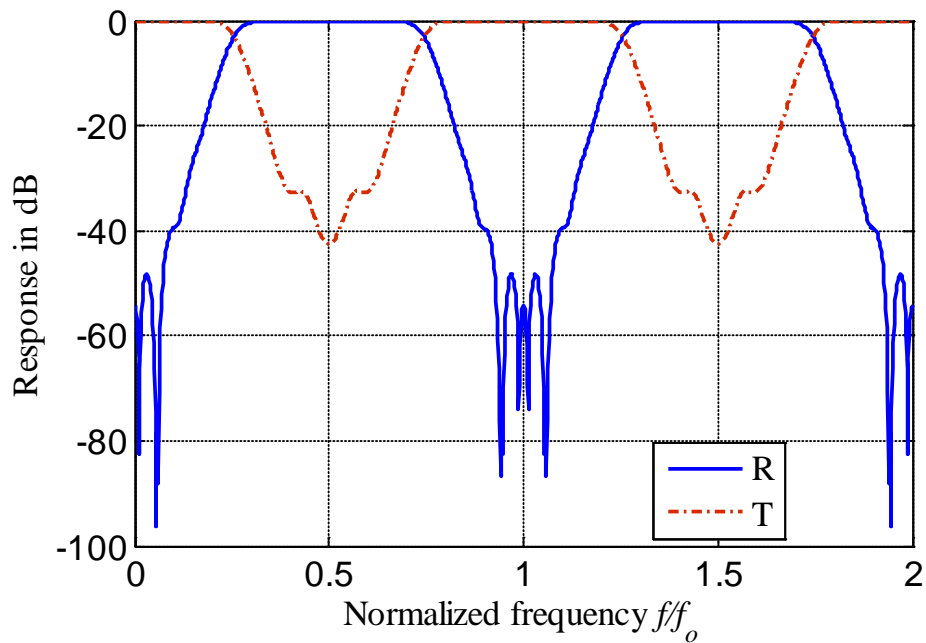
Fig. 6.14. The drop and through response of the optimized structure with 30 microcavities.
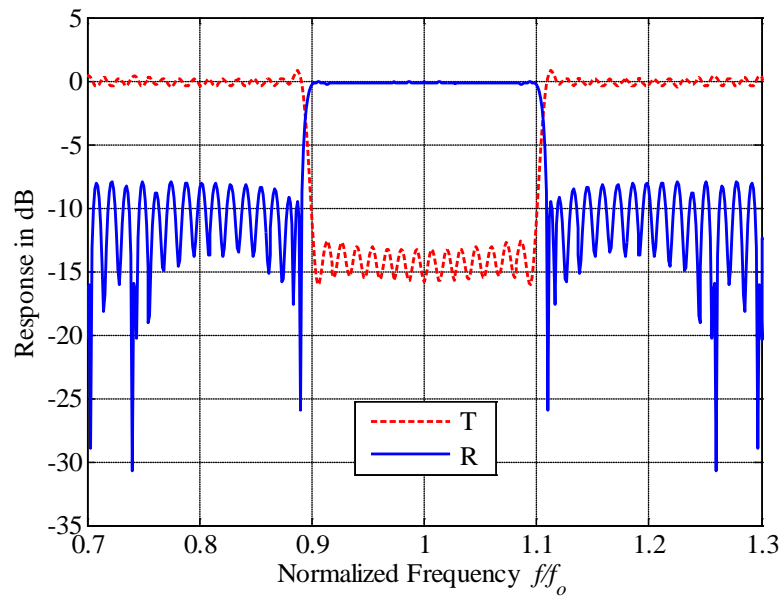
Fig. 6.15. The drop and through response of the optimized structure with 150 microcavities.
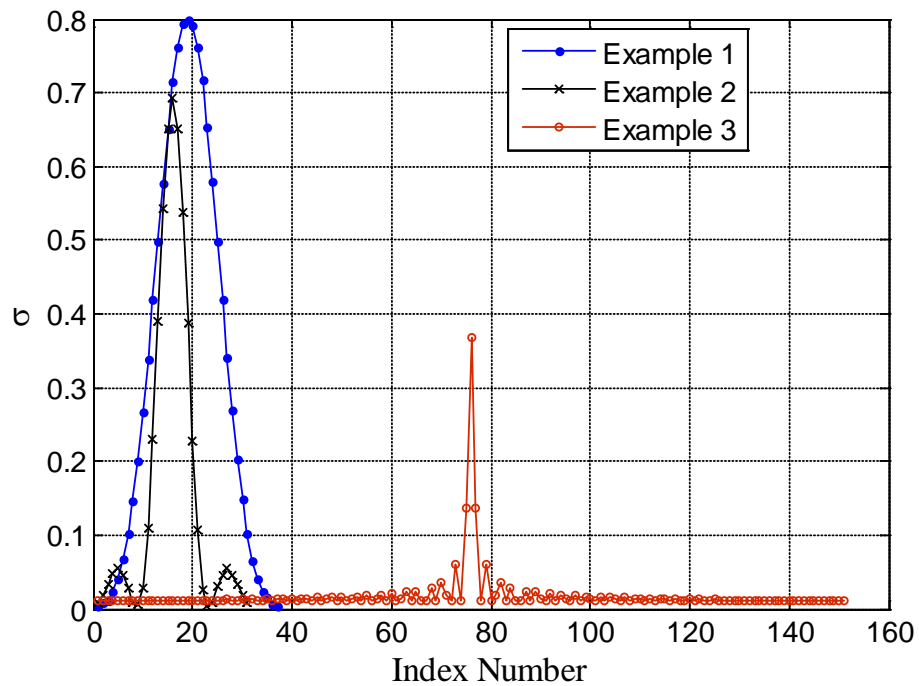
Fig. 6.16. The coupling coefficient of the optimized design of the 36, 30 and 150 cascaded microcavities [27].

6.5 SUMMARY

Two novel design procedures for filter design with a large number of coupled microcavities were introduced. These procedures are efficient and simple. Both approaches exploit convex optimization techniques for formulating the design problem. This formulation allows for fast and accurate solution of the design problem. The accuracy and the efficiency of these approaches allow for solving design problems with few hundreds of variables in less than one second.

6.6 REFERENCES

[1]   B. E. Little, S. T. Chu, H. A. Haus, J. Foresi, and J.-P. Laine, " Microring resonator channel dropping filters," *J. Lightwave Technol.*, vol. 15, pp. 998-1005, 1997.

[2]   F. C. Blom, D. R. Van Dijk, H. J. W. M. Hoesktra, A. Driessen, and T. J. A. Popma, "Experimental study of integrated-optics microcavity resonators: toward an all-optical switching device," *Appl. Phys. Lett.*, vol. 71, pp. 747-749, 1997.

[3]   B. E. Little, J. S. Foresi, G. Steinmeyer, E. R. Thoen, S. T. Chu, H. A. Haus, E. P. Ippen, L. C. Kimerling, and W. Greene, "Ultra-compact Si/SiO2 microring resonator optical channel dropping filters," *IEEE Photon. Technol. Lett.*, vol. 10, pp. 549-551, 1998.

[4]   Y. Yanagase, S. Suzuki, T. Kokubun, and S. T. Chu, "Vertical triple series-coupled microring resonator filter for passband flattening and expansion of free spectral range," *Jpn. J. Appl. Phys.*, vol. 41, pp. L141-L143, 2002.

[5]   C. Ozturk, A. Huntington, A. Aydinli, Y. T. Byun, and N. Dagli, "Filtering characteristics of hybrid integrated polymer and compound semiconductor waveguides," *J. Lightwave Technol.*, vol. 20, pp. 1530-1536, 2002.

[6]   C. K. Madsen and J. H. Zhao, *Optical Filter Design and Analysis: A Signal Processing Approach*. New York: Wiley, 1999.

[7]   T. Barwicz, M. A. Popović, M. R. Watts, P. T. Rakich, E. P. Ippen, and H. I. Smith, "Fabrication of add-drop filters based on frequency matched microring resonators," *J. Lightwave Technol.*, vol. 24, pp. 2207-2218, 2006.

[8]   F. Xia, M. Rooks, L. Sekaric, and Y. Vlasov, "Ultra-compact high order ring resonator filters using submicron silicon photonic wires for on-chip optical interconnects," *Opt. Express*, vol. 15, pp. 11934-11941, 2007.

[9]   B. E. Little, S. T. Chu, P. P. Absil, J. V. Hryniewicz, F. G. Johnson, F. Seiferth, D. Gill, V. Van, O. King, and M. Trakalo, "Very high order microring resonator filters for WDM applications," *IEEE Photon. Technol. Lett.*, vol. 16, pp. 2263-2265, 2004.

[10]   O. Schwelb, "Transmission, group delay, and dispersion in single-ring optical resonators and add/drop filters-a tutorial overview," *J. Lightwave Technol.*, vol. 22, pp. 1380-1394, 2004.

[11]   A. Melloni and M. Martinelli, "Synthesis of Direct-Coupled-Resonators Bandpass Filters for WDM Systems," *J. Lightwave Technol.*, vol. 20, pp. 296-303, 2002.

[12]   A. Melloni, "Synthesis of a parallel-coupled ring-resonator filter," *Opt. Lett.*, vol. 26, pp. 917-919, 2001.

[13]   P. Chak and J. E. Sipe, "Minimizing finite-size effects in artificial resonance tunneling structures," *Opt. Lett.,* vol. 31, pp. 2568-2570, 2006.

[14]   E. Dowling and D. MacFarlane, "Lightwave lattice filters for optically multiplexed communication systems," *J. Lightwave Technol.*, vol. 12, pp. 471-486, 1994.

[15]   C. K. Madsen, "General IIR Optical Filter Design for WDM Applications Using All-Pass Filters," *J. Lightwave Technol.*, vol. 18, pp. 860-868, 2000.

[16]   R. Orta, P. Savi, R. Tascone, and D. Trinchero, "Synthesis of multiple ring-resonator filters for optical systems," *IEEE Photon. Technol. Lett.*, vol. 7, pp. 1447-1449, 1995.

[17]   J. K. S. Poon, J. Scheuer, S. Mookherjea, G. T. Paloczi, Y. Huang, and A. Yariv, "Matrix analysis of microring coupled-resonator optical waveguides," *Opt. Express*, vol. 12, pp. 90-103, 2004.

[18]   B. E. Little, S. T. Chu, J. V. Hryniewicz, and P. P. Absil, "Filter synthesis for periodically coupled microring resonators," *Opt. Lett.*, vol. 25, pp. 344-346, 2000.

[19]   C. Ferrari, F. Morichetti, and A. Melloni, "Disorder in coupled-resonator optical waveguides," *J. Opt. Soc. Am. B*, vol. 26, pp. 858-866, 2009.

[20]   G. Matthaei, E. Jones, and L. Young, *Microwave Filters, Impedance-Matching Networks, and Coupling Structures*. Artech House Publishers, 1980.

[21]   S. Cohn, "Direct-Coupled-Resonator Filters," *Proc. of the IRE*, vol. 45, pp. 187-196, 1957.

[22]   Leo Young, "Direct-Coupled Cavity Filters for Wide and Narrow Bandwidths," *IEEE Trans. Microw. Theory Tech.*, vol. 11, pp. 162-178, 1963.

[23]   L. N. Binh, N. Q. Ngo, and S. F. Luk, "Graphical representation and analysis of the Z-shaped double-coupler optical resonator," *J. Lightwave Technol.*, vol. 11, pp. 1782-1792, 1993.

[24]   C. J. Kaalund and G.-D. Peng, "Pole-zero diagram approach to the design of ring resonator-based filters for photonic applications," *J. Lightwave Technol.*, vol. 22, pp. 1548-1559, 2004.

[25]   O. S. Ahmed, M. A. Swillam, M. H. Bakr, and X. Li, "Efficient design optimization of ring resonator-based optical filters," *IEEE J. of Lightwave. Technol.*, vol. 29, pp. 2812-2817, 2011.

[26]   S. Boyd and L. Vandenberghe, *Convex Optimization*. New York: Cambridge, 2004, ch. 4.

[27]   M. A. Swillam, O. S. Ahmed, M. H., Bakr, and X. Li, "Filter design using multiple coupled microcavities," *IEEE Photon. Technol. Lett.*, vol. 23, pp. 1160-1162, 2011.

[28]   H. Haus, *Waves and Fields in Optoelectronics*. New York: Prentice-Hall, 1984.

[29]   Matlab, 2005. Version 7.1.

[30]   M. A. Swillam, M. H. Bakr, and Xun Li, " The design of multilayer optical coatings using convex optimization," *J. Lightwave Technol.*, vol. 25, pp. 1078-1085, 2007.

[31]   Sturm, J.F. Using SeDuMi 1.02, a MATLAB toolbox for optimization over symmetric cones. *Optimization Methods and Software* 1999, vol. 11, pp.625-653,.Available from http://sedumi.ie.lehigh.edu/.

7 CONCLUSIONS AND FUTURE WORK

This thesis presented a thorough explanation of different techniques, algorithms, and applications developed and investigated over the last four years. The utilized techniques cover numerical and analytical modeling of electromagnetic structures. The developed algorithms are applied to microwave, terahertz, photonic, and nano-plamsonic structures. The thesis contributed to the modeling, sensitivity analysis, and optimization of EM based structures. We focused on the applications of these approaches to nano-plasmonic applications.

This thesis focused on the time-domain transmission line modeling (TLM) as a physics-based modeling technique towards multi-physics simulation. While most of the applications in the thesis are based on nano-plasmonics, applications of the TLM to mechanical and electrical systems are provided in the literature. In Chapter 2, we explained the theory of the TLM method, based on the work done at the University of Nottingham. We provide innovative applications of the TLM approach including the subwavelength structures. The performance measures of the simulation are provided through a number of challenging examples.

Pursuing a general TLM solver with integrated sensitivity calculations, we developed a memory efficient scheme (impulse sampling) for the TLM-based adjoint variable method. This approach is the ultimate efficient technique for sensitivity calculation in the TLM case. It preserves the accuracy and reduces the computational cost. The TLM approach is known for its computational overhead as the fields are

replaced by network voltage and current variables of increased size. We developed an optimized approach for AVM calculations that overcome redundant calculations and saves 90% of the required memory storage. The technique is applied for conventional stub-loaded algorithm as demonstrated in related publications. In Chapter 3, we provided the memory efficient formulation based on the utilized computational node discussed in Chapter 2. The technique is developed for 2D and 3D-TLM. We demonstrated the theory for general material with non-zero electrical and magnetic constitutive parameters.

Wide categories of materials have frequency-dependent constitutive parameters. We developed, to the best of our knowledge, the first dispersive AVM approach. It enables the application of the AVM approach to numerous fields consist dispersive materials, e.g. the design of nano-plasmonic structures. The dispersive AVM approach is also mandatory for problems that involve biological materials, which are naturally frequency dependent. Application of AVM to spectroscopy and imaging problems is limited to the frequency domain where the material constitutive parameters can be provided to the solver by simple substitution with the operating frequency. In Chapter 4, the AVM approach is developed for materials of general constitutive parameters (i.e. frequency dependent) in the time-domain. It is applied to common material models (Drude, Debye, and Lorentz). The theory can be extended though to any causal mathematical model. The developed theory exploits the Z-domain representation of the material constitutive parameters. It has been applied to the fields of metamaterial and nano-plasmonics.

Chapters 5 and 6 primarily discussed optimization algorithms based on analytical models that provide efficient computationally inexpensive modeling. In Chapter 5, we proposed an efficient terahertz time-domain spectroscopy approach to mitigate measurements uncertainty. The physics-based material models are utilized to develop parameter based optimization approach. The number of optimization variables over a wideband is reduced to few optimization parameters. Our approach has been demonstrated for the spectroscopy of carbon nano-tubes and organic compounds (e.g. naphthalene). We utilized the technique for characterization of highly doped semiconductors that exhibit plasmonic resonance in the terahertz regime.

We dedicated the last chapter (Chapter 6) of the thesis to present convex optimization approaches for photonics structures. We successfully proposed efficient approaches for the design optimization of coupled resonators. These approaches utilize simplified yet accurate analytical linear model to transform the design problem into linear program that can be solved for hundreds of variables in a fraction of a second. Our approach is demonstrated for the design of 150 coupled microcavities with an optimized flat pass-band filter response.

This thesis is a compilation of the work published in a number of peer-reviewed journals (9 articles), and presented in a number of international conferences (14 presentations).

7.1 FUTURE DIRECTIONS

I. The theory of dispersive AVM sensitivity approaches can be extended to the widely used numerical techniques (e.g. finite difference time-domain (FDTD) and finite element time-domain (FETD)) In this direction, our group has started the development of the dispersive AVM approach for FDTD technique. It represents natural extension to the work presented in this thesis. However, once the theory is developed for numerous computational techniques, it can be integrated to widely used commercial solvers.

II. The dispersive AVM theory has not been applied to some critical applications in nano-plasmonics (i.e. radiation-matter interaction in the nano-scale and optimization of nano-pillars and nano-rods). These are just examples of research directions that will be elevated by exploiting the dispersive AVM approach.

III. Our research in the modeling of transmission line models will suggest integration of the developed time-domain TLM approach with a frequency domain TLM approach towards hybrid numerical techniques. In hybrid techniques, time-domain solvers are utilized to estimate the early transient time response of the structure while the frequency domain solver is utilized to retrieve the low frequency responses. Using proper

mathematical base functions, the response throughout the entire spectrum can be predicted.

IV. In terahertz spectroscopy, the presented theory – in this thesis – suggests exceptional spectroscopy results once integrated with a robust terahertz source/detector system. Our approach can provide a high precision sample thickness. Collaboration with current research institutes with terhartz systems for measurements will be an asset.

V. Our work in convex optimization for couple resonator would be further pursued towards different coupled resonator configurations. While the presented technique utilizes the series coupling, array configuration of coupled resonators can be addressed similarly with the proper mathematical model approximations.

BIBLIOGRAPHY

- W. L. Barnes, A. Dereux, and T. W. Ebbesen, "Surface Plasmon subwavelength optics," *Nature*, vol. 424, pp. 824-830, 2003.

- S. I. Bozhevolnyi, V. S. Volkov, E. Devaux, and T. W. Ebbesen, "Channel Plasmon-Polariton guiding by subwavelength metal grooves," *Phys. Rev. Lett*., vol. 95, p. 046802, 2005.

- E. Ozbay, "Plasmonics: Merging photonics and electronics at nanoscale dimensions," *Science*, vol. 311, pp. 189-193, 2006.

- C. Genet and T. W. Ebbesen, "Light in tiny holes," *Nature*, vol. 445, pp. 39-46, 2007.

- F. J. Garcia-Vidal, L. Martin-Moreno, H. J. Lezec, and T. W. Ebbesen, "Focusing light with a single subwavelength aperture flanked by surface corrugations," *Appl. Phys. Lett*. vol. 83, pp.4500-4502, 2003.

- B. Guo, Q. Gan, G. Song, J. Gao, and L. Chen, "Numerical study of a high-resolution far-field scanning optical microscope via a surface plasmon modulated light source," *IEEE J. Lightwave Technol.*, vol. 25, pp. 830-833, 2007.

- H. Shi, C. Du, and X. Luo, "Focal length modulation based on a metallic slit surrounded with grooves in curved depths," *Appl. Phys. Lett*., vol. 91, p. 093111, 2007.

- H. Atwater,"The promise of plasmonics," *Sci. Am*, vol. 296, pp. 56-63, 2007.

- B. Lee, S. Kim, H. Kim, and Y. Lim, "The use of plasmonics in light beaming and focusing," *Prog. in Quantum Electronics*, vol. 34, pp. 47-87, 2010.

- Z. Sun and H. K. Kim, "Refractive transmission of light and beam shaping with metallic nano-optic lenses," *Appl. Phys. Lett.*, vol. 85, pp. 642-644, 2004.

- H. Shi, C. Wang, C. Du, X. Luo, X. Dong, and H. Gao, "Beam manipulating by metallic nano-slits with variant widths," *Opt. Express*, vol. 13, pp. 6815-6820, 2005.

- L. Verslegers, P. B. Catrysse, Z. Yu, and S. Fan, "Planar metallic nanoscale slit lenses for angle compensation," *Appl. Phys. Lett*. vol. 95, p. 071112, 2009.

- L. Verslegers, P. B. Catrysse, Z. Yu, J. S. White, E. S. Barnard, M. L. Brongersma, and S. Fan, "Planar lenses based on nanoscale slit arrays in a metallic film," *Nano Lett.*, vol. 9, pp. 235-238, 2009.

- D. Choi, Y. Lim, S. Roh, I. Lee, J. Jung, and B. Lee, "Optical beam focusing with a metal slit array arranged along a semicircular surface and its optimization with a genetic algorithm," *Appl. Opt.*, vol. 49, pp. A30-A35, 2010.

- J. Homola, S. S. Yee, and G. Gauglitz, "Surface plasmon resonance sensors: review," *Sens. Actuators B*, vol. 54, pp. 3-15, 1999.

- R. D. Harris and J. S. Wilkinson, "Waveguide surface plasmon resonance sensors," *Sens. Actuators B*, vol. 29, pp. 261-267, 1995.

- B. Luk'yanchuk, N. I. Zheludev, S. A. Maier, N. J. Halas, P. Nordlander, H.Giessen, and C. T. Chong, "The Fano resonance in plasmonic nanostructures and metamaterials," *Nature Mater.*, vol. 9, pp. 707-715, 2010.

- H. A. Atwater and A. Polman, "Plasmonics for improved photovoltaic devices," *Nature Mater.*, vol. 9, pp. 205-213, 2010.

- S. M. Williams, K. R. Rodriguez, S. Teeters-Kennedy, A. D. Stafford, S. R. Bishop, U. K. Lincoln, and J. V. Coe, "Use of the extraordinary infrared transmission of metallic subwavelength arrays to study the catalyzed reaction of methanol to formaldehyde on copper oxide," *J. Phys. Chem. B*, vol. 108, pp. 11833-11837, 2004.

- T. W. Ebbersen, H. J. Lezec, H. F. Ghaemi, T. Thio, and P. A. Wolff, "Extraordinary optical transmission through sub-wavelength hole arrays," *Nature*, vol. 391, pp. 667-669, 1998.

- S. A. Maier, *Plasmonics: Fundamentals and Applications*, Springer, 2007.

- S. A. Maier, M. L. Brongersma, P.G. Kik, S. Meltzer, A. A. G. Requicha, and H. A. Atwater, "Plasmonics- a route to nanoscale optical devices," *Adv. Mater.*, vol. 13, pp. 1501-1505, 2001.

- S. A. Maier and H. A. Atwater, "Plasmonics: Localization and guiding of electromagnetic energy in metal/dielectric structures," *J. Appl. Phys.*, vol. 98, pp. 1-10, 2005.

- G. Mie, "Beitrige zur Optik trüber Medien, speziell kolloidaler Metallösungen (Contributions to the optics of turbid media, especially colloidal metal suspensions)," *Ann. Phys.*, vol. 25, pp. 376-445, 1908.

- M. J. Kobrinsky, B. A. Block, J.-F. Zheng, B. C. Barnett, E. Mohammed, M. Reshotko, F. Robertson, S. List, I. Young, K. Cadien, "On chip optical interconnects," *Intel Techno. J.*, vol. 8, pp. 129-142, 2004.

- D. K. Gramotnev and S. I. Bozhevolnyi, "Plasmonics beyond the diffraction limit," *Nature Photon.*, vol. 4, pp. 83-91, 2010.

- R. Zia, J. A. Schuller, A. Chandran, and M. L Brongersma, "Plasmonics: the next chip-scale technology," *Mater. Today*, vol. 9, pp. 20-27, 2006.

- R. Appleby and H. B. Wallace, "Standoff detection of weapons and contraband in the 100 GHz to 1 THz region," *IEEE Trans. Antennas Propag.*, vol. 55, pp. 2944-2956, 2007.

- O. S. Ahmed, M. A. Swillam, M. H. Bakr, and Xun Li, "Modeling and design of nano-plasmonic structures using transmission line modeling," *Opt. Express*, vol. 18, pp. 21784-21797, 2010.

- O. S. Ahmed, M. A. Swillam, M. H. Bakr, and X. Li, "Transmission line modeling of nano-plasmonic devices," *Integrated Photonics Research, Silicon and Nanophotonics (IPRSN), OSA Technical Digest (CD): IMA3. 1-3, Toronto 2011.

- M. H. El Sherif, O. S. Ahmed, M. H. Bakr, "Derivative free optimization of nano-plasmonic structures," *The 31st Prog. In Electromag. Research Symposium* (PIERS), Kuala Lumpur, Malaysia 2012.

- O. S. Ahmed, M. H. Bakr, and X. Li, "A memory-efficient implementation of TLM-based adjoint sensitivity analysis," *IEEE Trans. Antennas Propag.*, vol. 60, pp. 2122-2125, 2012.

- O. S. Ahmed, M. H. Bakr, and X. Li, "Memory efficient adjoint sensitivity analysis exploiting 3D time domain transmission line modeling," *2012 IEEE MTT-S International Microwave Symposium Digest*, Montreal 2012.

- O. S. Ahmed, M. H. Bakr, M. A. Swillam, and X. Li, "Efficient sensitivity analysis of photonic structures with transmission line modeling," in *Proc. SPIE*, vol. 8412, Photonics North 2012, 841213, Montreal 2012.

- O. S. Ahmed, M. H. Bakr, X. Li, "Efficient formulation for TLM-based adjoint sensitivity analysis," *The 28th International Review of Progress in Applied Computational Electromagnetics* (ACES), Columbus, Ohio 2012.

- O. S. Ahmed, M. H. Bakr, X. Li, and T. Nomura, "Adjoint variable method for two-dimensional plasmonic structures," *Opt. Lett.*, vol. 37, pp. 3453-3455, 2012.

- O. S. Ahmed, M. H. Bakr, X. Li, and T. Nomura, "A time-domain adjoint variable method for materials with dispersive constitutive parameters*," IEEE Trans. Microwave Theory Tech.*, vol. 60, pp. 2959-2971, 2012.

- O. S. Ahmed, M. H. Bakr, X. Li, and T. Nomura, "Wideband sensitivity analysis of plasmonic structures," in *Proc. SPIE*, vol. 8619, Photonics West 2013, Physics and Simulation of Optoelectronic Devices XXI, San Francisco 2013.

- O. S. Ahmed, M. A. Swillam, M. H. Bakr, and X. Li, "Efficient optimization approach for accurate parameter extraction with terahertz time-domain spectroscopy," *IEEE J. of Lightwave Technol.*, vol. 28, pp. 1685−1692, 2010.

- O. S. Ahmed, M. A. Swillam, M. H. Bakr, and X. Li, "Accurate characterization of doped semiconductors with terahertz spectroscopy," in *Proc. SPIE*, vol. 8007, Photonics North 2011, 80071K, Ottawa 2011.

- O. S. Ahmed, M. A. Swillam, M. H., Bakr, and X. Li, "Efficient and accurate parameter extraction approach for terahertz time domain spectroscopy," in *Proc.*

SPIE, vol. 7938, Photonics West 2011, Terahertz Technology and Applications IV, 793805, San Francisco 2011.

- O. S. Ahmed, M. A. Swillam, M. H. Bakr, and X. Li, "Efficient design optimization of ring resonator-based optical filters," *IEEE J. of Lightwave. Technol.*, vol. 29, pp. 2812-2817, 2011.

- M. A. Swillam, O. S. Ahmed, M. H., Bakr, and X. Li, "Filter design using multiple coupled microcavities," *IEEE Photon. Technol. Lett.*, vol. 23, pp. 1160-1162, 2011.

- M. A. Swillam, O. S. Ahmed, and M. H. Bakr, "Efficient design of coupled microcavities at optical frequencies," *Micromachines*, vol. 3, pp. 204-217, 2012.

- M. A. Swillam, O. S. Ahmed, M. H. Bakr, and X. Li, "Microcavity filter design using convex optimization methodology," *Integrated Photonics Research, Silicon and Nanophotonics* (IPRSN), OSA Technical Digest (CD): IWD4. 1-3, Toronto 2011.

- O. S. Ahmed, M. A. Swillam, M. H. Bakr, and X. Li, "A perturbation approach for the design of coupled resonator optical waveguides (CROWs)," in *Proc. SPIE*, vol. 8264, Photonics West 2012, Integrated Optics: Devices, Materials, and Technologies XVI, 82640H, San Francisco 2012.

- M. A. Swillam, O. S. Ahmed, M. H. Bakr, and X. Li, "Highly efficient design methodology for very large scale coupled microcavities," in *Proc. SPIE*, vol. 8412, Photonics North 2012, 841215, Montreal 2012.

- A. Yariv, "Coupled-mode theory for guided-wave optics," *IEEE J. Quantum Electron.,* vol. QE-9, pp. 919-933, 1973.

- M. Yamada and K. Sakuda, "Analysis of almost-periodic distributed feedback slab waveguides via a fundamental matrix approach," *Appl. Opt.,* vol. 26, pp. 3474-3478, 1987.

- K. A. Winick, "Effective-index method and coupled-mode theory for almost-periodic waveguide gratings: A comparison," *Appl. Opt*., vol. 31, pp. 757-764, 1992.

- P. B. Catrysse and S. Fan, "Understanding the dispersion of coaxial plasmonic structures through a connection with the planar metal-insulator-metal geometry," *Appl. Phys. Lett*., vol. 94, p. 231111, 2009.

- J. Henzie, J. Lee, H.M. Lee, W. Hasan, T.W. Odom, "Nanofabrication of Plasmonic Structures", *Annu. Rev. Phys. Chem*., vol. 60, pp. 147-165, 2008.

- J. Melngailis, "Focused ion beam technology and applications," *J. Vac. Sci. Technol.,* vol. B5, pp. 469-495, 1987.

- S. Aksu, A. A. Yanik, R. Adato, A. Altar, M. Huang, and H. Altug, "High-throughput nanofabrication of infrared plasmonic nanoantenna arrays for vibrational nanospectroscopy," *Nano Lett.* Vol. 10, pp. 2511-2518, 2010.

- X. Li, *Optoelectronic devices: design, modeling, and simulation*. Cambridge University Press, New York, NY, USA, 2009.

- A. Taflove and S. C. Hagness, *Computational Electrodynamics: The Finite-Difference Time-Domain Method*, Third Edition, Artech House Publishers, Boston, 2005.

- G. V. Eleftheriades, O. Siddiqui, and A. Iyer, "Transmission line models for negative refractive index media and associated implementations without excess resonators," *IEEE Microwave Wireless Compon. Lett.*, vol. 13, pp. 53-55, 2003.

- A. J. Lowery, "New dynamic semiconductor laser model based on the transmission-line modeling method," *Proc. Inst. Elect. Eng.*, pt. J, vol. 134, pp. 281-289, 1987.

- P.B. Johns, and M. O'Brien, "'Use of transmission-line modelling method to solve non-linear lumped networks", *Radio Electron.-Eng.*, vol. 50, pp. 59-70, 1980.

- S. Hui, K. FUNG, and C. Christopoulos, "Decoupled simulation of multistage power electronics systems using transmission-line links," *23rd Annu. IEEE Power Electronics Specialist Conference*, Toledo, Spain, 1992, vol. 3, pp. 1324-1330.

- L. Vietzorreck, F. Coccetti, V. Chtchekatourov, P. Russer, "Modeling of MEMS Capacitive switches by TLM," *2000 IEEE MTT-S International Microwave Symposium Digest*, vol. 2, Boston, MA, 2000, pp.1221-1223.

- C. Christopoulos and J. Herring, "The application of transmission-line modeling (TLM) to electromagnetic compatibility problems," *IEEE Trans. on Electromagnetic Compatibility*, vol. 35, pp. 185-191, 1993.

- D. Vahldieck, "A hybrid drift-diffusion-TLM analysis of traveling-wave photodetectors," *IEEE Trans. Microwave Theory Tech.*, vol. 53, pp. 2700-2706, 2005.

- D. D. Cogan, *Transmission line matrix (TLM) techniques for diffusion applications*, CRC Press, 1998.

- De Cogan, Donard, William J. O'Connor, and Susan Pulko. *Transmission Line Matrix (TLM) in computational mechanics*. CRC Press, 2005.

- P. B. Johns and R. L. Beurle, "Numerical solution of 2-dimensional scattering problems using a transmission-line matrix," *Proc. Inst. Elec. Eng.*, vol. 118, pp.1203-1208, 1971.

- C. Christopoulos, *The Transmission-Line Modeling Method: TLM*, Wiley-IEEE Press, 1995.

- P. B. Johns, "A symmetrical condensed node for the TLM method," *IEEE Trans. Microwave Theory Tech.*, vol. 35, pp. 370-377, 1987.

- O. Jacquin, F. Ndagijimana, A. Cachard, and P. Benech, "Application of the TLM technique to integrated optic component modelling," *Int. J. of Numer. Model.*: *Electronic Networks, Devices and Fields*, vol. 14, pp. 95-105, 2001.

- W. J. R. Hoefer, "The transmission-line matrix method –theory and applications," *IEEE Trans. Microwave Theory Tech.*, vol. MTTT-33, pp. 882-893, 1985.

- P. B. Johns, "A simple, explicit and unconditionally stable numerical solution of the diffusion equation," *Int. J. Numer. Methods Eng.*, vol. 11, pp. 1307-1328, 1977.

- L. de Menezes and W. J. R. Hoefer, "Modeling frequency dependent dielectrics in TLM," *in IEEE Antennas Propagat.-S Symp. Dig.*, 1994, pp. 1140-1143.

- L. de Menezes and W. J. R. Hoefer, "Modeling nonlinear dispersive media in 2-D-TLM," *in 24th European Microwave Conference Proc.*, 1994, pp. 1739-1744.

- L. de Menezes and W. J. R. Hoefer, "Modeling of general constitutive relationships using SCN TLM," *IEEE Trans. Microwave Theory Tech.*, vol. 44, pp. 854-861, 1996.

- J. Paul, C. Christopoulos, and D. W. P. Thomas, "Generalized material models in TLM—Part I: Materials with frequency-dependent properties," *IEEE Trans. Antennas Propagat.*, vol. 47, pp. 1528-1534, 1999.

- J. Paul, C. Christopoulos, and D. W. P. Thomas, "Generalized material models in TLM—Part 2: Materials with anisotropic properties," *IEEE Trans. Antennas Propag.*, vol. 47, pp. 1535-1542, 1999

- J. Paul, C. Christopoulos, and D.W.P. Thomas, "Perfectly matched layer for transmission line modelling (TLM) method," *Electronics Lett.*, vol. 33, pp. 729-730, 1997.

- W. Greiner and J. Reinhardt, *Quantum Electrodynamics*, 4th ed., Berlin, Heidelberg: Springer Berlin Heidelberg, 2009.

- J. D. Jackson, *Classical Electrodynamics*, 3rd ed. New York: John Wiley, 1999.

- R. J. Luebbers, F. Hunsberger, and K. S. Kunz, "A frequency-dependent finite-difference time-domain formulation for transient propagation in plasma," *IEEE Trans. Antennas Propagat.*, vol. 39, pp. 29-34, 1991.

- J. P. Bérenger, "A perfectly matched layer for the absorption of electromagnetic waves," *J. Comput. Phys.*, vol. 114, pp. 185-200, 1994.

- C. Eswarappa and W. Hoefer, "Implementation of Berenger absorbing boundary conditions in TLM by interfacing FDTD perfectly matched layers," *Electronics Lett.*, vol. 31, p. 1264, 1995.

- S. Le Maguer, N. Peňa, and M. Ney, "Matched absorbing medium techniques for full-wave TLM simulation of microwave and millimeter-wave components," *Annals of Telecomm.*, vol. 53, pp. 115-129, 1998.

- B. Wang and G. P. Wang, "Plasmon bragg reflectors and nanocavities on flat metallic surfaces," *Appl. Phys. Lett.*, vol. 87, p. 013107, 2005.

- Z. Han, E. Forsberg, and S. He, "Surface plasmon Bragg gratings formed in metal-insulator-metal waveguides," *IEEE Photon. Tech. Lett.*, vol. 19, pp. 91-93, 2007.

- C. Sönnichsen, *Plasmons in metal nanostructures*, Ph.D. dissertation, Ludwig-Maximilians-Universtät München, (München, 2001).

- E. J. Zeman and G. C. Schatz, "An accurate electromagnetic theory study of surface enhancement factors for silver, gold, copper, lithium, sodium, aluminum, gallium, indium, zinc, and cadmium," *J. Phys. Chem.*, vol. 91, pp. 634–643, 1987.

- P. B. Johnson and R. W. Christy, "Optical constants of the noble metals," *Phys. Rev. B*, vol. 6, pp. 4370-4379, 1972.

- J. Park, H. Kim, and B. Lee, "High order plasmonic Bragg reflection in the metal-insulator-metal waveguide Bragg grating," *Opt. Express*, vol. 16, pp. 413-425, 2008.

- A. Hosseini, H. Nejati, and Y. Massoud, "Modeling and design methodology for metal-insulator-metal plasmonic Bragg reflectors," *Opt. Express*, vol. 16, 1475-1480, 2008.

- D. Z. Lin, C. Chang, Y. Chen, D. Yang, M. Lin, J. Yeh, J. Liu, C. Kuan, C. Yeh, and C. Lee, "Beaming light from a subwavelength metal slit surrounded by dielectric surface gratings," *Opt. Express*, vol. 14, pp. 3503-3511, 2006.

- S. Kim, Y. Lim, H. Kim, J. Park, and B. Lee, "Optical beam focusing by a single subwavelength metal slit surrounded by chirped dielectric surface gratings," *Appl. Phys. Let*t., vol. 92, p. 013103, 2008.

- E. D. Palik, Handbook of optical constants of solids. Academic Press, 1998.

- J. W. Bandler, Q. S. Cheng, S. A. Dakroury, A. S. Mohamed, M. H. Bakr, K.Madsen, and J. Sondergaard, "Space mapping: The state of the art," *IEEE Trans. Microwave Theory Tech*., vol. 52, pp. 337-361, 2004.

- P. Garcia and J. P. Webb, "Optimization of planar devices by the finite element method," *IEEE Trans. Microwave Theory Tech*., vol. 38, pp. 48-53, 1990.

- M. Gustafsson and S. He, "An optimization approach to two-dimensional time domain electromagnetic inverse problems," *Radio Sci*., vol. 35, pp. 525-536, 2000.

- N. Joachimowicz, C. Pichot, and J. P. Hugonin, "Inverse scattering: An iterative numerical method for electromagnetic imaging," *IEEE Trans. Antennas Propag*., vol. 39, pp. 1742-1753, 1991.

- E. J. Haug, K. K. Choi, and V. Komkov, *Design Sensitivity Analysis of Structural Systems*. Orlando, FL: Academic, 1986.

- H. Akel and J. P. Webb, "Design sensitivities for scattering-matrix calculation with tetrahedral edge elements," *IEEE Trans. Magn.,* vol. 36, pp. 1043-1046, 2000.

- J. P. Webb, "Design sensitivities using high-order tetrahedral vector elements," *IEEE Trans. Magn.,* vol. 37, pp. 3600-3603, 2001.

- J. P. Webb, "Design sensitivity of frequency response in 3-D finite-element analysis of microwave devices," *IEEE Trans. Magn*., vol. 38, pp. 1109-1112, 2002.

- G. Iuculano, V. A. Monaco, and P. Tiberio, "Network sensitivities in terms of scattering parameters," *Electron. Lett.*, vol. 7, pp. 53-55, 1971.

- J. W. Bandler, Q.-J. Zhang, and R. M. Biernacki, "A unified theory for frequency domain simulation and sensitivity analysis of linear and nonlinear circuits," *IEEE Trans. Microwave Theory Tech.*, vol. 36, pp. 1661-1669, 1988.

- Y. Chung, C. Cheon, I. Park, and S. Hahn, "Optimal shape design of microwave device using FDTD and design sensitivity analysis," *IEEE Trans. Microwave Theory Tech.*, vol. 48, pp. 2289-2296, 2000.

- Y. Chung, J. Ryu, C. Cheon, I. Park, and S. Hahn, "Optimal design method for microwave device using time domain method and design sensitivity analysis—Part I: FETD case," *IEEE Trans. Magn.,* vol. 37, pp. 3289-3293, 2001.

- Y. Chung, C. Cheon, I. Park, and S. Hahn, "Optimal design method for microwave device using time domain method and design sensitivity analysis—Part II: FDTD case," *IEEE Trans. Magn.,* vol. 37, pp. 3255-3259, 2001.

- M. H. Bakr and N. K. Nikolova, "An adjoint variable method for time-domain transmission line modeling with fixed structured grids," *IEEE Trans. Microwave Theory Tech.*, vol. 52, pp. 554-559, 2004

- N. K. Nikolova, H. W. Tam, and M. H. Bakr, "Sensitivity analysis with the FDTD method on structured grids," *IEEE Trans. Microwave Theory Tech.*, vol. 52, pp. 1207-1216, 2004

- M. H. Bakr, P. Zhao, and N. K. Nikolova, "Adjoint first order sensitivities of transient responses and their applications in the solution of inverse problems," *IEEE Trans. Antennas Propag.*, vol. 57, pp. 2137-2146, 2009.

- M. H. Bakr and N. K. Georgieva, "An adjoint variable method for frequency domain TLM problems with conducting boundaries," *IEEE Microwave wireless Comp. Lett.*, vol. 13, pp. 408-410, 2003.

- N. K. Georgieva, S. Glavic, M. H. Bakr, and J. W. Bandler, "Feasible adjoint sensitivity technique for EM design optimization," *IEEE Trans. Microwave Theory Tech.*, vol. 50, pp. 2751-2758, 2002.

- P.A.W. Basl, M.H. Bakr, and N. K. Nikolova, "Efficient estimation of adjoint sensitivities in TLM with dielectric discontinuities," *IEEE Microwave and Wireless Comp. Lett.*, vol. 15, pp. 89-91, 2005.

- M. H. Bakr and N. K. Nikolova,"An adjoint variable method for time-domain TLM with wide-band Johns matrix boundaries," *IEEE Trans. Microwave Theory Tech.*, vol. 52, pp. 678-685, 2004.

- P.A.W. Basl, M.H. Bakr, and N.K. Nikolova, "An AVM technique for 3D TLM with symmetric condensed nodes," *IEEE Microwave and Wireless Comp. Lett.*, vol. 15, pp. 618-620, 2005.

- M.H. Bakr, N.K. Nikolova, and P.A.W. Basl, "Self-Adjoint S-Parameter Sensitivities for Lossless Homogeneous TLM Problems," *International Journal of Numerical Modeling: Electronic Networks, Devices and Fields*, vol. 18, pp. 441-455, 2005.

- P.A.W. Basl, M.H. Bakr, and N.K. Nikolova, "Theory of self-adjoint S-parameter sensitivities for lossless nonhomogeneous transmission-line modeling problems," *IET Microwave Antennas Propag.*, vol. 2, pp. 211-220, 2008.

- N. Appannagaari, R. Edlinger, and B. Gray, "Optimetrics: Parametrics and Optimization Using Ansoft HFSS," Microwave Journal, Nov. 1999. [Online]. Available: http://www.ansoft.com/news/articles/MWJ.11.99.pdf. [Accessed 20 Jan. 2013].

- Press Release, "Sensitivity analysis and adapted optimization strategies for CST MICROWAVE STUDIO transient solver," May 2010. [Online]. Available: http://www.cst.com/Content/News/Documents/2010_5_TimeDomain2011_web.pdf. [Accessed 20 Jan. 2013]

- P. A. W. Basl, *An adjoint variable method for time-domain transmission line modeling*. Ph.D. dissertation, McMaster University, Hamilton, Ontario, Canada (Hamilton, 2007).

- J. Mu, H. Zhang, and W.-P. Huang, "A theoretical investigation of slot waveguide Bragg gratings," *IEEE J. Quantum Electron.*, vol. 44, pp. 622-62, 2008.

- H. Haus, *Waves and Fields in Optoelectronics*. Englewood Cliffs, NJ: Prentice-Hall, ch. 3, 1984.

- S. Ali, N. Nikolova, and M. Bakr, "Central adjoint variable method for sensitivity analysis with structured grid electromagnetic solvers," *IEEE Trans. on Magnetics*, vol. 40, pp. 1969-1971, 2004.

- A. Petosa, N. Simons, R. Siushansian, A. Ittipiboon, and M. Cuhaci, "Design and analysis of multisegment dielectric resonator antennas," *IEEE Trans. Antennas Propag.*, vol. 48, pp. 738-742, 2000.

- K. C. Gupta, R. Garg, and R. Chadha, *Computer-Aided Design of Microwave Circuits*. Dedham, MA: Artech House, 1981.

- H. Lee and T. Itoh, "A systematic optimum design of waveguide-to-microstrip transition," *IEEE Trans. Microwave Theory Tech.*, vol. 45, pp. 803-809, 1997.

- A. V. Chebykin, A. A. Orlov, A. V. Vozianova, S. I. Maslovski,Yu. S. Kivshar, and P. A. Belov, "Nonlocal effective medium model for multilayered metal-dielectric metamaterials," *Phys. Rev. B*, vol. 84, p. 115438, 2011.

- R. J. Luebbers, F. P. Hunsberger, K. S. Kunz, R. B. Standler, and M. Schneider, "A frequency-dependent finite-difference time-domain formulation for dispersive materials," *IEEE Trans. Electromagn. Compat.*, vol. 32, pp. 222-227,1990.

- D. Jiao and J.-M. Jin "Time-domain finite-element modeling of dispersive media,*" IEEE Microwave and Wireless Components Lett.*, vol. 11, pp. 220-222, 2001.

- E. Fear, S. C. Hagness, P. Meaney, M. Okoniewski, and M. Stuchly, "Enhancing breast tumor detection with near-field imaging,*" IEEE Microwave Mag.*, vol. 3, pp.48-56, 2002.

- V. Trenkic, C. Christopoulos, and T.M. Benson, "New symmetrical super-condensed node for the TLM method," *Electron. Lett.*, vol. 30, pp. 329-330, 1994.

- J. Paul, C. Christopoulos, and D. W. P. Thomas, "Generalized material models in TLM—Part 3: Materials with nonlinear properties," *IEEE Trans. Antennas Propag.*, vol. 50, pp. 997-1004, 2002.

- P. SO, "Exploit the parallel paradigm," *IEEE Microwave Mag.*, vol. 11, pp.79-85, 2010.

- F. Rossi and P. P. M. So "Hardware accelerated symmetric condensed node TLM procedure for NVIDIA graphics processing units," *IEEE Antennas Propag. Soc. Int. Symp*. (APSURSI'09), pp. 1-4, 2009.

- A. G. Radwan, M. H. Bakr, and N. K. Nikolova, "Transient adjoint sensitivities for discontinuities with Gaussian material distribution," *J. Progress in Electromagnetic Research* (PIER) B, vol. 27, pp. 1-19, 2011.

- J. B. Pendry, "Negative Refraction Makes a Perfect Lens," *Phys. Rev. Lett.*, vol. 85, pp. 3966-3969, 2000.

- R. W. Ziolkowski and E. Heyman, "Wave propagation in media having negative permittivity and permeability," *Phys. Rev. E*, vol. 64, p. 056625, 2001.

- M. G. Silveirinha and N. Engheta, "Tunneling of electromagnetic energy through subwavelength channels and bends using ε-near-zero materials," *Phys. Rev. Lett*., vol. 97, p. 157403,2006.

- S. Gabriel, R. W. Lau, and C. Gabriel, "The dielectric properties of biological tissues—III: Parametric models for the dielectric spectrum of tissues," *Phys. Medicine and Biology*, vol. 41, pp. 2271-2293, 1996.

- A. von Hippel. *Dielectrics and Waves.* The M.I.T. Press, 1954.

- C. F. Bohren and D. R. Huffman, *Absorption and Scattering of Light by Small Particles*. Wiley, New York, 1983, Ch. 9.

- B. M. Fischer, M. Walther, and P. Jepsen, "Far-infrared vibrational modes of DNA components studied by terahertz time domain spectroscopy," *Phys. Med. Biol.*, vol. 47, pp. 3807-3814, 2002.

- R. Siushansian and J. LoVetri, "A comparison of numerical techniques for modeling electromagnetic dispersive media," *IEEE Microwave Guided Wave Lett.*, vol. 5, pp.426-428, 1995.

- D. F. Kelley and R. J. Luebbers, "Piecewise linear recursive convolution for dispersive media using FDTD," *IEEE Trans. Antennas Propagat.*, vol. 44, pp. 792-797, 1996.

- C. Caloz and T. Itoh, *Electromagnetic Metamaterials, Transmission Line Theory and Microwave Applications*. New York: Wiley, 2005.

- X. -S. Lin and X. -G. Huang, "Tooth-shaped plasmonic waveguide filters with nanometeric sizes," *Opt. Lett*. vol. 33, pp. 2874-2876, 2008.

- A. E. Cetin, M. Turkmen, S. Aksu, and H. Altug,"Nanoparticle-based metamaterials as multiband plasmonic resonator antennas," *IEEE Trans. On Nanotech.,* vol. 11, pp. 208-212, 2012.

  - D. M. Sullivan, "Frequency-dependent FDTD methods using Z transforms," *IEEE Trans. Antennas Propagat.*, vol. 40, pp. 1223-1230, 1992.

- L. Duvillaret, F. Garet, and J. Coutaz, "A reliable method for extraction of material parameters in terahertz time-domain spectroscopy," *IEEE J. Sel. Topics Quantum Electron.*, vol. 2, pp. 739-746, 1996.

- L. Duvillaret, F. Garet, and J. L. Coutaz, "Highly precise determination of optical constants and sample thickness in terahertz Time-Domain spectroscopy," *Appl. Opt.*, vol. 38, pp. 409-415, 1999.

- T. D. Dorney, R. G. Baraniuk, and D. M. Mittleman, "Material parameter estimation with terahertz time-domain spectroscopy," *J. Opt. Soc. Am. A*, vol. 18, pp. 1562-1571, 2001.

- I. Pupeza, R. Wilk, and M. Koch, "Highly accurate optical material parameter determination with THz time-domain spectroscopy," *Opt. Express*, vol. 15, pp. 4335-4350, 2007.

- W. Withayachumnankul, G. Png, X. Yin, S. Atakaramians, I. Jones, H. Lin, S. Y. Ung, J. Balakrishnan, B. Ng, B. Ferguson, S. Mickan, B. Fischer, and D. Abbott, "T-Ray sensing and imaging," in *Proc. Of IEEE*, vol. 95, pp. 1528-1558, 2007.

- X. Chen, M. Ma, T. Ji, S. Wu, and Z. Zhu, "Optical properties of carbon materials in THz region," in Proc. of Joint 32nd International Conference on Infrared and Millimeter Waves, and the 15th International Conference on Terahertz Electronics. IRMMW-THz. 2007, pp. 550-552.

- D. Mittleman, *Sensing with Terahertz Radiation*. London: Springer, 2003, pp. 39-43

- H. Frolich, Theory of dielectrics: Dielectric constant and dielectric loss. USA: Clarendon P, 1958, pp. 98-103

- W. Zhu, C. Li, G. Zhang, and G. Fang, "The calculation of dielectric dispersive models in THz range with GA," *Microwave and Opt. Tech. Lett.*, vol. 49, pp. 2540-2545, 2007.

- P. T. Boggs and J. W. Tolle, "Sequential quadratic programming," *Acta Numerica*, vol. 4, pp. 1-51, 1995.

- M. M. Nazarov, A. P. Shkurinov, E. A. Kuleshov, V. V. Tuchin, "Terahertz time-domain spectroscopy of biological tissues," *Quantum Electron.*, vol. 38, pp. 647-654, 2008.

- J. Han, H. Xu, Z. Zhu, X. Yu, W. Li, "Terahertz spectroscopy of naphthalene, α-naphthol, β-naphthol, biphenyl and anthracene," *Chem. Phys. Lett.*, vol. 392, pp. 348-351, 2004.

- D. Grischkowsky, S. Keiding, M. van Exter, and Ch. Fattinger, "Far-infrared time-domain spectroscopy with terahertz beams of dielectrics and semiconductors," *J. Opt. Soc. Am. B*, vol. 7, pp. 2006-2015, 1990.

- M. van Exter and D. Grischkowsky, "Optical and electronic properties of doped silicon from 0.1 to 2 THz," *Appl. Phys. Lett.*, vol. 56, pp. 1694-1696, 1990.

- W. Withayachumnankul, B. M. Fischer, H. Lin, and D. Abott, "Uncertainty in terahertz time-domain spectroscopy measurement," *J. Opt. Soc. Am. B*, vol. 25, pp. 1059-1072, 2008.

- B. D. Kong, V. N. Sokolov, K. W. Kim, and R. J. Trew, "Terahertz emission mediated by surface Plasmon polaritons in doped semiconductors with surface grating," *J. Appl. Phys.*, vol. 103, p. 056101-3, 2008.

- L. Duvillaret, F. Garet, and J. Coutaz, "Influence of noise on the characterization of materials by terahertz time-domain spectroscopy," *J. Opt. Soc. Am. B*, vol. 17, pp. 452-461, 2000.

- B. E. Little, S. T. Chu, H. A. Haus, J. Foresi, and J.-P. Laine, " Microring resonator channel dropping filters," *J. Lightwave Technol.*, vol. 15, pp. 998-1005, 1997.

- F. C. Blom, D. R. Van Dijk, H. J. W. M. Hoesktra, A. Driessen, and T. J. A. Popma, "Experimental study of integrated-optics microcavity resonators: toward an all-optical switching device," *Appl. Phys. Lett.*, vol. 71, pp. 747-749, 1997.

- B. E. Little, J. S. Foresi, G. Steinmeyer, E. R. Thoen, S. T. Chu, H. A. Haus, E. P. Ippen, L. C. Kimerling, and W. Greene, "Ultra-compact Si/SiO2 microring resonator optical channel dropping filters," *IEEE Photon. Technol. Lett.*, vol. 10, pp. 549-551, 1998.

- Y. Yanagase, S. Suzuki, T. Kokubun, and S. T. Chu, "Vertical triple series-coupled microring resonator filter for passband flattening and expansion of free spectral range," *Jpn. J. Appl. Phys.*, vol. 41, pp. L141-L143, 2002.

- C. Ozturk, A. Huntington, A. Aydinli, Y. T. Byun, and N. Dagli, "Filtering characteristics of hybrid integrated polymer and compound semiconductor waveguides," *J. Lightwave Technol.*, vol. 20, pp. 1530-1536, 2002.

- C. K. Madsen and J. H. Zhao, *Optical Filter Design and Analysis: A Signal Processing Approach*. New York: Wiley, 1999.

- T. Barwicz, M. A. Popović, M. R. Watts, P. T. Rakich, E. P. Ippen, and H. I. Smith, "Fabrication of add-drop filters based on frequency matched microring resonators," *J. Lightwave Technol.*, vol. 24, pp. 2207-2218, 2006.

- F. Xia, M. Rooks, L. Sekaric, and Y. Vlasov, "Ultra-compact high order ring resonator filters using submicron silicon photonic wires for on-chip optical interconnects," *Opt. Express*, vol. 15, pp. 11934-11941, 2007.

- B. E. Little, S. T. Chu, P. P. Absil, J. V. Hryniewicz, F. G. Johnson, F. Seiferth, D. Gill, V. Van, O. King, and M. Trakalo, "Very high order microring resonator filters for WDM applications," *IEEE Photon. Technol. Lett.*, vol. 16, pp. 2263-2265, 2004.

- O. Schwelb, "Transmission, group delay, and dispersion in single-ring optical resonators and add/drop filters-a tutorial overview," *J. Lightwave Technol.*, vol. 22, pp. 1380-1394, 2004.

- A. Melloni and M. Martinelli, "Synthesis of Direct-Coupled-Resonators Bandpass Filters for WDM Systems," *J. Lightwave Technol.*, vol. 20, pp. 296-303, 2002.

- A. Melloni, "Synthesis of a parallel-coupled ring-resonator filter," *Opt. Lett.*, vol. 26, pp. 917-919, 2001.

- P. Chak and J. E. Sipe, "Minimizing finite-size effects in artificial resonance tunneling structures," *Opt. Lett.,* vol. 31, pp. 2568-2570, 2006.

- E. Dowling and D. MacFarlane, "Lightwave lattice filters for optically multiplexed communication systems," *J. Lightwave Technol.*, vol. 12, pp. 471-486, 1994.

- C. K. Madsen, "General IIR Optical Filter Design for WDM Applications Using All-Pass Filters," *J. Lightwave Technol.*, vol. 18, pp. 860-868, 2000.

- R. Orta, P. Savi, R. Tascone, and D. Trinchero, "Synthesis of multiple ring-resonator filters for optical systems," *IEEE Photon. Technol. Lett.*, vol. 7, pp. 1447-1449, 1995.

- J. K. S. Poon, J. Scheuer, S. Mookherjea, G. T. Paloczi, Y. Huang, and A. Yariv, "Matrix analysis of microring coupled-resonator optical waveguides," *Opt. Express*, vol. 12, pp. 90-103, 2004.

- B. E. Little, S. T. Chu, J. V. Hryniewicz, and P. P. Absil, "Filter synthesis for periodically coupled microring resonators," *Opt. Lett.*, vol. 25, pp. 344-346, 2000.

- C. Ferrari, F. Morichetti, and A. Melloni, "Disorder in coupled-resonator optical waveguides," *J. Opt. Soc. Am. B*, vol. 26, pp. 858-866, 2009.

- G. Matthaei, E. Jones, and L. Young, *Microwave Filters, Impedance-Matching Networks, and Coupling Structures*. Artech House Publishers, 1980.

- S. Cohn, "Direct-Coupled-Resonator Filters," *Proc. of the IRE*, vol. 45, pp. 187-196, 1957.

- Leo Young, "Direct-Coupled Cavity Filters for Wide and Narrow Bandwidths," *IEEE Trans. Microw. Theory Tech.*, vol. 11, pp. 162-178, 1963.

- L. N. Binh, N. Q. Ngo, and S. F. Luk, "Graphical representation and analysis of the Z-shaped double-coupler optical resonator," *J. Lightwave Technol.*, vol. 11, pp. 1782-1792, 1993.

- C. J. Kaalund and G.-D. Peng, "Pole-zero diagram approach to the design of ring resonator-based filters for photonic applications," *J. Lightwave Technol.*, vol. 22, pp. 1548-1559, 2004.

- S. Boyd and L. Vandenberghe, *Convex Optimization*. New York: Cambridge, 2004.

- H. Haus, *Waves and Fields in Optoelectronics*. New York: Prentice-Hall, 1984.

- Matlab, 2005. Version 7.1.

- M. A. Swillam, M. H. Bakr, and Xun Li, "The design of multilayer optical coatings using convex optimization," *J. Lightwave Technol.*, vol. 25, pp. 1078-1085, 2007.

- Sturm, J.F. Using SeDuMi 1.02, a MATLAB toolbox for optimization over symmetric cones. *Optimization Methods and Software* 1999, vol. 11, pp.625-653. Available from http://sedumi.ie.lehigh.edu/.